Détection de flux neutronique intense en vue d'applications d'astrophysique nucléaire

Vincent Lelasseux

Vincent Lelasseux. Détection de flux neutronique intense en vue d'applications d'astrophysique nucléaire. Other. Institut Polytechnique de Paris, 2022. English. NNT : 2022IPPAX092 . tel-04085190

HAL Id: tel-04085190
https://theses.hal.science/tel-04085190
Submitted on 28 Apr 2023

INSTITUT
POLYTECHNIQUE
DE PARIS

NNT : 2022IPPAX092

Thèse de doctorat

Detection of laser-driven high flux neutrons in view of nuclear astrophysical applications

Thèse de doctorat de l'Institut Polytechnique de Paris
préparée à l'École polytechnique

École doctorale n°626 École doctorale de l'Institut Polytechnique de Paris (EDIPP)
Spécialité de doctorat : Astronomie, astrophysique

Thèse présentée et soutenue à Palaiseau, le 28/09/2022, par

VINCENT LELASSEUX

Composition du Jury :

Ishay Pomerantz Professeur, Tel Aviv University	Président
Ceri Brenner Directrice de recherche, Centre for Accelerator Science	Rapporteur
Ishay Pomerantz Professeur, Tel Aviv University	Rapporteur
Satyabrata Kar Professeur, Queen's University Belfast	Examinateur
Paul McKenna Professeur, University of Strathclyde	Examinateur
Peter Thihrolf Professeur, Ludwig-Maximilians Universität München	Examinateur
Julien Fuchs Directeur de recherche, École Polytechnique	Directeur de thèse
Pär-Anders Söderström Directeur de recherche, ELI-NP	Invité

Remerciements

Je tiens par ces quelques mots plus personnels en début de manuscrit, à remercier toutes les personnes qui ont permis l'écriture de cette thèse, soit l'aboutissement non pas juste de quatre années de travail mais d'une vie entière d'étudiant. Sans la rencontre et les interactions avec toutes les différentes personnes qui vont être nommées ici, je ne serais pas la personne que je suis au moment où j'écris ces lignes.

Je vais commencer avec le commencement et sûrement les personnes les plus importantes de ces remerciements. Je tiens avant tout à remercier ma mère Nelly, mon père Philippe et mon frère Loïc, ainsi que tout le reste de ma famille, qui m'ont soutenu et me soutiennent inconditionnellement quels que soient les choix que je fais.

J'ai également une pensée pour tous les camarades de classe et les professeurs, en particulier des matières scientifiques, qui m'ont aidé à trouver et confirmer au fur et à mesure les sujets qui me passionnent le plus, que ce soit avant le baccalauréat, en école préparatoire, en école d'ingénieur ou en université. Avant d'arriver aux personnes plus liées à la thèse, je tiens particulièrement à remercier trois personnes qui m'ont fait découvrir le monde de la recherche académique et m'ont décidé à abandonner la voie de l'ingénierie pour celle de la recherche : Camille Ducoin et Olivier Stézowski puis Amel Korichi.

Concernant ces dernières années, mes premiers remerciements iront à toute l'équipe de recherche avec laquelle j'ai eu le plaisir de travailler. La première personne que je vais citer est bien évidemment Julien Fuchs. Je considère être chanceux d'avoir pu travailler et grandir en tant que scientifique sous son aile de chercheur plus qu'avisé. Je pense notamment à son dynamisme à tout épreuve qui le rend capable de mener de nombreux projets de recherches dans différents domaines en même temps qu'une vie de famille qui s'est enrichie de deux petits durant ces dernières années ! Travailler à ses côtés durant de nombreuses expériences a été des plus formateurs pour le jeune chercheur que je suis. La deuxième personne que je citerai est tout aussi évidement Alice Fazzini. Mener nos thèses en parallèle fut une véritable chance et elle a été durant toutes ces années une collègue et amie sur laquelle j'ai pu compter dans les moments joyeux comme plus difficiles. Je remercie également tous les autres membres de notre équipe de recherche qui ont toujours été très disponibles et d'excellents collègues. Je pense ici à Simon

Bolanos, Konstantin Burdonov, Emmanuel de Chefdebien, Raymond Diab, Vojtěch Horný, Yao Weipeng ainsi que Ronan Lelièvre à qui je souhaite toute la réussite durant sa propre thèse.

Je tiens maintenant à remercier les chercheurs hors du LULI qui m'ont grandement aidé pour la conception du détecteur de neutron tout au long de la thèse. Je remercie particulièrement Pär-Anders Söderström qui, en plus d'être membre invité du jury de thèse, fut d'une aide incroyale, ainsi que Soichiro Aogaki, Mirella Cerchez, Claude Deutsch, Marius Gugiu, Cătălin Matei, Florin Negoita, Sergey Pikuz, Florin Rotaru and Oswald Willi.

Je remercie aussi l'ensemble du LULI, le laboratoire de recherche qui m'a accueilli durant ces quatre dernières années. Je pense notamment à Patrick Audebert, directeur du laboratoire, Sébastien LePape, directeur adjoint, Elodie, Elorri, Myriam et Virginie pour leur aide avec l'administratif, Anthony, Cyril, Doina, Émilie, Fabien, Franck, Jacques, Jordan, Joseph, Loïc, Olivier et Yohann, qui permettent au LULI2000 d'être une installation où il est agréable de faire des expériences, Ambra, Bruno, Claude-Alban, Frédéric, Gabriel, Hanna, Isabeau, Jean-Raphael, Livia, Malkiel, Michel, Mickael, Paul, Pierre, Sophie, Thibault, Tommaso and Yannis, avec qui ce fut toujours un plaisir de discuter autour d'un repas ou d'un café. Merci spécialement à Sandra Dorard et Frederick Lefèvre sans qui les différentes expériences auraient été beaucoup plus compliquées à préparer.

Je pense également à tous ceux avec qui j'ai pu travailler durant les nombreuses expériences que ce soit au LULI2000, à Apollon ou dans les différentes installations à l'étranger. La liste est bien trop longue et je demande pardon à ceux que j'oublierais de citer ici mais mes sincères remerciements, en plus de ceux que j'ai déjà cités, à Adam, Amina, Guilhem, Jérôme, Maxence, Stanimir, ...

Puisqu'il y a quelques moments ces quatre dernières années durant lesquelles je n'ai pas travaillé, je remercie aussi tous ceux qui m'ont soutenu en dehors du travail à savoir les meilleurs amis du monde Marinne, Lucas, Sébastien, Baptiste, Vincent, ..., la fanfare CUC, et enfin le meilleur colloc Lucas.

Finalement, je tiens aussi à remercier ceux qui ont été là pour la dernière étape de cette thèse, qui ont pris le temps de lire l'entièreté de la thèse, ont participé à la soutenance et posé des questions fort intéressantes. Merci donc aux rapporteurs Ceri Brenner et Ishay Pomerantz ainsi qu'aux examinateurs Satyabrata Kar, Paul McKenna et Peter Thirolf. Enfin, merci à tous ceux qui prendront le temps de lire cette thèse, en espérant que son contenu vous intéressera et aidera.

Acknoledgments

I would like with these few more personal words at the beginning of the manuscript, to thank all the people who have made it possible for me to write this thesis, which is the culmination not just of four years of work but of an entire life as a student. Without meeting and interacting with all the different people who are going to be named here, I wouldn't be the person I am as I write these lines.

I will start with the beginning and surely the most important people of these thanks. Above all, I would like to thank my mother Nelly, my father Philippe and my brother Loïc, as well as all the rest of my family, who supported me and support me unconditionally whatever choices I make.

I also have a thought for all the classmates and teachers, especially science subjects, who helped me find and confirm as I went along the subjects that fascinate me the most, whether before the baccalaureate , preparatory school, engineering school or university. Before getting to the people more related to the thesis, I would particularly like to thank three people who introduced me to the world of academic research and made me decide to abandon the path of engineering for that of research: Camille Ducoin and Olivier Stézowski then Amel Korichi.

Concerning these last years, my first thanks will go to all the research team with whom I had the pleasure of working. The first person I will quote is obviously Julien Fuchs. I consider myself lucky to have been able to work and grow as a scientist under his wise researcher wing. I am thinking in particular of his unfailing dynamism which makes him capable of carrying out numerous research projects in different fields and at the same time have a family life which has been enriched by two little ones in recent years! Working alongside him during many experiments has been most formative for the young researcher that I am. The second person I will quote is just as obviously Alice Fazzini. Carrying out our theses in parallel was a real blessing and during all these years she has been a colleague and friend on whom I could count in happy and difficult times. I also thank all the other members of our research team who have always been very reliable and excellent colleagues. I am thinking here of Simon Bolanos, Konstantin Burdonov, Emmanuel de Chefdebien, Raymond Diab, Vojtěch Horný, Yao Weipeng as well as Ronan Lelièvre to whom I wish every success during his own thesis.

I would now like to thank the researchers outside LULI who greatly helped me with the design of the neutron detector throughout the thesis. I particularly thank Pär-Anders Söderström who, in addition to being a guest member of the thesis jury, was incredibly helpful, as well as Soichiro Aogaki, Mirella Cerchez, Claude Deutsch, Marius Gugiu, Cătălin Matei, Florin Negoita, Sergey Pikuz, Florin Rotaru and Oswald Willi.

I would also like to thank all of LULI, the research laboratory that has hosted me over the past four years. I am thinking in particular of Patrick Audebert, laboratory director, Sébastien LePape, deputy director, Elodie, Elorri, Myriam and Virginie for their help with administration, Anthony, Cyril, Doina, Émilie, Fabien, Franck, Jacques, Jordan, Joseph, Loïc, Olivier and Yohann, who allow the LULI2000 to be an installation where it is very pleasant to experiment, Ambra, Bruno, Claude-Alban, Frédéric, Gabriel, Hanna, Isabeau, Jean-Raphael, Livia, Malkiel, Michel, Mickael, Paul, Pierre, Sophie, Thibault, Tommaso and Yannis, with whom it was always a pleasure to chat over a meal or a coffee. Special thanks to Sandra Dorard and Frederick Lefèvre without whom the various experiments would have been much more complicated to prepare.

I am also thinking of all those with whom I was able to work during the numerous experiences whether at LULI2000, at Apollon or in the various installations abroad. The list is far too long and I apologize to those I forgot to mention here but my sincere thanks, in addition to those I have already mentioned, to Adam, Amina, Guilhem, Jérôme, Maxence, Stanimir, ...

Since there have been a few moments in the last four years during which I have not worked, I would also like to thank all those who have supported me outside of work, namely the best friends in the world Marinne, Lucas, Sébastien, Baptiste, Vincent, ..., the CUC brass band, and finally the best flatmate Lucas.

Finally, I would also like to thank those who were there for the last stage of this thesis, who took the time to read the entire thesis, participated in the defense and asked very interesting questions. Thanks therefore to the rapporteurs Ceri Brenner and Ishay Pomerantz and to the reviewers Satyabrata Kar, Paul McKenna and Peter Thirolf. Finally, thank you to all those who will take the time to read this thesis, hoping that its content will interest and help you.

Résumé

Le développement de diagnostics pour la physique nucléaire dans le cadre d'expériences avec des lasers de haute intensité est de prime importance pour explorer les possibilités offertes par les nouvelles et futures installations repoussant les limites d'intensité, qu'elles soient en France, en Europe ou ailleurs dans le monde. Cette thèse s'intéresse en particulier au développement de diagnostics neutron dans le contexte de travaux d'astrophysique nucléaire. En effet, nous avons durant celle-ci développé un compteur de neutrons à partir de pièces disponibles dans le commerce, ainsi que tous les scripts et simulations nécessaires pour définir quantitativement une émission de neutron durant une expérience. Nous avons également débuté le développement d'un détecteur de neutron à temps de vol pour mesurer les spectres d'énergie des neutrons émis. Ce second détecteur peut également être utilisé en tant que compteur grâce aux épais murs de béton présents autour des chambres expérimentales dans la plupart des installations.

Dans un premier chapitre, nous allons présenter les différentes notions nécessaires à la compréhension des mécanismes de production de protons et neutrons dans les installations laser de haute intensité. Nous aborderons également des éléments d'astrophysique nucléaire. Nous présenterons les grands principes de la nucléosynthèse en nous attardant plus spécifiquement sur le processus r pour ensuite montrer en quoi les lasers de haute intensité sont des outils intéressants pour son étude.

Le deuxième chapitre est quant à lui consacré à la conception d'un compteur de neutrons à haute efficacité adapté au voisinage de lasers de haute intensité, depuis les concepts utilisés jusqu'à sa construction et sa calibration. Ainsi, nous montrerons quelles solutions nous avons trouvées pour pouvoir utiliser des éléments disponibles dans le commerce pour construire un détecteur capable de supporter les conditions d'une salle d'expérience utilisant des lasers de haute intensité. Nous verrons également la mise au point d'un prototype et les tests que nous avons menés sur celui-ci, avec des sources radioactives et durant des expériences utilisant des lasers, afin de valider nos concepts. Nous présenterons les simulations Geant4 que nous avons menées pour mieux comprendre notre détecteur et optimiser ses dimensions. Enfin, nous expliciterons comment nous avons calibré le détecteur juste construit, en utilisant des sources de gammas et de neutrons, et en développant des scripts adaptés à l'analyse de ces données

de calibration.

Le troisième chapitre présente la première expérience durant laquelle nous avons utilisé le détecteur de neutrons développé durant le chapitre 2. Cette expérience a eu lieu au LULI2000 et les conditions excédaient sur certains points ce pour quoi le détecteur a été conçu, à savoir des expériences sur des installations type Apollon. Ainsi, le bruit a été un réel problème durant cette expérience mais nous avons tout de même pu démontrer que ce détecteur était capable de détecter et compter des neutrons durant des tirs haute intensité avec des impulsions picoseconde. En effet, les résultats obtenus par certaines unités du détecteur, qui correspondent par ailleurs aux résultats statistiques les plus forts, donnent des nombres de neutrons produits dans l'ordre de grandeur de ce qui était attendu. Nous avons également pu montrer que moins de neutrons étaient émis, ou du moins détectés, durant les tirs durant lesquels la cible secondaire était chauffée par une impulsion laser nanoseconde. Malgré plusieurs tentatives qui seront aussi exposées, l'importance de cette diminution n'est pas encore bien expliquée.

Le quatrième et dernier chapitre explique comment nous avons pu profiter de la mise en service de la salle SFA de l'installation Apollon pour utiliser certaines parties du détecteur développé précédemment pour les utiliser à la fois en tant que diagnostic neutron de temps de vol, ainsi qu'en tant que simple compteur. Nous verrons que, durant cette mise en service, nous n'avons été capable de caractériser que partiellement le faisceau de neutrons produit. En effet, les résultats obtenus en utilisant le détecteur en tant que compteur correspondent parfaitement aux attentes et ces résultats et la façon de les obtenir seront donc présentés. Cependant, les mesures réalisées sur la partie temps de vol durant cette campagne expérimentale ne sont pas satisfaisants. Nous présenterons par conséquent des tests réalisés a posteriori pour mieux comprendre le fonctionnement et les limites du détecteur dans ce mode de fonctionnement, ainsi que différentes solutions qui peuvent être mises en place pour pallier ces limitations. Enfin, une dernière partie montre différentes techniques appliquées infructueusement aux données obtenues durant la campagne expérimentale, pour essayer d'extraire des résultats sur la partie temps de vol malgré l'influence nocive des différentes émissions d'ondes lors des tirs laser sur notre détecteur.

Acronyms

MASER Microwave Amplification by Stimulated Emission of Radiation

LASER Light Amplification by Stimulated Emission of Radiation

CPA Chirped Pulse Amplification

OPA Optical Parametric Amplification

OPCPA Optical Parametric Chirped Pulse Amplification

TNSA Target Normal Sheath Acceleration

RPA Radiation Pressure Acceleration

CSA Collisionless Shock Acceleration

BOA Break Out Afterburner

PIC Particle-In-Cell

IRF Instantaneous Rest Frame

LS Light Sail

AGB Asymptotic Giant Branch

LANSCE Los Alamos Neutron Scattering Center

PIC Particle In Cell

PMTs PhotoMultiplier Tubes

PVT PolyVinylToluene

PS PolyStyrene

FRET Fluorescence Resonance Energy Transfer

EMP ElectroMagnetic Pulse

HDPE High Density PolyEthylen

TCC Target Chamber Center

HPGe High Purity Germanium

FWHM Full Width at Half Maximum

SHV Safe High Voltage

PCIe Peripheral Component Interconnect express

LEMO LEon MOuttet

FSSR Focusing Spectrometer with Spatial Resolution

IP Image Plate

RCF RadioChromic Films

PSL PhotoStimulated Luminescence

Contents

Introduction

The goal of this thesis is to develop neutron detection tools adapted to the high intensity laser environment. We will present in a first time the global context in which this thesis is taking place. In a second time, we will talk about the organisation of this manuscript and the objectives it tries to answer to.

Context

With the development of multi-PW lasers, such as Apollon or ELI-NP, the particle beams which can be produced by condensing light on a target reach new milestones. In particular, the proton and/or neutron beams those facilities will be able to produce should not only have characteristics interesting enough to challenge the well established particle accelerators but also to allow nuclear experimental physics capabilities able to study problems of nuclear physics which cannot be addressed in those conventional facilities.

To produce proton beams, the experimental teams working on laser facilities with intensities up to the PW usually use a very well known process called TNSA (1) to produce pulsed protons beams of typically up to 10^{13-14} particles. These have a 100 % spread spectrum with maximum energies up to a few tens of MeV. They are generated using typically laser pulses from a few tens of fs to 1 ps duration. According to simulations and some preparatory experiments (2), the advent of multi-PW lasers should allow the use of some other processes which could unlock the production of proton beams with maximum energies up to several hundreds of MeV, and also with the potential of a narrow energy spectrum.

Besides the interest of this type of source alone for experimental nuclear physics, producing protons with such high energies would allow the use of a very efficient neutron producing process, the spallation (3). Indeed, such facilities should be the place of production of neutron beams with unprecedented peak intensity, i.e. in the order of 10^{23} neutrons.cm^{-2}.s^{-1} (4), at a shooting rate of typically one shot per minute for most of the incoming facilities, which would allow experiment with significant statistic to work with.

Those new particle sources would be available in addition to the other possible uses a laser source can have, i.e. the production of electron beams, the use of part of the beams in several diagnostics, the possibility to produce several particle beams in any imaginable direction by using several laser arms, or simply the possibility to heat, ionize, or pressure secondary targets. Such commodities are indeed easy to implement at a laser facility when it can be complicated with a particle accelerating facility and could be of prime interest for various nuclear physics experiments.

The availability of those intense neutron sources could in turn allow the study of nuclides hardly reachable by the existing facilities. In particular, there is a nucleosynthesis process, the r-process, taking place far on the neutron-rich side of the nuclide map and for which experimental data to feed the models are nowadays extremely difficult if not impossible to get. Such neutron sources thanks to their unique peak intensities, could then help study nuclides nearer the r-process path (5; 6).

On the downside, the high intensity laser environment is a peculiar environment, very different from what nuclear physics experimenters are used to, especially in terms of noise level. Indeed, the production of a proton beam, by shooting on a target with a laser pulse, is always accompanied by the generation of a lot of others particles and waves. The two especially problematic productions for electronic diagnostics are the production of x-ray and gammas which can saturate diagnostics aimed to detect other type of particles, and the production of a powerful electromagnetic pulse which tends to shut down any electronic devices if those devices are not protected adequately.

In order to characterize the beams produced at those new facilities and perform measurements specific to nuclear experimental physics, we need diagnostics which can stand a repetition rate of one shot per minute, and which can still operate under the harsh conditions reigning in the experimental area during a shot. Due to the relative youth of nuclear experimental physics using high intensity lasers, detectors adapted to this field are still to be conceived and commissioned. It is in this context that we developed during this thesis neutron diagnostics adapted to the high intensity laser environment.

Manuscript plan

The first chapter presents the scientific context in which this thesis took place, and some of the theory needed to understand the following chapters. It starts with an history of the laser intensity progression and a state of the art of current facilities. It explains then proton acceleration through the most well known TNSA process but also exposes some of the others processes proposed and experimentally tested at high laser intensities. It subsequently presents neutron acceleration using the accelerated protons, through two families of process, the nuclear reactions and the spallation, and their application to the high intensity laser context.

Afterward, we present the astrophysical context in which the laser-drive neutron beams would be of interest. Here, we present the nucleosynthesis processes, and especially the r-process and explain through which aspect and to which extent those incoming neutron beams would experimentally be useful. We also talk about the use of neutron beams in another type of diagnostic which is the thermometry of warm dense matter using neutron resonance spectroscopy.

In a second chapter, we go through the different phases of conception of the high efficiency neutron counter we developed during this thesis. We explain the three main concepts behind the functioning of our detector, which are :

- the physic of scintillators which transform a part of an energy deposition into visible light which can be collected by photomultipliers and turned into an electronic signal,
- the boron loading of those scintillators to exploit an exothermic neutron capture reaction and focus the detection on the neutron and not on any energy deposing particle that goes through the scintillators,
- and the use of the thermalization to both increase the detection efficiency by increasing the neutron capture rate, and delay a part of the detection enough for the detector not to be affected anymore by the consequences of the laser shot other than the neutron production.

It also here that we present the Geant 4 (7) simulations used to dimension the whole detector array. A following section is dedicated to the preliminary tests we run on a prototype before building the whole detector and calibrate it both in energy and efficiency, which is the topic of the last section. The calibration part also presents the basis of the data analysis when using a scintillator/PMTs assembly technology.

The third chapter is dedicated to the experiment during which the commissioning of the neutron detector, built in the previous chapter, took place at the LULI2000 facility. We first explain the scientific motivation behind this experiment, apart from the detector commissioning, i.e. to measure a (p,n) reaction cross section depending on the target being whether in a solid state or in a plasma state. This implies some theory on how a cross section is measured experimentally and the effect of the electron cloud surrounding the nucleus on this measurements. We then detail the full design of the experiment at the LULI2000 facility, including that of the experimental setup, as well as of all the simulations and calculations done to prepare the experiment.

We finally present the data obtained during the experiment which is overwhelmingly polluted by the noise induced by the laser, and the saturation it induces on the PMTs. We also explain how we nonetheless managed to analyze those data and we especially emphasize on the strategies employed to counter the noise present in the traces obtained during the experiment, and the unresponsiveness induced by the PMT saturation after the gamma flash and by the electromagnetic pulse. We finally present the results we obtained in terms of neutron production and try to explain it with different explanations, although it still remains inconclusive.

In the fourth and last chapter, we detailed how we took advantage of the Short Focal Area (SFA) commissioning campaign at the Apollon facility to try and use parts of the detector previously built. The aim was here to use them as a neutron Time-Of-Flight (nToF) detector besides their counting ability. We first recall the present and future capacities of the Apollon facility and the design of the commissioning experiment with its numerous diagnostics in place. In the next section, we concentrate on the configuration of the neutron detectors as well as on preparatory calculations done to study what measurement we could expect. Another part of the section is dedicated to the calibration of those detector units, which is a bit different from the one applied to the neutron counter since those units are designed to work both as nToF units and counters.

The analysis of the Apollon data presented in the last section is divided in three different steps. The first one is dedicated to the counting measurements, performed using Geant4 simulations, and which give satisfactory results. The second one studies the PMT saturation thanks to the experimental data and additional tests run afterward, and propose some improvements done after the experiment or still to be done. The third and last one shows an unsuccessful attempt to retrieve exploitable data despite the saturation of the PMT due to the gamma flash.

Chapter 1

Context and theory

In this chapter, we will first present the state of the art of what is possible in terms of particle beam production using intense lasers, nowadays and in the near future. Then we will present some possible applications, especially in the astrophysical context.

1.1 Elements of high-intensity laser physics

1.1.1 Laser intensity progression

Described in 1917 by Albert Einstein, the stimulated emission principle has only been used experimentally for the first time in 1953 in a device based on Microwave Amplification by Stimulated Emission of Radiation (MASER) that was developped by Charles Townes, James P. Gordon and Herbert Zeiger(8). In the optical range, the first so-called Light Amplification by Stimulated Emission of Radiation (LASER) device has been put together by Theodore H. Maiman(9) and less than one year later, the first helium-neon laser was constructed by Ali Javan, William R. Bennett and Donald Herriott(10). From this point, this technology has constantly been improved to reach higher energies, shorter timescales and brighter intensities, as it can be seen in Fig.1.1.

Early techniques such as Q-switching or mode-locking allowed the laser to quickly reach a power around the MW. Energy densities were then reaching the limits of what the amplification media could endure. In 1985, Donna Strickland and Gerard Mourou found out about a technique used by radar scientists(12) and decided to adapt it to the light amplification domain(13). This technique now called Chirped Pulse Amplification (CPA), allowed to resolve the energy density issue and to keep the intensities going higher and higher. This method, presented in a schematic in Fig.1.2, consists in temporally stretching an initial short pulse produced by an oscillator. This is done by delaying the different parts of

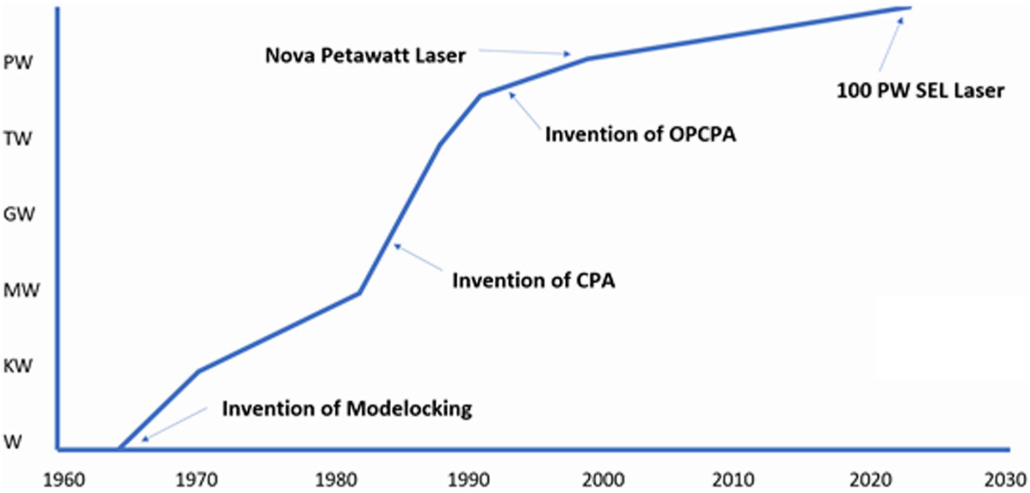

Figure 1.1: *Evolution of the maximum laser intensity around the world since its invention*(11)

its spectrum using usually gratings. The temporally larger pulse can then be amplified without reaching energy densities that would cause damages to the amplification medium. Finally, using a symmetric gratings system, the pulse can be temporally shortened to reach higher intensities.

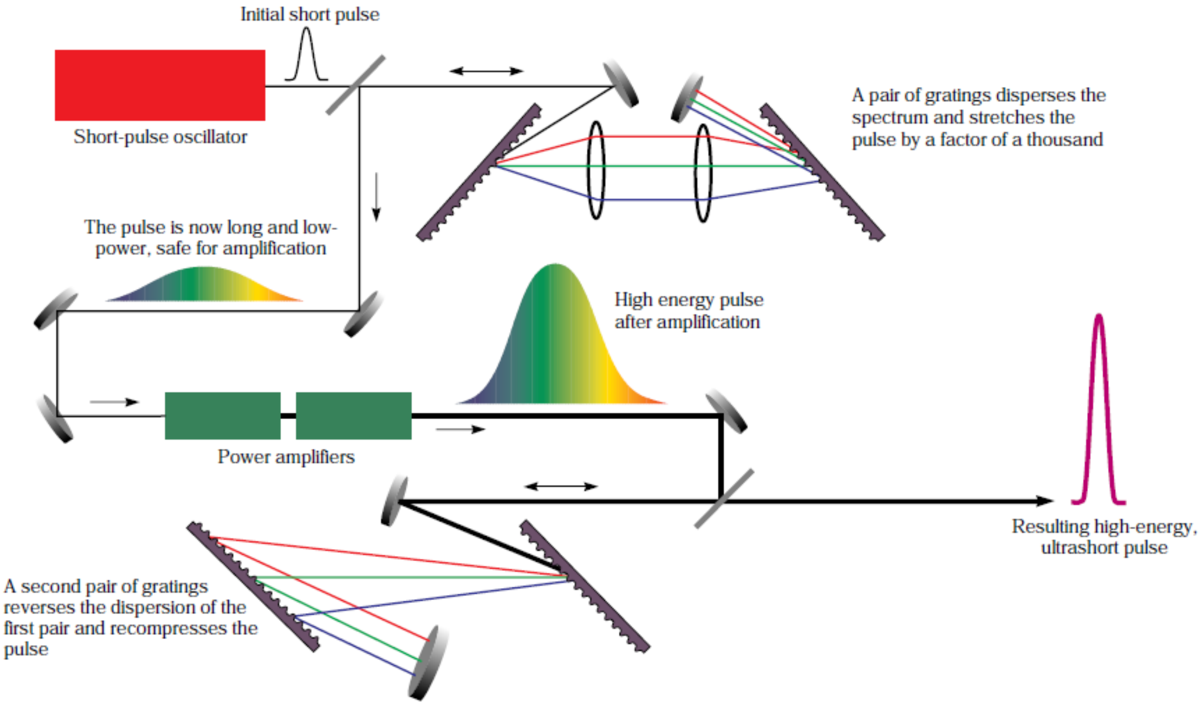

Figure 1.2: *Schematic of the CPA principle*(14)

In addition to this, there is another technique which can be combined efficiently with CPA. The Optical Parametric Amplification (OPA) is an amplification mechanism which doesn't rely on the population inversion of a medium but on nonlinear processes (15). In a nonlinear crystal material such as

Laser	Laboratory	Power	Energy	Pulse width	Amplifier crystal
NIF	LLNL	0.6 PW	1.8 MJ	3 ns	Nd:glass
NIF ARC	LLNL	0.5 PW	0.4-1.7 kJ	1.3-38 ps	Nd:glass
Titan	LLNL	0.4 PW	300 J	0.7 ps	Nd:glass
OMEGA EP	LLE	0.7 PW	0.5-2.3 kJ	0.7-100 ps	Nd:glass
Beamlet	SNL	1 PW	500 J	500 fs	Nd:glass
ALEPH	CSU	0.85 PW	10-26 J	30-45 fs	Ti:sapphire
Bella	LBNL	1.3 PW	40 J	30 fs	Ti:sapphire
Hercules	CUOS	0.5 PW	15 J	30 fs	Ti:sapphire
Diocles	UNL	0.7 PW	20 J	30 fs	Ti:sapphire
Texas PW	UTA	1.1 PW	155 J	140 fs	Ti:sapphire
Scarlet	OSU	0.4 PW	10 J	30 fs	Ti:sapphire
ALLS	UQ	0.5 PW	10 J	20 fs	Ti:sapphire

Table 1.1: *Overview of the PW laser facilities around the world (North America)(11)*

lithium niobate ($LiNbO_3$) or lithium triborate (LiB_3O_5), where two pulses with different frequencies ω_1 and ω_2, and which we will call respectively signal pulse and pump pulse, are injected, it is possible for some photons of the pump pulse to be converted into a photon with the frequency of the signal pulse and a so-called idler photon with a frequency $\omega_3 = \omega_2 - \omega_1$. In the end, the signal pulse has then been amplified. This technique has some advantages such as a very high gain per pass or the possibility to work over very large bandwidth. As long as the resulting idler pulse doesn't deposit its energy in the nonlinear crystal, there are also way less thermal effects since there is no population inversion. However, for this technique to work, the pump pulse needs to match precise requirements. Among them, since no energy is stored in the crystal with this technique, the pump pulse and the signal pulse need to be overlapping temporally which, can be difficult for ultra-short pulses. Since, in CPA, the pulses are temporally widened and have usually large bandwidth, those two techniques match very well. The fusion of these two techniques gave birth to the Optical Parametric Chirped Pulse Amplification (OPCPA) technique(16).

Nowadays, the highest intensity facilities use hybrid systems with a first stage using OPCPA and a last stage using conventional CPA with large bandwidth amplifier such as Ti:sapphire crystals(17). Indeed, energetically speaking, the OPCPA method is not as efficient as using classic amplifiers. So when it comes to the last stages, the difference matters. Besides, it also becomes very complicated to produce a pump beam with all the requirements needed for OPA at such levels of energy.

If we take a look at the existing and upcoming facilities around the world, there are several facilities with at least 1 PW laser as seen in Tables.1.1, 1.2 and 1.3, and some 10 PW or even higher will be available soon(11). It is also interesting to see that the most widespread technology is to use Ti:sapphire for the last amplifier stage. It is especially true for the commercial solutions installed by Thales or Amplitude Technologies(11). Another type of crystal often used in the last classic CPA stage is Nd:glass, especially

Laser	Laboratory	Power	Energy	Pulse width	Amplifier crystal
Vulcan PW	RAL	1 PW	500 J	500 fs	Nd:glass
Gemini	RAL	1 PW	30 J	30 fs	Ti:sapphire
Orion	AWE	1 PW	500 J	500 fs	Ti:sapphire
TARANIS	QUB	0.3 PW	3 J	10 fs	Nd:glass
SCAPA	US	0.35 PW	8.75 J	25 fs	Ti:sapphire
LMJ	CESTA	0.4 PW	1.4 MJ	3.5 ns	Nd:glass
PETAL	CESTA	1.15 PW	850 J	700 fs	Nd:glass
PHELIX	GSI	1 PW	400 J	400 fs	Nd:glass
Jeti200	Jena	0.3 PW	5.6 J	17 fs	Ti:sapphire
HI-BEF	XFEL	0.3 PW	8 J	25 fs	Ti:sapphire
PEARL	RAS	0.56 PW	24 J	43 fs	DKDP
FEMTA	RFNC	1 PW	100 J	100 fs	DKDP
VEGA	CLPU	1 PW	30 J	30 fs	Ti:sapphire
L3 HAPLS	ELI-BL	1 PW	30 J	30 fs	Ti:sapphire
HPLS	ELI-NP	10 PW	244 J	24 fs	Ti:sapphire

Table 1.2: *Overview of the PW laser facilities around the world (Europe) (11)*

Laser	Laboratory	Power	Energy	Pulse width	Amplifier crystal
SG-II	SIOM	5 PW	150 J	30 fs	KDP
Qiangguang	SIOM	2 PW	52 J	26 fs	Ti:sapphire
	SIOM	1 PW	32 J	32 fs	LBO
XG-III	LFRC	0.75 PW	20 J	26.8 fs	Ti:sapphire
SG-IV	LFRC	0.5 PW	1.5 MJ	3 ns	Nd:glass
CAEP-PW	Mianyang	4.9 PW	91.1 J	18.6 fs	LBO
XL-III	IOP	1.16 PW	32 J	28 fs	Ti:sapphire
LFEX	ILE	2 PW	2 kJ	1 ps	Nd:glass
J-KAREN	KPSI	0.85 PW	28.4 J	33 fs	Ti:sapphire
HERMES	SACLA	0.5 PW	12.5 J	25 fs	Ti:sapphire
	CoReLS	4.2 PW	83 J	19.4 fs	Ti:sapphire
EXLS	ETRI	1.4 PW	31 J	22 fs	Ti:sapphire
	RRCAT	1 PW	25 J	25 fs	Ti:sapphire

Table 1.3: *Overview of the PW laser facilities around the world (Asia) (11)*

for highest energy facilities. We can also see that there are some facilities having PW class laser using only OPCPA with KDP or LBO crystals. One of the main noticeable aspect of this overview is that the number of facilities having PW class laser is pretty important. Hence such intensities become available to an increasing number of scientists to experiment with.

1.1.2 Proton acceleration

Those intense lasers can have many applications. A very active research field is for instance the use of such pulses to produce electron beams using laser wakefield acceleration(18; 19; 20; 21; 22; 23). More in our interest is the possibility to accelerate ions, especially protons. This possibility has been demonstrated experimentally as soon as 1999 by researchers working with the VULCAN laser with intensities on target around 5.10^{19} W.cm^2(24). This result was quickly reproduced by a team of the Lawrence Livermore National Laboratory with intensities on target even higher(25). However, the physics behind those accelerated particles has been subject to a scientific debate during almost a decade.

This debate finds its roots in the fact that there are several complex phenomena leading to this acceleration. It is nowadays better understood, and we know that several different processes can compete depending on the laser intensity, the thickness target and some other parameters. The scientific consensus nowadays is that there are four main processes that can lead to proton or ion acceleration(26):

- the Target Normal Sheath Acceleration (TNSA),
- the Radiation Pressure Acceleration (RPA),
- the Collisionless Shock Acceleration (CSA),
- and the Break Out Afterburner (BOA).

Depending on the laser-matter interaction conditions, those processes can coexist and there is no clear boundary between two regions where different processes dominate. We will here present those different processes and the experimental conditions needed for them to take place.

Target Normal Sheath Acceleration

The most commonly used process to accelerate protons nowadays is TNSA. To do so, targets with thicknesses from a few microns to a few tens of microns are usually irradiated with pulses of intensity of at least 10^{18} W.cm^{-2}. At such high intensities for the main pulse, we have to consider some parasitic laser light which comes before the main pulse, such as amplified spontaneous emission or the increasing intensity laser light coming in front of the main pulse for at least hundreds of picoseconds, called prepulse, and which can play a major role in the laser target dynamics. Indeed, those light emissions coming ahead of the main pulse on the target are enough to ionize the front side of the target and create a plasma in front of it. Hence, when the main pulse arrives, the target is actually a solid target with a plasma cloud in front of it, which is called preplasma.

This preplasma has some time to expand from the target front surface, then its density increases the nearer we are from the target surface. When the main pulse arrives, it will propagate inside this preplasma until it reaches the surface from where it can no longer propagate, i.e. the surface where the electron density is equal to the critical density :

$$n_e = n_c = \frac{\gamma_e m_e 4\pi^2}{\mu_0 e^2 \lambda^2} \tag{1.1}$$

Where n_e is the electron density, n_c the critical density, γ_e is the Lorentz factor of the electrons, m_e the electron mass, μ_0 the permeability of free space, e the electron charge and λ the laser wavelength. In this region, simulations(27) have shown that, twice every laser period, the ponderomotive force accelerates batches of electrons to create a hot electrons population which has roughly a Boltzmann distribution with a temperature constant equal to :

$$k_B T_{hot} = m_e c^2 \left(\sqrt{1 + \frac{I\lambda}{1.37 \times 10^{18}}} - 1 \right) \tag{1.2}$$

Where c is the speed of light, I the laser intensity in W.cm^{-2} and λ the laser wavelength in μm. A lot of work has been done to characterize this hot electrons population with different, more or less refined, laws describing it(27; 28; 29; 30; 31). Absorbed laser energy is mainly sent in the production of those energetic electrons and the laser absorption can go as high as 60% with a laser normal incidence and even 90% if the laser incidence is 45°(32). Those bunches of hot electrons are sent in the target mainly in the target normal direction even if the laser pulse comes with an angle on the target(33). However, depending on the plasma conditions, this direction can vary quite a lot(34).

Then, two different effects have opposite influences on this hot electron beam(35). On one side, since this current exceeds the Alfvén limit by several orders of magnitude, the self-generated magnetic field tends to bend the electron toward the source. On the other side, scattering tends to broaden this flow of electrons. Even though it is still an active field of research, it seems that the magnetic effect is preponderant on the first 10 to 20 μm where the shockwave caused by the laser interaction has partly ionized the target, and that scattering is preponderant further away in the target, as shown in Fig.1.3. It is also important to notice that this hot electrons journey induces a return current which depends on the target material properties and which is primordial for the hot electrons not to be completely stopped by the electric field they would create without it(36).

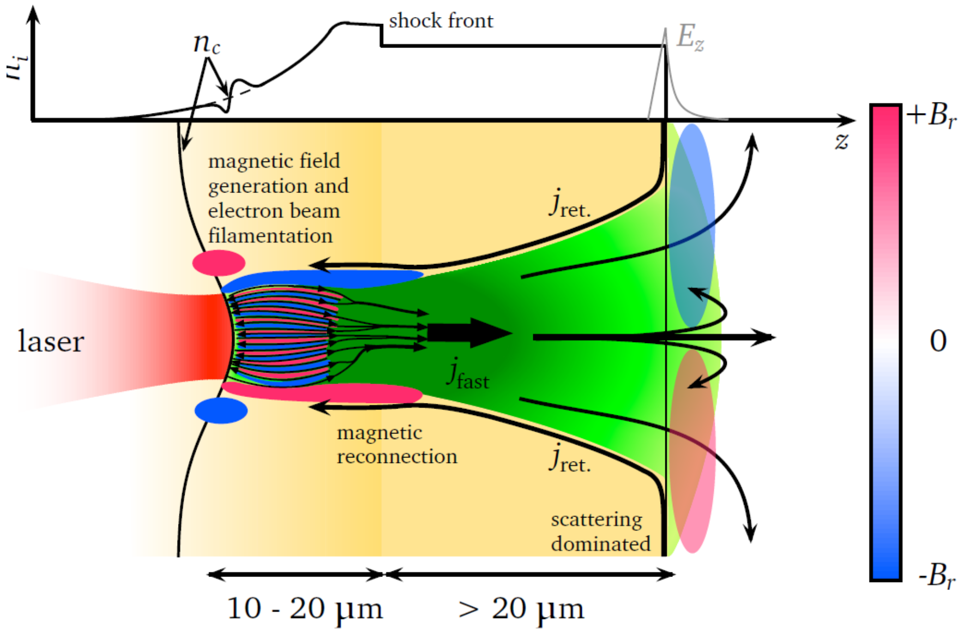

Figure 1.3: View of the main processes happening during the hot electrons transport through the target during TNSA(35)

Finally, the hot electrons population reaches the rear side of the target and approximately 4% of it goes into the vacuum(37). It will creates on this side an electric field which is analytically calculable with some assumptions. First we can assume that all the hot electrons generated on the front side reached the rear side. This gives a total number of hot electrons and an overall electron density on the rear side respectively equal to(38) :

$$n_0 = \frac{\eta E_L}{c\tau_L \pi r_0^2 k_B T_{hot}} \tag{1.3}$$

$$n_{e,0} = \frac{r_0^2}{(r_0 + d\tan\frac{\theta}{2})^2} n_0 \tag{1.4}$$

Where n_0 is the total number of hot electrons, η the fraction of laser energy converted into hot electrons kinetic energy, E_L the laser energy, τ_L the laser pulse temporal length, r_0 the focal spot radius, and $n_{e,0}$ is the electronic density on the rear side integrated along the target normal axis, d the target thickness and θ the angular broadening of the electron beam. In one dimension, Poisson's equation and the electronic Boltzmann distribution gives then(39) :

$$\epsilon_0 \frac{\partial^2 \Phi}{\partial z^2} = e n_e(z) = e n_{e,0} \exp\left(\frac{e\Phi(z)}{k_B T_{hot}}\right) \tag{1.5}$$

Where ϵ_0 is the permittivity of free space, Φ the electric potential and n_e the electronic density. Using the conditions $\Phi(0) = 0$ and $\partial\Phi/\partial z \to 0$ when $z \to +\infty$, it is possible to solve Eq.1.5. The electric potential and electric field are then given by :

$$\Phi(z) = -\frac{2k_B T_{hot}}{e} \ln\left(1 + \frac{z}{\sqrt{2}\lambda_D}\right) \tag{1.6}$$

$$E(z) = \frac{2k_B T_{hot}}{e} \frac{1}{z + \sqrt{2}\lambda_D} \tag{1.7}$$

$$\lambda_D = \sqrt{\frac{\epsilon_0 k_B T_{hot}}{e^2 n_{e,0}}} \tag{1.8}$$

Where λ_D is the Debye length. What is of particular interest here is the maximum value the electric field reaches for $z = 0$. Numerical applications for standard cases give an electric field on the rear side of the target that is less than one order of magnitude lower than the laser electric field. This electric field is actually of the order of TV.m^{-1}. This value is way higher than the ionization threshold of any atom. Atoms on the rear side of the target are then instantly ionized as soon as the hot electrons reach the vacuum boundary. The ions created are then accelerated by the very same electric field they have been ionized by. On the contrary, a part of the electrons sent in the vacuum are stopped by this electric field and sent back in the target.

Now that we have described the instant the electrons reached the vacuum, the evolution of the resulting plasma is a bit more complicated to describe. In most of the works on this subject(35), the expansion of this initial plasma is seen as an isothermal expansion and then, quasi-neutrality and a constant temperature are assumed. Besides, even though those models are one-dimensional and experiments have clearly shown that TNSA is at least a two-dimensional process, it successfully explains experimental data from several facilities(38). A simulation and theoretical work on this subject has been done by Mora(39; 40; 41). An interesting feature of this model is that it gives the electrons and ions population kinetic behaviour at any time as shown in Fig.1.4, and especially we can have analytically the maximum ion kinetic energy at any time :

$$E_{max}(\tau) = 2Zk_B T_{hot} \ln^2\left(\tau + \sqrt{1+\tau^2}\right) \tag{1.9}$$

$$\tau = \frac{\omega_{pi} t}{\sqrt{2\exp(1)}} = \frac{t}{\sqrt{2\exp(1)}} \sqrt{\frac{n_{e,0} Z e^2}{m_i \epsilon_0}} \tag{1.10}$$

Where E_{max} is the maximum ion energy, ω_{pi} the ion plasma frequency, Z the ion charge number and m_i the ion mass. With Fig.1.4, Mora gives also standard numerical values for some parameters. Indeed, standard values can be $n_{e,0} = 10^{19}$ cm^{-3}, $\omega_{pi}^{-1} = 240$ fs, $\lambda_D = 2.35$ μm, the target thickness $L = 47$ μm and t = 12 ps. As we can see in Eq.1.9, the maximum ion kinetic energy diverges with time so it is necessary to determine the temporal limit for which this model is valid, i.e. the time during which ions can be accelerated. It has been shown by Fuchs et al(42) empirically and using Particle In Cell (PIC) simulations, that this acceleration time can be written :

$$\tau_{acc} = \alpha(\tau_L + \tau_{min}) \tag{1.11}$$

Where τ_{acc} is the time during which the ions can be considered accelerated, $\tau_{min} = 60$ fs is a constant and α is a variable which depends on the laser intensity. It varies linearly from 3 at I = 2.10^{18} W.cm^{-2} to 1.3 at I = 3.10^{19} W.cm^{-2} and it is constant and equal to 1.3 for higher intensities.

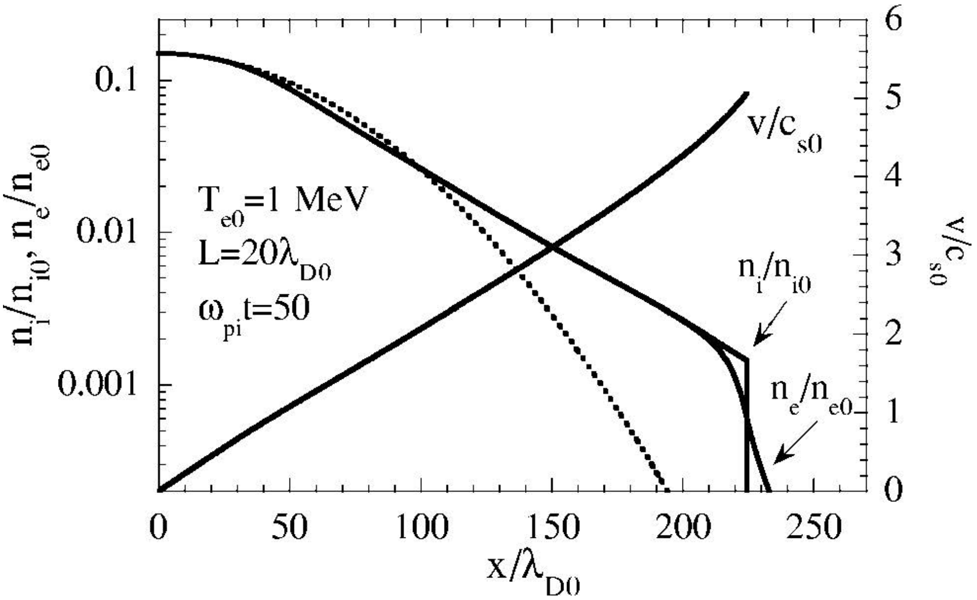

Figure 1.4: Ion and electron densities and ion velocity as function of distance from the target rear side. λ_0 is the initial Debye length, L the target thickness, T_{e0} the temperature constant of the electron population in its initial state (noted T_{hot} in the text), n_{i0} the initial ion density(41).

In the end, as it can be deduced from Fig.1.4, the ion energy spectrum is an exponentially decreasing one with a maximum energy cutoff. The main ions population accelerated is usually a protons population coming from water vapour and hydrocarbon contamination present on the target surface which is always present if no special target treatment has been operated(43). This doesn't change with the target material and is due to the fact that protons have the highest charge to mass ratio and then are more easily accelerated by the sheath electric field.

Radiation Pressure Acceleration

Experimentally speaking, the TNSA mechanism has been the most employed experimentally. However, already in early PIC simulations(27), the important role radiation pressure could play on particle acceleration was identified. For linear polarisation, the ponderomotive force has an oscillating part which accelerates bunches of hot electrons which will then play a key part in the TNSA process. However, when a circular polarisation is used, the ponderomotive force is steady and the consequences are totally different. Another condition for the following process to happen is to have a contrast good enough not to generate an expanding plasma on the front side of the target before the main pulse arrives.

If a circularly polarized intense laser pulse arrives on a step-boundary thick target with an electronic density higher than the critical density of the laser expressed in Eq.1.1, a steady ponderomotive force will rapidly push the electrons in the target(27). Since ions didn't have time to move yet, it will leave the front layer of the target positively charged, which will give rise to an electric field holding those electrons back. Then, an equilibrium is found where electrons are piled-up in a position for which the ponderomotive force and the electric field that has emerged by the charge depletion cancel each other's effect on the piled-up electrons. A representation of this equilibrium is shown in Fig.1.5.

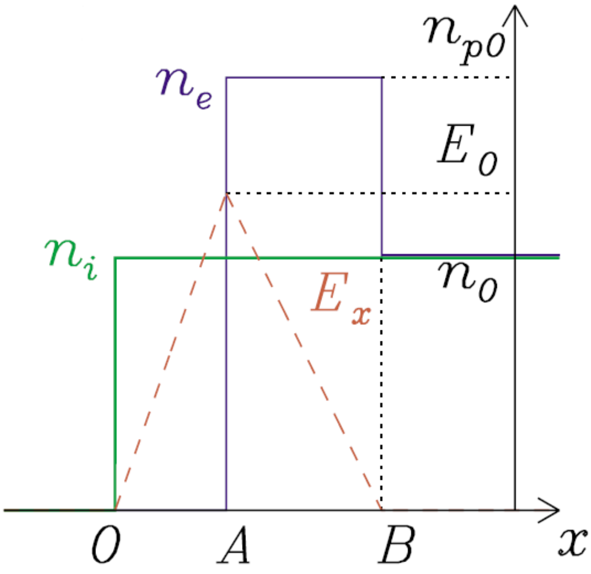

Figure 1.5: *Ion and electron densities n_i and n_e when the electric field E_x generated by the new electronic position balances the ponderomotive force and the ion population didn't have time to move yet*(44).

The ions are then accelerated by a quasi-static electric field resulting from this equilibrium(45). This process is often called hole-boring. Lots of analytical models built to explain the PIC simulations consider a perfect reflection of the laser in the instantaneous rest frame (IRF) of the target(46; 47; 48; 49). Using the momentum and energy conservation in the IRF, one finds:

$$P_{rad} = \frac{2I}{c}\frac{1-\beta_b}{1+\beta_b} = 2\gamma_b^2 m_i n_i v_b^2 \tag{1.12}$$

$$\beta_{imax} = 2\beta_b = 2\sqrt{\frac{I}{m_i n_i c^3}} \tag{1.13}$$

Where P_{rad} is the radiation pressure in the IRF, I the laser intensity, $\beta_b = v_b/c$, $\gamma_b = (1-\beta_b)^{\frac{1}{2}}$ the Lorentz factor of the foil, v_b the hole-boring velocity, $\beta_{imax} = v_{imax}/c$ is the maximum ion velocity, m_i the ion mass and n_i the ion density. The ions initially positioned between A and B in Fig.1.5, i.e. where the laser evanescence happens, are accelerated as a bunch by the piled-up electrons and reach velocities from v_b to v_{imax}.

If the target is thin enough, the piled-up electrons population, which is in the equilibrium state presented in Fig.1.5, can be directly toward the rear side of the target, i.e. toward the B position that corresponds to the target rear side. This will give place to another process called Light Sail (LS)(50). In such a regime, the bunch with the piled-up electrons and the accelerated ions can keep on being accelerated by the radiation pressure of the laser as long as the laser pulse lasts. We then have two different ion populations. A first one, which had an original position between O and A in Fig.1.5, is poorly accelerated and is called the tail. A second one, which had an original position between A and B in Fig.1.5, is greatly accelerated and is called the sail(51).

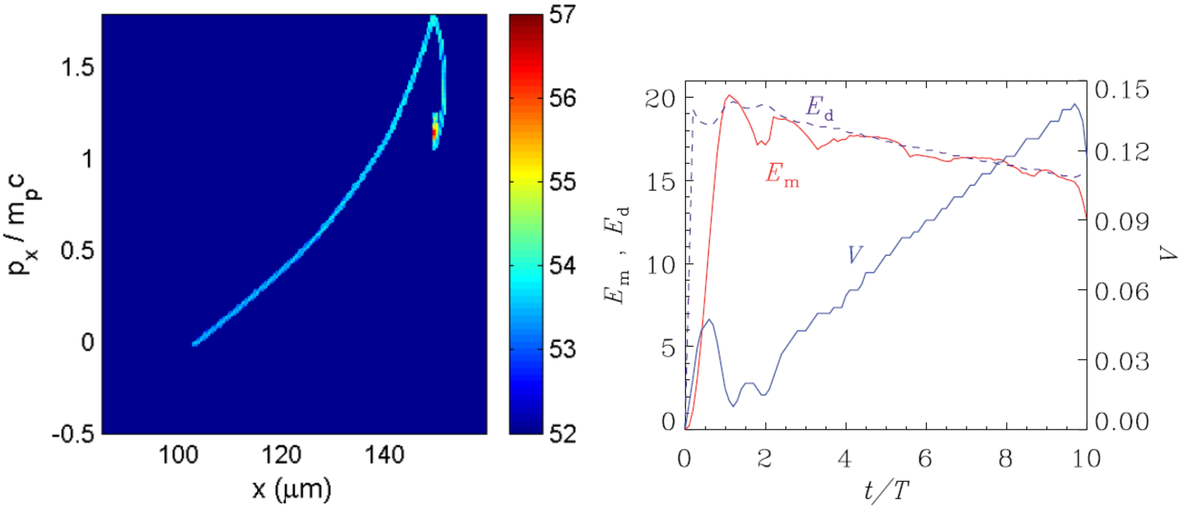

Figure 1.6: *Simulation of the RPA acceleration of ions: On the left, proton phase space after 400 fs for a 150 nm proton foil with a* 8.10^{28} m^{-3} *density irradiated by 64 fs circularly polarized pulse with a* 2.10^{21} $W.cm^{-2}$ *peak intensity*(52)*. On the right, temporal evolution of the peak of the electrostatic field called here* E_m *in red, of the velocity of the peak position* V *in blue and of* $E_d(t) = E_m(0)(1+V(t)/v)/(1+V(t)/c)$*, for dimensionless parameters which can correspond to a 40 nm thick* ^{12}C *foil with a* $1.1.10^{29}$ m^{-3} *density irradiated by a 800 nm laser with a* 3.10^{20} $W.cm^{-2}$(51)

The sail and the tail can clearly be identified in the proton phase space presented in Fig.1.6. This last process is of the uppermost interest since it can produce quasi monoenergetic ion beams with energies way higher than what is reachable with TNSA. Simulations show protons reaching GeV energies with a laser intensity around 10^{23} W.cm^{-2}(53). Besides, the ion energy depends a lot on how long the accelerating conditions last(50; 26). However, the requirements for this process to exist are quite complex since are needed a circular polarization, an exceptional contrast and an ultrathin target. Some simulations(54) have shown that linear polarization might also work but for intensities higher than 10^{23} W.cm^{-2}. Experimentally speaking, beams with particles partially accelerated by RPA have been reported for intensities between 5.10^{19} W.cm^{-2} and $6.1.10^{20}$ W.cm^{-2}(55; 56; 57).

Collisionless Shock Acceleration

As it can be seen in Fig.1.3, the creation of the plasma pushed by the laser ponderomotive force creates a shock wave which travels in the target. It travels at a lower velocity than the electrons through the target, so it takes more time to reach the rear side of the target. Like for hole boring in radiation pressure acceleration, since the electron momentum is negligible, the conservation of momentum implies :

$$(1+R)\frac{I}{c} = m_i n_i v_{shock}^2 \tag{1.14}$$

Where R is the reflection efficiency. For a target thicker than 30 μm and for a 10^{20} W.cm^{-2} laser intensity, the Mach number of the the shock wave is around 1. When the target is thinner, its Mach number increases(58). The mechanism that creates fast ions is the fact that ions can reflect on the shock wave. By using the shock wave referential, it is easy to find that in the laboratory referential, the velocity of such reflected ions is $v_i = 2v_{shock}$. Then, this acceleration mechanism dominates if the velocity of the ions it accelerates is higher than the ones accelerated by classic TNSA. This gives the condition(58) :

$$L \leq 4\lambda_D \frac{M^2}{Z} \tag{1.15}$$

Where L is the target thickness, λ_D the Debye length of the sheath electric field, M the Mach number and Z the ion charge number. This implies that this process can dominate only for thin target. This process can be recognized by the shape of its ion spectrum. Indeed, when reaching the rear side, the spectrum of the ions accelerated this way is narrow ranged since it depends on the shock velocity. Then, it changes into a plateau when the ions reaches the sheath accelerating field(58). Such a feature has been found in experimental spectra from several teams(59; 60; 61; 62), obtained by using targets with low density, around ten times the critical density for instance(63).

Break Out Afterburner

This process has been conceptualized by Yin et al(64) and involves several phases. For this process to happen, one needs to use ultrathin targets. The target thickness used in Yin's simulation was 30 nm. Hence, the contrast of the laser must be really good to avoid to destroy the target before the main pulse arrival. In the first phase happens a classic TNSA phase. In a second time, since we are using a very thin target, the proportion of hot electrons begins to be non negligible and even though the target is still opaque, the electron skin depth becomes comparable to the target thickness. All the electrons of the target are then susceptible to become hot electrons so the conversion efficiency of the laser into hot electrons is enhanced. Besides, on the rear surface, ions see both the sheath electric field and the ponderomotive pressure coming directly from the laser. This second stage is called enhanced TNSA. On a third and final phase, the electron plasma expands so much that its density goes below the critical density, as it has been shown experimentally(65). The laser can then interact with all the hot electrons in the target and in the sheath field. This induces a longitudinal electric field as high as in the previous phases but taking place over a much longer distance. This allow to accelerate ions to much higher energies than TNSA. A scaling law(66) to get the maximum ion energy has been proposed to be :

$$E_{max} = (1 + 2\alpha) Z T_{hot} \tag{1.16}$$

Where α is an empirical parameter estimated to be 3. Experimentally, several teams have reported BOA which is also called TNSA in the relativistic transparency regime(65; 67; 68; 69).

As one could expect from the complexity and variety of the physical phenomena happening in laser-matter interaction, some others acceleration processes have been proposed with sometimes experimental evidences. For instance, some processes have been proposed for acceleration in near-critical and underdense plasmas(26) such as Magnetic Vortex Acceleration(70).

1.1.3 Neutron acceleration

Now that we saw that it is possible, using laser-matter interaction, to produce proton beams with a maximum energy which can go from tens of MeVs to hundreds of MeVs or even GeVs for the most optimistic scenarii, we can use those proton beams to produce neutron beams using correct converters. As shown in Fig.1.7, there are two main setup families to produce neutrons using a laser. We can either use a single target (see 1.7b) in which ions are accelerated and interact in the very same target to produce neutrons. For instance, thermonuclear fusion can be induced by the implosion of a capsule containing deuterium and tritium and this can produce neutrons. It is something well-documented at facilities aiming for Inertial Confinement Fusion such as the National Ignition Facility(71; 72; 73) or the Laser MegaJoule. On more modest facilities, the deuterium fusion can also be used to produce neutrons by accelerating, from the front face of a deuterated plastic target, deuterium ions which can then interact with other deuterium nuclei in the same target to produce neutrons(74; 75). The fusion reactions of interest and the respective neutron kinetic energies are given by Eqs.1.17 and 1.18:

$$d + d \longrightarrow n +^3 He + 3.26\ MeV \qquad E_n = 2.5\ MeV \tag{1.17}$$

$$d + t \longrightarrow n +^4 He + 17.6\ MeV \qquad E_n = 14.1\ MeV \tag{1.18}$$

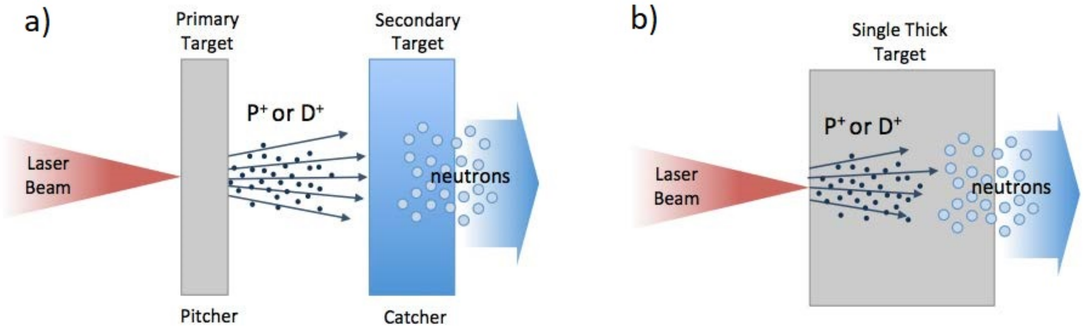

Figure 1.7: *Possible setups for laser-driven neutrons generation*(76)

Another possible setup is to accelerate particles in a first target usually called pitcher, as shown in Fig.1.7a, and send this beam in another target where the neutrons will actually be produced. This second target is usually called the catcher. For instance, a laser-driven electron beam can be sent in a target where it will create gammas by Bremsstrahlung. If the second target is chosen wisely, those gammas can then induce photonuclear reactions, where neutrons are produced. Several experimental teams have used this process with lasers from 10 TW to 1.3 PW to produce photoneutron beams with intensities reaching up to 10^{21} neutrons.cm^{-2}.s^{-1}(77; 78; 79; 80). Even though such peak intensities are quite remarkable, we will focus in this thesis on neutrons produced by ion beams, and especially proton beams, which should offer in a near future the possibility to produce even higher yields as we will show.

A classic way to produce neutron beams is to use secondary targets with nuclei with a good cross section for the (p,n) reactions, which are nuclear reactions that capture a proton and emit a neutron. This technique is very effective for proton energy in the MeV range. For energies of hundreds of MeVs or higher, another process becomes way more interesting, this process is called spallation and it will also be discussed in this section.

Neutrons produced by nuclear reactions

In order to have an efficient converter, we need to choose nuclei that fulfill several conditions. First and foremost, the cross section of the (p,n) reaction needs to be as high as possible. Besides, it is important that this cross section is high especially for low energy protons. Indeed, as it has been shown previously, the TNSA process produces protons with an exponentially decreasing energy spectrum (see Fig.1.4). Besides, protons can scatter in the catcher target and see their energy decrease going through this one. To fulfill this condition, the (p,n) reaction needs to have a positive, or at least a low in absolute value, Q-value, which is the amount of energy absorbed (if it is negative) or produced (if it is positive) during the nuclear reaction.

Another important point to help in the choice of the target material is the fact that to have the highest fluence possible, one needs to produce a beam as directional as possible. The directionality of the beam can also be important for radioprotection issues in some applications. To do so, it is important to choose a nucleus as light as possible. Indeed, the directionality of the produced beam depends greatly on the mass ratio between the protons forming the incoming beam and the target component.

There are only four stable nuclei with a positive (p,n) Q-value and those nuclei are ^{40}K, ^{50}V, ^{138}La and ^{176}Lu. However, those four nuclei have all very low natural abundances, are quite heavy and as it can be seen in Fig.1.8, have high cross sections for the (p,n) reaction at quite high proton energies.

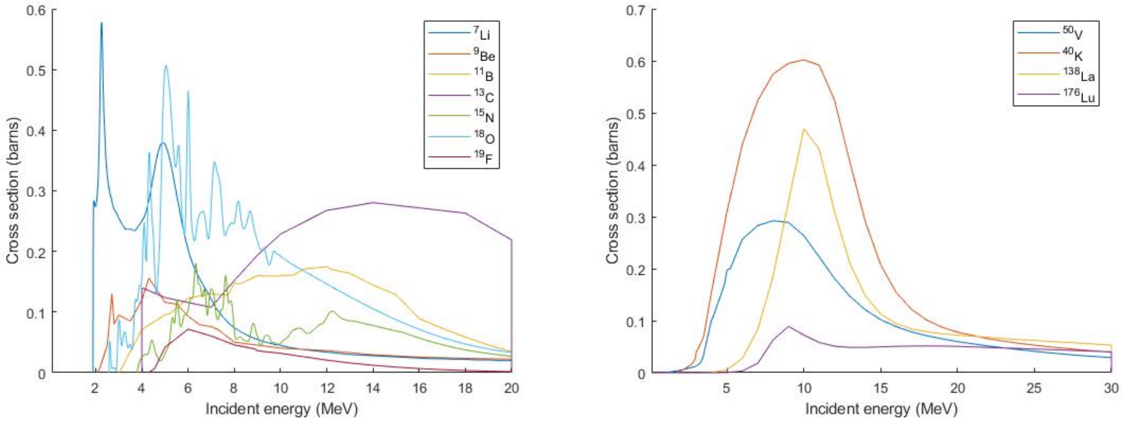

Figure 1.8: *Cross section of (p,n) reaction for several nuclei(81; 82)*

If we look at the cross sections for low mass nuclei, it appears that three nuclei fulfill all the conditions we just set. Those three nuclei are ^{7}Li, ^{9}Be and ^{18}O. If we check the natural abundances, ^{9}Be is the only stable isotope and ^{7}Li makes up 92.5% of natural lithium but ^{18}O represents only 0.2% of natural oxygen. Besides, oxygen is naturally a gas and that would complicate the target making. The Q-values for the two last reactions are -1644.24 keV for ^{7}Li(p,n)^{7}Be and -1850.4 keV for ^{9}Be(p,n)^{9}B.

Another aspect to consider is the engineering of the target. Those secondary targets have to be able to resist the mechanical constraints implied by receiving proton and electron beams produced by the laser. Metallic lithium has a very low melting temperature, i.e. 182°C, which means that a cooling system must be designed if the target is to be used for a lot of shots. Besides, as any alkali metal, it has an exothermic reaction with water. This makes this metal not easy to manipulate. A solution to this problems is to use a compound crystal containing lithium instead of metal lithium. One widely used for laser-driven neutron experiments is lithium fluoride. The melting temperature of this crystal is 848°C which is way better than metal lithium but it has a low thermal conductivity of 13.89 W.m^{-1}.K^{-1}, and as shown in Fig.1.8, fluorine can contribute to the neutron production with energetic enough protons, i.e. more than 4235.13 keV protons.

Metallic beryllium has a melting temperature of 845°C and a thermal conductivity of 218 W.m^{-1}.K^{-1}. So even though its neutron yield is lower than the lithium one, beryllium becomes interesting if the catcher is to be used an important number of time. This is something to consider especially for high repetition rate laser systems. In such cases, the deposition of hydrogen in the catcher target can also become a problem and lead to the deformation of the target, a process call blistering(83).

However, for very high intensity lasers such as Apollon, the repetition rate is only one shot per minute, so such considerations are not necessary.

Spallation

The highest neutron overall productions and intensities are reach during thermonuclear explosion tests but those neutron productions cannot be used for experimental purposes for obvious reasons. Then apart from laser driven neutron sources, the neutron sources for experimental purposes reaching the highest intensities use proton accelerators and spallation. Indeed, such facilities started to exceed in performance the experimental fission reactors in the 1980s' as it can be seen in Fig.1.9. The European Spallation Project which is being built using this design aims to reach a peak flux of 2.10^{17} thermal neutrons.cm^{-2}.s^{-1}(84).

Those facilities are usually composed of a linear accelerator which can accelerate protons up to an energy between 0.5 GeV to 2 GeV. This very energetic proton beam is then sent on a heavy nuclei target for the spallation process(86; 87) to happen and then produces very intense neutron beam. Such a process has never been used yet with a laser-driven proton beam due to the high proton energy needed for this process to happen.

As specified by the Encyclopedia Britannica, a classic definition for spallation is a "high-energy nuclear reaction in which a target nucleus struck by an incident (bombarding) particle of energy greater than about 50 million electron volts (MeV) ejects numerous lighter particles and becomes a product nucleus correspondingly lighter than the original nucleus". This value of 50 MeV can be explained using

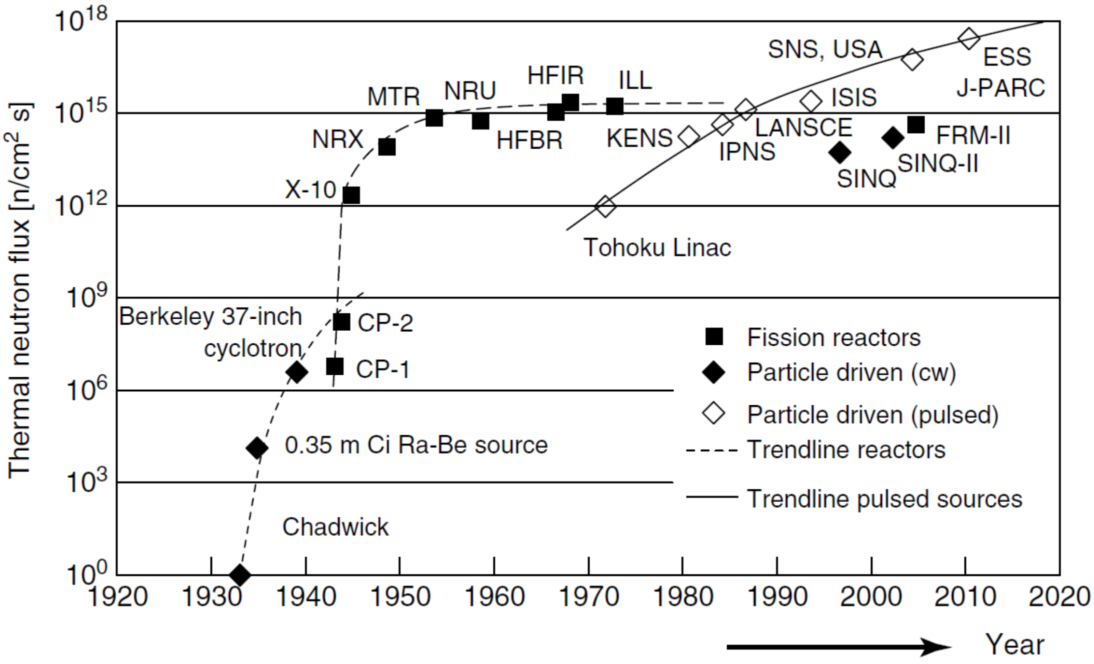

Figure 1.9: *Evolution of maximal thermal fluxes in research facilities*(85)

the De Broglie wavelength of a proton with such an energy :

$$\lambda = \frac{h}{p_p} = \frac{h}{\sqrt{2m_pE_p}} = 4.0 \times 10^{-15}\ m \tag{1.19}$$

Where λ is the De Broglie wavelength of a 50 MeV proton, h the Planck constant, m_p the proton mass and E_p its energy. This length is to be compared to the distance between two nucleons which is usually around 1-2.10−15 m. Hence, protons with energy equal to or higher than 50 MeV are able to interact with an individual nucleon inside a nucleus. This prevents the possibility to consider that the proton is captured by the target nucleus to form a compound nucleus which will de-excite itself by emitting particles, which is usually the case for nuclear reactions including a light incoming particle and a non-light nucleus. On the contrary, it will lead to the existence of the first phase of the spallation.

The spallation process has two main phases represented in Fig.1.10 which are presented in Filges and Goldenbaum's book (86). In the first phase, called the intranuclear cascade, the incoming particle is energetic enough to interact with individual nucleons as we have shown. This will create secondary particles with energy from 20 MeV up to the energy of the incoming particle. Among those secondary particles which can either be protons, neutrons or pions, some will stay in the nucleus and interact with other nucleons to take part in the intranuclear cascade, and some will be ejected from the nucleus to potentially interact with other nuclei. The second possibility induces what is called an internuclear cascade. The intranuclear cascade takes place on a timescale of 10^{-18} s. There is then a transition phase

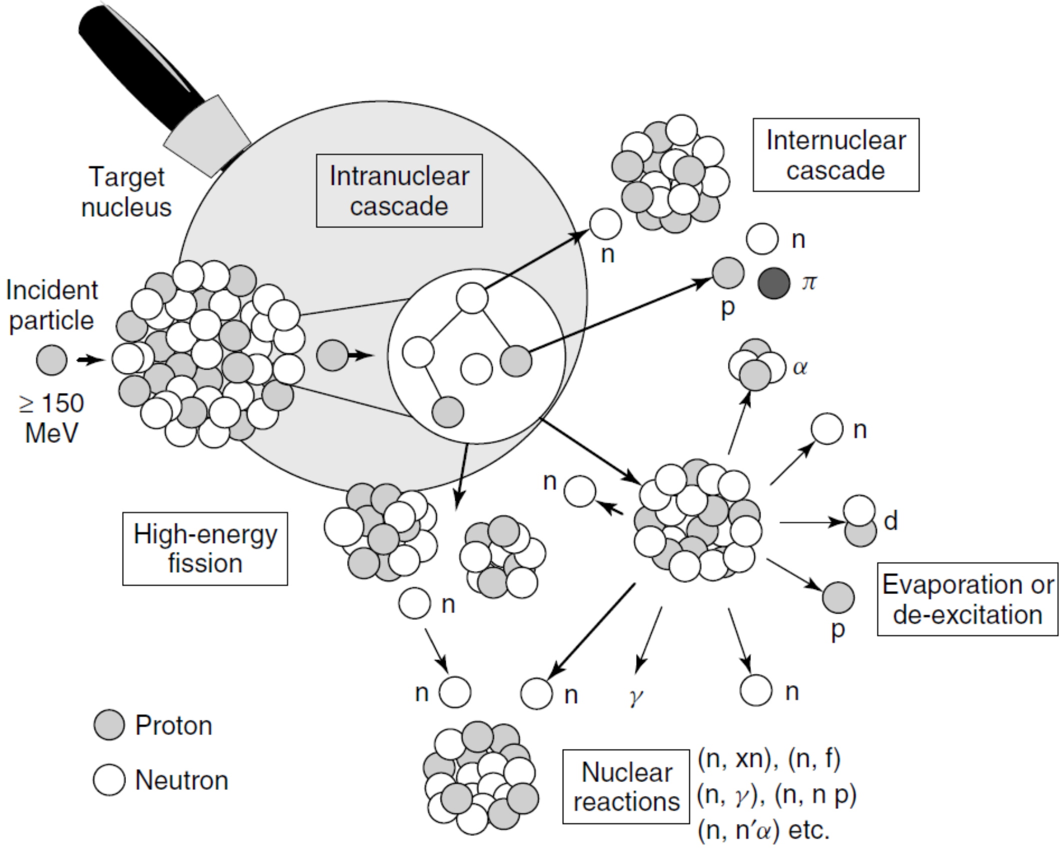

Figure 1.10: *Sketch with the different mechanisms composing the spallation process*(*86*)

called pre-equilibrium during which some low energy particles leave the nucleus which stays in a highly excited. In reality, those two phases overlap temporally but they are usually considered as two different phases.

The second main phase of the spallation process is the evaporation. Indeed, after the first two phases, the resulting nucleus is highly excited and has to de-excite. As shown in Fig.1.10, it can fission but in such a case, the process is no more called a spallation process but a high energy fission. The other way for this nucleus to de-excite is to emit low energy particles, mainly neutrons. As in the first two phases, the designation low energy particles means particles with a less than 20 MeV energy.

A variety of particles can be emitted by the spallation process such as protons, deuterium and tritium ions, alpha particles and gammas, especially during the evaporation phase. However, since they are massive neutral particles, neutrons are really efficient to cool down the excited nuclei and are not affected by the Coulombian potential barrier around the nuclei. Hence, their emission is very probable. That is one of the reasons why this process is really efficient to produce neutron beams. This is well characterized by the neutron yields shown in Fig.1.11 and 1.12.

Another aspect in favor of this process is the very important increase of the inelastic cross section of

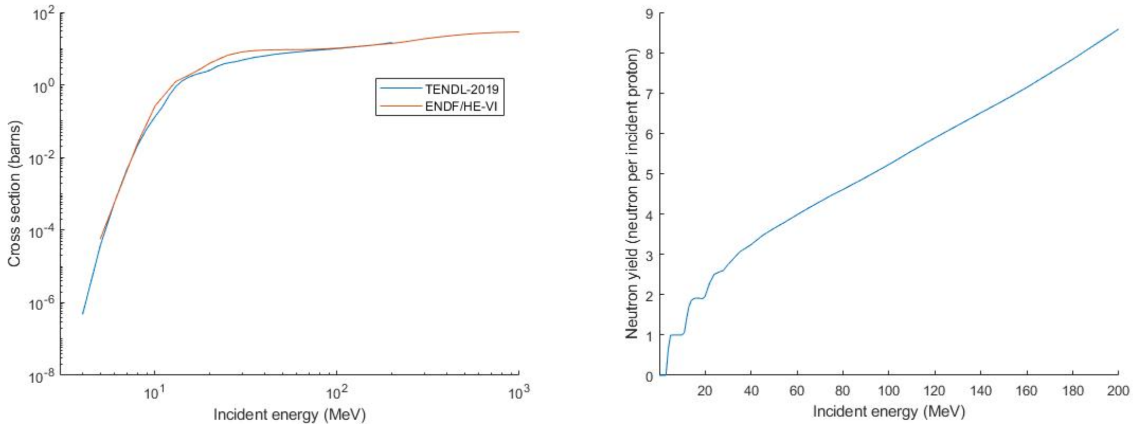

Figure 1.11: *Cross section of (p,xn) reaction for ^{208}Pb from two databases on the left and corresponding yield from TENDL-2019 on the right*(81; 82)

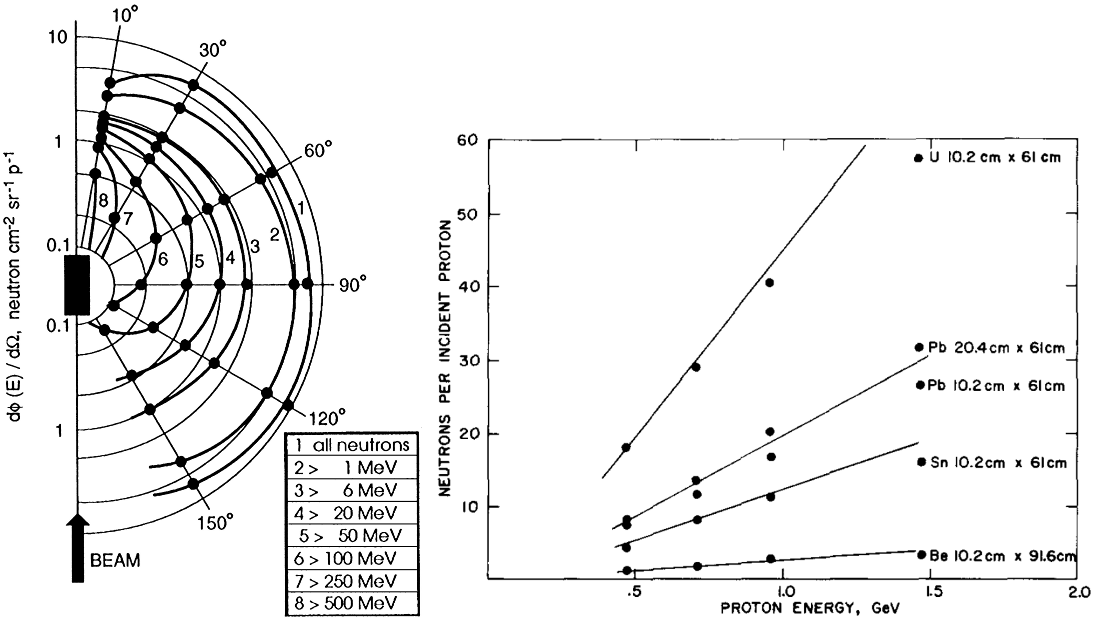

Figure 1.12: *Experimental angular neutron distribution for a 20 cm diameter lead target bombarded by 2 GeV protons on the left*(3) *and experimental neutron yield according to the proton beam energy for various targets on the right*(88)

proton on ^{208}Pb especially between 10 MeV and a few hundreds MeV as shown in Fig.1.11. If we now consider the resulting neutron beam, we can see in Fig.1.13 that the neutron spectrum peaks around 2 MeV, like it is for a fission reactor source. However, unlike a fission reactor source, a whole population of high energy neutrons is emitted. Those neutrons are produced during the first phase of the spallation process and, as it can be seen Fig.1.12, are very directional. On the contrary, lower energy neutrons are mostly produced during the second phase and almost isotropically. Those high energy neutrons could be of interest but above all, they must be taken into account when it comes to radiological protection. So spallation is a really interesting process to produce high intensity neutron sources. On the downside,

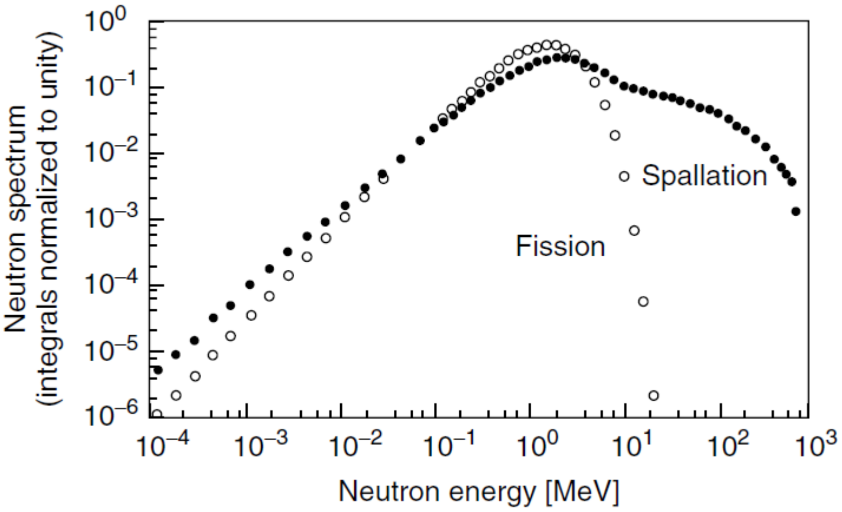

Figure 1.13: *Typical neutron spectra of thermal neutron fission of* ^{235}U *and spallation of 800 MeV protons on a 10 cm diameter tungsten target*(86)

the very high energy protons and the radiological measures it requires makes such a source only suited for significant research facilities.

Application to laser facilities

No laser-driven neutron beams using spallation have been reported yet. However, the promises of RPA and the incoming multi-PW facilities have motivated some numerical preparatory studies(4; 89). Some preparatory experiments have also been performed(90; 91). Some others are planned in a near future(92).

To achieve the numerical studies, both papers(4; 89) have used the combination of two codes. Each code was used to simulate the physics in each target in the pitcher-catcher setup shown in Fig.1.7a. To simulate the interaction between the laser and the first target, they used a PIC code called CALDER-CIRC(93). For the second stage, they used the Monte Carlo code FLUKA to simulate the interaction between the proton beam and the secondary target. The laser beam characteristics range from 0.6 to 6 PW, with a 20 fs pulse duration on a 5 μm focal spot. Using a Gaussian pulse, this gives an intensity of 2.10^{21} W.cm^{-2} to 2.10^{22} W.cm^{-2}. The primary targets are plastic targets with a thickness around 100 nm, ranging from 64 to 192 nm. The proton and carbon spectrum produced in the two extreme cases are shown in Fig.1.14.

There are some discussions about the preplasma influence on the final proton spectrum. The preplasma, hence the proton spectrum, should greatly depend on the laser temporal profile and the use of plasma mirror might be necessary to enhance the contrast. The resulting proton spectra are then used as input for the second set of simulations using FLUKA. Both papers show that the neutron production

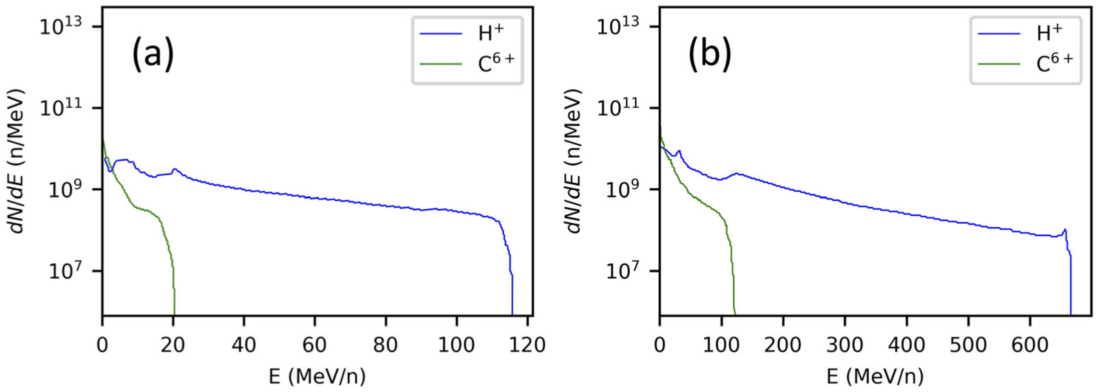

Figure 1.14: *Proton and carbon spectra obtained using CALDER simulations for a 0.6 PW scenario (a) and a 6 PW scenario (b)(4)*

depends greatly on the thickness of the secondary target.

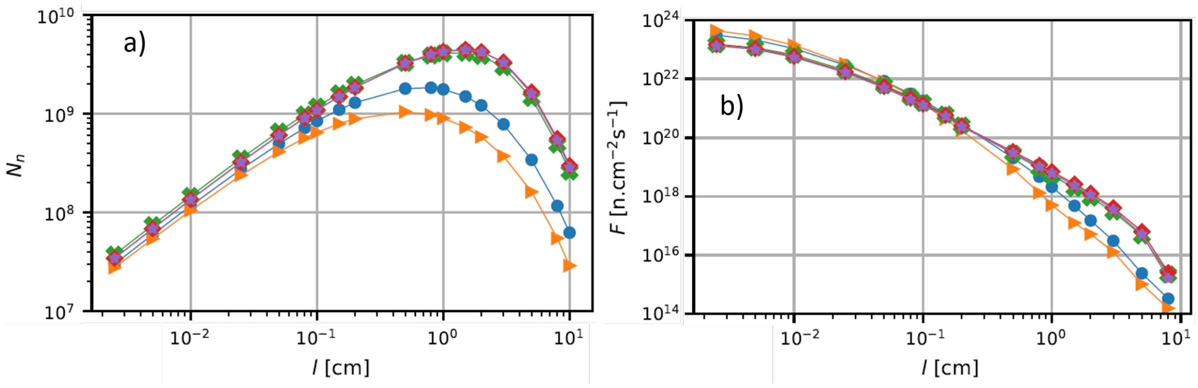

Figure 1.15: *Number a) and peak flux b) of the neutron production on the rear side of the catcher target depending on its thickness for different proton spectra(89)*

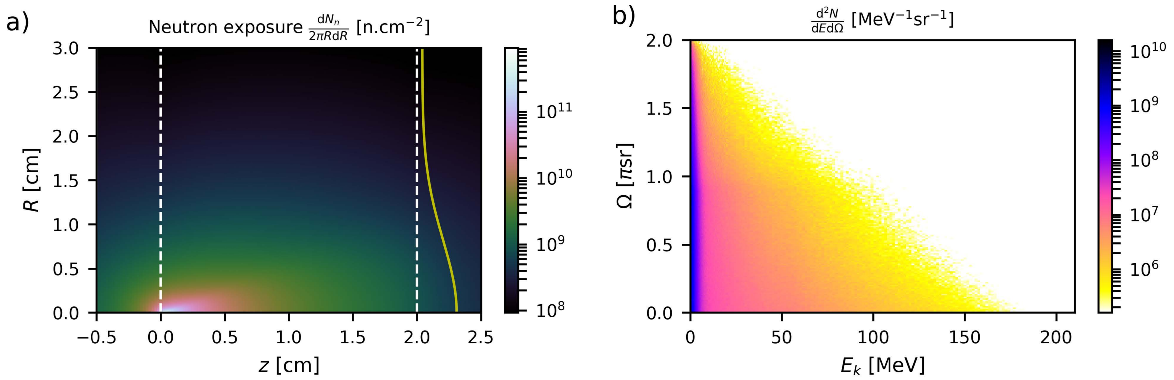

Figure 1.16: *a) spatially presents the integrated over time neutron fluence for a 2 cm thick lead converter. The limits of the target are represented by the white dashed line and the yellow curve shows the gaussian fit of the fluence on the rear side of the target. This case corresponds to the one presented in red in Fig.1.15. b) presents the integrated over time energy spectrum of the neutrons coming out of the rear face of the target(89).*

Figs.1.15 and 1.16 present the characteristics of the neutrons generated with proton beams we can expect from multi-PW facilities. The different cases presented in Fig.1.15 correspond to targets with different thicknesses and density profiles. We clearly see a difference of evolution between the overall neutron production and the neutron peak flux. This is well represented with Fig.1.16a, the highest fluences are located on the front part of the target. However if the target thickness is too reduced, a part of the high energy protons will be able to go through the target and participate less in the neutron production. Hence, depending on what neutron beam characteristic is wanted for experiments, the target thickness of the catcher target needs to be optimized. Still, those studies show the possibility to reach peak neutron fluxes in the order of 10^{23} neutrons.cm^{-2}.s^{-1}.

The neutron energy spectrum also plays a key role in nuclear astrophysical experiments. The neutron energy spectra obtained with those configurations peaks around 1 MeV. Depending on what nuclear astrophysical process one wants to study, the energy of the particles at play can vary considerably. The temperature at which the r-process is estimated to happen is around 1.2 GK(6). If we assume a Maxwell-Boltzmann distribution, it gives a mean energy of 100 keV which is not so far from the peak energy obtain by Martinez et al(4). Hence, those new neutrons beams could have some uses in the study of nuclear astrophysics.

1.2 Astrophysical interest

As we have seen in the previous section, the accelerator-based neutron beam facilities reach peak intensities in the order of 10^{17} neutrons.cm^{-2}.s^{-1}. Meanwhile, laser-based facilities have already reached peak intensities around 10^{21} neutrons.cm^{-2}.s^{-1} and incoming facilities could reach 10^{23} neutrons.cm^{-2}.s^{-1} (4; 89). Such new tools open the study of events out of reach until now, which require really high neutron fluences. It happens that there are some astrophysical events where such neutron fluences are reached and those events are considered as the main responsible for the nucleosynthesis of the heaviest nuclides naturally existing. In a first time, we will present some basics about the nucleosynthesis and especially about the r-process. In a second time, we will talk about some other possible applications of the laser-driven neutron beams.

1.2.1 Nucleosynthesis and the r-process

After the Big Bang, the universe rapidly cooled down but during the first 20 minutes, it was hot and dense enough for a primordial nucleosynthesis to happen(94). Fusions of light elements led to the primordial abundances shown in Table.1.4. Those values are derived from observations but the models reproduce well those results except for ^{7}Li(95). For the rest, ^{6}Li should have an abundance around 10^{-12} according to the models and the rest should represent not more than 10^{-15}(94). Such values differ quite a lot from

Nucleus	Abundance
^{1}H	0.7551±0.0040
^{4}He	0.2449±0.0040
^{2}H	$2.45\pm0.04\times10^{-5}$
^{3}He	$(0.9\text{-}1.3)\times10^{-5}$
^{7}Li	$1.58\pm0.31\times10^{-10}$

Table 1.4: *Primordial abundances after the Big Bang nucleosynthesis(94).*

the Solar system abundances represented in Fig.1.17. This means that most of the heavier than lithium elements have been produced later.

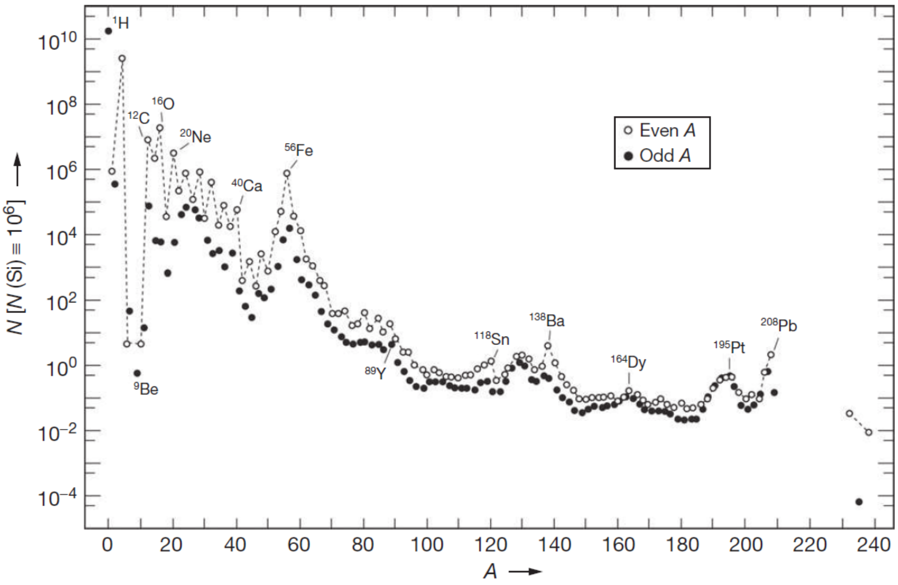

Figure 1.17: *Solar system abundances by mass number(96).*

In fact, most of this heavy elements are produced in the stars in the very end of their life. To understand it, we will first go through the different phases that a star experienced during its life. Most of what is presented in this section is explained in deeper length in the book Nuclear Physics of Stars(6).

Nucleosynthesis in massive stars

The first and longest phase of a star life is the hydrostatic hydrogen burning. Indeed, to stay in hydrostatic equilibrium and not collapse, a star produces energy by fusing protons into heavier elements, mainly helium nuclei. For low mass nuclei, the binding energy per nucleon tends to increase when the nucleus mass increases, until the iron peak. Hence, fusing light nuclei will produce energy. Depending on the temperature of the star, during this first phase, this is done by following one of those three sequences of nuclear reactions :

$$p(p,e^+\nu)d(p,\gamma)^3He(^3He,2p)\alpha \qquad pp1 \qquad (1.20)$$

$$p(p,e^+\nu)d(p,\gamma)^3He(\alpha,\gamma)^7Be(e^-,\nu)^7Li(p,\alpha)\alpha \qquad pp2 \qquad (1.21)$$

$$p(p,e^+\nu)d(p,\gamma)^3He(\alpha,\gamma)^7Be(p,\gamma)^8B(e^+\nu)^8Be(\alpha)\alpha \qquad pp3 \qquad (1.22)$$

Where p is an ^{1}H hydrogen nucleus, d a ^{2}H deuterium nucleus, α a ^{4}He nucleus, e^+ a positron, e^- an electron and ν a neutrino. When there is only one term in the parenthesis, it means that it is a natural decay and only the emitted particle are then written. The half-life of ^{8}B and ^{8}Be are respectively 770 ms and 8.2×10^{-17} s. Those three sequences named pp1, pp2 and pp3 all produce ^{4}He nuclei. The predominance of one or another is temperature dependent as described in Fig.1.18. Another interesting feature is that in the second step of the sequences, deuterium is used. Even though it is also created during the first step, the deuterium abundance depends on the equilibrium of the first and second reactions. It happens that for most of the stars, this equilibrium sets an abundance around 10^{-17}-10^{-18} relatively to hydrogen, which is lower than the primordial deuterium abundance. Consequently, most of the primordial deuterium has been consumed in those sequences.

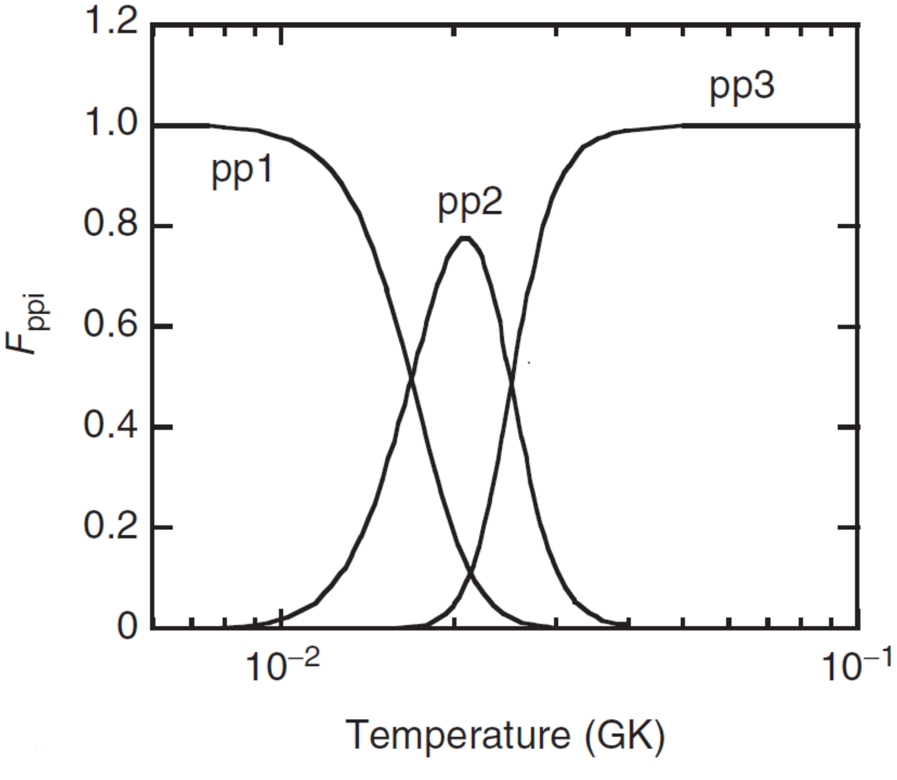

Figure 1.18: *Fraction F_{ppi} of ^{4}He nuclei produced by each nuclear reaction sequences according to the temperature (6).*

Besides, those three sequences are the only ones which can generate energy if the star consists only of hydrogen and helium. However, for stars not formed in the very early ages of the universe, heavier elements are also present in their composition. In particular, they can contain carbon, nitrogen and oxygen nuclei. Those nuclides can participate in cycles called CNO cycles which produces ^{4}He using protons :

$$^{12}C(p,\gamma)^{13}N(e^{+}\nu)^{13}C(p,\gamma)^{14}N(p,\gamma)^{15}O(e^{+}\nu)^{15}N(p\alpha)^{12}C \qquad CNO1 \tag{1.23}$$

$$^{14}N(p,\gamma)^{15}O(e^{+}\nu)^{15}N(p,\gamma)^{16}O(p,\gamma)^{17}F(e^{+}\nu)^{17}O(p,\alpha)^{14}N \qquad CNO2 \tag{1.24}$$

$$^{15}N(p,\gamma)^{16}O(p,\gamma)^{17}F(e^{+}\nu)^{17}O(p,\gamma)^{18}F(e^{+}\nu)^{18}O(p,\alpha)^{15}N \qquad CNO3 \tag{1.25}$$

$$^{16}O(p,\gamma)^{17}F(e^{+}\nu)^{17}O(p,\gamma)^{18}F(e^{+}\nu)^{18}O(p,\gamma)^{19}F(p,\alpha)^{16}O \qquad CNO4 \tag{1.26}$$

Even though all those cycles seem different, they all absorb four protons and emit one ^{4}He nucleus, two positrons and two neutrinos. The half-lives at play here are 9.965 min for ^{13}N, 122.24 s for ^{15}O, 64.49 s for ^{17}F and 109.77 min for ^{18}F. We can see that those cycles have some nuclei in common and that the choice of the cycle depends on the probability for some nuclei to participate in a (p,γ) or a (p,α) reaction. Those probabilities depend once again on the temperature. Hence, the abundances of all those nuclei can change depending on the temperature of the region those processes take place in. Some others processes, including proton captures with heavier nuclei, can lead to ^{4}He production but not in a proportion as important as the processes already exposed.

At some point, there is not enough hydrogen in the core to produce enough energy to counter the gravitational pressure. Consequently, the core starts to shrink and the temperature rises so much that it becomes possible to enter a new phase called hydrostatic helium burning. During this phase, helium, which is at this moment the most abundant nuclide in the core, will take part in nuclear reactions to produce heavier nuclei and enough energy to sustain the hydrostatic equilibrium. The main reactions which take place during this phase have the following equations and Q-values(6):

$$^{4}He(\alpha\alpha,\gamma)^{12}C \qquad (Q = 7274.7\ keV) \tag{1.27}$$

$$^{12}C(\alpha,\gamma)^{16}O \qquad (Q = 7161.9\ keV) \tag{1.28}$$

$$^{16}O(\alpha,\gamma)^{20}Ne \qquad (Q = 4729.8\ keV) \tag{1.29}$$

$$^{20}Ne(\alpha,\gamma)^{24}Mg \qquad (Q = 9316.6\ keV) \tag{1.30}$$

Since the reaction defined by Eq.1.28 correspond to a simultaneous fusion of three α particles, it is very improbable. In reality, fusion of two ^{4}He nuclei create an highly unstable ^{8}Be nucleus. Even though its half-life is really low, the ^{8}Be abundance is not null due to those fusions. Then, it is possible for an ^{4}He nucleus to interact with ^{8}Be nucleus inducing the reaction ^{8}Be(α,γ)^{12}C. Again, the lightest nuclides are consumed and turn into heavier nuclides. For the other nuclides, there is an equilibrium between their creation thanks to lighter nuclides and their annihilation to produce heavier nuclides. This equilibrium depends on the temperature which is typically between 0.1 GK and 0.4 GK for massive stars at this stage. In the end, the ratio between the abundances of those nuclides are mainly due to this phases. For stars lighter than 9 solar masses, this phase is the latest hydrostatic one. Indeed, the electron degeneracy pressure prevents those lighter stars to reach pressure and temperature conditions sufficient to trigger the next burning stages.

For heavier stars, when all the helium is consumed in the core of the star, the core instantly shrinks and the temperature rises up to reach a point at which fusion of the next lighter nuclides is possible. The main abundances at this stage are for the nuclei ^{12}C and ^{16}O. Around 0.85 GK, ^{12}C fusion can start in massive stars. The mass difference between the two ^{12}C nuclei and the resulting ^{24}Mg is excited with an energy around 14 MeV which is high enough for light particles to be emitted instead of just gammas. The most probable reactions are then:

$$^{12}C(^{12}C,p)^{23}Na \qquad (Q = 2241\ keV) \tag{1.31}$$

$$^{12}C(^{12}C,\alpha)^{20}Ne \qquad (Q = 4617\ keV) \tag{1.32}$$

$$^{12}C(^{12}C,n)^{23}Mg \qquad (Q = -2599\ keV) \tag{1.33}$$

The secondary particles then quickly react with most probably ^{12}C or ^{16}O. Once again, those reactions go on until all the carbon fuel is consumed. This stage is the last hydrostatic one for stars with masses between 9 and 11 solar masses. Then, once again, the stellar core shrinks and the temperature rises up. One could expect the next stage to be oxygen burning since the core is now mainly made of ^{16}O, ^{20}Ne, ^{23}Na and ^{24}Mg. However, the temperature in the stellar core reaches now more than 1 GK and the photodisintegration of ^{20}Ne becomes the most probable reaction with the equation and Q-value that follow :

$$^{20}Ne(\gamma,\alpha)^{16}O \qquad (Q = -4730\ keV) \tag{1.34}$$

As we can notice, this reaction is endothermic. However, the ^{4}He nucleus produced will quickly be captured by another nucleus through a reaction with most of the time a positive Q-value higher in absolute. Hence, this neon burning will keep the hydrostatic equilibrium until the next phase which is finally the oxygen burning. The most abundant nuclides are now ^{16}O, ^{24}Mg and ^{28}Si. Typical temperature in the stellar core are between 1.5 and 2.7 GK. Two ^{16}O nuclei can now fuse to produce a ^{32}Si nucleus in an highly excited state since the mass difference is around 16.5 MeV. It will then emit through a variety of channels light particles which will be captured quickly in mainly exothermic reactions. Once the oxygen is depleted, we can enter the final hydrostatic stage of the most massive stars, the silicon burning. The most abundant nuclides are, at the beginning of this stage, ^{28}Si and ^{32}S and the temperature is between 2.8 and 4.1 GK. The fusion of two of those nuclei is highly improbable even at those temperatures. As during the neon burning, the most probable reactions are photodisintegration ones. Some ^{28}Si and ^{32}S nuclei will be ripped off light particles and turn into lighter nuclei for which the particle separation energy is even lower, and then which will go through disintegration themselves, etc. The light particles produced can then be captured by heavier and heavier nuclides through a quite complicated scheme until the stablest nuclides which are around the so-called iron peak. The main paths and evolution of the abundances are presented in Fig.1.19.

The outage of silicon fuel finally leaves a stellar core mainly composed of iron and which doesn't collapse as long as electron degeneracy pressure is strong enough to counter the gravitational pressure. In the very end of its life, a massive star is then composed of several layers with different pressure and temperature conditions and corresponding to each burning stage as shown in Fig.1.20.

When the mass of the iron core reaches the Chandrasekhar limit which is around 1.4 solar masses, the electron degeneracy pressure is not sufficient anymore counter the gravitational pressure and the core will collapse and trigger a supernova. The first effect is that the supernova will eject in the interstellar medium the products of the ongoing nucleosynthesis in the different layers. Besides, the shockwave produced by the core collapse will dramatically increase the temperature and speed up the burning for a short amount of time. This is especially true in the silicon burning layer where nuclei around the iron peak will be produced in massive quantities. This explains most of the release of those nuclides in the interstellar medium, since the iron produced earlier in the star life is stuck in the collapsing core which will become a neutron star.

After the shockwave, the different layers will be crossed by a neutrino-driven wind that bring protons and neutrons ripped from the proto neutron star. It is estimated that 10% of the iron core mass is transformed in neutrino radiation. This will give rise to a process called νp-process(97). Successive captures of protons and neutrons, whose ratio is determined by neutrino transitions, will transform typically iron nuclides into heavier nuclides. This process explains the synthesis of nuclides between the iron peak and the region A$\approx$100.

Besides, supernovae accelerate some particles to velocities near the speed of light. Those cosmic rays

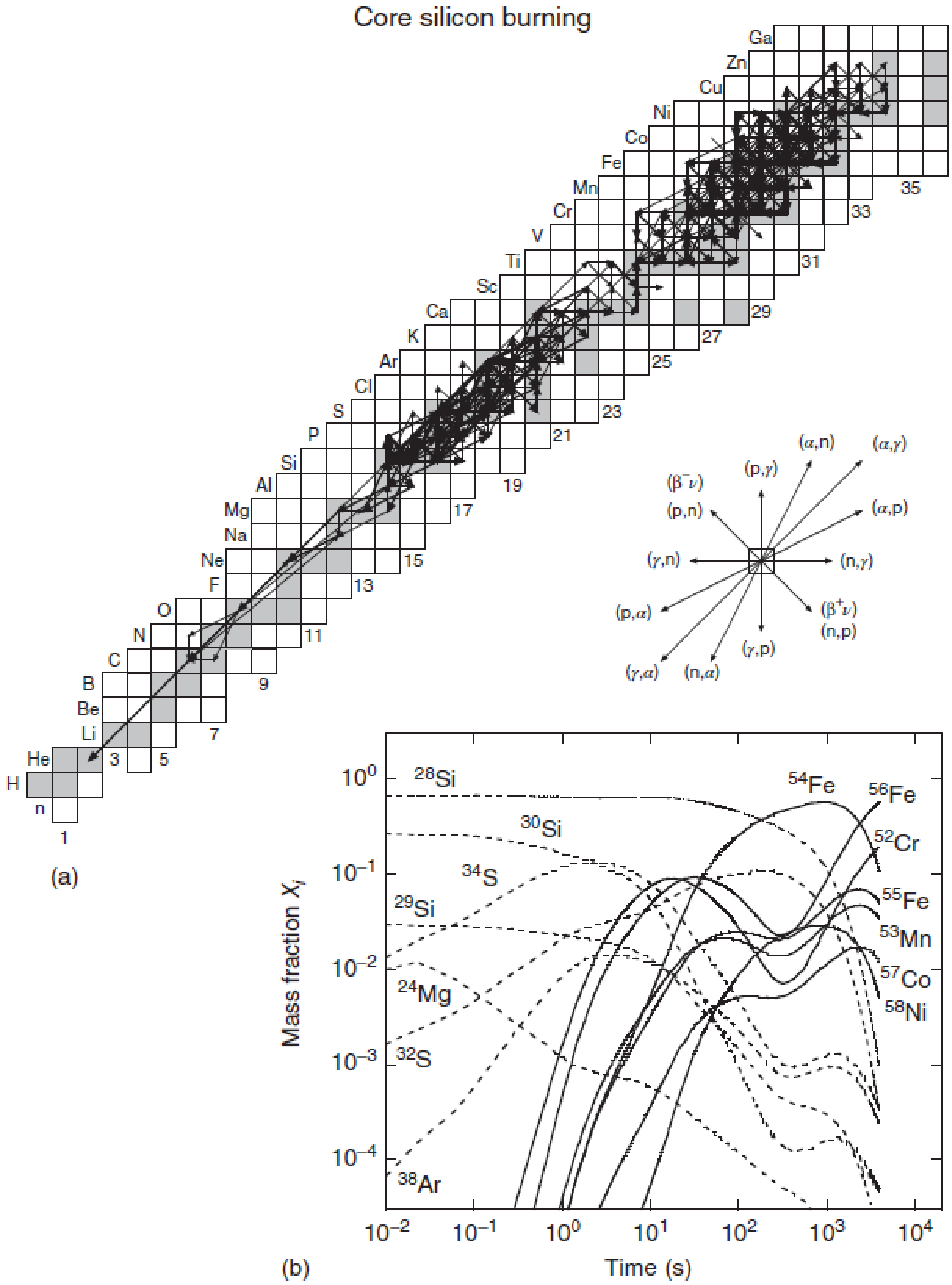

Figure 1.19: *(a) represents the most probable reactions happening during the silicon burning with arrows whose size increases with the integrated probability over time. (b) represents the corresponding abundances evolution. Those results come from a numerical simulation for the silicon burning phase of a 25 solar mass star with a solar initial metallicity(6).*

are energetic enough to break nuclei in the interstellar medium. In particular, those cosmic rays breaking for instance carbon nuclei are seen as responsible for the most of boron and beryllium production.

We have now explained nucleosynthesis of nuclides from helium up to the region A≈100 thanks to

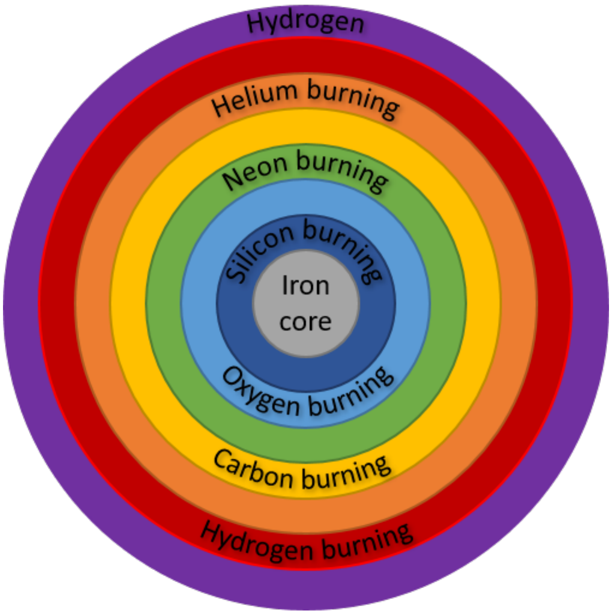

Figure 1.20: *Schematic of the states of nuclear processes happening in a massive star at the very end of its life.*

the nuclear reactions happening in very massive stars which are believed to have been very common in the first population of stars.

Nucleosynthesis in low-mass stars

The first phases in a low-mass star are the same than for a massive one. However, in such a star, electron degeneracy pressure is enough to counter the gravity pressure, often after the helium burning phase. So, in the last part of their life, those low-mass stars, which weight less than 9 solar masses, become part of the Asymptotic Giant Branch (AGB). This happens when they have burned enough hydrogen to have an helium core. While the core shrink, its temperature increases and this will cause the expansion of the outer layers which will cool down, and will stop the hydrogen burning. The star is then a red giant. The helium burning starts in the core and the temperature of the star in the outer layers rises again. Once the helium burning in the core is done, it keeps going on in a layer around a carbon and oxygen core which doesn’t collapse. The helium burning is the main energy source of this giant until the helium layer runs out of fuel. The star cools off again and the energy of the star is then only coming from a thin layer of hydrogen burning. This hydrogen burning is not enough to sustain the existence of an helium burning layer. On the contrary, helium will stack with time until it can ignite again. There is then a new helium burning phase, which increases the temperature in the whole star, which induces a stronger hydrogen burning, until the helium is consumed again and the cycle goes again.

This cyclic pattern has tremendous consequences on the spatial evolution of the star and those so-called thermal pulses can mix up different layers in convection patterns that are still not fully understood.

This mix up is called a dredge up. In particular, protons are able to plunge and reach the ^{12}C and ^{16}O core. The protons will then induce the following nuclear reactions :

$$^{12}C(p,\gamma)^{13}N(e^{+}\nu)^{13}C(p,\gamma)^{14}N \tag{1.35}$$

This gives birth to small regions at the border between the helium layer and the core with the nuclides ^{13}C and ^{14}N. Depending on the temperature, those new nuclides can release neutrons thanks to the following reactions :

$$^{13}C(\alpha,n)^{16}O \tag{1.36}$$
$$^{14}N(\alpha,\gamma)^{18}F(e^{+}\nu)^{18}O(\alpha,\gamma)^{22}Ne(\alpha,n)^{25}Mg \tag{1.37}$$
$$\tag{1.38}$$

The existence of those neutrons allows the possibility to have another nucleosynthesis process called the s-process. Indeed, the neutrons are not sensitive to the coulombian potential of heavy ions. For stars which contain heavy nuclides produced in older generations of stars, it is possible to have neutrons captured by those heavy nuclides. This is especially the case for ^{56}Fe which represents the main population of such heavy nuclides. After this capture, the resulting nucleus is either stable or can go through a β^{-} decay to become stable. Such captures are not very probable. However, such a star goes through several dredges up over hundreds of thousands of years. Over this long period of time, heavier and heavier stable nuclides can be produced and this can go up to ^{208}Pb and ^{209}Bi after which the nuclides are no more stable. The mixing during the dredges up allows those heavier nuclides to reach the outer layer of the star. Then, they can be ejected in the interstellar medium through the important stellar winds this type of star produces before ending as a white dwarf.

In the end of their lives, those stars have expelled all their outer layers through stellar winds and become carbon-oxygen white dwarfs. In a binary system, it is possible that this white dwarf accretes matter from a its companion until it reaches the Chandrasekhar mass. This will trigger a supernova of type Ia. There is still a lot of work ongoing to understand those events, especially depending on the nature of the companion(98; 99). However during such events, it is believed that, in a matter of seconds, the carbon and oxygen of the white dwarfs, will go through burning, up to the iron peak for most of the nuclei. Finally, those supernovae contribute to the abundances of nuclides from ^{28}Si up to the iron peak, and especially ^{56}Ni, thanks to the fact that the white dwarfs explode completely and spread their whole resulting material in the interstellar medium.

R-process

We have now been able to explain the nucleosynthesis of most of the nuclides up to ^{208}Pb. However, for the nuclides above A ≈ 100, the processes already exposed are not enough to explain the observed abundances. Besides, still no process explains the natural existence of the thorium, uranium and plutonium nuclides. For heavy nuclides, absorption of a charged particle is really improbable. That is why this r-process is driven by neutron captures, like the s-process. However, if the neutron capture rate is low enough to see unstable produced nuclides to decay back to stable nuclides during the s-process, it is not the case for the r-process. Indeed, this process is driven by a large neutron flux during a short period of time in an expanding medium. Several sites have been proposed to host the r-process(100). Looking at the properties we just exposed, an astrophysical site comes to mind quickly. Indeed, the neutrino driven wind which happens during a supernova can create a very high neutron flux. However, some calculations have shown that the quantities of heavy nuclides which can be produced during those events are not enough to explain the abundances observed in the solar system(101). Even though the astrophysical site remains still quite a mystery, the most probable site is considered to be neutron star mergers or neutron star/black hole mergers(102).

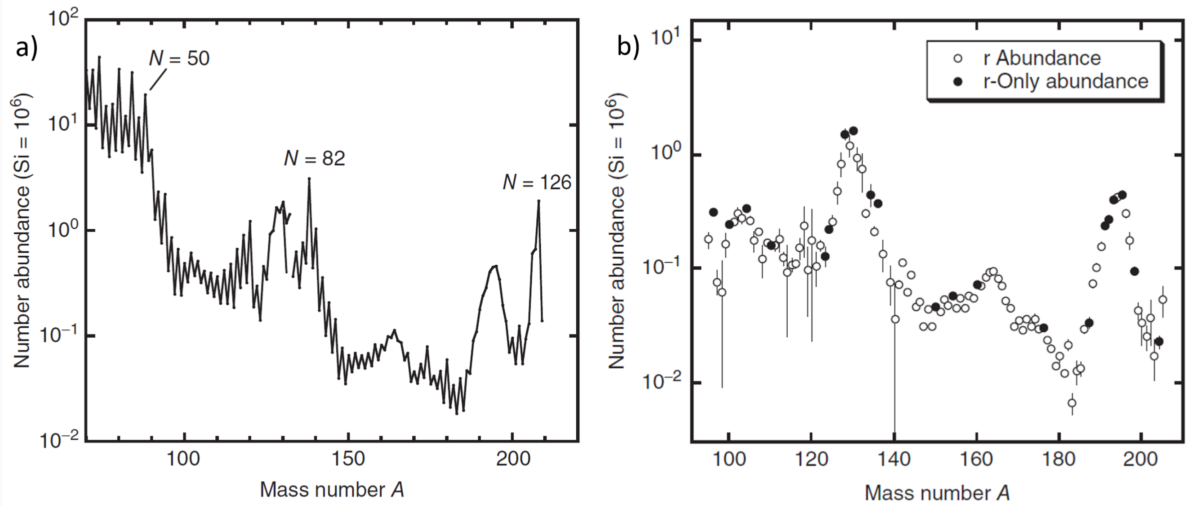

Figure 1.21: *a) represents the solar system abundances of heavy nuclides. b) represents the r-process contribution to those abundances. The "r-Only abundances" correspond to nuclei for which the s-process, and other processes, contribute to less than 3% of the final abundance. The abundances are here presented normalized to the silicon abundance with this one set to 10^6 (6)*

As it can be seen in Fig.1.21a, solar system abundances present some peaks which can be explained by nuclear properties. Indeed, the very narrow peaks around A = 84, 138 or 208 can be associated to neutron magic numbers 50, 82 and 126. In the nuclear shell model, those magic numbers correspond to numbers of protons or neutrons for which a shell is complete, which makes the corresponding nuclide particularly stable(103). The cross-sections around those peaks are influenced by those nuclear stability properties.

Hence, the equilibrium reached during the s-process can explain those features. However, the two peaks around A = 130 and 195 cannot be explained by such properties of those nuclides. Those peaks are even more outstanding if we remove from the solar system abundances the calculated contribution of the s-process as shown in Fig.1.21b. They are then a feature of this r-process.

During the r-process, the abundance of each nuclides is the result of an equilibrium between three main reactions which are (n,γ), (γ,n) and ($e^-\nu$) also called β^- decay. During the r-process, the neutron flux is so important that the neutron capture rate is important enough to produce nuclides far away from the stability valley. Beginning with nuclide seeds in the iron peak, the r-process path will first go away from the stability, the β^- decay half-life being high enough and the (γ,n) probability being low enough in comparison of the (n,γ) probability. It goes away until the (n,γ) and (γ,n) reaction rates reach an equilibrium. The nuclides, for which this equilibrium is reached are called waiting points and represent the main abundances for any given Z. At those waiting points, a part of the population will go through β^- decay to reach a higher Z. These two principles are the basic bricks of the r-process.

The two peaks around A = 130 and 195 give insight on the r-process path. Indeed, for elements for which a neutron magic number is reachable on the neutron-rich side, the waiting point tends to be on the isotope with this magic number of neutrons and more stable than for other elements, i.e. less prone to β^- decay. When the conditions of the r-process end, both (n,γ) and (γ,n) reactions stop. Hence, the important population on those waiting points will mainly decay through β^- decays as it is shown in Fig.1.22. The offset between the s-process peaks and the r-process peaks is an hint on how far from the stability valley the r-process path is.

The heaviest region reached by the r-process depends on the duration of the r-process conditions. If this duration is too short, the r-process will stop before reaching the heaviest regions possible. If not, it seems that the region around $A \approx 260$ and $Z \approx 94$ is the heaviest region reachable by this process. There is no experimental data to prove it since those nuclides are experimentally unreachable, but nuclear models tell that fission becomes predominant in such a region. If the r-process duration is long enough, this gives rise to an exponential fission cycle since the two nuclei produced by a fission event become seeds for the r-process. Fig.1.23 shows the complete path of the r-process if the r-process duration is long enough. All those durations depend on the temperature and the neutron flux which can vary a lot.

The classical model used to reproduce the r-process makes several assumptions. First of all, it assumes a constant temperature and neutron density. Besides, the termination of the neutron flow is considered instantaneous. Finally, it assumes that the waiting points and the flow between nuclides do not change during the whole r-process event. To reproduce the solar system abundances, and especially the different peaks, the classical model uses an addition of several r-process components with different parameters.

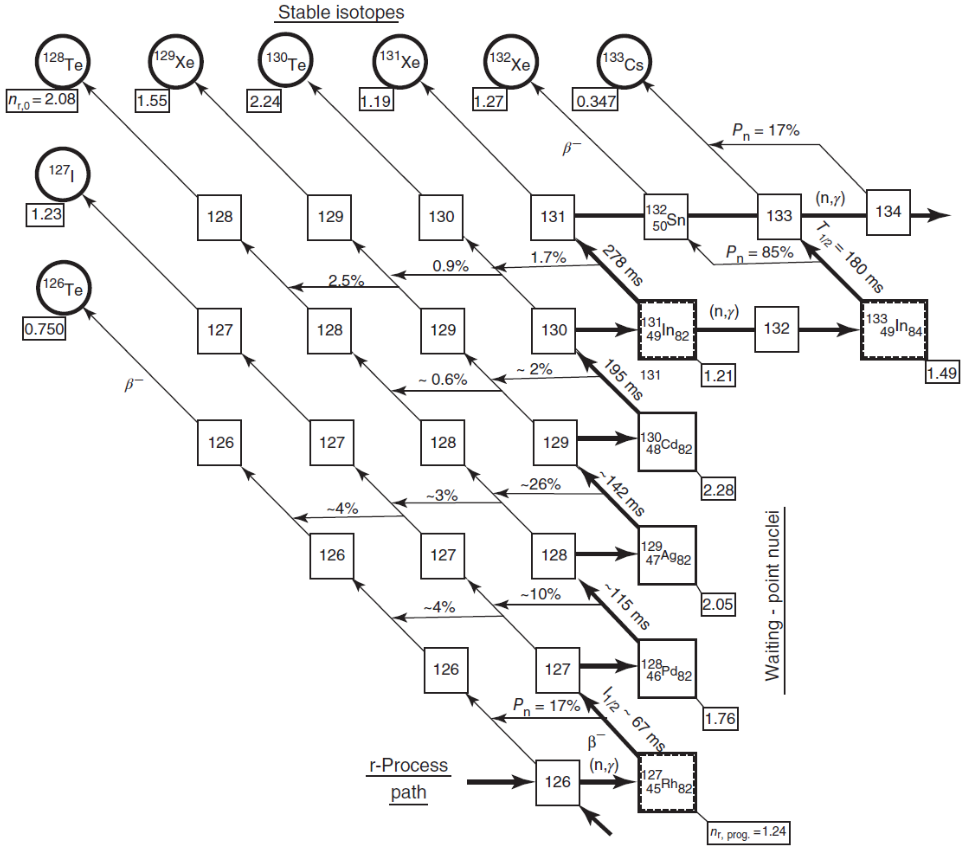

Figure 1.22: R-process path near a neutron magic number. The main waiting point nuclides are fully written in the squares. The resulting stable nuclei are presented in circles. The thick arrows represents the main r-process path with the associated half-lives written next to the β^- decay arrows. The thin arrows represent the decay paths after the r-process is done(6).

Those parameters range from 1.2 to 1.35 GK for the temperature, 3.10^{20} to 3.10^{22} cm^{-3} for the neutron density and 1.5 to 2.5 s for the duration. Fig.1.23 shows all the main r-process path possible.

Laser-driven neutron and r-process

We have now explained the main nucleosynthesis processes. Since the r-process path is so far from the stability valley, all the data feeding the nucleosynthesis models comes from nuclear models and not experimental data. Apart from the time duration, neutron beams which we will be able to produce thanks to the incoming laser facilities have characteristics close enough from what the r-process requires(see section 1.1.3). The main hurdle is to able to produce neutron-rich enough isotopes to reach the r-process path. We will here discuss the results of an extensive study about which nuclides would be reachable using the incoming laser-driven neutron beam(5).

However, this study suffers from optimistic assumptions. Indeed, this study suppose laser-driven neutron beams with 10^{12} neutrons which is way more than the $\sim 10^9$ neutrons from Horny's simulations

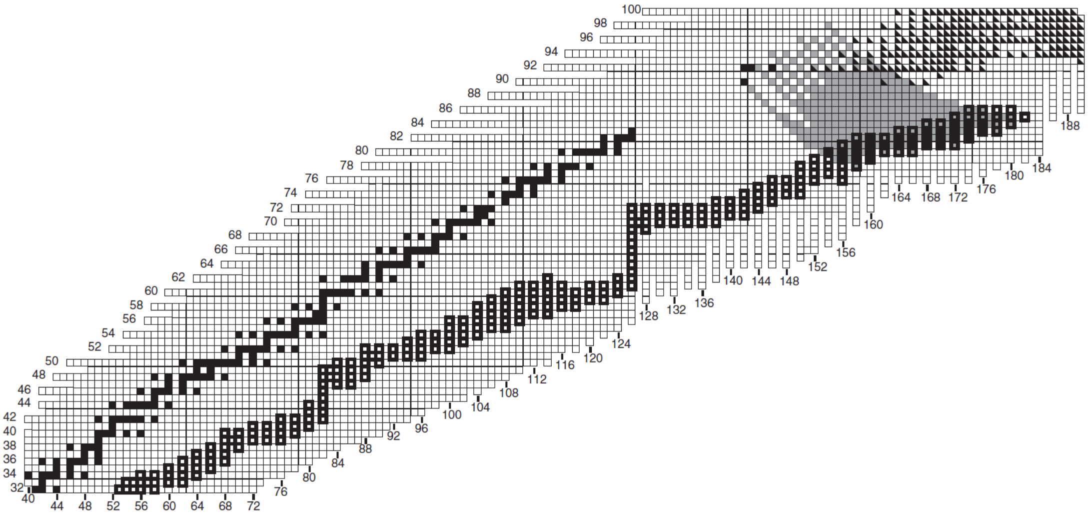

Figure 1.23: *Path of an addition of several r-process components. The main waiting point nuclides are represented by the large open and solid squares. Each contributes of at least 1% of the abundance of a stable or long-lived nuclide. The stable or long-lived nuclei are represented by the dark not large squares. Grey squares shows the decay path of nuclides contributing to the ^{232}Th, ^{234}U, ^{235}U and ^{238}U populations. Nuclides that predominantly fission are shown as triangles(6).*

(89). Besides, the neutron beam is considered mono energetic which is far from the truth as we have seen(see section 1.1.3). However, they also have done some studies with 10^{10} neutrons per pulse which is still higher than what could be obtained in the near future, but is still more realistic.

Fig.1.24 shows that for one shot, we can have two consecutive neutron captures but three consecutive captures is not really probable. This production always increases when the neutron energy decreases. Hence, it might be interesting to moderate the neutron even though it would induce a decrease of the neutron peak flux.

Fig.1.25 shows the isotope production for and after 10^4 shots with pulses of 10^{10} neutrons at 1 Hz repetition rate. This way, it would be possible to reach isotopes produced by three consecutive neutron captures. This can rise up to four consecutive neutron captures for pulses with 10^{12} neutrons. Even though it is still interesting to be able to produce such nuclides, those nuclides are not the main important ones in the r-process. However, more studies need to be done to be able to see what can be achieved with the laser-driven neutron beams which should have large energy spectra. In particular, it might be interesting to see if a modification of the neutron spectrum could have an interesting effect on the isotope production.

1.2.2 Neutron resonance spectroscopy

Another interesting use of laser-driven neutron beams could be the thermometry of warm dense matter using neutron resonance spectroscopy(104; 105; 106; 107). Indeed, the measure of a temperature is

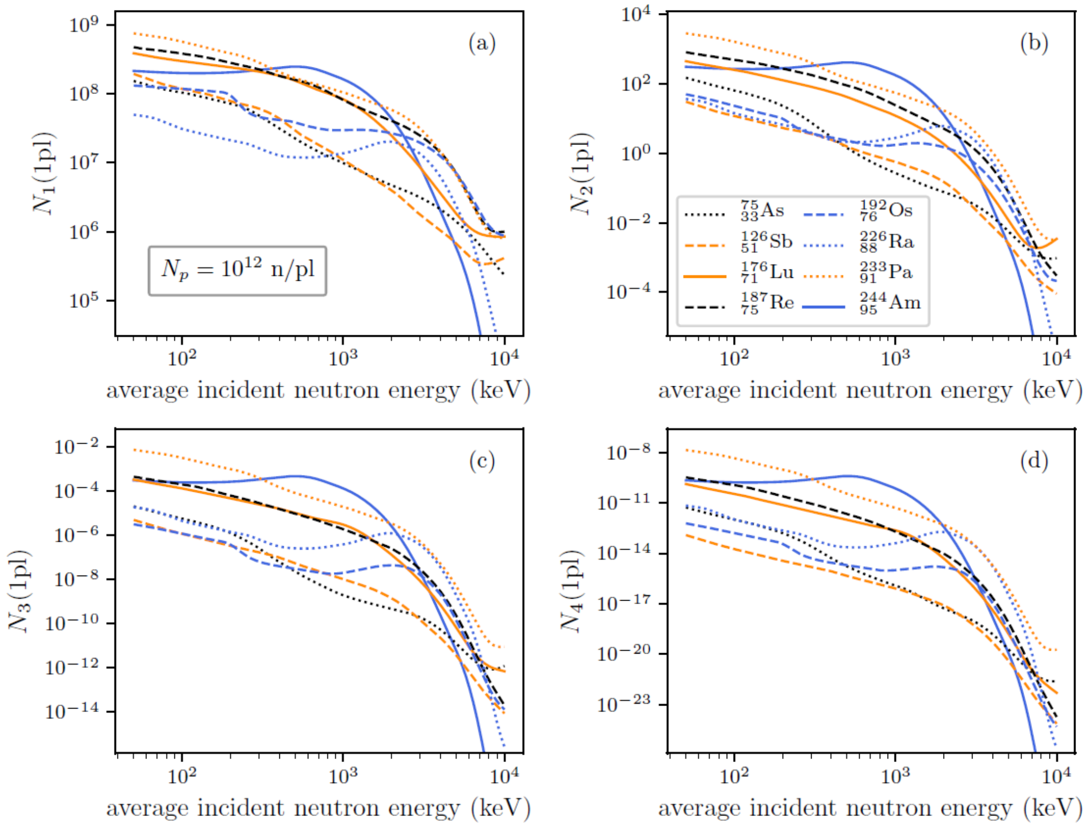

Figure 1.24: *Isotope production after one pulse (1pl) with 10^{12} neutrons. N_1, N_2, N_3 and N_4 correspond to the isotopes produced by respectively 1, 2, 3 and 4 consecutive neutron captures. This production is represented according to the energy of the neutrons. The seed nuclides are presented in the legend of (b). This production doesn't take into account the radioactive decay of the produced isotopes since the pulse temporal length is considered way shorter than their half-lives(5).*

something often needed in an experiment, especially to determine the material equation of state which is of prime interest in several fields. There are several ways to measure the temperature at a surface. However, if one wants to dynamically measure the temperature inside a bulk, it becomes more complicated. There are techniques using x-ray scattering(108) which are often used but which might be not adapted depending on the target thickness or nature. Other existing techniques, like thermocouples which is also often used, all have their drawbacks. Even if on the downside, there is the need to use a dopant, neutron resonance spectroscopy can achieve a temporally and spatially resolved thermometry. To do so, the region to measure in the target needs to be locally doped with an appropriate isotope.

The idea behind this technique is pretty simple. It uses the resonances of neutron capture reactions. If the resonance is in a low enough energy range and if this resonance is narrow enough, it is possible to measure the influence of Doppler effects on the cross section of the reaction as shown in Fig.1.26. This can be done by sending a neutron beam with a broad energy spectrum on the target to measure, and then probe it using a time of flight detector or any detector that can energetically resolved the neutron beam.

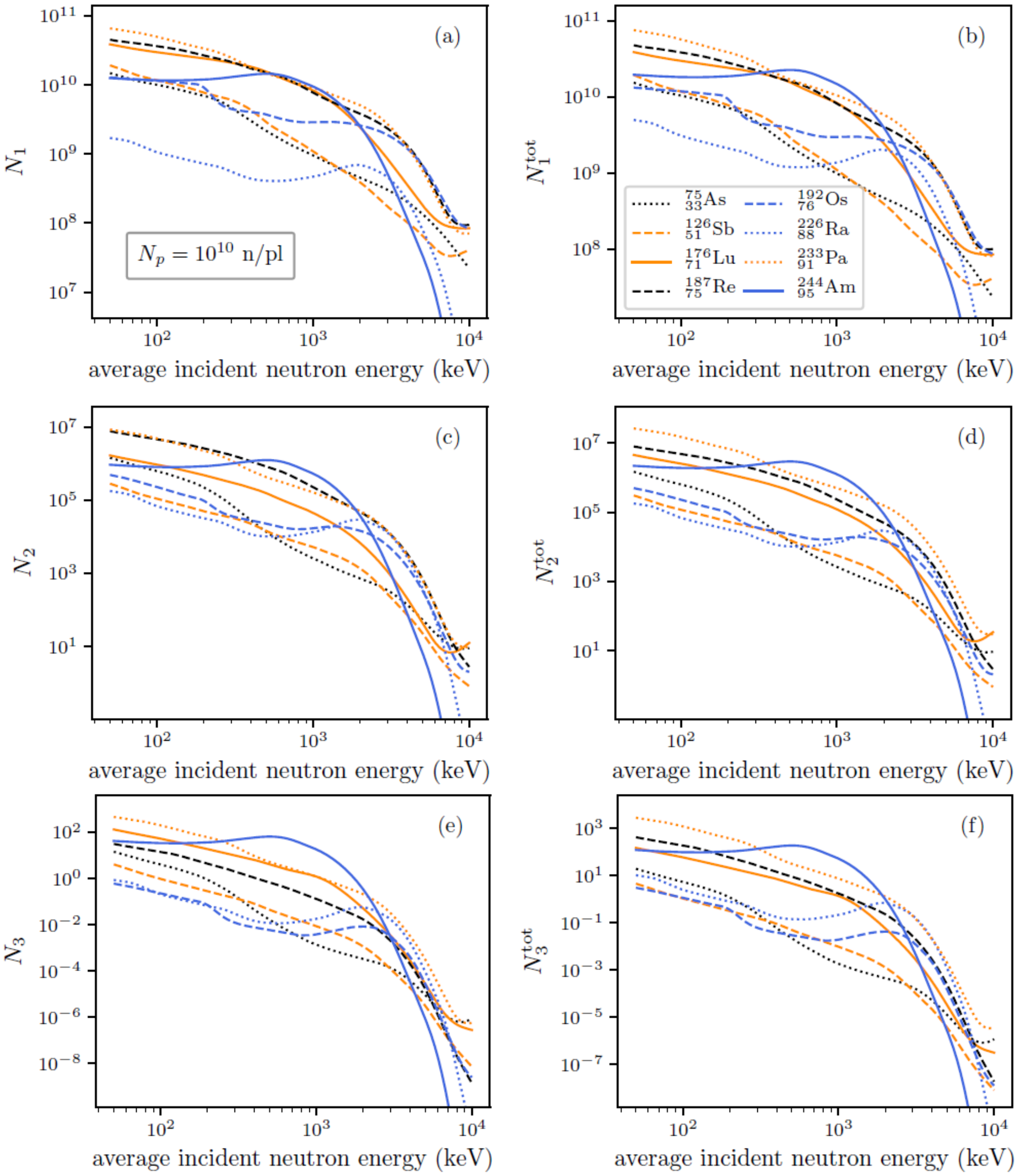

Figure 1.25: *Isotope production after 10^4 pulses with 10^{10} neutrons at 1 Hz repetition rate. N_1, N_2 and N_3 correspond to the isotopes produced by respectively 1, 2 and 3 consecutive neutron captures at the end of those shots. N_1^{tot}, N_2^{tot} and N_3^{tot} correspond to the time-integrated production of the corresponding isotopes. This production is represented according to the energy of the neutrons. The seed nuclides are presented in the legend of (b)(5).*

One can then see the width and position of the resonance in the neutron spectrum. The temperature of the target will tend to broaden the resonance width and it is possible to retrieve the temperature of the sample in the doped region. This technique has already been used experimentally(109; 110). It is even possible to measure the velocity of the region if this one is shocked for example(111).

Until now, this type of measurement has always been done at accelerator facilities, such as the Los Alamos Neutron Scattering Center (LANSCE). Being able to use such a technique at laser facilities would

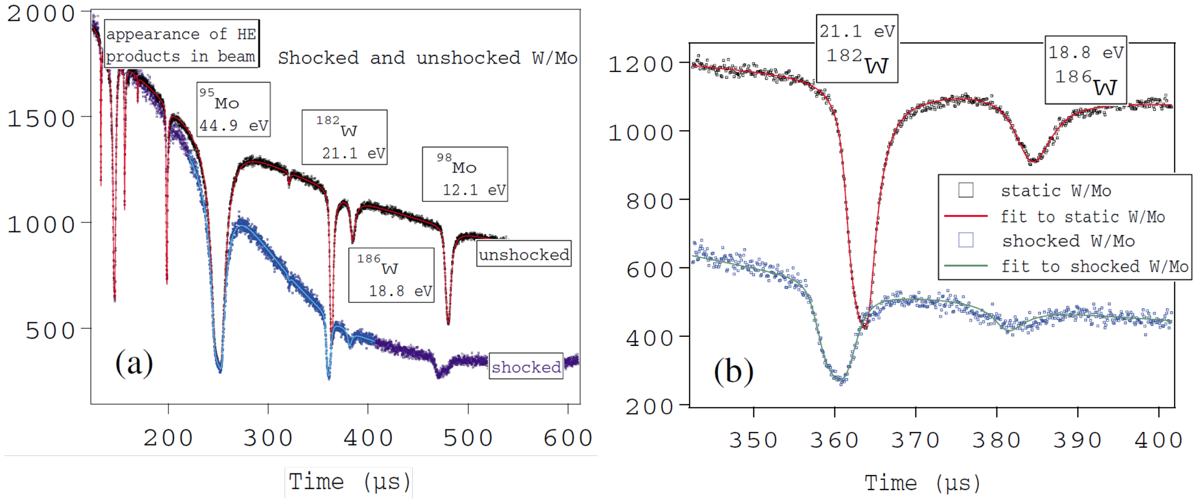

Figure 1.26: *Time of flight spectra of neutrons which went through a molybdenum target doped with* ^{182}*W. The red curve correspond to the solid target unshocked and the blue one to the shocked target.*(111)

be of great interest, especially since lasers can also be used to study equations of state(106), and are way less expensive to build than accelerators. Epithermal laser-driven neutron source with characteristics good enough to be used for this technique, have already been developed(112). Besides, analysis has shown that laser-driven neutron beams associated with time of flight neutron detectors could in principle have even better detection characteristics than the ones reached at LANSCE(113). However, the use of time of flight detectors in a high intensity laser is not something trivial and could cause issue in the development of this technique(114).

To conclude, the increase in statistic that the incoming brighter neutron beams will bring could help to overcome the difficulties encountered to implement this technique in a laser environment.

In summary, we have seen that the incoming upgrade of the laser intensity at upcoming facilities, which will allow to greatly increase of brightness for the laser-driven neutron, should impact several applications in different research domains. Besides, in the very long term, the mastering of laser-driven neutron beams could even reduce the cost of boron neutron capture therapy in the treatment of cancer(115; 116) by avoiding the need to use accelerators(117). However, before any possible application of those neutron beams, there is first a need to develop neutron detectors adapted to those beams and to the high intensity laser environment.

Chapter 2

The neutron detector

In this chapter, we will present the development of a neutron counter adapted to the high intensity laser environment we are working with. In a first section, we will start by talking about the concepts behind our design and some preparatory simulations. Then, a second section will present the prototype testing we did before building this detector. A last part will be dedicated to the calibration of the detector.

2.1 Concept

2.1.1 The scintillators

The most widespread and well-known type of high efficiency neutron detectors are the gas proportional detectors(118). The nuclides usually used by this type of detector are ^{3}He, ^{6}Li, ^{10}B or Gd. Those detectors usually consist of a tube filled with ^{3}He or BF$_3$ gas in which a wire goes through(119). Thermal neutrons react with the chosen nuclide and the energy released by this reaction will ionize atoms in the vicinity. An high voltage is applied between this wire and the outer shell of the tube. This allow to accumulate the created charges and therefore electronically detect the energy deposited thanks to the neutron capture reaction(120), as shown in Fig.2.1.

However, there is a major downside to this technology. The electronic employed, especially the preamplifiers, is very sensitive and prone to picking up noise. Besides, since a few years, there is a worldwide shortage of ^{3}He which is the most efficient gas for this technology, since it has the highest absorption cross sections for thermal neutrons, except for some isotopes of cadmium, europium, samarium and gadolinium which are not gases. That is why another type of detector became more popular, the scintillation neutron detectors. This category of detectors includes a large variety of scintillating materials, either liquid, crystals, plastic, glass or scintillation fibers. Those scintillating materials are usually coupled with

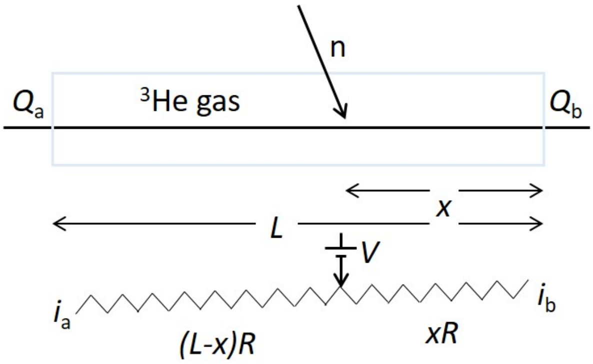

Figure 2.1: *Representation of a* ^3He *gas proportional counter and sketch of its equivalent electronic circuit* (120)

PhotoMultiplier Tubes (PMTs) which are less sensitive to the noise generated in a high intensity laser environment than the gas proportional detectors electronics.

Organic scintillators using a plastic or liquid matrix have an especially useful feature for our purpose. Indeed, those scintillators have a particularly fast response time, i.e. of a few nanoseconds(121). This is almost mandatory when dealing with intense particle beams. Besides, those technologies have a modest cost in regard of some other solutions.

When it comes to detect neutrons, there are mainly two types of neutrons to consider. First, there are thermal neutrons which have a kinetic energy of less than 1 eV. They cannot deposit enough energy by elastic collision to be detected. So their main way to ionize atoms that leads to detection, is to use some neutron-capture reactions which have a high cross section and a positive Q-value. This can be done by adding ^{6}Li or ^{10}B nuclei to either liquid or plastic scintillators. Second, fast neutrons which have an energy around 1 MeV or more, are way less susceptible to take part in neutron-capture reactions. Elastic scattering with low-mass nuclei is way more probable for such particles as shown in Fig.2.2. This can produce detectable ionization. Hence, hydrogen-rich material are well-suited do detect such neutrons.

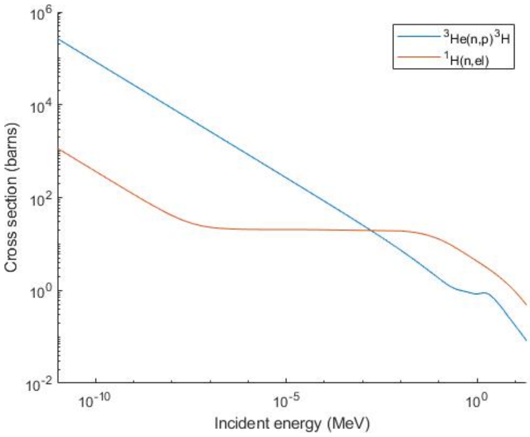

Figure 2.2: *Cross sections of* $^3He(n,p)^3H$ *and elastic scattering on* ^1H(81)

Many liquids scintillators suffer from a considerable quenching effect if oxygen is dissolved in them (122) so they need an airtight enclosure. On the contrary, plastic scintillator are easily available in any kind of shape. So from now on, we will only talk about the plastic organic scintillators which is the solution we went with for.

The plastic matrices used commercially are usually made of polystyrene (PS) or polyvinyltoluene (PVT)(123). Fluorescence occurs in plastic when energy is deposited by some ionizing energy radiation. However, this effect is not useful since the fluorescence yield is very low and the plastic is not transparent to its own emission which has a wavelength between 300nm to 350nm. Hence, some aromatic compounds with much higher fluorescence yield are added to this bulk to make it much brighter. Those compounds, called primary fluors, usually represent around 1% by weight. Such a high concentration allows a non-radiative energy transfer called Forster transfer or fluorescence resonance energy transfer (FRET) between the bulk and the added primary fluors within. Since the efficiency of this transfer is inversely proportional to the sixth power of the distance between the emitter and the receiver, a high concentration is needed to allow this energy transfer. The primary fluors can then emit a strong fluorescence light generally in the 350nm-400nm wavelengths. However, this fluorescence light is still quickly absorbed by the PVT matrix since the mean path for such light is usually less than 10cm. To be able to build a scintillator on a meter scale, one needs to decrease the bulk attenuation. To do so, another aromatic compound is usually used as a spectrum shifter. This spectrum shifter represents around 0.01% by weight so the energy transfer between the primary fluors and the spectrum shifter is mainly radiative. In the end, the emitted fluorescence spectrum is typically a spectrum between 400 nm and 500 nm.

Figs.2.3 shows emission and absorption spectra of PVT, b-PBD and POPOP which are commonly used synthetic polymer or aromatic compounds as respectively matrix, primary fluor and spectrum shifter. b-PBD stands for butyl-phenyl-bipheny-oxydiazole and POPOP for 1,4-bis(5-phenyloxazol-2-yl)benzene. This shift between the absorption spectrum and the emission spectrum for those fluorescent materials is called the Stokes shift. The energy difference is usually taken out thanks to vibrational relaxation, in the form of phonons. Figs.2.4 shows the chemical formulas of those three compounds.

The solution we went for is the boron loaded plastic scintillator EJ-254 from Eljen Technology. Indeed, from the three industrial companies which sell plastic scintillators, one is Nuclear Enterprise Ltd (124) and no longer exists, the last one is Saint-Gobain and doesn't sell anymore the BC-454 model which was its only boron loaded plastic scintillator model. We don't exactly know the composition of this particular plastic scintillator, especially its aromatic compounds, since it is an industrial secret. However, looking at its emission spectrum which is in Fig.2.5 and its specifications presented in Table.2.1, we can safely assume that it works the way we presented.

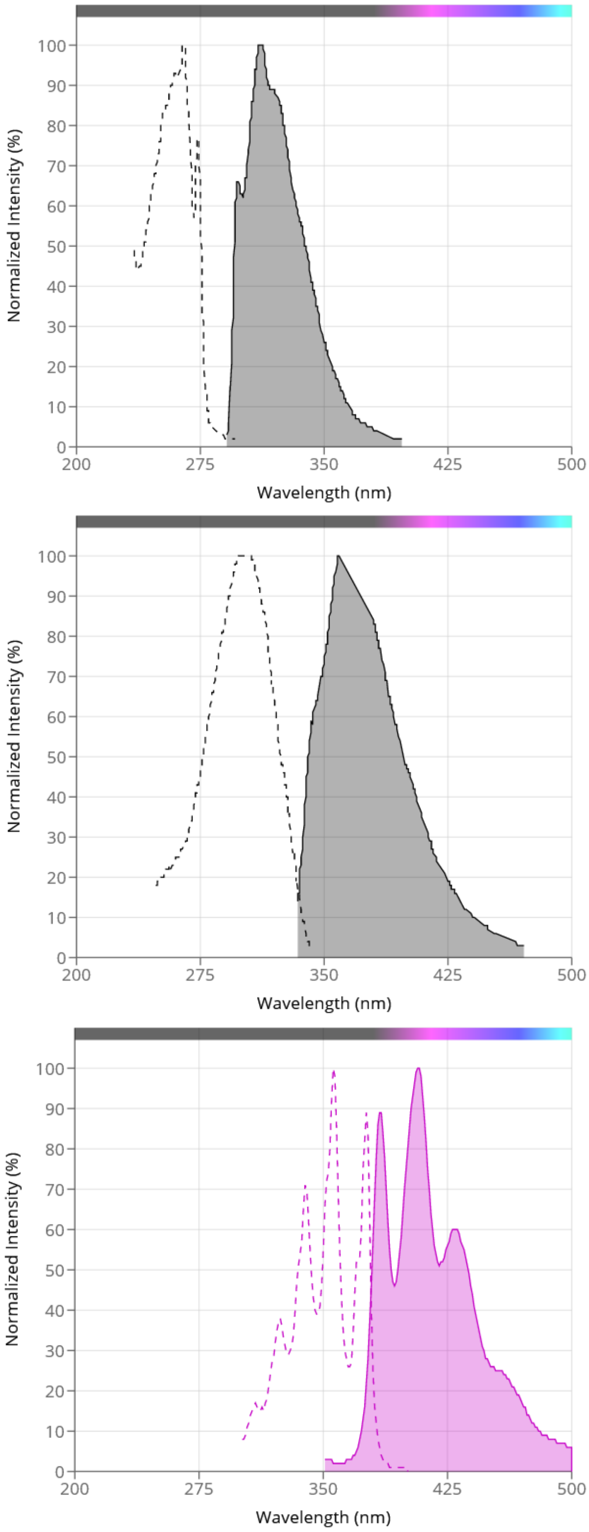

Figure 2.3: *Emission and absorption spectra of PVT, b-PBD and POPOP from top to bottom. Emission spectra are represented with thick lines and plain areas when absorption spectra used dashed lines.*

We also see on the specifications that the light output of this scintillator is only 60% of that of anthracene. Indeed, anthracene is the scintillator with the highest light output known and serves then as

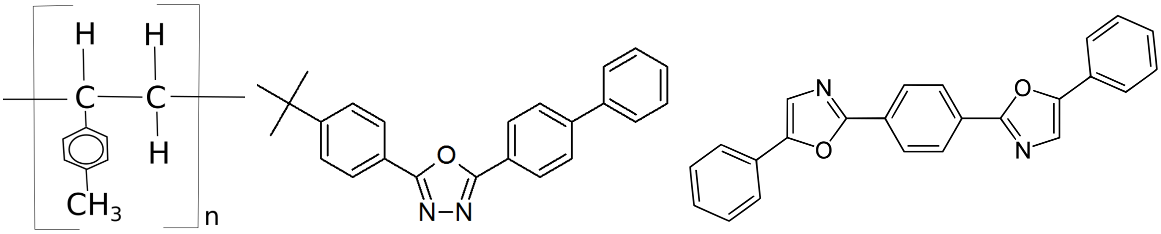

Figure 2.4: Chemical formulas from left to right of PVT, b-PBD and POPOP. PVT is a synthetic polymer and b-PBD and POPOP are aromatic compounds.

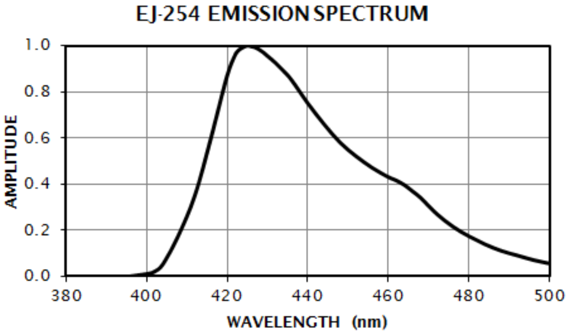

Figure 2.5: Emission spectrum of the EJ-254 plastic scintillator

standard to measure the light output of other scintillators. However, this organic crystal has a decay time around 30ns which is way worse than what we can reach with those plastic scintillators as seen in Table.2.1. For our purpose of working with high intensity signals, anthracene is then not our best option.

2.1.2 Boron loading

In order to boost the energy deposition from neutrons, one can use some neutron capture reactions with a positive Q-value. There are three main reactions for thermal neutrons with a positive Q-value and a high cross section as shown in Fig.2.6 and 2.7. Those reactions have the equations that follows :

$$^{10}\mathrm{B} + \mathrm{n} \longrightarrow ^{7}\mathrm{Li} + \alpha \qquad (\mathrm{Q} = 2789.91\mathrm{keV}) \tag{2.1}$$

$$^{6}\mathrm{Li} + \mathrm{n} \longrightarrow ^{3}\mathrm{H} + \alpha \qquad (\mathrm{Q} = 4783.47\mathrm{keV}) \tag{2.2}$$

$$^{3}\mathrm{He} + \mathrm{n} \longrightarrow ^{3}\mathrm{H} + \mathrm{p} \qquad (\mathrm{Q} = 763.75\mathrm{keV}) \tag{2.3}$$

Moreover, Gadolinium is an element with several stable isotopes with also positive Q-values and high cross sections for thermal neutron capture. Those isotopes are ^{155}Gd and ^{157}Gd. The associated radiative capture Q-values are respectively 8536.35 keV and 7937.39 keV.

A detector designed for neutrons and especially thermal neutrons uses one of those four elements

PROPERTIES	EJ-254-1%
Light Output (% Anthracene)	60
Scintillation Efficiency (photons/1MeV e^-)	9200
Wavelength of Maximum Emission (nm)	425
Rise Time (ns)	0.85
Decay Time (ns)	1.51
Pulse Width, FWHM (ns)	2.24
No. of H Atoms per cm^3 ($x10^{22}$)	5.16
No. of C Atoms per cm^3 ($x10^{22}$)	4.62
No. of ^{10}B Atoms per cm^3 ($x10^{20}$)	1.14
No. of Electrons per cm^3 ($x10^{23}$)	3.33
Density ($g.cm^{-3}$)	1.021
Polymer Base	Polyvinyltoluene
Refractive Index	1.58
Softening Point	75°C
Vapor Pressure	Vacuum-compatible
Coefficient of Linear Expansion	7.8 x 10^{-5} below 67°C
Light Output vs. Temperature	At 60°C, L.O. = 95% of that at 20°C No change from 20°C to -60°C
Temperature Range	-20°C to 60°C

Table 2.1: *Specifications given by Eljen Technology for the EJ254 scintillator(125)*

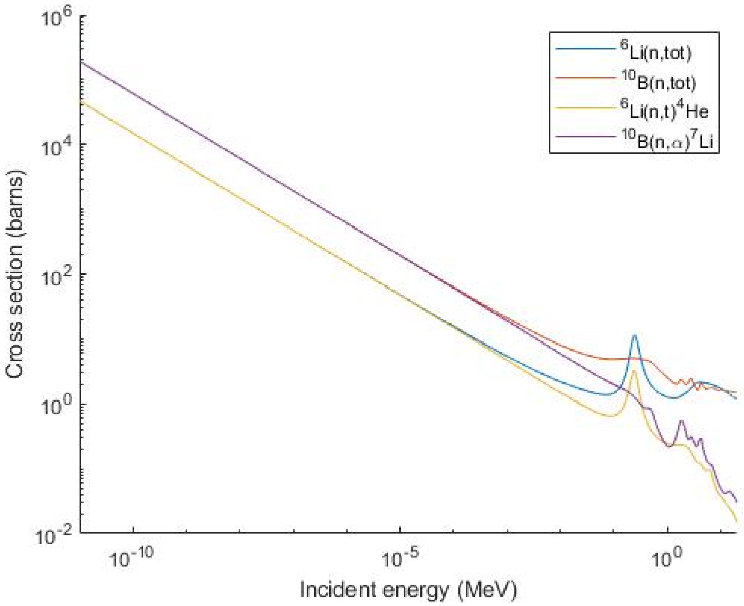

Figure 2.6: *Cross sections of neutron capture and (n,α) or (n,t) reactions for respectively ^{6}Li and ^{10}B(81)*

to increase energy deposition and differentiate energy depositions due to neutrons from ones due to gammas or other ionizing particles. We can then look at what is available from manufacturers, i.e. Saint-Gobain and Eljen Technology. Gadolinium enriched detectors are only liquid scintillators which we dismissed for reasons explained above. ^{3}He is used in the gas proportional counter we already talked about. ^{6}Li can be found in liquid scintillator but also in lithium compound enriched with a ZnS:(Ag)

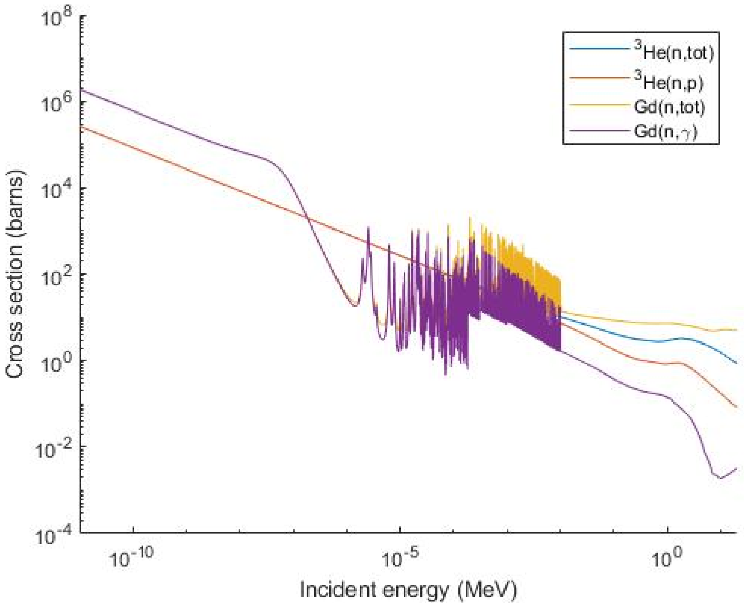

Figure 2.7: *Cross sections of neutron capture and (n,p) or (n,γ) reactions for respectively ^3He and natural Gd(81)*

fluorescent powder. However, the decay time for this technology is 200 ns which is really long compared to what is possible with plastic scintillators. Saint-Gobain also sells a glass scintillator enriched with ^{6}Li but its performances in decay time and light output are not as good as the EJ-254 ones. The best technology for our purpose is then the boron loading plastic scintillator.

The reaction which has for equation 2.1 can leave the ^{7}Li residual nucleus either in the ground state or the first excited state which has an energy level equal to 477.61 keV. Indeed, we can see Fig.2.8 that the second excited state has an energy level equal to 4630 keV which is higher than the Q-value and the kinetic energy the neutron can usually bring. When we look at the cross sections for the two possible ending states as shown in Fig.2.9, we can see that for neutron kinetic energies up to 10keV, the ^{7}Li residual nucleus is in the first excited state 93.7% of the time. The Q-value is then 2789.91 - 477.61 = 2312.30 keV. The excited ^{7}Li nucleus deexcites itself with a half-life of 73 fs emitting a 477,595 keV gamma which have only a very little chance to deposit its energy inside the scintillator

We can calculate the recoil energy for both the ^{7}Li nucleus and the α particle using the conservation of energy and momentum. Since there are only two products, the incoming neutron, the alpha and the ^{7}Li nucleus produced stay in the same plane. If we consider the laboratory referential with the ^{10}B nucleus

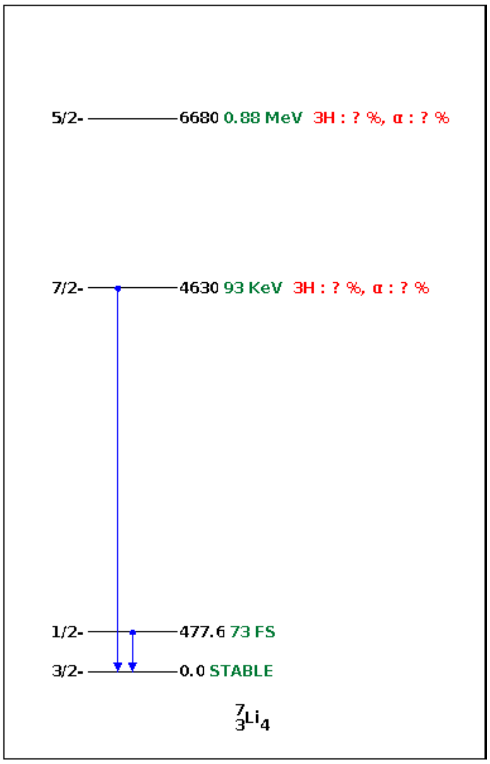

Figure 2.8: *Level scheme of the* ^{7}Li *nucleus*(126)

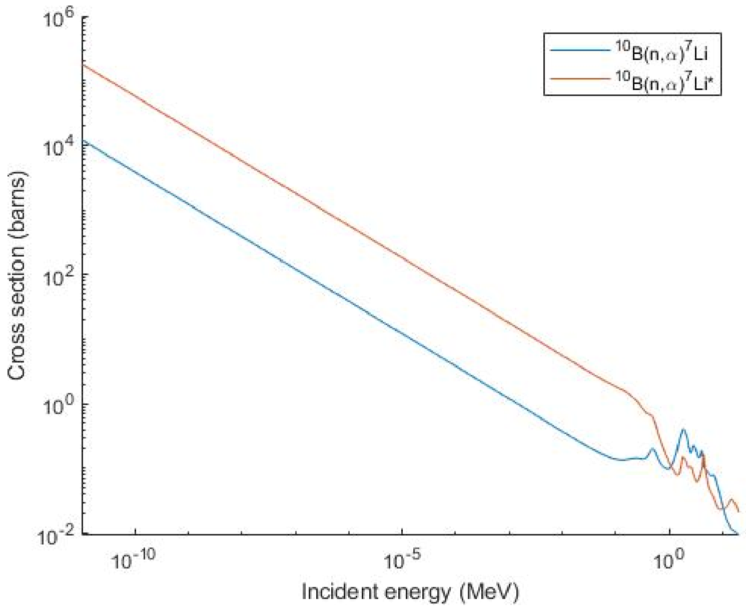

Figure 2.9: *Cross sections of* $^{10}B(n,\alpha)^{7}Li$ *and* $^{10}B(n,\alpha)^{7}Li^{*}$(81)

immobile in this one, and the x axis being in the incoming neutron direction, we can write :

$$Q = T_{Li} + T_{\alpha} - T_{n} \tag{2.4}$$

$$p_{n}c = p_{Li}c\ cos\theta_{Li} + p_{\alpha}c\ cos\theta_{\alpha} \tag{2.5}$$

$$0 = p_{Li}c\ sin\theta_{Li} + p_{\alpha}c\ sin\theta_{\alpha} \tag{2.6}$$

Q is the Q-value. T_n, T_{Li} and T_α are the kinetic energies of respectively the incoming neutron and the outgoing ^{7}Li nucleus and α particle. p_n, p_{Li} and p_α are the momentums of the same particles. θ_{Li} and θ_α are the angle of the outgoing direction of the corresponding particles. Using the relativistic definition of the momentum, we can write :

$$(p_nc)^2 - 2p_{Li}p_nc^2cos\theta_{Li} + (p_{Li}c)^2 = (p_\alpha c)^2 \tag{2.7}$$

$$p_ic = \sqrt{T_i(T_i + 2M_ic^2)} \tag{2.8}$$

$$\begin{aligned} T_\alpha(T_\alpha + 2M_\alpha c^2) =& T_n(T_n + 2M_nc^2) \\ & - 2\sqrt{T_n(T_n + 2M_nc^2)}\sqrt{T_{Li}(T_{Li} + 2M_{Li})c^2}cos\theta_{Li} \\ & + T_{Li}(T_{Li} + 2M_{Li}c^2) \end{aligned} \tag{2.9}$$

M_n, M_{Li} and M_α are the masses of respectively the incoming neutron and the outgoing ^{7}Li nucleus and α particle. c is the speed of light. Since the incoming neutron is almost always thermal, it has a very low kinetic energy in comparison with the Q-value and other recoil energies. We can then consider it null and simplify a lot the equations, especially equation 2.9.

$$T_{Li}(T_{Li} + 2M_{Li}c^2) = T_\alpha(T_\alpha + 2M_\alpha c^2) \tag{2.10}$$

$$Q = T_{Li} + T_\alpha \tag{2.11}$$

$$T_\alpha = \frac{Q(Q + 2M_{Li}c^2)}{2(M_\alpha + M_{Li})c^2 + 2Q} = 1466.5 \text{ keV} \tag{2.12}$$

$$T_{Li} = \frac{Q(Q + 2M_\alpha c^2)}{2(M_\alpha + M_{Li})c^2 + 2Q} = 845.8 \text{ keV} \tag{2.13}$$

To conclude, when a neutron reacts with a ^{10}B nucleus, there is 93.7% chance to produce a ^{7}Li residual nucleus with a 1466.5 keV recoil energy, an alpha particle with a 845.8 keV kinetic energy and a 477.6 keV gamma. There is also a 6.3% chance to produce a ^{7}Li residual nucleus with a 1769.4 keV recoil energy and an alpha particle with a 1020.5 keV kinetic energy. According to SRIM calculation (127), the expected range for such α particles or ^{7}Li ion is around 5 μm so all the energy is deposited in the doped scintillator almost all the time. According to the Birks' formula(128), only a part of this energy will be converted in light and be detected by the PMTs. This proportion will be determined later on during the calibration process.

But first, it can be interesting to thermalize the incoming neutrons to increase our detector sensitivity.

2.1.3 Thermalization

Interest

In the high intensity laser environment we are working with here, there is two main advantages to moderate the neutrons that we want to detect. The first advantage is true for all kind of environment. As it can be seen in the Figs.2.6 and 2.7, all neutron detectors using neutron-capture reactions are way more efficient for thermal neutrons than for rapid ones. Indeed, the cross sections for those reactions increase tremendously with the decrease of the neutron energy.

Another advantage of thermalization is specific to our subject. Thermalization takes time and will delay the actual detection of the neutron in comparison of the time they enter the detector. This is of particular interest since during an high intensity laser shot, there is two phenomena which can disturb a lot the detectors for some time. First, there is the production of a huge amount of ionizing radiations, especially gamma rays, which tend to totally overflow the scintillators, even with a lot of protection. Secondly, such a laser generates a very important electromagnetic pulse (EMP) which has the bad habit to induce a lot of noise or even worse in all electronic systems. Even though all electronic parts are put in Faraday cages and all the wires are protected in metallic sockets, it can still induce some problems in the detected signals for some time after the shots. Hence, being able to delay at least a part of the signal to detect, until the detectors are back online and working properly is a huge asset. It is then very easy using expected neutron spectrum and Geant4 simulations to retrieve an original number of neutrons. Shots with a huge amount of noise will increase the error bars but should not prevent us from making a measure.

When a neutron has an elastic shock with a nucleus, we can calculate the speed ratio between the original and later speed. Indeed, if we consider a ratio of mass A between the mass of the neutron and the mass of the hit nucleus, and that the neutron doesn't have a relativistic speed, we can write the following equation due to conservation of the energy and momentum in the laboratory referential:

$$v_n^2 = v_{n'}^2 + A v_A^2 \tag{2.14}$$

$$A^2 v_A^2 = v_n^2 - 2 v_n v_{n'} cos\theta_{n'} + v_{n'}^2 \tag{2.15}$$

v_n, $v_{n'}$ and v_A are the speed of respectively the incoming neutron, the outgoing neutron and the recoil speed of the nucleus. $\theta_{n'}$ is the angle of the neutron deviation in the laboratory referential. After some calculations, we can find out that :

$$\begin{aligned}\left(\frac{v_{n'}}{v_n}\right)^2 &= \frac{A^2 + 2Acos\theta_{n'}\sqrt{1 - \frac{sin^2\theta_{n'}}{2A}} + 1 - 2sin^2\theta_{n'}}{(A+1)^2} \\ &= 1 - \frac{2A\left(cos\theta_{n'}\sqrt{1 - \frac{sin^2\theta_{n'}}{2A}} - 1\right) - 2sin^2\theta_{n'}}{(A+1)^2}\end{aligned} \tag{2.16}$$

The equation 2.16 shows us that, for any angular deviation, the bigger A ratio, the smaller the decrease of the neutron speed. Hence, for a same atomic density, hydrogen is the most effective nucleus to slow down neutrons. Moreover, the higher the atomic density, the more probable it will be for a neutron to have an elastic collision with an hydrogen nucleus. That is why we went with High Density PolyEthylen (HDPE) as moderator since it combines the two qualities we just talked about.

Dimensioning simulations

With this detector, we aim to have an efficiency as high as possible while taking into account the constraints the high intensity laser environment impose. To have a maximum angular coverage with a reasonable amount of scintillating material, it is important to be close from the neutron source, surrounding it. The best is to be able to place the detector inside the interaction chamber. This imply some constraints especially spatially.

First the height is limited both from the height of the chamber and the fact that the laser paths are often going through the top part of the chamber before being sent to the Target Chamber Center (TCC) as it can be seen in the example Fig.. That is why we decided to set a maximum height for the detector which is 60 cm. Second, some space is also needed in the middle of the chamber to accommodate the target holding system and some optical systems that might be needed to place the target and the laser focus, or to some diagnostics. We decided to set a 40 cm diameter free cylinder around the TCC.

We also need to accommodate some paths in the horizontal plane for some potential paths for either intense lasers or diagnostics's views. That is why we decided to design a modular assembly of detector parts cut in a cylinder with an inner diameter of 40 cm and a height of 60 cm. Then, for any needed path in the horizontal plane, we can remove the corresponding parts to empty the space.

To set the other geometrical parameters of the detector, we used GEANT4 simulations (7; 129; 130). GEANT4 is a very well-known and used Monte-Carlo simulation toolkit to simulate the passage of energetic particle through matter. All the simulations have been done with the version 10.5.

To begin, we used a modified version of the code developed for the BRIKEN project (131; 132; 133). In order to use accurate cross-section for scattering and nuclear reactions for neutrons below 20 MeV,

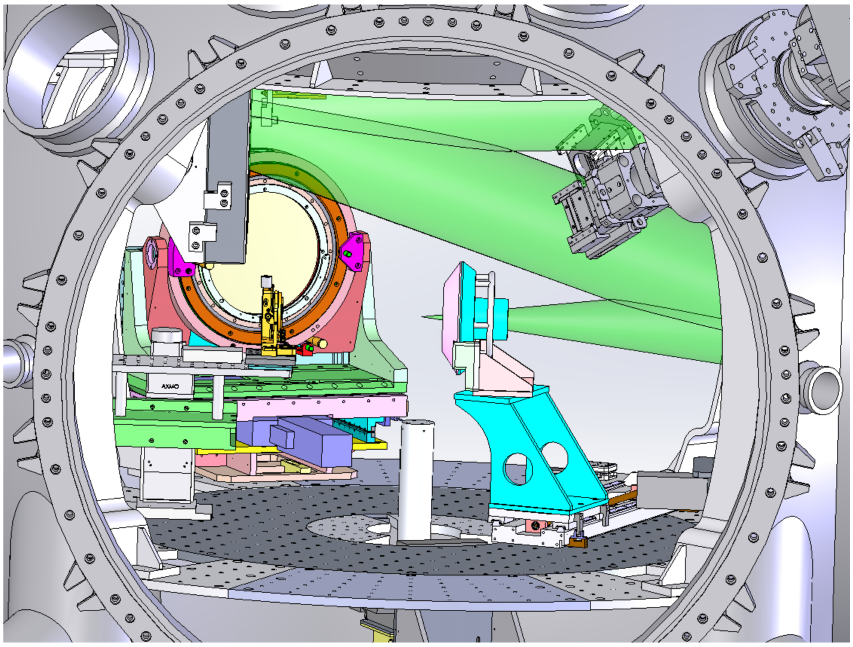

Figure 2.10: *CAD side view of an experimental chamber, the MILKA chamber of the LULI2000 facility. The laser path is represented in green.*

we used the NeutronHP physics list. To handle more generic interactions, we also used the physics lists G4DecayPhysics, G4RadioactiveDecayPhysics and G4EmStandardPhysics.

In a first approximation, we used a cylindrical geometry of HDPE with a 40 cm inner diameter, a 65 cm outer diameter and a 60 cm height. Ten scintillating units with a 2,54 cm diameter and a 60 cm height are disposed in the HDPE cylinder on a 50 cm circle. HDPE was set as a CH_2 material with a density of 0.95 $g.cm^{-3}$. The scintillating units were composed a 0,102 cm thick layer of stainless steel and a 2.438 diameter cylinder of scintillating material. The scintillating material was simulated using the C, H and ^{10}B proportion and the density given in Table 2.1. A more precise composition of the EJ-254 plastic scintillator is not publicly available since it is commercially protected. We will only consider the deposited energy in the scintillator and not the production of light since attempts to do so using GEANT4 have underestimated it a lot (134; 135).

We can then monitor the energy deposited in the scintillating unit in different configurations and use this to optimize the dimensions that remain unfixed. An energy deposition is here defined by the sum of all the interactions which deposit some energy in the matrix of one defined scintillator. For the first simulations, we used isotropic neutron sources with monoenergetic distributions in steps of 100 keV ranging from 1 MeV to 1,5 MeV. The number of scintillators was by default equal to 10, the external diameter of the HDPE cylinder to 65 cm and the diameter of the circle the scintillators are placed on to 50 cm.

Fig.2.12 has several interesting features. First of all, we can clearly see a main peak at 2312 keV which

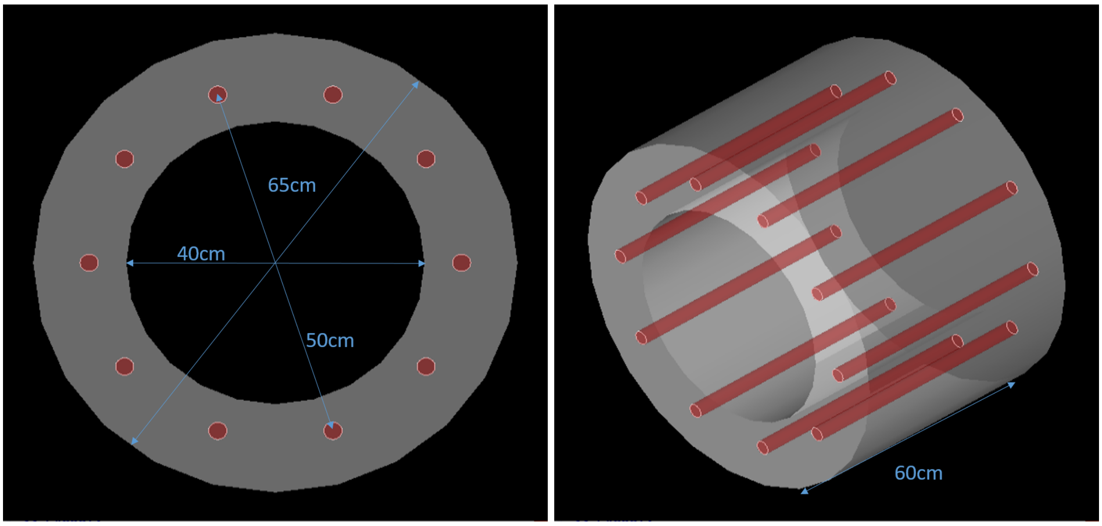

Figure 2.11: Views of the geometry used for the first simulations. In grey is the HDPE cylinder. In red are the scintillating units. The blue indications give the length of several dimensions.

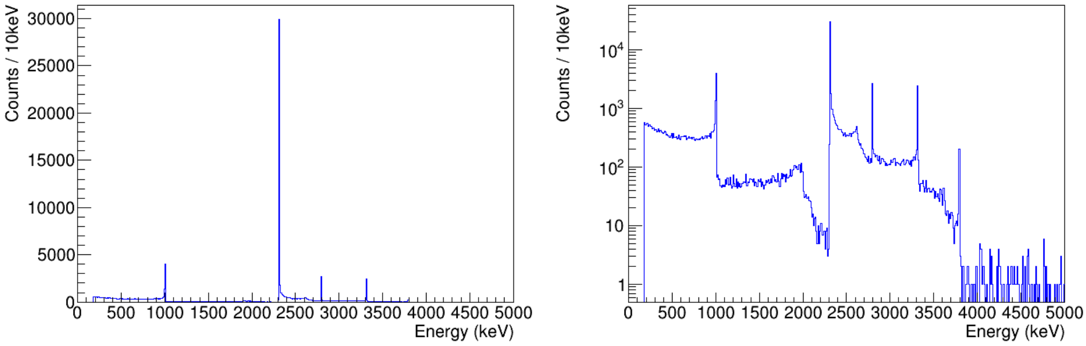

Figure 2.12: Histogram counting energy deposition in the scintillating units according to the energy deposited in both linear and logarithmic scale for 1 million events using an isotropic 1 MeV neutron source and the setup shown Fig.2.11.

corresponds to the Q-value of the ^{10}B(n,α)^{7}Li*. This totally makes sense since it is the most probable nuclear reaction and that the products have an overwhelming chance to deposit their recoil energy in the scintillator due to their 5 μm mean range. The second most important peak is at 2790 keV which corresponds to the Q-value of the less probable ^{10}B(n,α)^{7}Li reaction. An other interesting peak is seen at 1 MeV. It corresponds to the neutrons which entirely thermalized in the PVT matrix without reacting with any ^{10}B nucleus. In the same logic, we can also see two peaks at 3312 keV and 3790 keV for neutrons which entirely thermalized in the PVT matrix but also reacted with a ^{10}B through the corresponding channel. Below 1 MeV and between the four highest energy peaks, there are energy depositions which mainly corresponds to neutron thermalizing only partly in the PVT matrix and react or not. A last interesting feature of this histogram is the bump located next 2623 keV. Indeed, if we calculate the Compton edge energy of the 477,61 keV gamma emitted by the excited ^{7}Li nucleus after the most probable reaction, Eq.2.17 gives us 311.16 keV. Added to the Q-value of the reaction that generates this gamma, we found an energy of 2623,46 keV. Then, this bump surely corresponds to the Compton edge associated to this gamma. One could even argue that the 2790 keV peak could contain events where the neutron capture produced an excited ^{7}Li nucleus, and the produced gamma deposited all its energy through photoelectric effect in the PVT matrix. This photoelectric effect is however very unlikely to happen with nuclei with so low Z.

$$E_e = \frac{2E_\gamma^2}{2E_\gamma + m_e} \tag{2.17}$$

From now on, we will assume that the behaviour of the height of the main peak represents well the behaviour of the overall efficiency of the detector. It is especially true since that, for other energy depositions where proton, carbon nuclei or gamma are vector in the energy deposition in the PVT matrix, we do not know the scintillating efficiency. So the 2312 keV peak is indeed the main contributor of the neutron peak that we should see in the energy histogram retrieved from the PMTs signal. We define for the next figures the height of the main peak as the number of events in the 10 keV wide bin corresponding to the energies between 2310 and 2320 keV.

In Figs.2.13, we fix every parameters and look at the influence of each free parameter one by one. Fig.2.13(a) shows the evolution of the peak height according to the number of scintillators. As one could expect, the peak height increases linearly with the number of scintillators when it is low enough. However, we see that over 15 scintillators, the gain in efficiency when we add units is not as good. That effect becomes really strong above 30 scintillators. Fig.2.13(b) shows the evolution of the peak height according to the HDPE cylinder external diameter. We see here that after a great increase, the peak height reaches a plateau which means that there is no use to add more HDPE to collect the backscattered neutrons. For all the other parameters set to default, it looks that this plateau is reached as soon as 65 cm.

Fig.2.13(c) shows the evolution of the peak height according to the scintillator ring diameter. This one is a bit more complicated and reaches a seemingly neutron energy dependent maximum. Besides, the peaks corresponding to the deposition of the kinetic energy of the incoming neutrons evolve differently when the scintillator ring diameter approaches the value of the internal diameter of the HDPE cylinder. As it can be seen on Figs.2.14, the peak corresponding to the sum of the Q-value of the main reaction and the kinetic energy of the incoming neutrons is no longer negligible in comparison of the main peak, for a scintillator ring diameter equal to 45 cm. If we consider that the efficiency evolves with the sum of the height of those two peaks and not only the one of the main peak, it would look that the smaller the scintillator ring diameter, the bigger the efficiency. However, we don't know how efficiently a proton hit

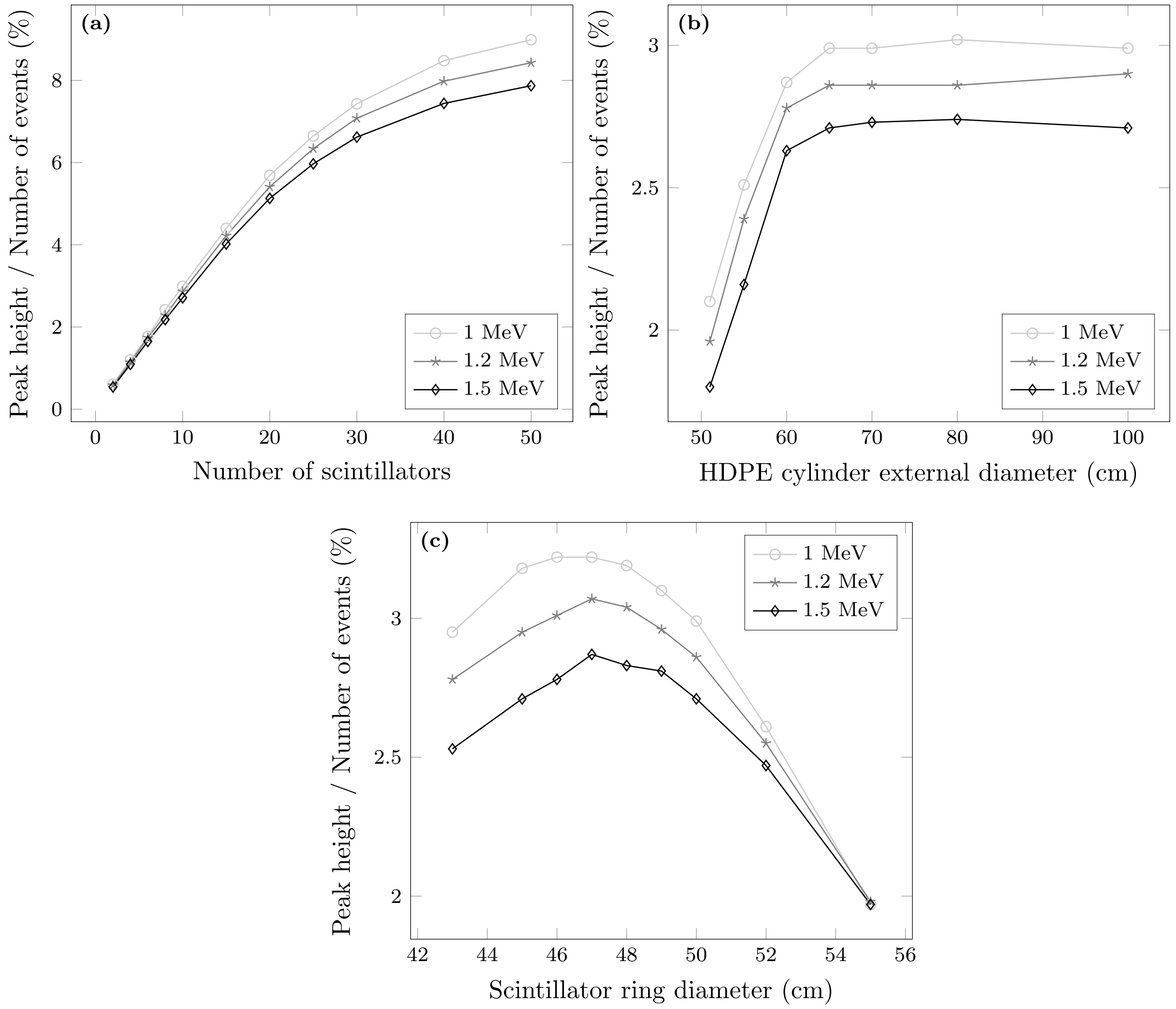

Figure 2.13: *Evolution of the main peak height according to several parameters for 1 MeV, 1.2 MeV and 1.5 MeV neutrons.* (*a*) *shows the according to the number of scintillators,* (*b*) *the external diameter of the HDPE cylinder and* (*c*) *the diameter of the circle the scintillator are placed on.*

by the thermalizing neutron will transmit its recoil energy to ionize its environment and produce light. Still, we know that this efficiency is not null and that there is a chance that those events will not be in the neutron peak we are expecting to see. Besides, the same thing happens for the peak corresponding to the neutron thermalizing in the PVT matrix without reacting with a ^{10}B nucleus. Then, it seems more reasonable to try to avoid such a problem by choosing a scintillator ring diameter for which those events are negligible and most of the neutrons which react have been thermalized in the HDPE moderator. However, we still want to have an efficiency as great as possible. In the end, we decided to go with a scintillator ring diameter equal to 48 cm.

An important feature of the thermalization is the time it takes for the neutron to slow down before being captured by a ^{10}B nucleus. Indeed, in case our detector is unresponsive for some time after the shot, we need to know the evolution of the detection rate. This would be required to be able to retrieve

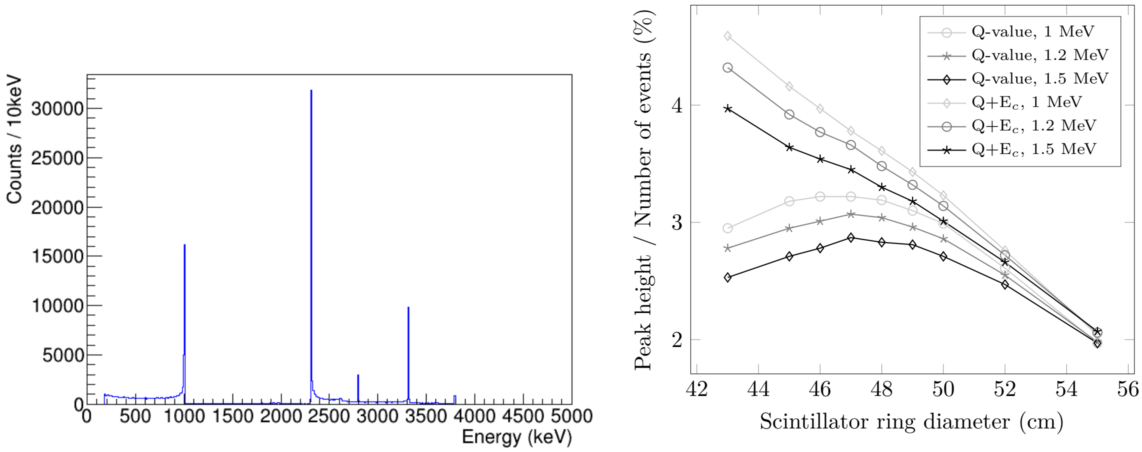

Figure 2.14: *On the left, histogram counting energy deposition in the scintillating units according to the energy deposited for 1 million events using an isotropic 1 MeV neutron source and the setup shown in Fig.2.11 except for the scintillator ring diameter here equal to 45 cm. On the right, evolution of both the main peak height and the addition of two peak heights, according to the scintillator ring diameter. The two peaks in question are the main peak and the peak corresponding to the main reaction Q-value plus the kinetic energy of the incoming neutron. Those two peaks are the ones at 2312 keV and 3312 keV for the histogram shown here on the left.*

the right number of emitted neutrons.

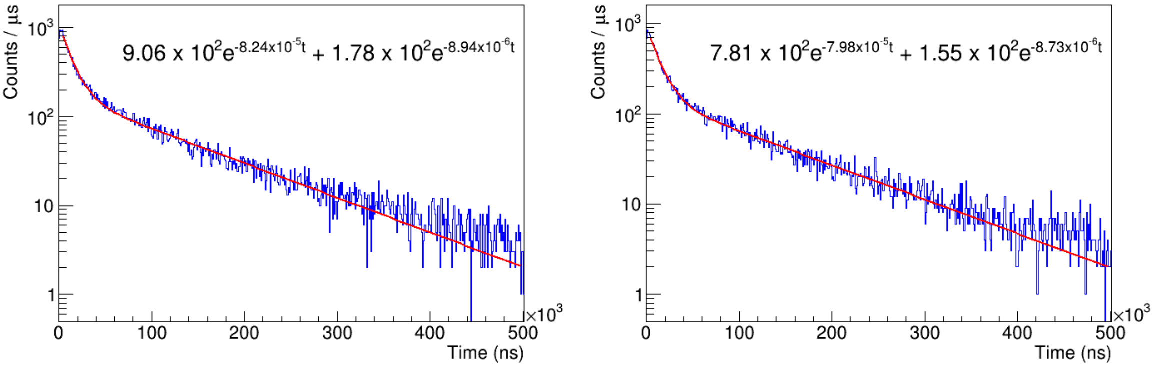

Figure 2.15: *Histograms counting energy deposition in the scintillating units according to the time of the last interaction. Those are the result of a 1 million events Geant4 simulation using the setup shown in Fig.2.11, except for the scintillator ring diameter here equal to 48 cm, and an isotropic respectively 1 MeV and 1.5 MeV neutron source for the left and right histogram. Only the energy deposition which are in the main peak with an energy between 2310 keV and 2320 keV were considered in the drawing of those wo histograms. The equations written on both histograms correspond to the fitting function.*

For less than 2 μs, the detection rate increases and it then decreases exponentially. As it can be seen in Fig.2.15, it seems that the best function to fit this decrease is the sum of two exponential. Tab.2.2 gives the fitting parameters for the fitting function given by the equation 2.18, according to the neutron energy. Hence, for neutrons with energy between 1 MeV and 1.5 MeV, the thermalization process has two time constant giving the decay of the detection rate. Those two constants are approximately equal to 12 μs and 110 μs. For any expected spectrum, this kind of simulation might have to be done in order to retrieve

Energy (MeV)	a_0	$1/t_0$ (ns^{-1})	a_1	$1/t_1$ (ns^{-1})
1	$9.06(21).10^{2}$	$8.24(23).10^{-5}$	$1.78(4).10^{2}$	$8.94(12).10^{-6}$
1.1	$8.75(20).10^{2}$	$8.47(21).10^{-5}$	$1.79(3).10^{2}$	$9.01(11).10^{-6}$
1.2	$8.39(20).10^{2}$	$8.12(23).10^{-5}$	$1.70(4).10^{2}$	$8.83(11).10^{-6}$
1.3	$8.37(20).10^{2}$	$8.39(24).10^{-5}$	$1.71(4).10^{2}$	$9.07(11).10^{-6}$
1.4	$7.79(19).10^{2}$	$8.16(24).10^{-5}$	$1.70(4).10^{2}$	$9.11(11).10^{-6}$
1.5	$7.81(18).10^{2}$	$7.98(20).10^{-5}$	$1.55(3).10^{2}$	$8.73(11).10^{-6}$

Table 2.2: *Fitting parameters for the time evolution of the energy deposition in the scintillating units for for several neutron energies.*

a correct number of neutrons.

$$f(t) = a_0 e^{-\frac{t}{t_0}} + a_1 e^{-\frac{t}{t_1}} \tag{2.18}$$

To summarize, the dimensions of the detector which has been set at the end of this study are an outer PET diameter of 65 cm, an inner PET diameter of 40 cm, an height of 60 cm and a scintillator ring diameter of 48 cm.

2.2 Preliminary tests

Before committing to build the whole detector assembly, we decided to build a prototype unit in order to test its response, first to continuous gamma and neutron sources and second to real experimental conditions implying intense laser-matter interaction. It was also the opportunity to start developing an analysis method of the signals we would get from such an assembly. The prototype consisted of a 50 mm long and 30 mm diameter cylindrical scintillator associated with two PMTs, one at each end of the cylinder as shown in Fig.2.16. The scintillator model was EJ-254 1% boron loaded. The PMTs model was PMS XP2972 from Philips. Those PMTs have a 29 mm cylinder shape and are 100 mm long without the electronic pins nor the voltage divider part.

In order to use it as close as possible from the laser matter interaction point during a real experiment, the assembly was enclosed in a vacuum-tight and light-tight aluminum housing. The housing was totally hermetic so the components inside were kept under atmospheric pressure in any circumstance. To keep a good contact between both the PMTs and the scintillator, a spring was set between one of the PMT and the capsule wall. A drawing of this prototype is presented in Fig.2.16.

2.2.1 Prototype testing with continuous neutron and gamma sources

First, the prototype was tested using a ^{137}Cs gamma source, placed right next to the scintillator, next to the middle part of the capsule wall. This source had an activity of 313 kBq and emitted gammas with a 661.66 keV energy. Like for the 477.61 keV gammas possibly emitted after a neutron capture on ^{10}B,

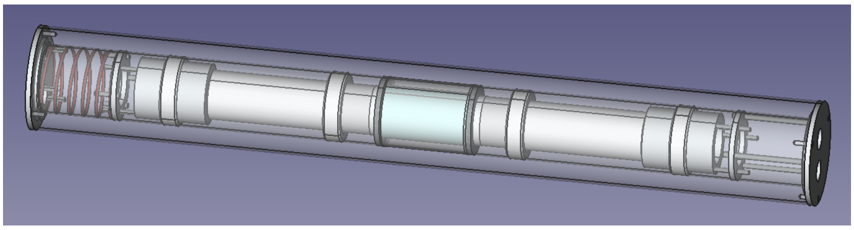

Figure 2.16: CAD drawing of the prototype used for the preliminary tests.

photoelectric absorption of those 661.66 keV gammas is very unlikely. As shown in Fig.2.17, there are indeed several orders of magnitude between the probabilities of photoelectric absorption and Compton scattering at those energies. Hence we won't be able to see any clear photoelectric peak. However, we can see the Compton edges which, according to Eq.2.17, corresponds to a 477.34 keV energy. As a reminder, this energy corresponds to the energy transferred during a 180° scattering of the incoming particle, i.e. the gamma, which is the maximum energy which can be transferred this way.

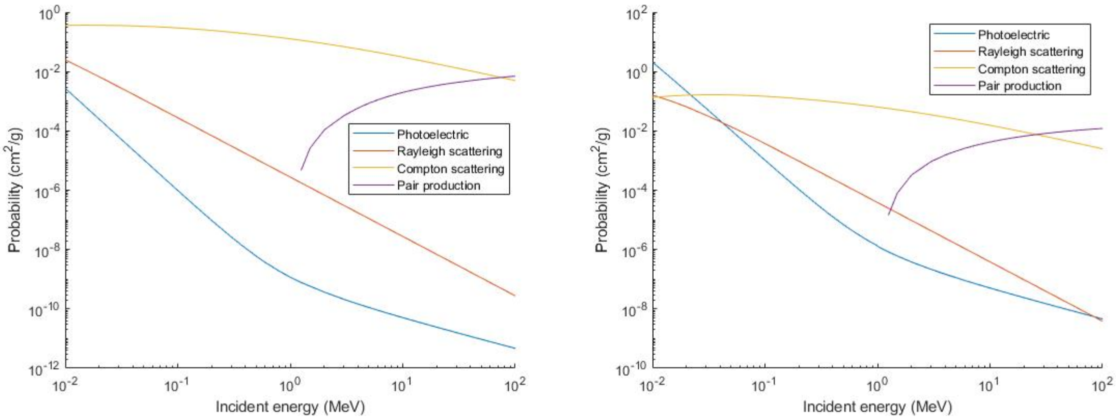

Figure 2.17: Probability of interaction of a photon with an atom according to the the photon energy for different types of interaction. The probabilities are for an hydrogen atom on the left and a carbon atom on the right(136).

One of the first tests to do with this prototype was to have working together two PMTs in a particular mode called coincidence counting mode. Indeed, the idea behind the use of two PMTs is to be able to reduce the potential electronic noise that the conditions of intense laser-matter interaction might induce. Since those two PMTs are collecting light from the same scintillator, one on each end, and that this scintillator emits its light in a few ns window as shown in Table.2.1, a positive signal on one PMT should correspond to another positive signal with characteristics near enough in amplitude and time position. If not, the detected signal is surely noise. In our analysis scripts, we then have a temporal condition on the proximity of signal detection from each PMT.

The two PMTs were biased with a 1.2 kV high voltage and the reading out was done using CAEN VX1730B digitizer units. This digitizer has a sampling frequency of 500 MS/s and a resolution of 14 bits on either a 0.5 or 2 V range. The card was operated with the Digital Pulse Processing-Pulse Shape Discrimination (DPP-PSD) firmware version 4.17. So the integration of each peak is done automatically by the firmware. The thresholds used to define a peak have been chosen manually. Those thresholds need to meet two qualities. They have to be low enough to see the signal and some electronic noise in the low energy part. They also have to be high enough not to have the noise representing a too important proportion of the recorded peaks and flood the signal or even saturate the cards. Their definition is then an incremental process until reaching a satisfying value.

For the energy calibration, we set the 477.34 keV Compton edge location at 80% height on the high energy side of the energy deposition distribution. This value of 80% has been found to well represent the Compton edge location for low Z scintillators by detecting the gammas fully backscattered by a scintillator using a High Purity Germanium (HPGe) detector(137). With this energy calibration, we obtained the two PMTs responses presented in Fig.2.18. The energy calibration will be presented more extensively in section 2.3.2. The unit for the light amount/energy measured by the PMTs is keV$_{ee}$ where $_{ee}$ stands for electron equivalent. This means that what we measure here relates to the energy deposited in the electron population of the scintillator.

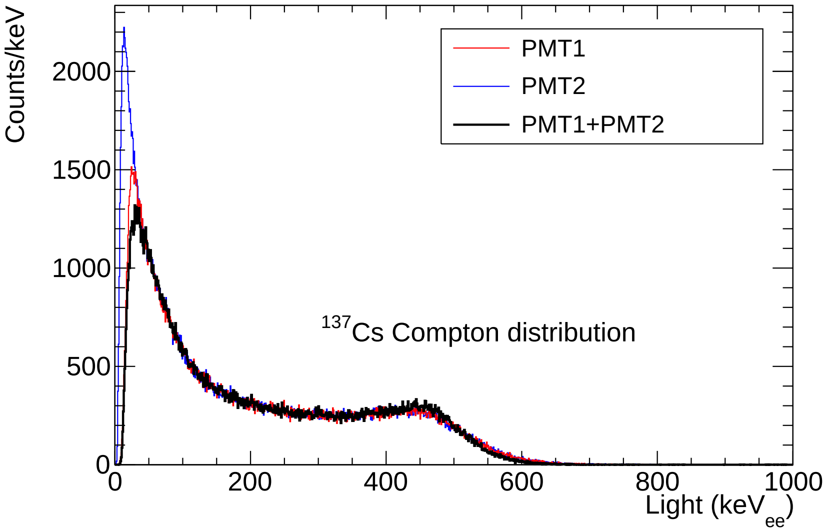

Figure 2.18: *Histogram of the light collected by the prototype detector exposed to a ^{137}Cs gamma source. Blue and red curves each correspond to an individual PMT response. The black curve correspond to events coincident in both PMTs and for which the two PMTs energies have been summed and rescaled along the x-axis.*

We see that the responses of the two PMTs are very similar. However, we see that, even though we used the same thresholds, the low energy part is very different from one PMT to the other. This implies that the noise signal depends a lot on the PMT. The black curve represents the events coincident within a 5 ns window and with an energy proportional to the sum of the energy from the two PMTs. The energy has been rescaled to have the Compton edge of the black curve at the right energy. The resulting curve is really similar to the two precedent ones. This implies that almost no positive events are lost by this coincidence check. It is even a bit more well-defined in the higher energy part with a slightly sharper Compton edge. The low energy part is also slightly lower which is either a reduction of the electronic noise or a loss of some real energy depositions in the scintillator which are important enough to trigger one of the two PMTs. This possible loss of low energy events is not an issue since the energy deposition corresponding to neutron capture events should be high enough. The consequences on the results if the noise is higher in energy will be discussed later. This calibration result for which noise is not really strong compared to what can be experienced at high energy lasers, confirm that time coincidence can be used to select events and reduce possible noise during the future experiments.

To evaluate the neutron response, we used the PuBe neutron source described in Ref(138), with a moderator. The PuBe neutron source is based on two reactions described by the following equations :

$$^{239/240}Pu \longrightarrow ^{235/236}U + \alpha \qquad (Q = 5244.50/5255.75\ keV) \tag{2.19}$$

$$^{9}Be + \alpha \longrightarrow ^{12}C + n \qquad (Q = 5702.05\ keV) \tag{2.20}$$

This neutron source can then only emit one neutron per alpha decay. This neutron can also be produced in coincidence with a 4.4 MeV gamma produced by the ^{12}C nucleus excited in the first state. The energy of the produced neutrons is of several MeVs. However, we have seen that the boron neutron capture cross section decreases a lot when the energy increases. Hence, we used a moderator to slow down those neutrons to thermal energies. The PuBe source was placed 30 cm away from the prototype unit and a 10 cm thick HDPE moderator was placed in between. We also placed 5 cm of lead to reduce the influence of the 4.4 MeV gammas. Using the same energy calibration and the time coincidence condition, we have been able to produce the histogram presented in Fig.2.19.

As we could expect, the neutron signal is represented by a peak in this kind of histogram. This peak is centered on an energy value which corresponds to the portion of the Q-value which has been transmitted through the kinetic recoil energy of the α particle and ^{7}Li nucleus to the surrounding electrons. We see that in this case, the peak is centered on an 83.81(11) keV$_{ee}$ energy with a full width at half maximum (FWHM) of 28.55 keV$_{ee}$. This value is way lower than the Q-value, however it is high enough to be clearly separated from the noise. The value given by the constructor for the 5% boron loaded scintillator is 76 keV$_{ee}$. Since the 1% boron loaded scintillator which we are using here has a better scintillation efficiency, this value of 83.81(11) keV$_{ee}$ is not surprising. Furthermore, the time coincidence condition shows here much more clearly its efficiency to reduce noise signal. The neutron peaks is besides more well-defined in the combination of the two PMTs signal.

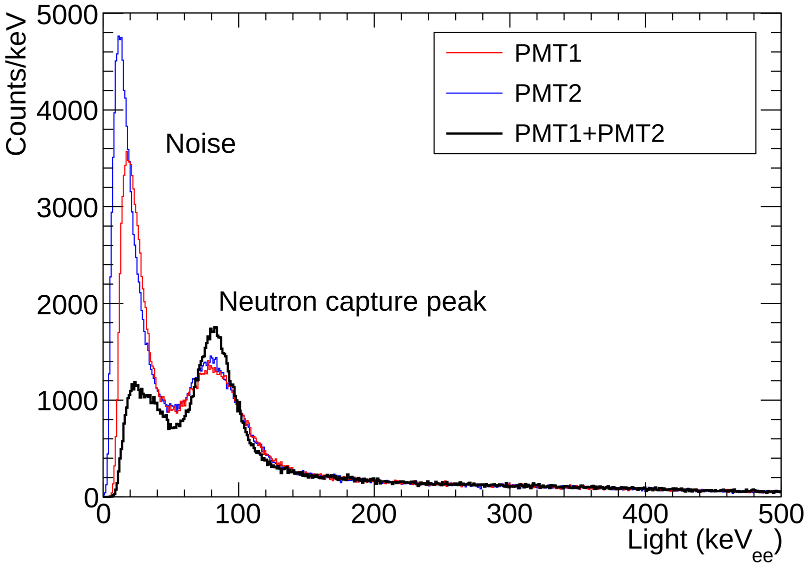

Figure 2.19: *Histogram of the light collected by the prototype detector exposed to a PuBe neutron source. Blue and red curves each correspond to an individual PMT response. The black curve corresponds to events coincident in both PMTs and for which the two PMTs energies have been summed and rescaled along the x-axis.*

2.2.2 Laser environment test

In order to test the response of the detector to the prompt gammas and x-rays generated after the laser irradiation, through a combinaison of synchrotron and Bremsstrahlung emission(139; 140; 141), and the EMP(142; 143; 144) generated by the laser-matter interaction, we have been able to use the prototype during an experiment were proton beams were generated for another purpose. This experiment was taking place at the Arcturus laser of the Heinrich Heine Universität of Düsseldorf(145). This laser has a typical pulse duration of 30 fs for an energy of 1.5 to 1.7 J on a focal spot of 5 μm. This gives a maximum intensity on target around 10^{20} W.cm^{-2}. The excellent contrast obtained thanks to a plasma mirror system makes it a good facility to generate high-energy proton beams(145). During the experiment we had the opportunity to piggyback to test the response of our prototype to this environment, the protons were used to irradiate mammalian cells and study their potential for proton therapy(146). The target used to produce protons was a 5 μm thick titanium foil. Our prototype was set horizontally 30 cm away from the target chamber center and 15 cm below the equatorial plane as described in Fig.2.20.

The two PMTs were biased with a 1 kV high voltage and the reading out was done using a Teledyne Lecroy oscilloscope with a maximum rate of 500 MS.s^{-1}. Some sets of traces recorded over 5 ms are displayed in Fig.2.21. The first noticeable feature is the very important peak corresponding either to the EMP or the energy deposition of the prompt gammas and x-rays in the scintillator inducing light emission within. However this peak seems to decrease very fast, faster than what is measurable with

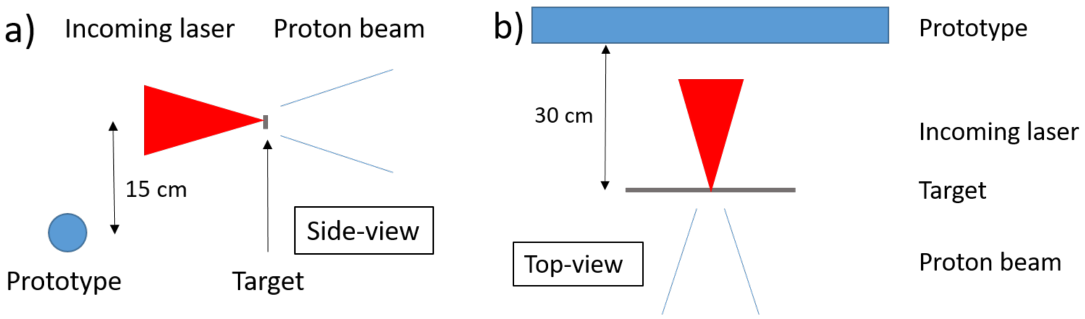

Figure 2.20: *Sketch of the setup used in Düsseldorf to test the laser environment response of our prototype. a) is a side-view and b) a top-view.*

those records. Then, the baseline tends to have some issue to come back to its precise initial value and might even go through some rebounds which take place on a long time scale, i.e. a few hundreds of μs. However, this doesn't seem to prevent the detection of some energy depositions which we supposed was due to some cosmic background or gammas produced after the shot outside the chamber by delayed (n,γ) reactions for instance. The important here is that such detection seems possible even though the initial value of the baseline isn't reached and that the height of the noise induced after the shot is way lower than the one of a real energy deposition. Indeed, this is especially proven by the energy deposition detected less than 0.5 ms after the EMP/prompt gamma peak even though the baseline did not come back to its pre shot value.

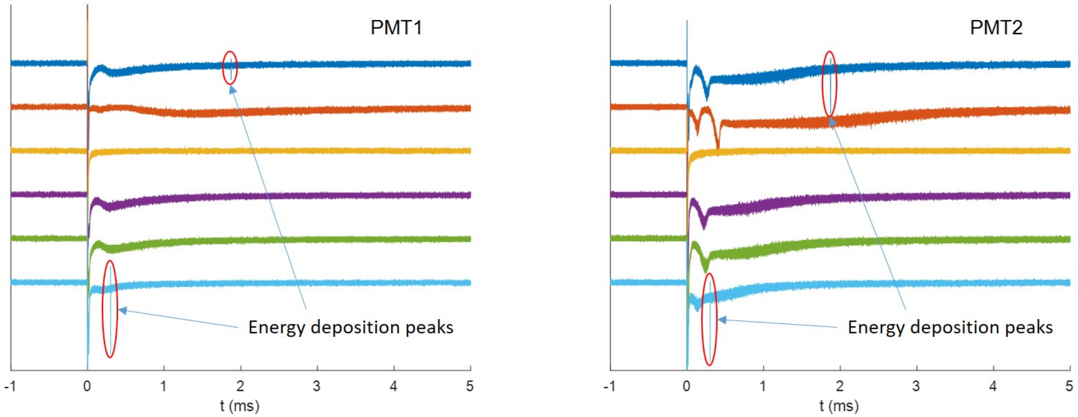

Figure 2.21: *Set of traces recorded for different shots over 5 ms. On the left are shown the traces for one PMT and for the other PMT on the right.*

To evaluate the unresponsive time of the prototype, we zoomed on the first peak region. The result of the superposition of traces from 12 different shots recorded over 10 μs is shown in Fig.2.22. We can see that the baseline comes back in the vicinity of the pre shot value as soon as 1 μs after the shot. Besides, before 1 μs, the temporal features of the traces evolution seem to be constant which means that it should depend on the PMT structure and its associated electronics. However, the rebound happening after has a much more random position and width.

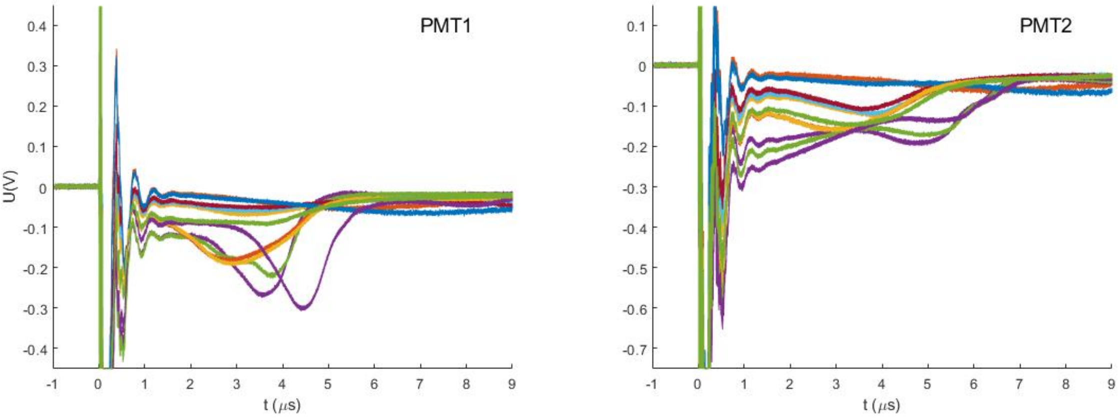

Figure 2.22: Set of traces recorded for different shots over 10 μs. On the left are shown the traces for one PMT and for the other PMT on the right.

In order to have a first idea of the energy deposition event shape, we also zoomed on some of those events as shown in Fig.2.23. As it was already shown with the ^{137}Cs gamma source and the PuBe neutron source, the main peaks of each PMTs are coincident with each other within a 5 ns window. We can also note that the FWHM of an event main peak is in the order of 8 timesteps, i.e. 16 ns. This is a bit higher than one could expect from the specifications of the scintillator and the PMTs used. Indeed, the EJ-254 scintillator has a pulse width of 2.24 ns and the XP2972 PMT has a time response FWHM of 3 ns. It could mean that the PMTs did not totally come back to their normal state. Another interesting feature is the clear positive rebound which exists after the main peak. We won't really use this but it is worth noting that there are electronic effects which don't correspond to a physical signal.

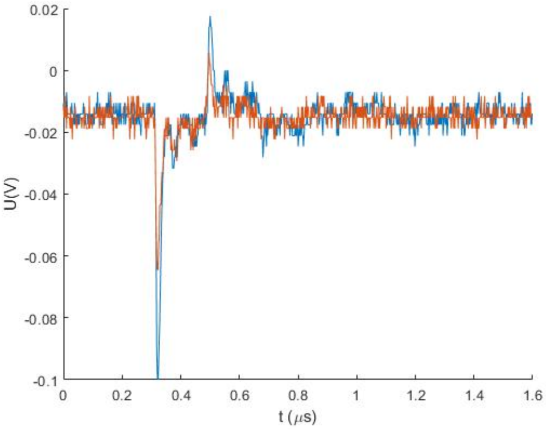

Figure 2.23: Zoom on an energy deposition event with the superposition of the two PMTs traces.

In the end, this test was conclusive. Indeed, even if the PMTs seem to struggle to come back to the exact pre shot baseline value, the prototype seemed able to detect some energy deposition events before the baseline stabilizes to its at-rest value. Besides, the temporal width of seemingly electronic rebounds are very different from the one of an energy deposition event. There are still some unresolved questions. Does the energy calibration we do using sources still stands in those experimental conditions for example. However, this test was positive enough for us to choose to build the full detector designed in the previous section.

2.3 Calibration

2.3.1 Technical specifications

Before building and calibrating the full detector designed earlier, there were still a few technical choices to make. First of all, as already explained, for the scintillator, we decided to go with the EJ-254 boron loaded model. Eljen Technology proposes three different percentages of boron loading which are 5%, 2.5% and 1%. The light output of the scintillator decreases when the boron loading increases. Indeed, the light output is 48% Anthracene for 5% boron loading when it is 60% for 1% boron loading as shown in Table.2.1(125). It is then easier to differentiate from noise neutron events with the 1% boron loaded scintillator. So, even though the overall efficiency of the detector is lowered by the fact that there are five time less nuclei to capture neutrons, we decided to go with the conservative choice and selected the EJ-254 1% boron loaded scintillator. For the dimension, we decided to associate two 200 mm long EJ-254 rods with a 25.4 mm diameter, 200 mm being the maximum length proposed by Eljen Technology. The edges were diamond milled and polished. The total scintillator length is then 40 cm which leaves 20 cm for the PMTs and the electronic connections.

To couple the scintillators between them and with the PMTs, we used EJ-560 optical interfaces which have a transmission coefficient higher than 90% on all the EJ-254 emission spectrum according to the enterprise data. Those optical interfaces are only 3 mm thick. Since the XP2972 PMTs used for the prototype were quite bulky, we decided to go for the PMT model 9112B from ET enterprise associated with its C673A voltage divider. This PMT has a 25 mm diameter and is only 43 mm long without the pins and has specifications almost identical to the XP2972. Even with the voltage divider and the electronic connectors, this fits in the 100 mm left on each end of the scintillator parts. Each ensemble scintillators-PMTs-electronic parts has been wrapped in TYVEK high-reflectivity paper(147), then placed between two HDPE semi-cylindrical shells with notches to keep the different pieces stuck to each other. A schematic of this assembly is presented in Fig.2.24.

Instead of using a voluminous HDPE cylinder, we decided to cut it into trapezoidal prisms which

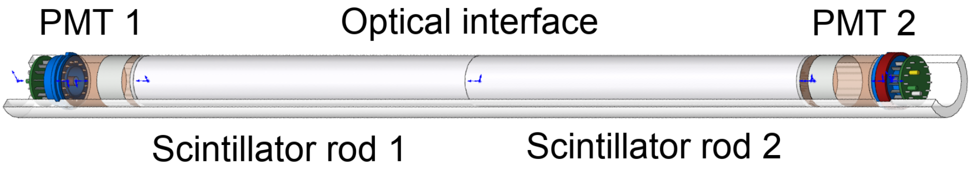

Figure 2.24: Schematic of a scintillator-PMTs assembly in half its HDPE shell.

contain each one a scintillator-PMTs assembly. This results in a modular assembly that is much more easy to manipulate, transport, install, etc. Besides, it allows us to imagine different configurations, depending on the experimental setup. A full cylinder can be assembled with 24 modules. The scintillator-PMTs assemblies presented in Fig.2.24 are then placed into those HDPE modules in which a cylindrical hole has been manufactured for the assemblies to exactly fit in. The hole doesn't reach the bottom part of the HDPE module and the top part has then to be sealed to be vacuum tight. This is done with a flange equipped with vacuum safe feedthroughs for both high voltage and signal cables of both PMTs. The LEon MOuttet (LEMO) standard has been used for those feedthroughs. This top part is presented in a schematic in Fig.2.25. The cables coming from the bottom PMT which are not represented on the schematic, are running in between the two HDPE shells where a free space has been set for it.

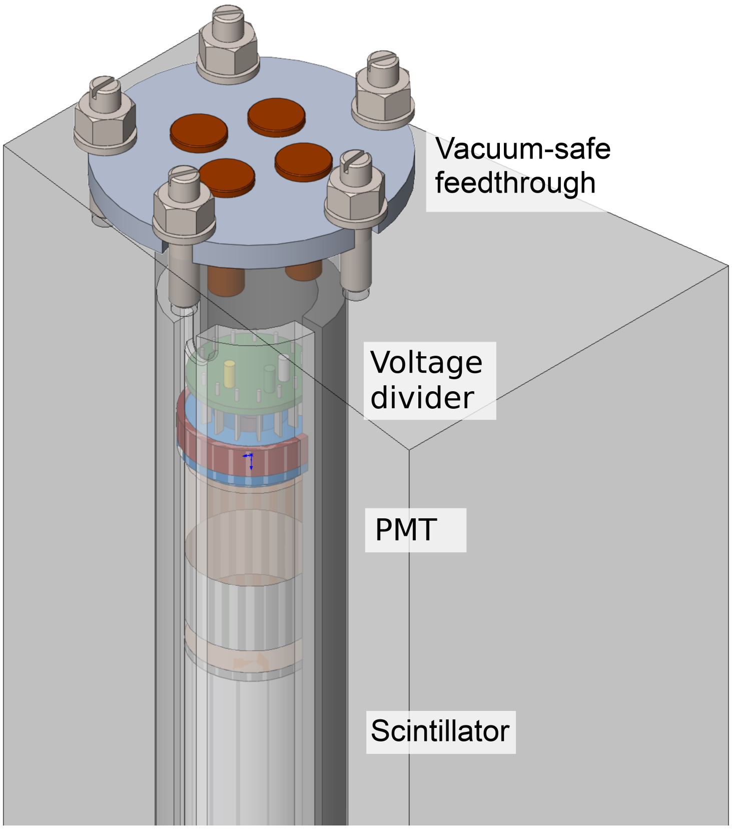

Figure 2.25: Schematic zoom on the top part of a detector module.

For considerations which are explained later in the commissioning experiment setup section 3.2.2, 15 of those units have been built for now. The calibration of the modules, both in energy and efficiency, has been done using the geometry setup that was elaborated for the LULI2000 experiment. All the units have been assembled and calibrated at the IFIN-HH facility, where radioactive sources were available.

2.3.2 Energy calibration

For the energy calibration, the PMTs were biased using two 24 channels CAEN A7030SN boards in a CAEN SY5527LC power supply system. The connection between the PMTs and the power supply was done using cables with Safe High Voltage (SHV) to LEMO connectors. For the signal part, the PMTs, were connected through LEMO-LEMO cables to three CAEN V1730SB cards. Those digitizers have 16 channels with a 14-bit resolution and a 500 MS.s^{-1} sampling frequency. The cards were connected between each others using a daisy chain of short optical fibers with the first and last boards connected with longer optical fibers to a Peripheral Component Interconnect express (PCIe) card installed in a dedicated data acquisition computer.

For the energy calibration, the same ^{137}Cs source used for the prototype has been placed at an height of 40 cm in the center of the modules assembly as shown in Fig.2.26.

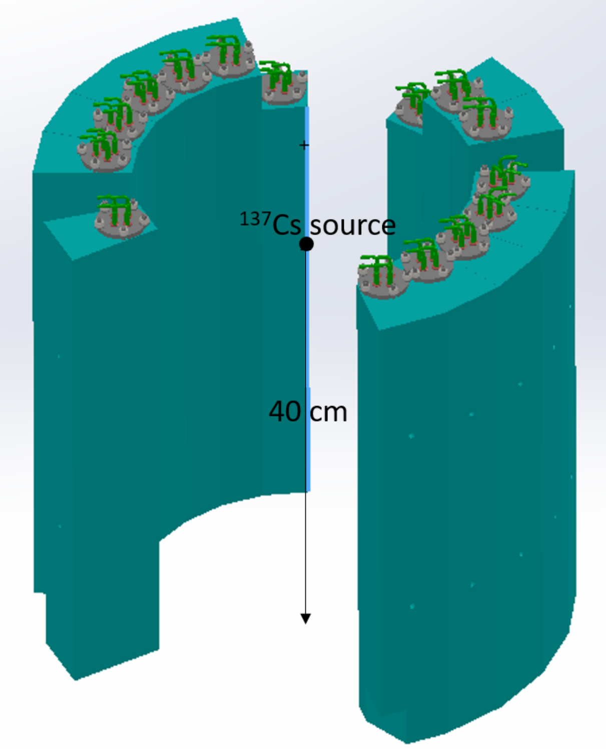

Figure 2.26: *Schematic of the detector array setup and placement of the radioactive source*

To work with the DPP-PSD firmware version 4.17 which was installed on the digitizer, CAEN proposes a software solution called Compass. To treat a lot of events, the raw traces are not recorded and only a few data which are calculated directly on the digitizers are saved. For each treated peak, only six values are stored.

First, to detect a peak on a channel, the digitizer checks if the digitized voltage value gets too far from a baseline value. On each channel, the baseline value is continuously calculated by the card by averaging the input value over a constant number of steps. This allows to have an evolution of the baseline over long period of time if the temperature, or any other reason, causes an effect on the at rest voltage value. Then, the input value is considered far enough from the baseline to induce a trigger if the absolute difference between those two values is higher than a determined threshold. Those thresholds are user determined for each channel and are usually set at the very edge of the mean noise width. This is to be able to see some noise signal without overloading the card with it, and to try not to lose any real signal. Once a trigger is reached, the baseline stops actualizing, the search for a trigger also stops and some on-card calculations are done on the incoming input values and some past ones which have been kept in memory. A temporal representation of this and of a few parameters is shown in Fig.2.27.

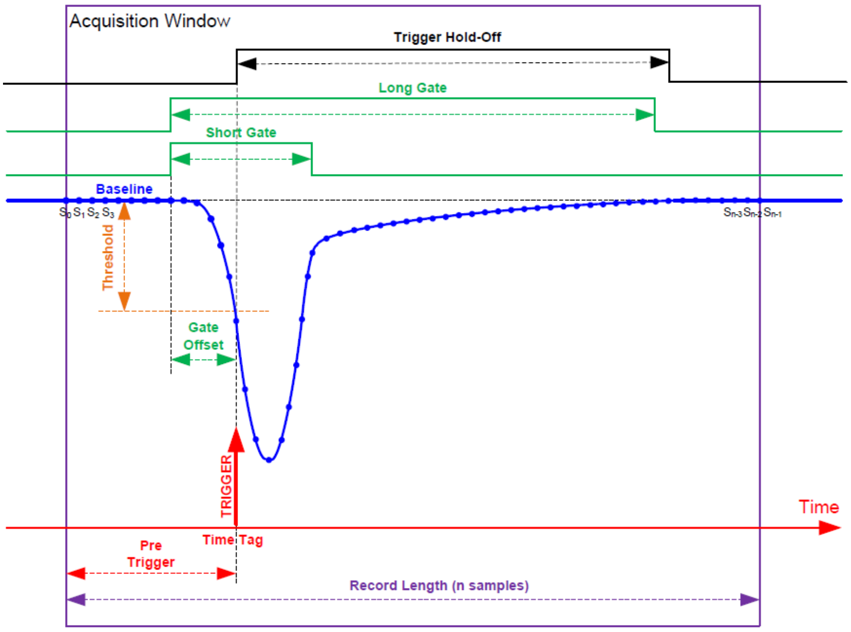

Figure 2.27: *Sketch of the data analysis logic of the CAEN digitizers with several key parameters.*(148)

The card will integrate the difference between the input signal and the baseline value over two different temporal windows, a short temporal window called short gate and a longer one called long gate. The length of those gates are constant. Besides those gates starts a few steps before the trigger timestep in order not to lose the first part of the peak which is often not high enough to induce a trigger. The impossibility for the card to trigger again lasts a few steps after the end of the long gate. Besides, with the card we used, there is another security which prevents a trigger to happen if the difference between the input value and the frozen baseline did not come back down to half the threshold value. In the end, the six values which are saved for each peak are :

- Channel, which is the channel number
- Timestamp, which corresponds to the timestep on which the card triggers
- Board, which is the card number
- Energy, which is the integral on the long gate
- EnergyShort, which is the integral on the short gate
- Flags, which is an information on the pile-up

The flag value changes if the difference between the input value and the baseline comes lower than the threshold and increases again over the threshold before the ability for this channel to trigger has been enabled again, i.e. if a second peak is located in the trigger hold-off time period represented in Fig.2.27. In most of the cases, this happens when two peaks are located in the same long gate window. Both will then be integrated in the same Energy value. Such events are what is called pile-up. The timestamp value is here limited at a 2 ns resolution since it is the width of the timesteps for the card we used.

Using the energy (long gate) data which are not calibrated yet, we can draw the histogram represented in Fig.2.28a. We see that the resulting shape is quite different from what we obtained with the prototype even without calibration factors. In fact, we seem to have two different Compton edges. However, considering the higher energy part as the "real" Compton edge, we have been able to reconstruct a quite satisfactory Compton scattering spectrum when combining the data from the two PMTs as shown with the black histogram in Fig.2.28b. For the calibration of each module, we are finally using three factors for the energy calibration. For each event, the resulting energy is then :

$$E_{ee} = A_{\Sigma} \frac{A_1 * E_1 + A_2 * E_2}{2} \tag{2.21}$$

Where E_1 and E_2 are the values calculated on-board by the digitizer, A_1 and A_2 are calibration factors defined with this "high energy" Compton edge and A_{Σ} is a final calibration factor. Even though the definition of A_1 is a bit unsound, the result is quite satisfactory for most of the modules. For two particular PMTs, the noise is way more important and it has been difficult to define this "high energy" Compton edge, these are namely PMT D of detector unit 1 and PMT U of detector unit 15. D stands for down and U for up, the PMT U being the one next to the vacuum-tight flange. A last one had some electronics issues we were not able to solve and presented a considerable leakage current each time it was put under tension. The detector unit 8 has then never been functional. We didn't have the opportunity to solve those issues before the commissioning experiment. Indeed, due to the covid situation, the calibration of the instrument actually took place after the experiment because of the impossibility to travel and the severe delays in the shipment of some pieces of the detector array.

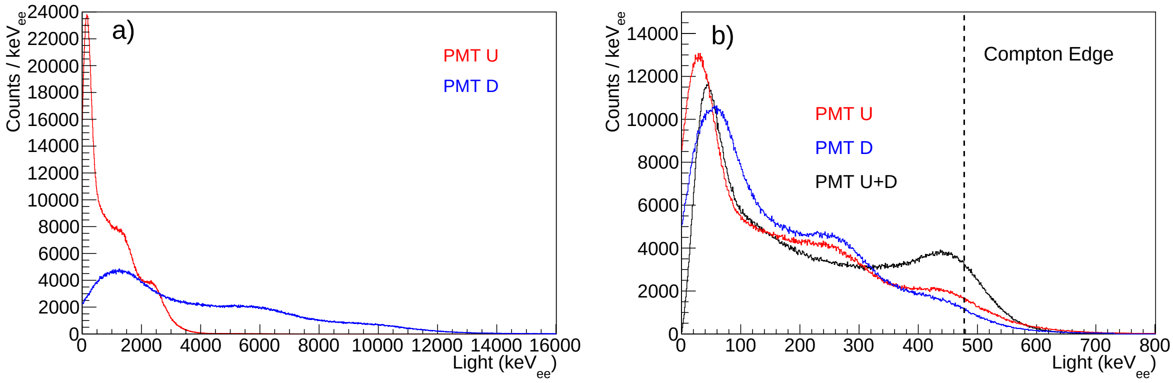

Figure 2.28: *a) Histograms of the light collected by the two individual PMTs of module 2 without any energy calibration. b) Same histograms with an approximate energy calibration in red and blue. In black is the combination of those two histograms recalibrated with the Compton edge energy at 80% height of the Compton distribution.*

To explain the structure of the histogram we measured in Fig.2.28, we did some additional tests. First of all, we found a clue of what was happening by looking at the energy distribution between the two PMTs, as shown in Fig.2.29 for the detector unit 2. In this figure, the x axis represents the fraction E1/(E1+E2) where E1 is the light amount collected during an event by the PMT U/PMT1 and E2 by the PMT D/PMT2. E1 and E2 are the same values than the ones presented in Fig.2.28b. If everything was perfect, we should have seen a narrow peak around 0.5 since the light is produced isotropically after an energy deposition. However, since the scintillator assembly is 40 cm long we could have imagined a relatively broad peak not centered exactly on 0.5 but a bit on the upper PMT side. Indeed, if we assume a linear loss with the distance the light has to travel before reaching the PMT, we could explain the broadness of the peak by the dependence of the energy distribution on where the energy deposition took place. The fact that the peak is not centered would have been explained by the fact that the radioactive source has been set a bit closer from one side than the other as shown in Fig.2.26. Since the detector height is 40 cm in the assembly, which is itself 60 cm tall, the irradiation center, located at a 40 cm height, is not located at the detector mid-height. However, what we see here are two distinct peaks with one a little bit higher than the other.

To fully understand what is happening, we decided to use a collimated source to see the dependence of the different histograms on the energy deposition localisation. A schematic of the setup we used is presented in Fig.2.30. This test was done using the detector unit 4.

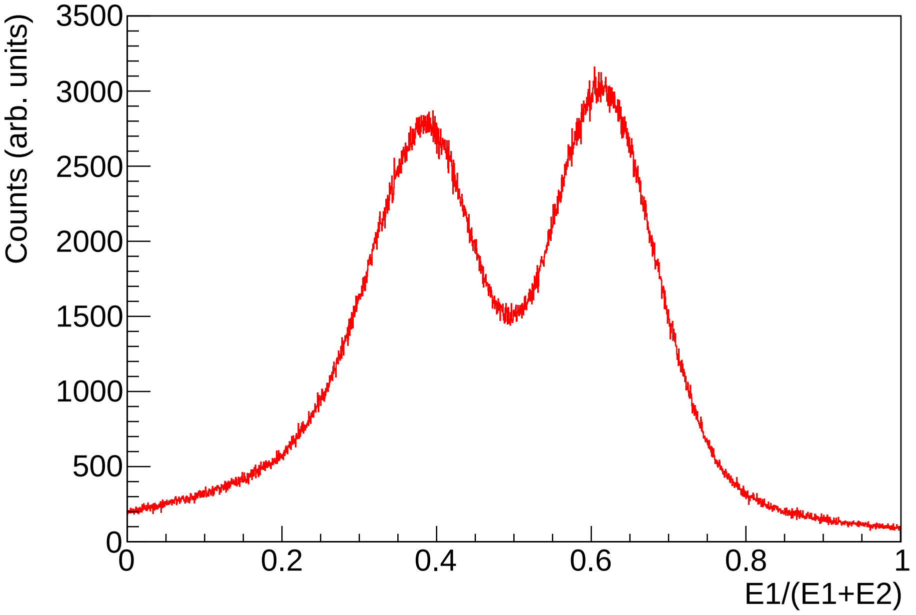

Figure 2.29: *Histogram of the energy distribution between the two PMTs for the detector unit 2. E1 is the amount of light collected by PMT U and E2 the amount of light collected by PMT D.*

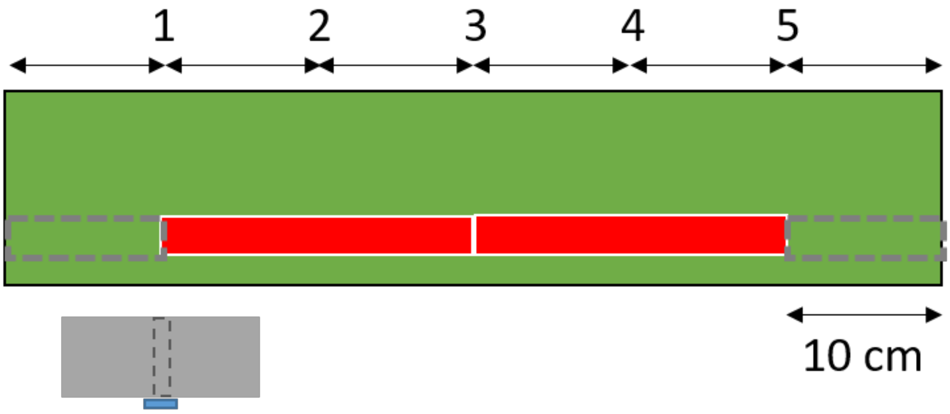

Figure 2.30: *Drawing of the setup used to test the dependence of the light collected by each PMT on the localisation of the energy deposition in the scintillator. The scintillator rods are in red, the HDPE is in green. In grey is a holed lead brick serving as collimator. The hole had a 1 cm diameter and the lead thickness was 5 cm. The* ^{137}*Cs gamma source is represented by the blue rectangle. The numbers 1 to 5 represents the different localisations of the collimated gamma source. The 10 cm grey dashed rectangle on each side represents where the PMTs and their electronics are located. PMT1 is on the left on this sketch and PMT2 on the right.*

To figure out more easily what is happening, we decided to use higher thresholds to only see the highest part of the Compton scattering spectrum and have a narrower energy span. As it can be seen in Fig.2.31, the histogram obtained when combining the two PMTs data doesn't depend on the gamma source position and shows only the higher part of the Compton scattering spectrum. This is really positive and shows that the calibration we did is accurate and not position-dependent.

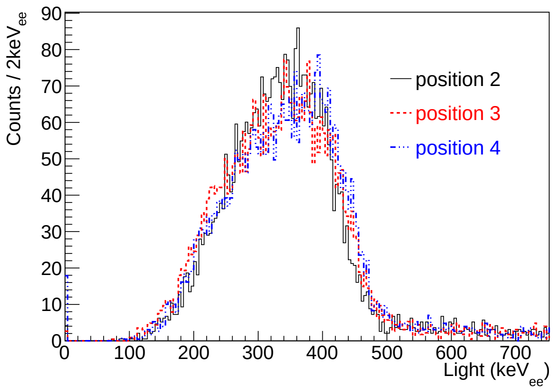

Figure 2.31: *Histograms of light collected by the detector unit 4 when combining the signals obtained by the two PMTs, for three different positions of the collimated source. The histograms are normalized to the position 1 histogram not represented here.*

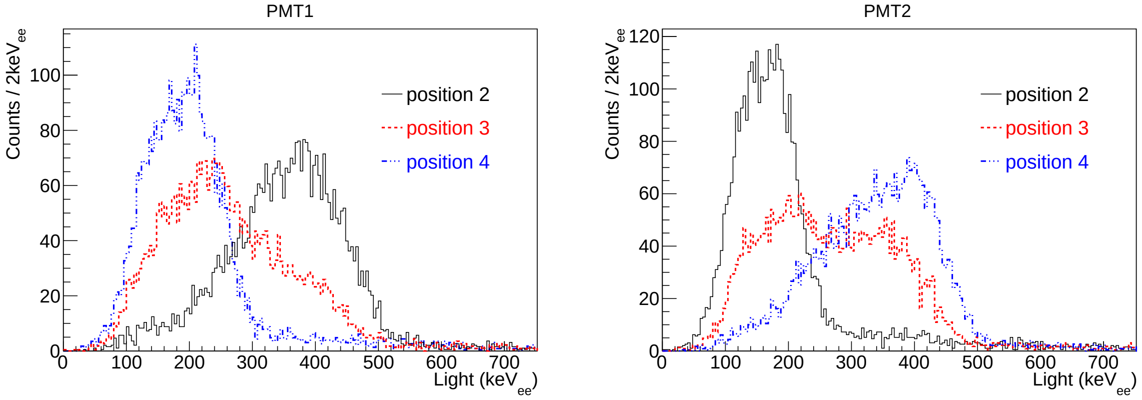

Figure 2.32: *Histograms of the light collected by the two individual PMTs of the module 4, PMT1 on the right and PMT2 on the left. The three different histograms correspond to three different positions explicit in Fig.2.30. The histograms are normalized to the position 1 histogram not represented here.*

However, when we look at the histograms representing the contribution of each PMT, the result is very position dependent as we can see in Fig.2.32. The light collection is way more important in the PMT located on the side of the energy deposition for positions 2 and 4. It is even possible to consider the result for position 3 as the addition of two contributions. It even seems that the gamma source was not exactly centered for position 3, and was a bit on the PMT2 side. Hence, it seems that the optical binding between the two scintillator rods is not as good as we could expect. Positions 1 and 5 tends to give the same conclusions in terms of light distribution between the two PMTs. In fact, as shown in Fig.2.33, the difference is even greater for position 1 and 5.

To summarize, it seems that the geometry of the detector has two effects on the collected light. Firstly, inside a scintillator rod, the nearer from one PMT the energy deposition is, the greater the part of this PMT in the light collection. This effect could be explained by the light absorption of the scintillator material. Secondly, depending on which scintillator rod the energy deposition happens, the PMT associated

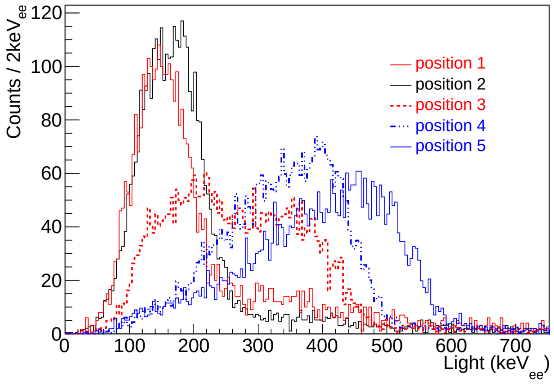

Figure 2.33: *Histogram of light collected by the PMT2 of the detector unit 4 for the five different positions of the collimated source. The histograms are normalized to the position 1 histogram.*

Module	A_1	A_2	A_Σ
1	0.2646	0.1073	1.2306
2	0.1838	0.0446	1.2424
3	0.0726	0.1131	1.2098
4	0.0691	0.1238	1.2697
5	0.0656	0.0577	1.2512
6	0.0690	0.1561	1.3210
7	0.1122	0.1087	1.1819
9	0.0748	0.1482	1.2270
10	0.1139	0.0633	1.3400
11	0.0928	0.0844	1.5276
12	0.0938	0.0542	1.2892
13	0.1588	0.0527	1.2074
14	0.1151	0.0794	1.2805
15	0.0696	0.0758	1.2144

Table 2.3: *Energy calibration factors*

to this rod will receive way more light than the other PMT. This effect can be explained by the not optimal optical connection between the two scintillator rods. This is this second effect which is responsible for the seemingly double Compton edge.

In the end, we managed to have an adequate energy for all the detector units, except detector unit 8 which had a PMT not working. The calibration factors exhibited in Eq.2.21 are given in Table.2.3.

2.3.3 Efficiency calibration

As we did with the prototype, we used here a PuBe neutron source(138) to first characterize the neutron detection characteristics and then the neutron detection efficiency. As a first step, we used the same setup than the one we used with the ^{137}Cs gamma source, i.e. CAEN V1730SB cards for the signal and CAEN A7030SN boards in a CAEN SY5527LC power supply system for the high voltage. However, this time, we used a function of the digitizers that allows to store the traces of the peaks which triggered the system.

As shown in Fig.2.27, there is a record length which we set here at 496 timesteps, i.e. 992 ns.

Doing so, we were able to define the typical shape of the signal detected by the PMTs after the capture of a thermal neutron in the boron loaded scintillators. This typical shape is shown in Fig.2.34. It shows that a constant gate of 30 ns is enough to integrate the full signal. To do so, a selection on the energy of the events has been set using the energy calibration we just explained. However, we can also notice a minor peak before the main mean peak and which doesn't appear in the typical trace presented in Fig.2.34. It corresponds to noise peaks that have not been eliminated despite the energy selection.

If we fit the rising and decaying part of this mean pulse shape with respectively the functions $ae^{-\frac{t-b}{\tau}}$ and $ae^{\frac{t-b}{\tau}}$, we found a rising time constant of 3.26(07) ns and a decay time constant of 7.47(11) ns. According to the manufacturers, the PMT has a single electron FWHM of 3.1 ns and the scintillator rising time and decay time are respectively 0.85 ns and 1.51 ns. Since we don't know the exact definition of the rising time and decay time given by the constructor, we can only say that the the time characteristics of the pulses we measure are in the expected range. We can also note that the temporal constants don't change much from a PMT to another. Hence, the variations in the energy calibration factors mainly come from variations in the mean height of the peaks from one PMT to another.

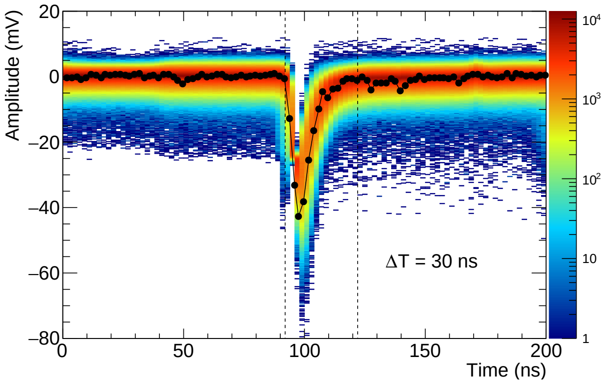

Figure 2.34: *Typical pulse shape of the PMT signal after the capture of a thermal neutron by a scintillating unit. The colored histogram shows the accumulation of approximately 150 000 traces and in black is represented one typical trace. The black points correspond to the actual sampling points. Those traces were recorded using the detector unit 7.*

During the experimental shots, we will not use such a system where the card triggers when a peak is detected. Indeed, we will on the contrary trigger all the cards just before the laser shot and record all the traces for 1 ms. Hence, we needed to develop a script to detect the different peaks along several 1 ms long traces and integrate them. We used this set of recorded traces to develop the integrating part of the code and adapt the energy calibration to this custom way of integrating.

To integrate the peak signal from the recorded traces partly represented in Fig.2.34, we tested two methods. First, for both methods, we decided to find the entry of the maximum value of the peak instead of the triggering one. Hence, in a first time, we tried integrating the peak on a fixed temporal window of 15 timesteps, i.e. 30 ns, centered on the peak maximal value timestep. In a second time, we tried the method to delimit the peak duration more precisely. To do so, we only kept the steps for which the signal difference from the baseline was at least 10% the peak height. The baseline is here calculated as the mean signal value of the first 40 steps. We can see the difference between the two windows with an example in Fig.2.35. The default value of the long gate used for the on-board integration is 300 ns which is way longer than the peak duration we are expecting.

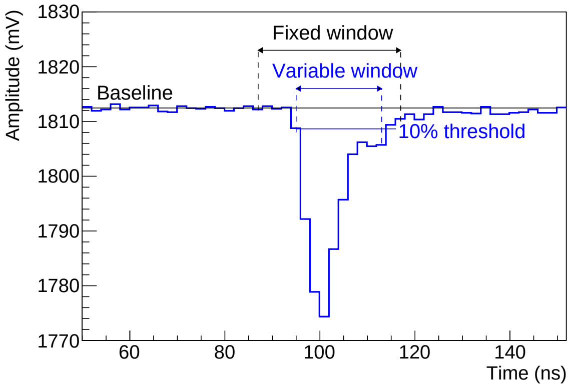

Figure 2.35: *Example of a recorded trace with the different time windows used to integrate the peak. The baseline and the 10% threshold used to define the variable time window are also represented respectively in black and blue.*

As we can see in Fig.2.36a, the on-board integration seems less precise than our customs methods. Indeed, the neutron peak is sharper in both our methods in comparison with the on-board calculation. The noise energy is also better-defined. Between the two custom methods, the variable time window one seems a bit better than the fixed window one, especially if we look into the delimitation between the noise and the neutron peak. What we call here neutron peak is really different from the peaks we can detect on the traces such as in Fig.2.34. Indeed, to summarize, we can associate a light amount/energy to the peaks detected on the traces by integrating them. Then, if we count the number of peaks according to their light amount, we see that a lot of them have a light amount around ∼100 keV, which corresponds to a neutron capture reaction as we can see with the prototype in Fig.2.19 or here in Fig.2.36a. This is this feature on the histogram that we call neutron peak.

We want to separate as much as possible the noise from the neutron peak and the computing time is not an issue for the size of the data we will have to analyze. Hence, we decided to go with the variable time window method which seems to give the best results. We also see that in the calibration conditions, the mean width of the integration window is equal to 12 timesteps, i.e. 24 ns, and vary in majority between 8 and 17 timesteps. To keep the same energy calibration, since we don't integrate on the same time window, we added a final energy calibration factor. It is the same for all the PMTs since it depends primarily on

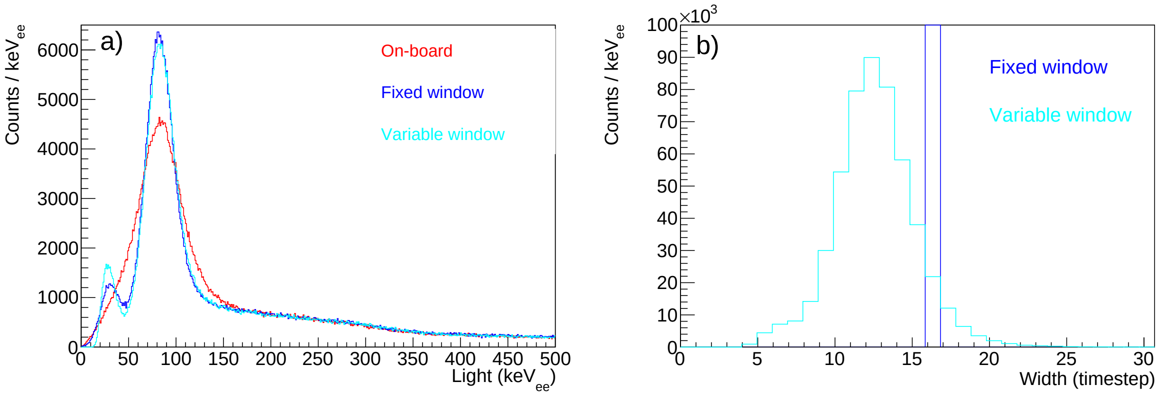

Figure 2.36: *a) shows histograms of the light collected by the PMTs of the detector unit 12. The three different histograms correspond to three different integration methods, the on-board method and the fixed and variable window custom methods. Energy calibration is corrected for the two custom histograms. b) represents the width of the integration time window for the two custom methods.*

the method we chose and it is equal to 0.6145. This factor is applied for each peak integration on the traces we do and has been defined using the histograms shown in Fig.2.36a to have the mean energy of the neutron peak obtained with the different methods of integration always the same.

With the custom integration method ready and the energy calibration corrected, we have been able to calibrate the efficiency of our detector units. To do so, we used the same setup. However, instead of triggering the digitizers on the measured signal, we triggered externally all the channel of all the cards at the same time to record 5.10^5 samples each, i.e. 1 ms worth of signal. We triggered all the channels 736 times to have an overall recording duration time of 0.736 s. This already represented 23 Go of data.

This step led us to develop two things. First, we finalized developing the traces analysis script which can be used during the laser experiments. Second, we defined thresholds in a more precise way than what could be done previously. The script we developed is composed of two main parts.

The first part corresponds to the peak detection. For each traces, we run through the whole trace and search for a peak. We consider there is a peak if the signal value differs from the baseline more than a threshold value. This baseline is recalculated for each timestep and is defined as the mean value of the signal over 40 steps, starting 41 steps before the timestep we are looking into. Indeed, we exclude from this calculation the previous step to avoid to have the beginning of a peak influencing the baseline value. Once the threshold value is excedeed, we look for the timestep for which the signal value differs the most from the baseline value, in the 20 next timesteps, i.e. a 40 ns window. We considered this as the peak maximum and integrate the peak with the integration method we have already explained. All the data which can be used to define this peak are then stored. Those data are the baseline value, the peak maximum timestep, the first timestep in the peak according to the 10% limit, the last timestep in the peak, the peak height and the peak integral multiplied by the corresponding PMT energy calibration factor and the integration method factor. When this is done, we start looking for another peak, starting at the first timestep for which the difference between the signal value and the peak baseline value is lower than the threshold, or the timestep right after the last timestep in the peak depending on which is the first. The most important values are represented in Fig.2.37.

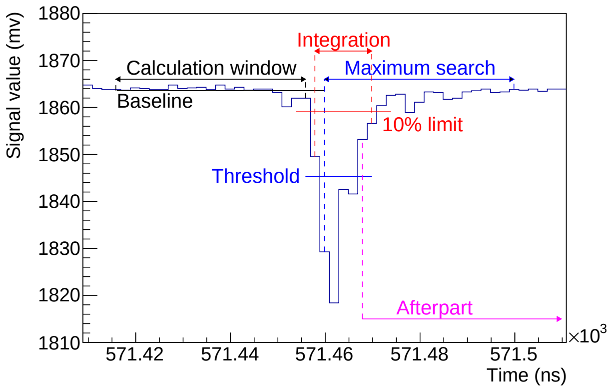

Figure 2.37: *Example, on part of a recorded trace of detector unit 6, of the peak search and integration process. Principal values of interest are represented with dashed line for timesteps, arrows for time windows and simple line for signal values. The order of the process is the following : Calculation window/Baseline, Threshold, Maximum search, 10% limit, Integration and Afterpart.*

Once this part is done, we check for the coincidences between the peaks found on the traces of the two associated PMTs. If the maximum timesteps of the two peaks are within an 8 ns window, the two peaks are considered representing a real energy deposition event and their contribution is added to the different histograms. The main histogram of interest is of course the one representing the number of events according to their associated light amount/energy. The value of 8 ns has been chosen because it is half the mean FWHM of a pulse induced by a neutron capture as shown in Fig.2.34.

At this step, we then set thresholds values. The efficiency that are calculated later in this section are of course dependent on all the parameters that we have fixed and also dependent of the energy spectrum of the PuBe neutron source we used. The threshold values are presented in Table.2.4. We can see that those thresholds vary a lot from one PMT to the other. Indeed, they depend primarily on the noise level which is very PMT dependent.

Using our custom analysis script on the 0.736 s worth of data collection, we have been able to obtain the histogram of counts per energy per neutron emitted by the PuBe source, for each detector unit. From this, we can fit the neutron peak that appears using a Gaussian profile for the peak and a decreasing exponential for the noise. Then, the integral of the Gaussian profile gives us the number of neutrons detected per neutron emitted, i.e. the efficiency of the detector unit. Hence, we found the efficiencies of each detector unit for this PuBe source and the parameters we set. Those are shown in Table.2.5.

We see that the characteristics of the neutron peak and the efficiency are of the same order for almost

Detector unit	PMT 1	PMT 2
1	100	160
2	18	70
3	200	75
4	110	35
5	40	200
6	150	30
7	30	40
9	170	30
10	100	200
11	160	130
12	150	25
13	75	250
14	60	70
15	250	170

Table 2.4: *Thresholds used for the calibration in efficiency. The thresholds are here defined in term of channel which is related to the voltage by* $1\ channel = 0.122\ mV$.

Detector unit	E (keV$_{ee}$)	ΔE (keV$_{ee}$)	Efficiency (%)
1	95.6(37)	30.2(91)	0.030(17)
2	104.8(11)	43.2(33)	0.299(43)
3	114.9(11)	45.9(29)	0.320(40)
4	109.7(11)	42.9(24)	0.363(42)
5	119.9(20)	64.0(54)	0.402(57)
6	105.0(11)	43.7(25)	0.420(48)
7	104.7(15)	46.8(36)	0.359(51)
9	110.0(12)	46.1(30)	0.338(43)
10	121.4(17)	66.6(63)	0.325(53)
11	99.9(12)	50.3(36)	0.366(47)
12	100.3(12)	49.3(34)	0.354(46)
13	99.7(10)	48.3(21)	0.365(35)
14	108.1(18)	35.8(19)	0.390(44)
15	99.3(50)	41.4 (13)	0.039(22)
Total			4.37(59)

Table 2.5: *Efficiency and neutron peak characteristics for the 14 working detector units during the calibration with a PuBe neutron source. Errors shown are from the fit of the neutron peak.*

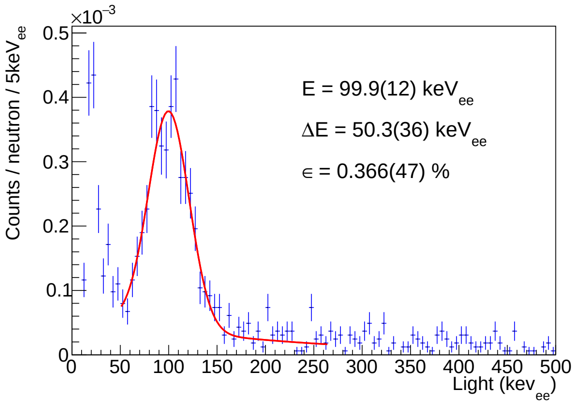

Figure 2.38: *Histogram of the light collected by the detector unit 11*

all detector units. However, in comparison with the other units, the efficiencies of detector units 1 and 15 are 10 times lower. This is due to the really important noise existing on one PMT of each detector unit, which prevent us to see a clear neutron peak over the background noise signal. We believe that those PMTs have been damaged during or after the commissioning experiment because those units were working perfectly fine during the experiment.

In summary, we now have an energy calibration and an efficiency calibration for all the detector units. One has to keep in mind that the efficiency calibration depends on the parameters we used and on the neutron energy spectrum. Hence, for each analysis, one needs to redo this calibration with others parameters if those have changed. Besides, simulations, using Geant4 for instance, need to be done to take into account the effect of the neutron energy spectrum on the efficiency.

Chapter 3

The LULI2000 experiment : commissioning of the neutron detector

In this chapter, we will present the experiment in which the detector we designed in the last chapter, has been used for the first time. We will first present the scientific motivations behind this experiment. A second section will present the design of this experiment and the preliminary studies that have been done. Finally we will present the analysis of the data and the result we got out of it.

3.1 Scientific motivations

3.1.1 Astronomical context

As we have have seen in section 1.2.1, nuclear reactions between charged particle are of prime interest to understand stellar nucleosynthesis. To model the nuclides production, it is then necessary to know the cross sections of all the nuclear reactions involved in the stellar environment. Indeed, the reaction rate for a reaction between two massive particle 0 and 1 is given by the equations(6):

$$r_{01} = \frac{N_0 N_1 \langle \sigma v \rangle_{01}}{1 + \delta_{01}} \tag{3.1}$$

$$N_A \langle \sigma v \rangle_{01} = \sqrt{\frac{8}{\pi m_{01}}} \frac{N_A}{(kT)^{\frac{3}{2}}} \int_0^\infty E \sigma(E) e^{-\frac{E}{kT}} dE \tag{3.2}$$

Where r_{01} is the reaction rate between the two particles 0 and 1, N_0 and N_1 are the densities of the interacting particles, δ_{01} is the Kronecker symbol, $\langle \sigma v \rangle_{01}$ is the reaction rate per particle pair, N_A the Avogadro constant, $m_{01} = m_0 m_1/(m_0+m_1)$ the reduced mass, $v=\sqrt{2E/m_{01}}$ the relative velocity between the two particles, E the center of mass energy, k the Boltzmann constant, T the temperature and σ the reaction cross section. N$_A$ is present in Eq.3.2 because it is generally the value $N_A\langle\sigma v\rangle_{01}$ in cm^{3}mol^{-1}s^{-1} which is used in the literature. To model the cross section of a nuclear reaction involving two charged particles, astrophysicists have introduced the astrophysical S-factor defined by the following equation(149):

$$\sigma(E) = \frac{1}{E}e^{-2\pi\eta}S(E) \tag{3.3}$$

Where S(E) is the astrophysical S-factor, σ(E) the cross section of the reaction, e$^{-2\pi\eta}$ the Gamow factor and η the Sommerfeld parameter (see below). This S-factor has been introduced for astrophysicists to manipulate a factor which depends way less on the energy than the cross section. It can then be extrapolated more reliably from the energy range for which data are confirmed experimentally to the lower energy Gamow peak for which most of the reactions in the stellar medium happen(150). Typically, for the sun, this Gamow peak extends from 3 to 10 keV(151). The Gamow factor approximates the tunnel effect probability through the Coulomb barrier. The Sommerfeld parameter is given by the following equation(152):

$$\eta(E) = \frac{Z_0 Z_1 e^2}{\hbar v} = \frac{Z_0 Z_1 e^2}{\hbar}\sqrt{\frac{m_{01}}{2E}} \tag{3.4}$$

Where Z$_0$ and Z$_1$ are the charge numbers of the two particles, e the elementary charge and $\hbar$ the reduced Planck constant. The Gamow factor and the Sommerfeld parameter are written for bare nucleus. However, either in the stellar medium or in a solid experimental target, the nuclei are surrounded by electron clouds. Since the electrons are negatively charged, this will have an effect on the Coulomb potential as shown in Fig.3.1.

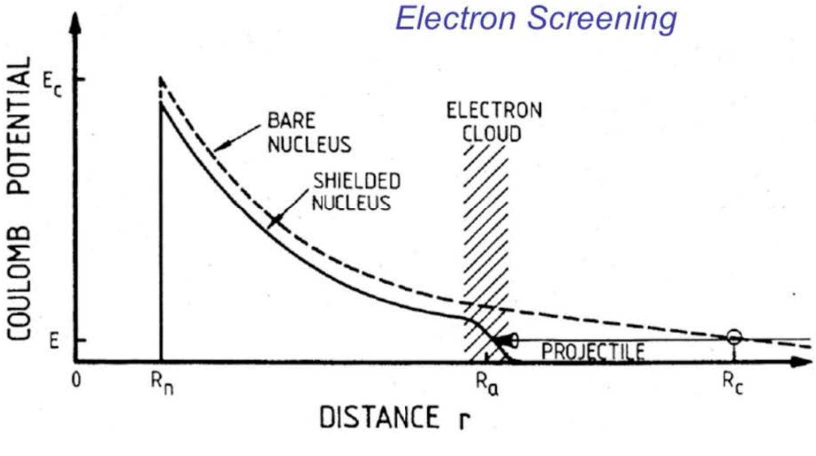

Figure 3.1: Representation of the influence of the electrons surrounding a nucleus on the Coulomb potential an incoming particle will see(153)

Salpeter(154) has shown that this influence can be modelled simply with an alteration of the center of mass energy. The Gamow factor becomes then:

$$exp\left[-2\pi\eta(E+U_e)\right] = exp\left[-\frac{2\pi Z_0 Z_1 e^2}{\hbar}\sqrt{\frac{m_{01}}{2(E+U_e)}}\right] \tag{3.5}$$

Where U$_e$ is defined as the screening potential. It is then possible to define an enhancement factor relative to the laboratory conditions(155) :

$$f_{lab}(E) = \frac{\sigma_{lab}(E)}{\sigma_b(E)} = \frac{\sigma_b(E+U_e)}{\sigma_b(E)} \tag{3.6}$$

Where f$_{lab}$ is the enhancement factor, σ_{lab} the cross section that can be measured in the experimental condition and σ_b the cross section for the bare nuclei. We can consider that most of the time, U$_e$ is very small in comparison of E, and S varies slowly with E. Hence, we can establish the following relation:

$$\begin{aligned} f_{lab}(E) &= \frac{E}{E+U_e}\frac{S(E+U_e)}{S(E)} exp\left[-\frac{2\pi Z_0 Z_1 e^2}{\hbar}\left(\sqrt{\frac{m_{01}}{2(E+U_e)}} - \sqrt{\frac{m_{01}}{2E}}\right)\right] \\ &= \frac{E}{E+U_e}\frac{S(E+U_e)}{S(E)} exp\left[-\frac{2\pi Z_0 Z_1 e^2}{\hbar}\sqrt{\frac{m_{01}}{2E}}\left(\left(1+\frac{U_e}{E}\right)^{-\frac{1}{2}} - 1\right)\right] \\ &\approx exp\left[\pi\eta(E)\frac{U_e}{E}\right] \end{aligned} \tag{3.7}$$

In the same way, we can also define an enhancement factor for the stellar environment. Indeed, each nucleus in the stellar environment is surrounded by an electron cloud at a distance given by the Debye-Hückel radius R$_D$(154):

$$R_D = \sqrt{\frac{kT}{4\pi e^2 \rho N_A \zeta^2}} \tag{3.8}$$

$$\zeta^2 = \frac{Z^2+Z}{A} \tag{3.9}$$

Where T is the temperature of the stellar medium and Z and A are respectively the proton number and the mass number of the nuclide. We can then find that the stellar enhancement factor f$_s$ is given by(6):

$$f_s = exp\left[\frac{Z_0 Z_1 e^2}{R_D kT}\right] \tag{3.10}$$

Hence, if we know the cross section for a bare nucleus, it is possible to calculate the cross sections in the stellar medium. For reactions including light nuclei, i.e. ^{1}H to ^{11}B, this screening potential ranges from less than 20 eV to a few hundreds of eV(150; 152). For most of the experiments, there is no need to take this effect into account because the energy of the particle in those experiments are way higher than the screening potential and the enhancement factor is equal to one. However, in the astronomical context, most of the particles taking part in nuclear reactions have an energy in the so-called Gamow peak. For the Sun, the mean energy of this Gamow peak is around 6 keV(6). Consequently, it becomes important for some reactions to know with precision those enhancement and of course, the corresponding cross-sections for bare nuclei.

3.1.2 Experimental investigations

Since it is impossible to measure directly the cross sections of bare nuclei, we can't measure an enhancement factor by measuring the two corresponding cross sections directly. To study electron screening, one must then study situations where the strength of this effect varies and retrieve from those variations the overall strength of this effect, i.e. the screening potential value.

To do so, experimental teams have run experiments using different methods to see variations in the screening potential. The most straightforward method is to calculate the S factor for energies as low as possible. Knowing that this value varies very slowly with the energy, any deviation in the measurement of this value at low energy can be considered as an effect of the electron screening(153). Several teams have done such measurements(156; 157; 158). An example of such measurement is shown in Fig.3.2.

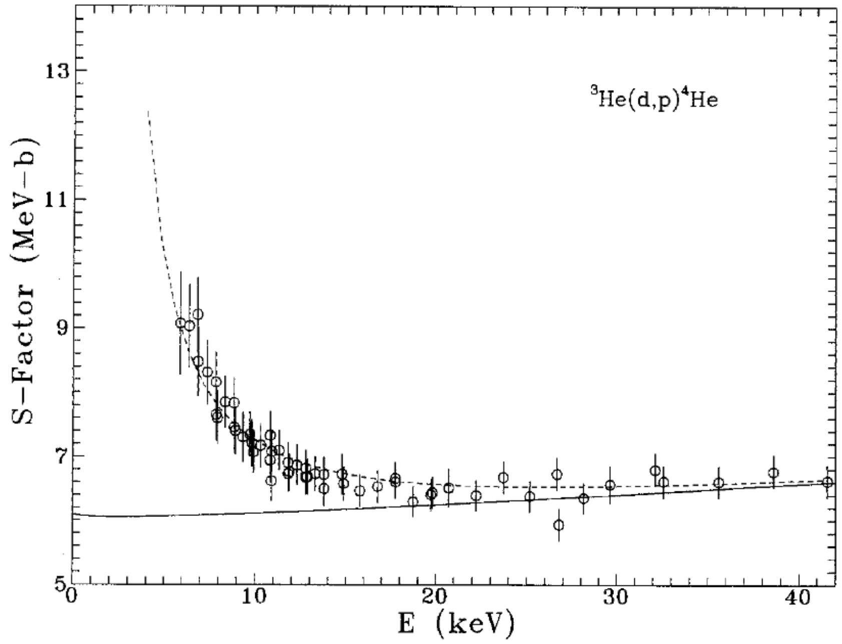

Figure 3.2: *Evolution of the S factor according to the energy. The solid curve represent the bare nuclide case while the dashed line gives the enhancement due to the electron screening in a solid target. The circles shows the experimental measures(156)*

However, for a lot of reactions implying light nuclides, this effect is not measurable. Hence, some teams are boosting this electron screening by using targets which will increase the electron population around some nuclides and then boost the electron screening effect(158; 159). Some other teams have used an indirect method called the Trojan Horse Method which the study of reaction with at least three products to retrieve information on reaction with less products(160; 161; 162). Most of those experimental measurements have find values for screening potential higher than what the theory calculates(152).

It is also possible to look into heavier nuclides. The cross section of reactions implying charged particle and heavier nuclides are way less important. However, the electron screening effect in such cases is much stronger. Indeed, the difference between the screening potential for a proton and a nuclide with a mass around 50 in different targets can reach a few tens of keV(155). The screening potential can for instance be changed by using targets in which the nuclide of interest will be mixed with another nuclide with a different electronegativity. It is then possible to use ion beams at higher energies than what is needed for light nuclides.

Hence, we decided to study reaction with nuclides in this mass range. Besides, since electron screening for (p,n) reactions had already been investigated(155), it was the opportunity for us to test our detector and be able to compare our measurements to some data which were close from our possible experimental setup. Still, the main difference is that in laser facilities, we can easily use one beam to ionize the target and study the electron screening in a plasma state which is closer to the stellar conditions than what has been done with solid target until now.

3.2 Design of the experiment

3.2.1 The LULI2000 facility

The LULI2000 facility is an intense laser system located in the École Polytechnique laboratories in Palaiseau. This system is composed of 4 laser chains :

- the NORTH chain which can deliver an energy up to 1 kJ at 1.053 μm in the ns regime,
- the SOUTH chain which can be used in two modes. It can deliver the same specifications than the NORTH in the nano2000 configuration. It can also be used in the pico2000 configuration for which the pulse is compressed using the CPA technique(13). Then , the energy delivered is limited to 80 J in 1 ps in order not to damage the gratings.
- the blue chain which can deliver around 50 J during 1 ns,
- and the black chain which can deliver around 10 J in 1 ps.

All chains are based on neodynium glass amplificators so the natural wavelength is 1.053 μm. Except for the black one, all chains can be doubled in frequency and then deliver pulses at 0.53 μm wavelength. When using the NORTH and SOUTH chains in the nano2000 configuration at full energy, the waiting time between two shots is 90 minutes. However, when only using the SOUTH chain in the pico2000 configuration, this waiting time can be lowered to 60 minutes. The facility uses 4 independent laser oscillators which allows differentiated temporal shapes for every chain over a duration of 1 ns to 15 ns.

There are two experimental areas within the LULI2000 facility, each dedicated to one configuration of the SOUTH chain. The experimental area #1 allows the experimental teams to use the NORTH chain, the SOUTH chain in the pico2000 configuration and the blue chain. As shown in Fig.3.3, the experimental chamber which has for name MILKA is a spherical one with a 2 m diameter. Besides the laser system, an electromagnetic pulser can be implemented. This can allow the production of magnetic fields up to 30 T.

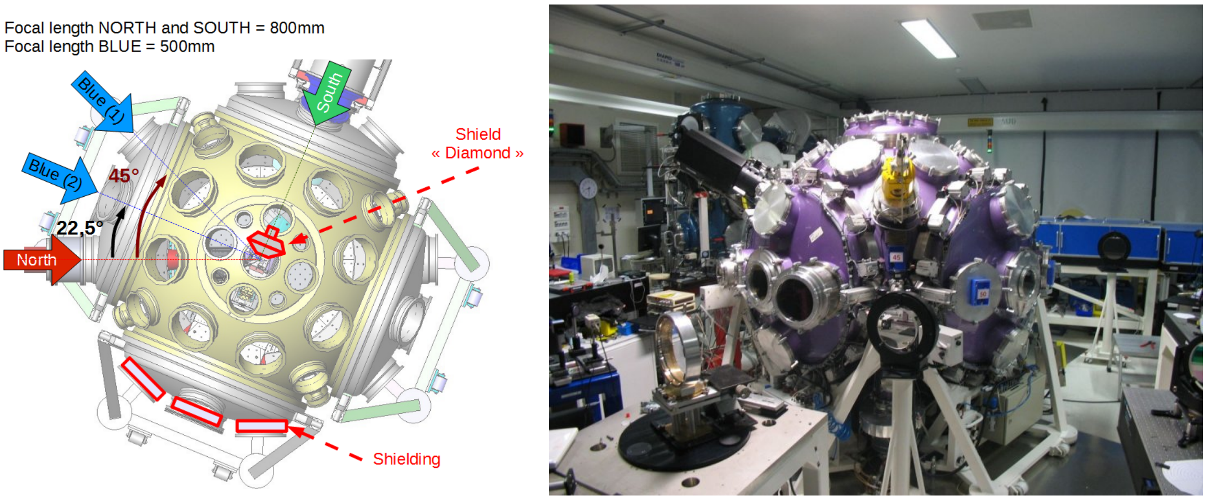

Figure 3.3: Schematic top view and actual photo of the experimental area #1 with the MILKA experimental chamber. The usual path of each laser beam is represented on the schematic view.

The experimental area #2 allows the use of the NORTH chain, the SOUTH chain in the nano2000 configuration, the blue chain and the black one. The experimental chamber associated to this area is cylindrical and a bit smaller than MILKA. An electromagnetic pulser can also be implemented in this area.

3.2.2 Setup

Since the idea is to study a (p,n) reaction, we want first to produce a proton beam as bright as possible. To do so, the best is to use the SOUTH chain in the pico2000 configuration in the experimental area #1. Besides, all the radioprotection equipment needed to do such an experiment is already installed in this

Potassium		Vanadium		Lanthanum		Lutetium	
Iso	Abundance	Iso	Abundance	Iso	Abundance	Iso	Abundance
^{39}K	93.258%	^{50}V	0.25%	^{138}La	0.089%	^{175}Lu	97.41%
^{40}K	0.012%	^{51}V	99.75%	^{139}La	99.911%	^{176}Lu	2.59%
^{41}K	6.730%						

Table 3.1: *Natural abundances for several elements. Iso stands here for isotope.*

area. Since we want to study the reaction in both solid and plasma state, we will need for some shots to heat up the target in which the proton beam will be send. The higher the ionization rate, the more important should be the effect we want to study. That is why we want to heat as much as possible the target. For that, we decided to use the NORTH chain since it has way more energy than the blue one.

Also, effects we want to study like electron screening have way more influence for incoming protons with a low energy. Hence, we want to study (p,n) reaction happening for protons with energies as low as possible. To do so, we want (p,n) reaction with no energy threshold i.e. with a positive Q-value. Among nuclei stable enough to be present naturally, only 4 have a positive Q-value for the (p,n) reaction. Those nuclei are ^{40}K, ^{50}V, ^{138}La and ^{176}Lu and the respective Q-values are 528.5 keV, 255.7 keV, 269.4 keV and 411.7 keV. Looking at the abundances of those isotopes as shown in Table.3.1, we see that those isotopes are pretty rare, especially ^{40}K. Besides potassium reacts violently with water so we discarded this nucleus.

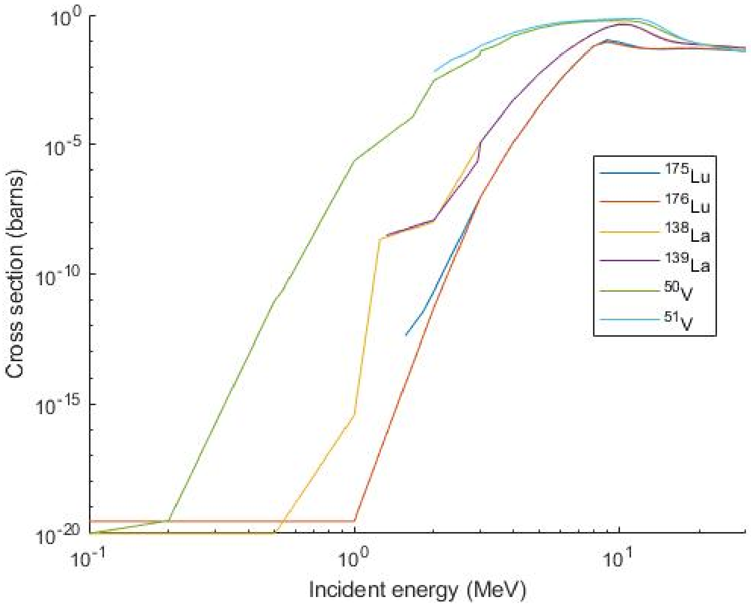

Figure 3.4: *Cross sections of (p,n) reactions for ^{50}V, ^{51}V, ^{138}La, ^{139}La, ^{175}Lu and ^{176}Lu(82)*

Only looking at the abundances, it seems, that ^{176}Lu would be the best candidates to investigate. However, when we take into account the cross sections of the (p,n) reactions shown in Fig.3.4, ^{50}V has a cross section several orders of magnitude higher than the ^{176}Lu one. Besides, the ^{176}Lu(p,n) cross section exhibits a narrow resonance not shown here around 0.81 MeV which would complicate and restrict the study of the changes on the cross section(163).The Q-value of the (p,n) reactions for ^{51}V, ^{139}La and ^{175}Lu are respectively -1534.8 keV, -1060.7 keV and -1466.3 keV. Those Q-values being quite similar, this has no incidence on the choice of the target. Below those energies no other reactions produce neutrons so only the reaction of interest would be measured. So we decided to go with targets composed of natural vanadium.

To produce proton beams using a picosecond laser pulse, there is two main possibilities. We can shoot in a gas jet and use Coulombian explosion to eject protons orthogonally from the laser propagation direction(164). Another possibility is to shoot on a solid thin sheet to use the TNSA mechanism to get on the rear side of the target a high energy proton beam(see section1.1.2). Figs.3.5 shows that both techniques give proton beams with spectrum decreasing exponentially when the energy increase until reaching a maximum cutoff energy. The main difference is that the cutoff energy and the proton number are way higher for the TNSA method.

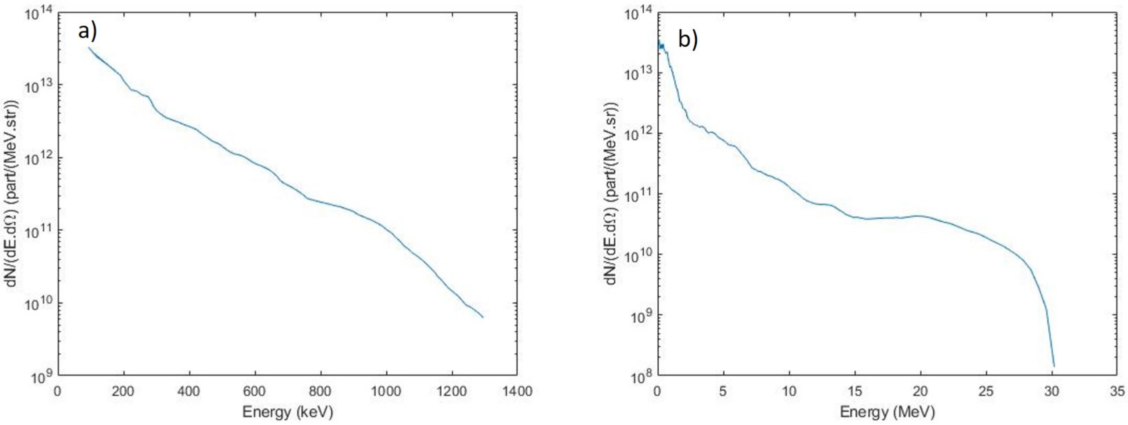

Figure 3.5: *Proton spectra obtained through two different methods. The left one has been produced shooting on a gas jet (Coulombian explosion) and the right one shooting on a solid target (TNSA). The TNSA spectrum has been obtained at the LULI2000 facility during our experiment and the Coulombian explosion one at the Jupiter laser facility using Titan which has specifications almost similar to the LULI2000 facility, during another experiment of our group.*

For our purpose, we don't need a priori high energy protons so it would seem like using the gas jet is our best option here. However, calculations which will be presented later show that we need protons with energy of at least a few MeV to be able to detect any product of the reactions we want to study. Besides, by changing the size of the focal spot on the target, it is possible to modulate the cutoff energy of a spectrum obtained using TNSA, without changing the spectrum otherwise(165). So we chose as primary target aluminized PET to produce the proton beam by the TNSA mechanism. These will go into a secondary vanadium target where the (p,n) reaction will occur. After a few tests, we saw during the experiment that the best thickness for the PET sheet to reach the highest energy possible, i.e. to get the widest range of energy possible, was 23μm. So the primary target has been set to a 23μm PET sheet with a 300 nm aluminum layer on the front face, i.e. on the face the laser hits. The aluminum layer is here to absorb more efficiently than the PET the laser energy.

To have the most homogeneous heating possible of the secondary target, we decided to use a thin vanadium target. This should not have a big incidence on the number of neutrons produce by low energy protons since according to SRIM calculations(127), the mean free path of a 1 MeV proton in a vanadium foil is 8.15 μm. Besides, the energy spectrum of the protons generated by the laser-matter interaction is not as stable as what can be done with accelerators. Then, it's important to monitor on every shot the proton energy spectrum. Having a thin vanadium target will allow enough protons to go through and allow us to retrieve enough information to build the proton spectrum on every shot. The width of the vanadium target has been defined thanks to simulations that will be presented in the next section.

For the distance between the two targets, they need to be close enough to limit the dispersion of the proton beam and then be able to heat the secondary target on a big enough surface considering this dispersion. On the contrary, the two targets needs to be far enough for the expansion of the vanadium target during its heating not to reach the primary target and prevent the proton beam generation. We decided to set the minimum distance to fulfill the second condition, at 500 μm. Hence, considering a maximum divergence of 50°(166), this gives us a disk with a 466 μm diameter on the secondary target. The reachable intensities using the north ns beam are then between $5.86.10^{13}$ W.cm^{-2} for 100 J and $3.52.10^{14}$ W.cm^{-2} for 600 J. A sketch of the targets setup is shown in Fig.3.6.

Now that our target system has been defined, we present the diagnostics used for this experiment. There are only three characteristics that we want to measure. Those three characteristics are the number of neutrons produced, the energy spectrum of the proton beam which produces those neutrons and the ionization degree of the target.

To monitor the ionization degree of the target, we decided to measure the temperature of the target using a Focusing Spectrometer with Spatial Resolution (FSSR)(167). This x-ray spectrometer measures the x-rays emitted from the hot target and it can spatially resolve the emission along one axis using a spherically bent crystal and a detecting device which is here an Image Plate (IP)(168). It allows to retrieve both the size of the plasma and its temperature thanks to the relative height of the different lines in the spectrum. Another interesting aspect of this diagnostic is that it can look at the plasma from anywhere in the experimental room as long as a clean line of sight is available. In order to maximize the available angular coverage for the neutron detector, we decided to place this diagnostic under the NORTH beam path in the chamber(see Fig.3.9).

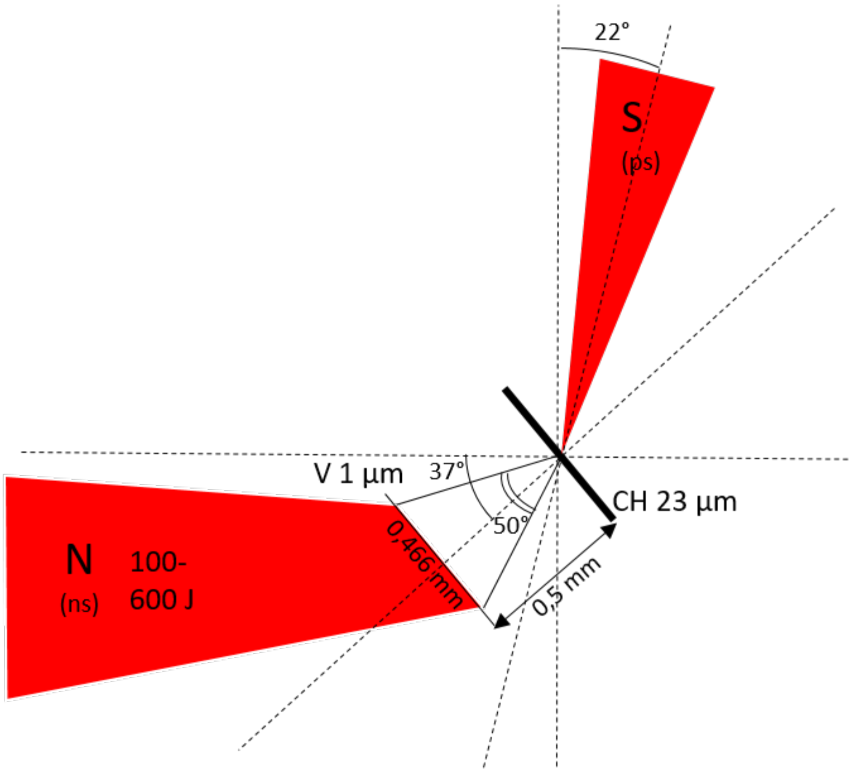

Figure 3.6: *Sketch of the targets setup with angles and distances between those.*

To monitor the proton energy spectrum, we used a magnetic spectrometer. This device consists here of two pairs of magnets which deflects protons coming out an assembly slit-collimator. An IP(169) is also use as detecting device here and its position depends on which energy range we want to monitor. The highest energy part of the proton beam is emitted normally to the aluminized PET target. Hence, the magnetic spectrometer needs to be placed on this path, as shown in Fig.3.7.

Finally, including the new constraints due to the laser paths and other elements in the chamber to the design we already established thanks to the Geant4 simulations (see section 2.1.3), we can now set the final design of our neutron detector. A CAD representation is shown Fig.3.8. The biggest hole in angular coverage in the upper right side of the top view is due to the path of the picosecond laser beam. It is especially due to a lead shield which is visible in Fig.3.3 and which has the purpose to protect the experimental and technical teams from the proton beam which comes out from the front face of the PET target(170). Another angular space on the left side of the top view has been freed for the nanosecond laser beam path. For alignment purposes, it has also been necessary to let two spaces on the opposite side of the laser paths, here on the right side and on the bottom left side of the top view. Besides, we can see that it has also been necessary to reduce the height of two modules on the bottom left side of the top view. This is due to a large mirror mount used to direct the SOUTH beam downward to the off-axis parabola. Moreover, the module in the middle of the batch on the bottom left side of the top view has

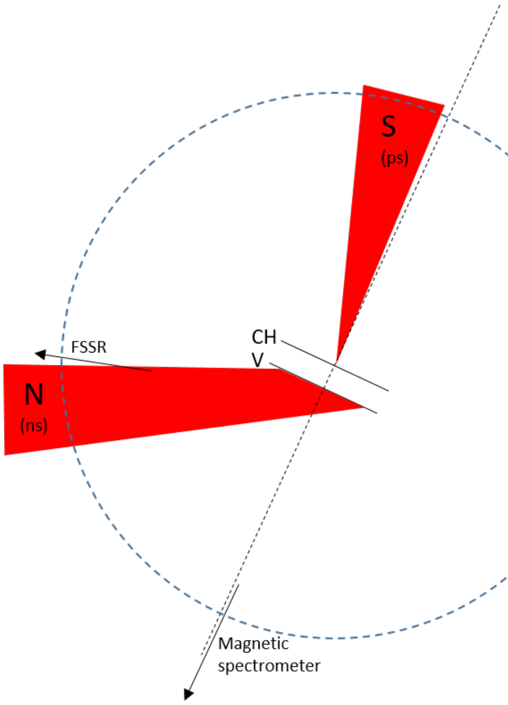

Figure 3.7: *Sketch of the setup*

been machined to have a little hole at the target height. This is to allow a part of the proton beam to go through and reach the magnetic spectrometer placed further away.

The setup with the diagnostics is summarized in Fig.3.7. Figs.3.9 and 3.10 show some captioned photos of the actual setup during the experiment. One important feature which has not been addressed yet is the white piece of plastic between the targets assembly and the lead shield. This piece has for very important purpose to stop the protons generated out the front face of the PET target before they reach the lead shield. Indeed, stopping protons with energy of several MeVs in lead would generate a lot of neutrons while it shouldn't in plastic. Without this, our neutron detector would have been flooded by those unwanted neutrons.

3.2.3 Preparatory simulations

In order to know what we could expect from this experiment and what parameters we should set, we did some calculations and simulations before the experiment.

Production of neutrons

Knowing the efficiency of our detector, we also needed to know the neutron production per shot according to the maximum proton energy. Indeed, since we are able to control this maximum energy by changing the size of the focal spot and since the cross section of the (p,n) reaction for both isotopes of

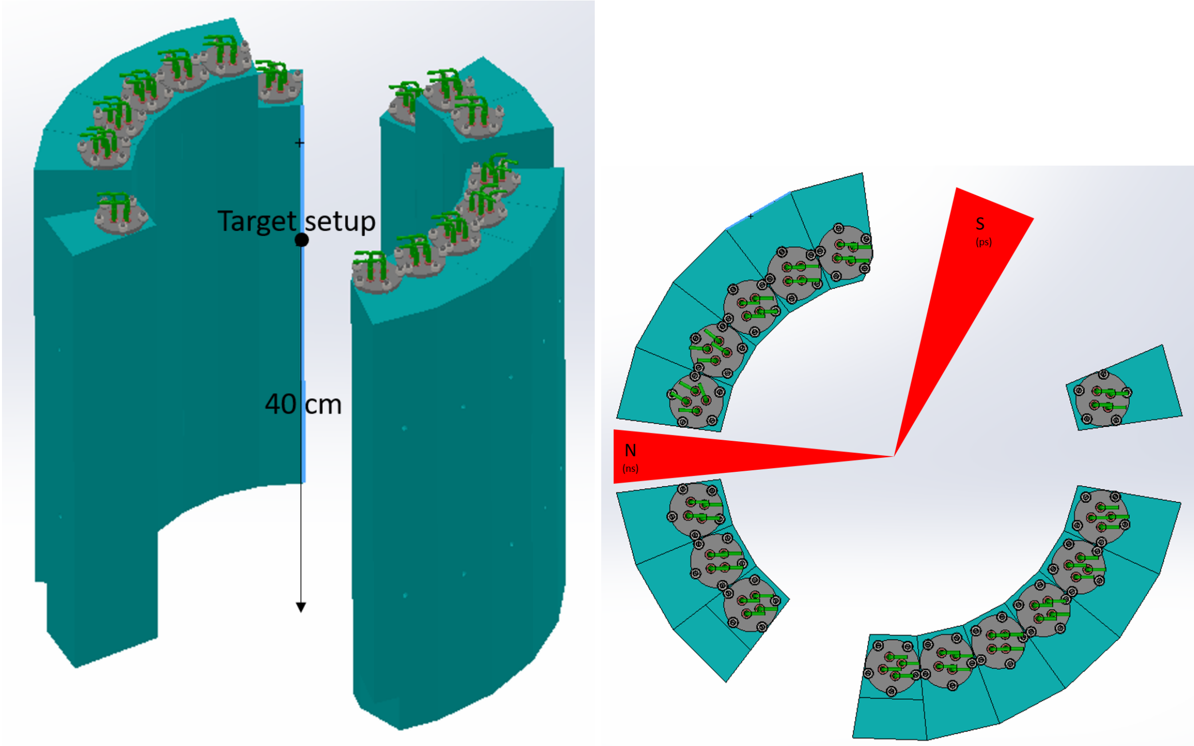

Figure 3.8: *CAD representations of the neutron detector design used during the LULI2000 experiment. The right image is a top view while the left one is more from the side.*

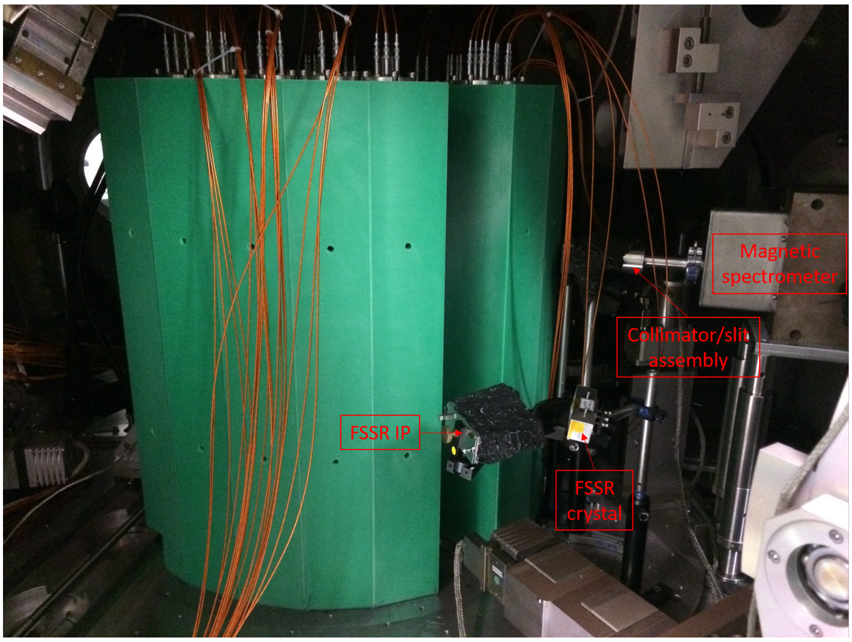

Figure 3.9: *Captioned side view of the experimental setup*

vanadium varies a lot according to the energy, controlling the maximum energy of the proton beam was the most efficient way for setting a neutron production which could be detected by the neutron detector without overloading it.

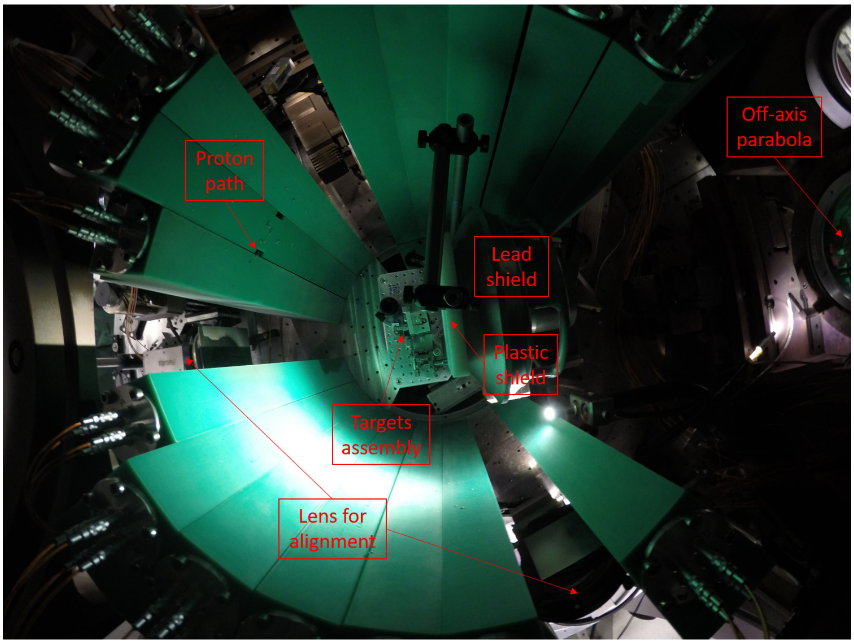

Figure 3.10: *Captioned top view of the experimental setup*

To estimate this neutron production, we used the database TENDL-2019(82) and proton spectra from shots obtained on the LULI2000 facility with the very same pico2000 configuration during another experiment of our group. The proton spectrum we used was measured using RadioChromic Films (RCF)s stacks(171). This RCFs stack allows to know the proton flux at several discrete energies. We can then fit the measured point with a Boltzmann distribution (see section 1.1.2) which stops at a maximum cutoff energy to have a fair estimation of the proton spectrum. This proton spectrum is shown in Fig.3.11. Other measures(38; 171) with RCF stacks have shown that the maximum proton energy is between 20 and 30 MeV in those experimental conditions, with the focal spot size reduced at its minimum, i.e. $\sim$5 μm.

Using this fit, we tested several different cutoff energies to see their effect on neutron production. Since all the protons produced on the rear face will interact with the secondary target, we had to define the overall number of protons produced on the rear side from this spectrum. To do so, we used the evolution of the half-angle of the proton cone beam according to the proton energy(166). For a given proton energy, we then assumed the isotropy of the proton emission within the boundary of the cone define by the energy dependent half-angle. This gave us a number of protons for each 100 keV energy bins represented in Fig.3.12 for several maximum cutoff energies.

For the lowest energies, since TENDL only give a few points and the cross section variation between those energies is of several orders of magnitudes, a linear interpolation was not accurate enough. Hence, we used a custom interpolation to have a more credible cross section. For energies of less than 1 MeV, we did an interpolation to the power 18, between 1 and 2 MeV, to the power 9 and between 2 and 3 MeV,

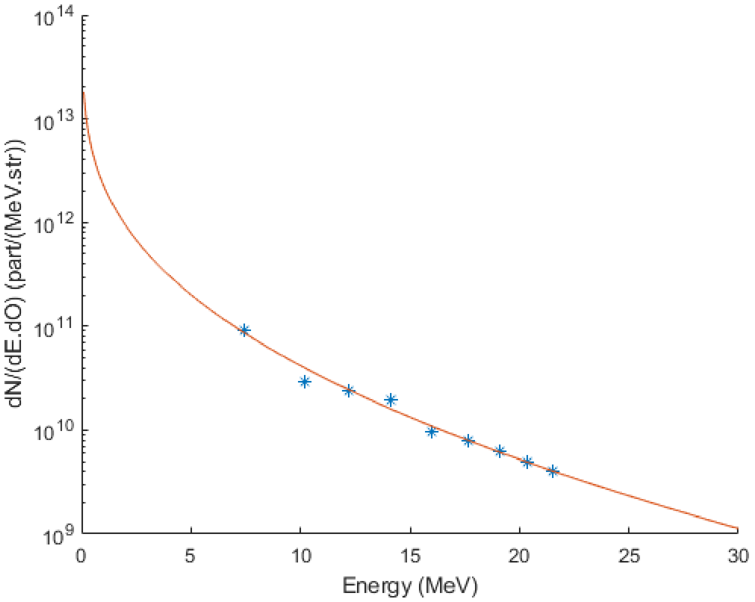

Figure 3.11: *Measured proton fluxes using RCFs stack represented by the blue stars and its fitted Boltzmann distribution proton spectrum represented by the red curve. The cutoff energy for the fitted curve is here set at 30 MeV which is higher than what has been measured with the RCFs stack.*

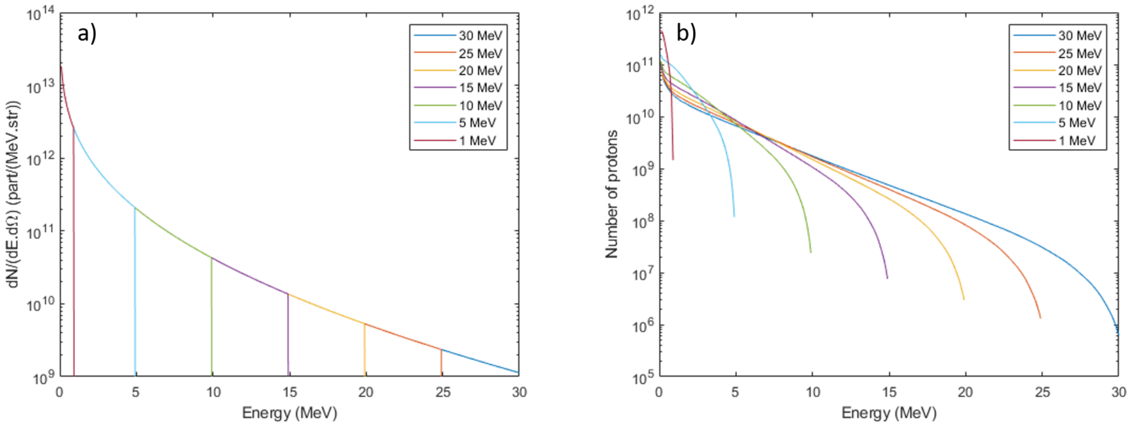

Figure 3.12: *Proton spectra with several cutoff energy on the left and associated overall number of proton according to their energy with 100 keV energy bins on the right.*

to the power 4. For the others energies, a classic linear interpolation seemed accurate enough. Both interpolations for the cross section of the reactions ^{50}V(p,n) and ^{51}V(p,n) are represented in Fig.3.13.

Besides, to take into account the energy loss induced by the travelling in the vanadium target, we used stopping power data from SRIM(127). Using timesteps of 1 fs, we have then been able to calculate for each batch of protons, according to their energy, the number of reactions at each timesteps and the mean energy loss. Running this until the protons go out of the target or stop in it, we have been able to calculate a number of reactions, i.e. a number of neutrons since at such low energies, only (p,n) reactions

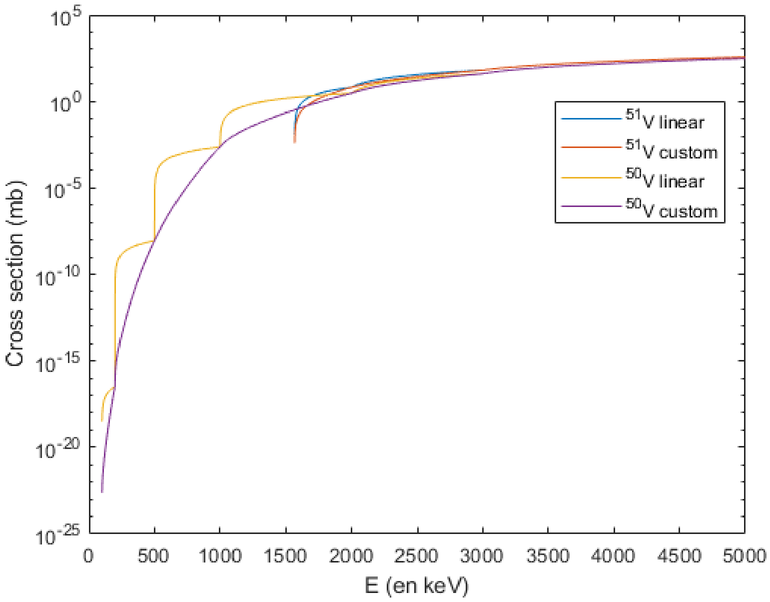

Figure 3.13: *Cross section of the reactions* $^{50}V(p,n)^{50}Cr$ *and* $^{51}V(p,n)^{51}Cr$ *extracted from TENDL-2019(82) with a linear interpolation and a seemingly more realistic custom interpolation.*

participate in the neutron production. We run this script for a 1 μm thick solid natural vanadium target. Thanks to simulations we will present after, we also have been able to use this script on a density map for an heated target. However, this shouldn't be so accurate since no plasma effect are taken into account in this case, especially on the stopping power.

Those calculations have been crucial in the proton target design. Indeed, it shows that it will not be possible to see any neutrons for a maximum energy cutoff below 2 MeV. Hence, a gas jet design for the proton emitting target was not conceivable (see Fig.3.5). We also see that most of the neutrons we will see will be emitted by the isotope ^{51}V. However, a solid target with a varying focal spot diameter seems perfect. Indeed, it would allow us to measure neutron numbers from 10^4 to more than 10^6 which seems totally feasible even if we take into dome detector dead time due to the EMP and prompt gamma emission.

During the gamma test at Dusseldorf, the fastest energy deposition we saw was located 300 μs after the prompt gamma flash. We only saw four of those energy depositions over 58 shots with recording times of 5 ms and the baseline was back in the vicinity of its original value 1 μs after the prompt gamma/EMP peak. Hence, if we want to estimate the number of neutrons we will be able to detect, it seems very conservative to assume that neutron capture can be detected as soon as a 50 μs after the shot. Even with this assumption, according to Table.2.2, if we consider that the neutrons have a 1 MeV energy and the proton beam a 20 MeV cutoff energy, there are still 21485 neutrons to be detected, i.e. 939 neutron detections according to the efficiency calibration.

Energy	Solid cold target			Hot target		
(MeV)	^{50}V(p,n)*	^{51}V(p,n)*	Total	^{50}V(p,n)*	^{51}V(p,n)*	Total
1	$1.33.10^{-5}$	0	$1.33.10^{-5}$	$1.32.10^{-5}$	0	$1.32.10^{-5}$
1.5	$2.07.10^{-2}$	0	$2.07.10^{-2}$	$2.08.10^{-2}$	0	$2.08.10^{-2}$
2	$4.67.10^{-1}$	$1.09.10^{2}$	$1.10.10^{2}$	$4.78.10^{-1}$	$1.11.10^{2}$	$1.11.10^{2}$
3	$1.68.10^{1}$	$1.15.10^{4}$	$1.15.10^{4}$	$1.71.10^{1}$	$1.17.10^{4}$	$1.17.10^{4}$
4	$9.58.10^{1}$	$6.04.10^{4}$	$6.05.10^{4}$	$9.80.10^{1}$	$6.18.10^{4}$	$6.19.10^{4}$
5	$2.68.10^{2}$	$1.56.10^{5}$	$1.56.10^{5}$	$2.77.10^{2}$	$1.61.10^{5}$	$1.61.10^{5}$
10	$1.61.10^{3}$	$8.07.10^{5}$	$8.09.10^{5}$	$1.68.10^{3}$	$8.41.10^{5}$	$8.43.10^{5}$
15	$2.45.10^{3}$	$1.20.10^{6}$	$1.20.10^{6}$	$2.54.10^{3}$	$1.24.10^{6}$	$1.25.10^{6}$
20	$2.80.10^{3}$	$1.39.10^{6}$	$1.39.10^{6}$	$2.90.10^{3}$	$1.44.10^{6}$	$1.44.10^{6}$
25	$2.92.10^{3}$	$1.46.10^{6}$	$1.47.10^{6}$	$3.03.10^{3}$	$1.51.10^{6}$	$1.52.10^{6}$
30	$2.92.10^{3}$	$1.48.10^{6}$	$1.48.10^{6}$	$3.02.10^{3}$	$1.52.10^{6}$	$1.53.10^{6}$

Table 3.2: *Number of (p,n) reactions per shot with proton energy spectra with different energy cutoffs as presented in Fig.3.12b. Are shown the number of reactions according to the reacting nuclide for two cases. The two cases are a 1 μm thick solid cold natural vanadium target and a 1 μm thick natural vanadium target heated on its rear side by a 600 J 1 ns laser pulse. The laser hit the target exactly when the neutron are emitted 5 mm away from the front side of the vanadium target.*

On a more concerning note, using a laser-driven multi-MeV proton beam which can vary quite a lot shot to shot, to detect a screening potential which should be of a few tens of keV seems challenging. Hence, the more statistic per shot we can have, the better.

Expected ionization

In order to have the highest screening effect, we had to aim for the highest ionization rate. For practical reasons, it was only possible to irradiate the vanadium target from the rear side. To see what ionization rate we could expect, we did some simulations using MULTI(172). MULTI is a one-dimensional code which treats radiation transfer and hydrodynamics and has been developed to compute the extreme thermodynamic conditions existing during a laser matter interaction event.

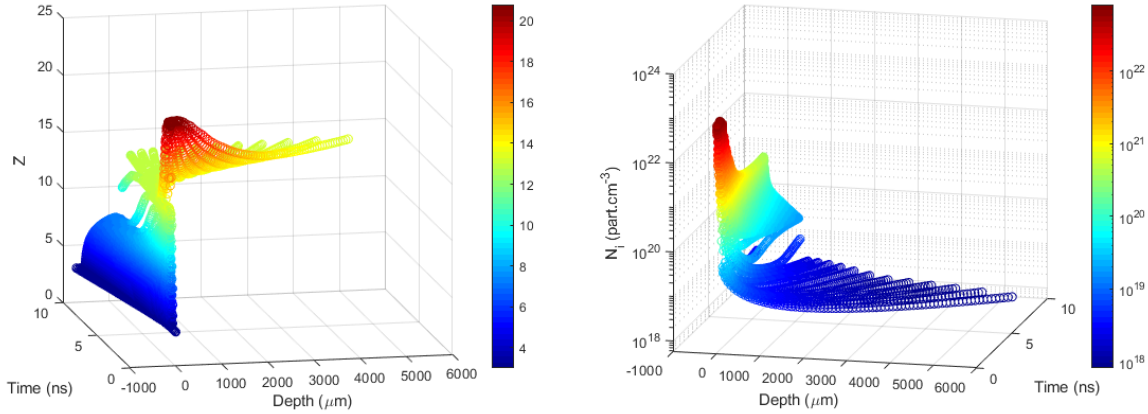

Figure 3.14: *Evolution of the ionization rate on the left and the density on the right of the target according to the time and the depth. These results are for a 1 μm thick vanadium target and $1.0.10^{14}$ W.cm^{-2} irradiation.*

Simulations were run for several target thicknesses and irradiation strengths. Fig.3.14 shows some results for a 1 μm thick target and an irradiation of 1.0.10^{-14} W.cm^{-2}. This irradiation corresponds to 170 J during 1 ns on a 466 μm focal spot. We need a quite large focal spot to be able to heat the target everywhere the proton beam will span. Those simulations shows that even 10 ns after the shot on the vanadium target, there is still a part of the target which isn't ionized and most of the ions in the dense part of the target have an ionization rate around 3, which is the minimum value in the simulation. However, we also can see that there is a good part of the target in term of depth which is 10 to 100 times less dense than the dense part but for which the ionization rate climbs up around 8. For earlier times, it is a bit more complicated to say anything without a zoom-in.

If we assume a uniform electronic charge within the atomic radius, theory gives us(173):

$$U_e = \frac{Z_0 Z_1 e^2}{4\pi\epsilon_0 R_a} \tag{3.11}$$

Where Z_0 and Z_1 are the charge of the nucleus and the incoming particle, e the elementary charge, ϵ_0 the permittivity of free vacuum and R_a the radius of the nucleus. For solid vanadium, we then have a theoretical value for U_e equal to 245.39 eV. It goes down to 160.03 eV for the ion vanadium ionized 8 times. This would give us a change in screening potential of only 85.36 eV. However, as the experiments have already shown(152; 173; 159), this value is way underestimated by theory and the difference in screening should be more in the tens of keV range.

So, in a first time, we assume that the electron screening effect was proportional to the ionization rate. In order to chose our parameters, we compared the sum over the whole target thickness of the product of density with ionization rate. This product is represented in Fig.3.15.

As a safeguard, we also didn't want a target thinner than 1 μm not to blow the target before the full ns pulse can be absorbed. This figure shows clearly that the best is to shoot the proton target as soon as the north bean hits the vanadium target. We neglect here the ps scale time to produce the proton beam(35) and the protons travel tens of ps scale time between the two targets since this is way faster than the ns scale of the hydrodynamics implied in the secondary target. This goes well with the fact that if we had to wait, the x-rays emitted by the heated vanadium could have blown up the proton producing target. Also the best thickness seems clearly to be 1 μm.

With all those results, we have been able to finalize the setup of with the two targets which is presented as a sketch in Fig.3.6. Now that all the parameters needed to do the experiments were set and that we know what proton maximum energy we would need to get a detectable neutron production, we were all set to perform the experiment at the LULI2000 facility.

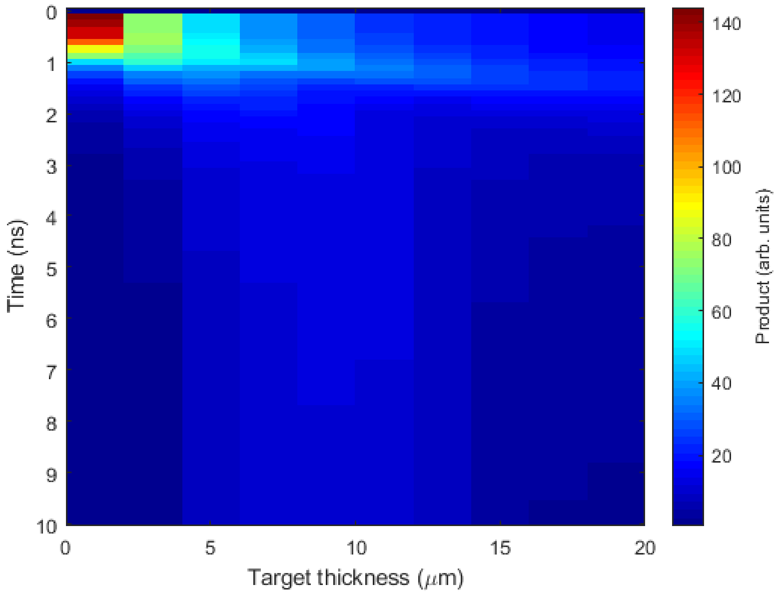

Figure 3.15: *Evolution of the sum over the thickness of the product of the density and the ionization rate. This product is represented according to the target thickness and the time after the shot.*

3.3 Analysis and results

During July 2019, we then have been able to implement the setup described section 3.2.2 and shoot with different set of parameters. In the next sections, we will present the results we got during this month of experiment and the analysis we did on the data obtained.

3.3.1 PMT response to prompt gamma flash/EMP

The first major hurdle we encountered during the experiment is the PMT response to the prompt gamma flash/EMP. Indeed, a feature we have not been able to detect and characterize during the Düsseldorf test is that the PMTs can be unresponsive even though their voltage comes back to the at-rest voltage value. With the laser parameter we were using during the LULI2000 experiment, this unresponsive time we didn't plan for, can last from around 100 μs to more than 1 ms in the worst case. Since the recording duration was 1 ms, there are thus some detector units which were totally unresponsive. This duration seems angle-dependent and we observed that the detector units in the direction of the ps beam were more affected than the other units. PMTs on the up side are also often more affected since they are nearer to the equatorial plane than the PMTs on the down side (see Fig.3.8). But most of all, the behaviour is strongly PMT dependent.

Fig;3.17 shows examples of the traces we have been able to record for a shot with a good neutron production. We see that the prompt gamma flash/EMP induced peak totally saturates the electronics

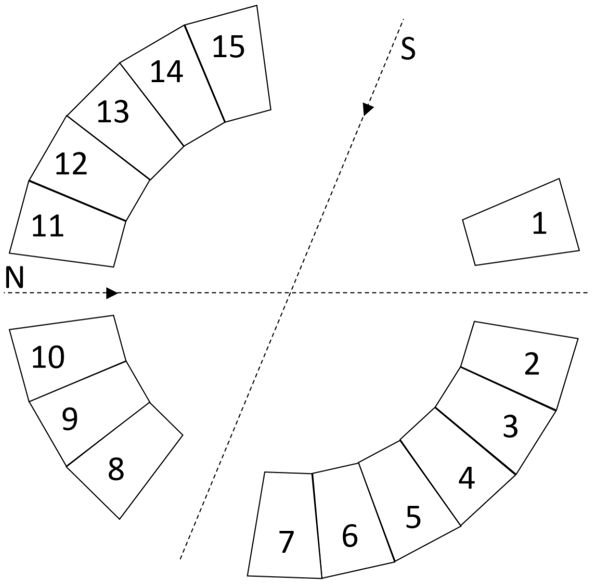

Figure 3.16: *Sketch of the detector setup with the two beams directions and the detector units labels.*

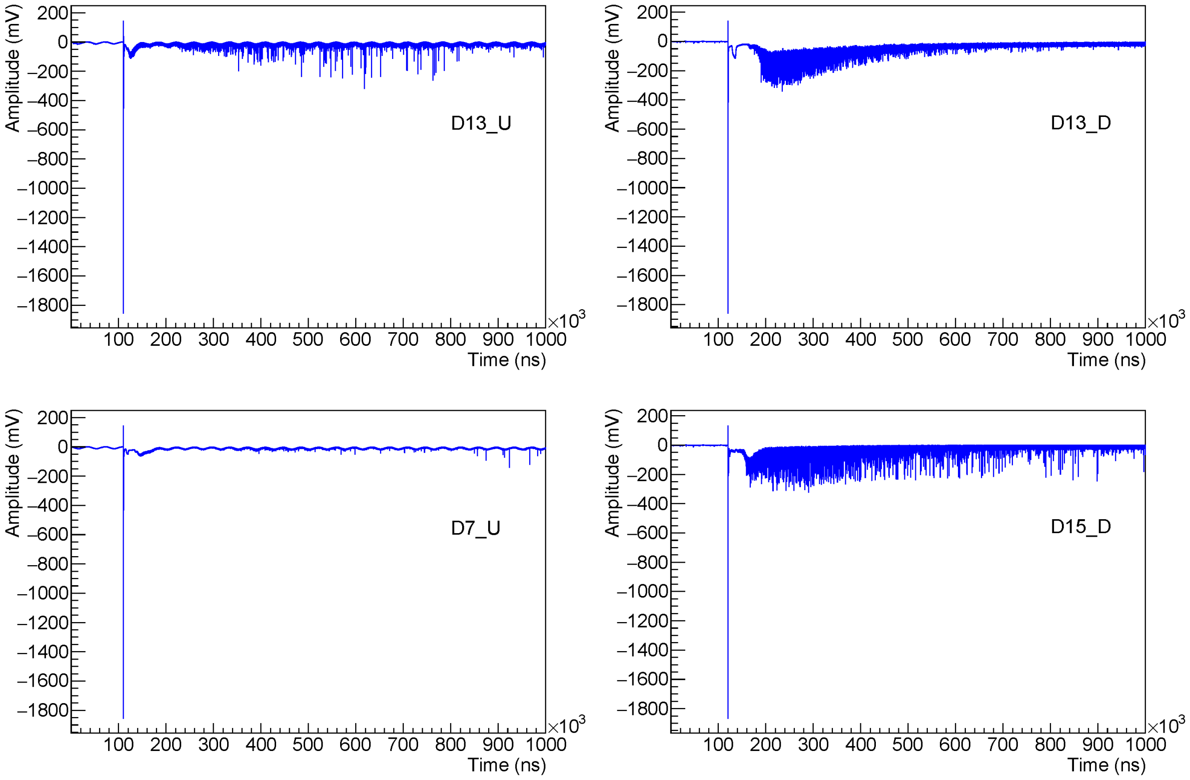

Figure 3.17: *Examples of traces obtained from different detector units and PMTs during shot 28. During this shot, the proton energy cutoff was 16.31 MeV and a 1 μm solid vanadium target was in place.*

since it reaches the card limit set at 2 V_{pp}. We see that, after this peak, there is a period during which the signal comes back to values near the at-rest baseline value. This unresponsive period duration varies from ∼100 μs for D15_D and D13_D to almost 1 ms for D7_U. In the labels, D stands for detector unit, 7 stands for the number of the detector units as presented in Fig.3.16 and U or D stands for up or down depending on which PMT we are looking into. After this unresponsive time, we see that the maximum peak height increases more or less rapidly to reach values between 250 mV and 300 mV. As seen in Fig.2.34, the mean peak height for a neutron detection is around 50 mV in normal condition. Then, the maximum peak height decreases on the scale of a few hundreds of μs as shown with the trace of D13_D in Fig.3.17, or stays at the same higher peak height as expected for the whole recording time.

Another important feature of the recorded signal which needs to be addressed is that the electronic noise after the shot is way higher than what could exist during the calibration measurements. Hence, the thresholds will need a readjustment and this will have an impact on the efficiency which has been presented in section 2.3.3. Also, since the electronic noise is more important, it should be more difficult to differentiate the neutron peak from the noise.

As it can be deduced from Figs.3.16 and 3.17, the duration of the time window during which the maximum peak height is first at the noise level and then increases to reach a maximum value, seems to mainly depend on the position of the PMT. As a reminder, we have shown in section 2.3.2 that the light distribution between the two coupled PMTs depends strongly on which scintillator cylinder the energy deposition takes place in. Hence, PMTs on the upper side should indeed receive more light than the ones on the down side.

However, the time it takes for this maximum peak height to decrease is really PMT dependent. We can draw two conclusions from this. First, since for some PMTs, the maximum peak height comes back to what we can expect of a regular neutron capture event, most of those peaks probably corresponds to neutron capture events even though their height is higher than expected. Second, the characteristics of the neutron peak in the energy histograms will probably be different. The peaks which have a higher height than expected will most probably also have higher integrals and, hence, higher associated energies. Then, the best case scenario is that the mean peak height stays constant and high for both coupled PMTs. This way, the peak should be located at higher energy than during calibration. For all other cases, the mean neutron peak height varies in time for at least one of the two PMTs and hence the definition itself of the peak is more complicated.

The sinusoidal signal we see on the PMTs U comes from a defect on the V1730SB card we used with those PMTs. The card has been afterward sent back to CAEN which found the issue and corrected it. This has no effect on the recording apart from this sinusoidal signal.

3.3.2 Procedure

With those new facts in mind, we established procedures during the experiment and then during the analysis of the data in order to ensure the nature and quality of our measurements.

During the experiment

As a reminder(165), during this experiment, the parameter we decided to play with to change the energy proton spectrum, in particular its maximum energy, was the size of the picosecond beam focal spot. Then, for a given energy spectrum the idea was to compare the number of neutrons detected when the secondary vanadium target was either in a solid state (cold shot) or a plasma state (hot shot). To ensure that what we were detecting with the detector were neutrons produced by the vanadium target, we decided to also do a third series of shot without any vanadium target for a given S-beam focal spot size and proton spectrum. To check the influence on the detector of the N-beam used to heat the secondary target, we also did some shots only with the north beam.

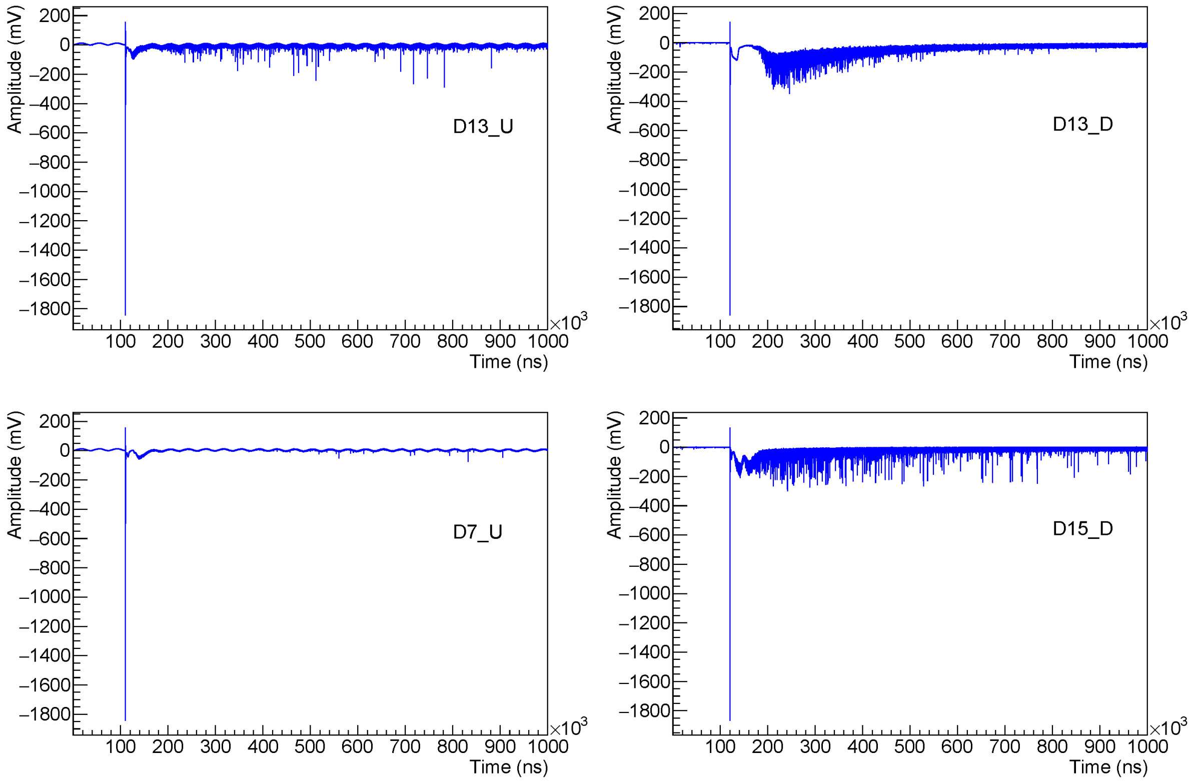

Figure 3.18: *Examples of traces obtained from different detector units and PMTs during shot 27. During this shot, the proton energy cutoff was 16.06 MeV and there was no vanadium target in place in place.*

Fig.3.18 shows examples of traces for the same PMTs, obtained during shot 27 which had the same parameters than the shot 28 for which the traces are shown in Fig.3.17, except for the vanadium target which was here removed. We see that the main behaviour is the same for each PMT. However, we can already seen that there are less peaks in those traces in comparison with the shot 28, as expected. The existence of peaks on those traces can be explained by several noise sources. It can either correspond to energy deposition from other energetic particles such as gammas which would have been delayed by bouncing around in the room or chamber. It could also be neutron capture by neutrons produced by other processes than the (p,n) reaction in the vanadium. For instance, the energy thresholds for the (p,n) reaction with ^{12}C and ^{13}C which represent the main components with ^{1}H of the HDPE, where most of the protons are stopped, are respectively 19.6 MeV and 3.2 MeV. For shots 28 and 27, the energy cutoffs for the proton spectrum were respectively 16.31 and 16.06 MeV. Hence, it is possible to have neutron production (p,n) reactions with ^{13}C in the detector bulk. It is even possible to see (γ,n) reactions either in the HDPE of the detector or in the chamber walls.

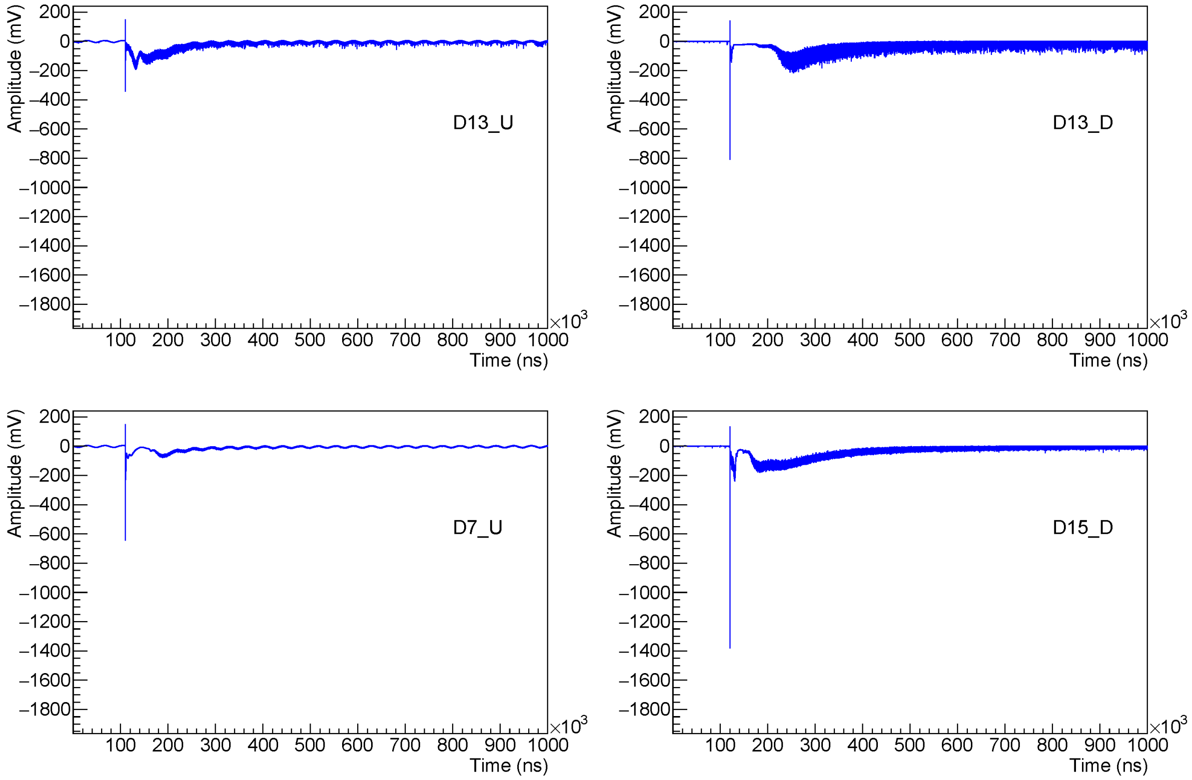

Figure 3.19: Examples of traces obtained from different detector units and PMTs during shot 54. During this shot, only the north beam was fired on a 1 μm vanadium target.

Fig.3.19 shows examples of traces for the same PMTs, obtained during shot 54 for which only the north beam was fired. The north beam also creates a prompt gamma flash/EMP peak although not as important as during a south beam shot. Also, the north beam generates electronic noise at an height which seems to totally depend on the PMT. Indeed, no angular or U/D dependence can be seen when we examine all the different traces. On a brighter side, we don't see any 200 mV-high peak during those shots. Hence, the addition of the north beam should not have an important effect, apart from a possible higher electronic noise depending on the PMT.

Analysis of the traces

In addition to the decisions taken during the experiment, we had to elaborate an analysis procedure to ensure the nature of what we had been able to measure. For all the detector units, we first had to set new thresholds which were more adapted to the changing noise level. Since the noise level is higher and depends on the time for some PMTs, this is the most complicated part. To do so, we can in a first time directly look at the traces and choose as threshold the half of the mean height of the noise. After that, we can try to improve those thresholds by looking at the histogram where the number of peaks is represented according to its energy, and have the neutron peak as clear as possible above the noise.

We also need a temporal selection since the PMTs are unresponsive or not reponsive in a satisfying way for some time after the shot. According to simulations, some results of which are shown in Fig.2.15, we know that the neutron detection rate should decrease according to the sum of two exponentials. In the range of neutron energy we are interested in, their two half lifes are around 12 and 110 μs. Taking into account the dead time duration which lasts at least 100 μs, the detection rate should then be fittable by a decreasing exponential with a half life of 110 μs.

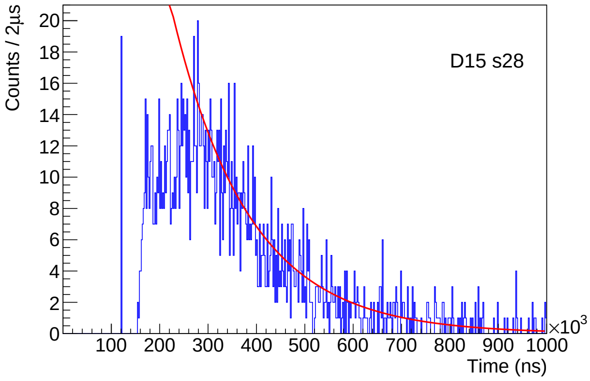

Figure 3.20: *Histogram of the light collected by the detector unit 15 according to the time during shot 28. The red curve represents a decreasing exponential with a half-life of 110 μs.*

As shown in Fig.3.20, we see the prompt gamma flash/EMP peak and then, after some dead time, the peak detection rate increases until reaching a peak and decreasing. If we represent a decreasing exponential with a 110 μs half-life and the right amplitude, we see a satisfactory agreement between this exponential and the detection rate after some time. Using this, we can define a time cutoff value after which we consider that the detector unit functions satisfyingly.

After those different steps, we can obtain the histogram presented in Fig.3.21. This histogram is what we can obtain in the best case scenario. Indeed, for the two PMTs of detector unit 15, the maximum peak height was staying high for the full recording time after its increase. Hence, we can see that the mean energy of the neutron peak is around 150 keV instead of around a 100 keV.

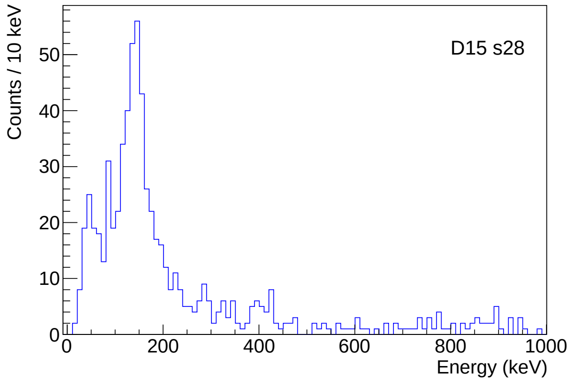

Figure 3.21: *Histogram of the light collected by the detector unit 15 according to the energy during shot 28. All the peaks detected before the timestep 170000 are excluded from this histogram.*

In the example presented in Fig.3.21, the neutron peak is clear, however, depending on the recovery time of the PMTs, the statistic available varied a lot from a detector unit to the other and, in the end, not all traces were exploitable since it can be impossible to define a clear peak apart from the noise in some cases.

To measure the neutrons produced in the vanadium, the idea is now to compare the histograms obtained for shots with and without the vanadium, and for equivalent proton spectra. Hence, we need at this step to know the proton spectrum for each shot.

Proton analysis

To measure the proton spectra, we used a magnetic spectrometer. As shown in Fig.3.22, this magnetic spectrometer is composed of a slit and a collimator at the proton entrance, of two pairs of magnets that deviate the protons according to their energy and of an IP(174) to measure the proton energy deposition. For the IPs, we used the Fuji BAS-TR model, several calibrations of which can be found in the literature(175; 176; 177; 178; 179; 169).

For such a spectrometer, if we consider a homogenous magnetic field in between the magnets, no magnetic field outside and a Larmor radius way bigger than the size of the magnets, the position of the energy deposition of a proton with a given energy is given by the following equation :

$$x = \frac{eBl_B\left(D_B + \frac{l_B}{2}\right)}{\sqrt{2m_pE_p}} \tag{3.12}$$

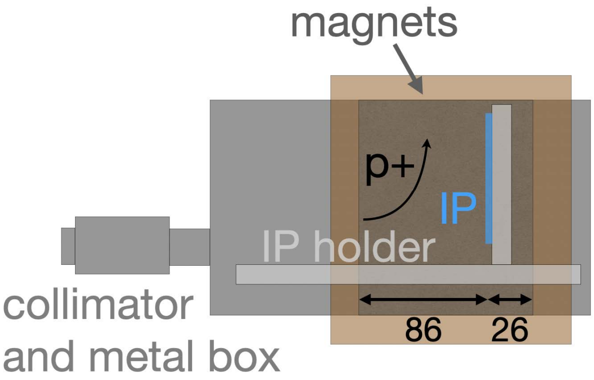

Figure 3.22: Sketch of the magnetic spectrometer used during the LULI2000 experiment.

Where x is the distance between the energy deposition position and the zero order, i.e. where the non-deviated particles, such as the gammas, deposit their energy, e is the elementary charge, B the magnetic field between the magnets, l_B the length of the magnets, D_B the algebric distance between the IP and the back of the magnets, m_p the proton mass and E_p the proton energy. Using different filters and SRIM calculations(127), we have determined during the experiment the calibration curve which is shown in Fig.3.23.

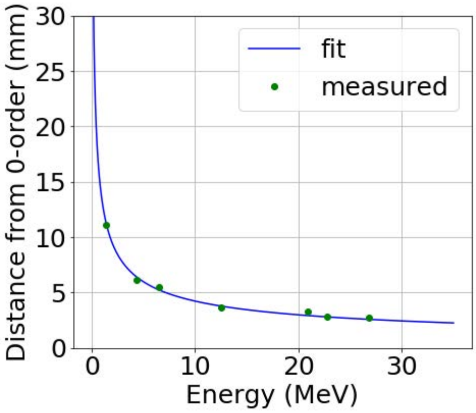

Figure 3.23: Distance from the zero order according to the proton energy. Experimental points are in green and the blue curve represents the fit using Eq3.12 with D_B^{fit}=-25.3 mm et B^{fit}=0.56 T.

The filters used were pieces of 25, 150 and 300 μm thick aluminum, 250 μm thick gold, 1 mm thick lead, 1 mm thick copper and 1.1 mm thick tantalum with cutoff energies of respectively 1.44, 4.36, 6.55, 12.53, 20.89, 22.80 and 26.86 MeV for the protons. We used B and D_B as fitting parameters. Indeed, the measure of D_B with a ruler might not be exact and B corresponds to a magnetic field which cannot be precisely measured since it corresponds to an idealized one. Finally, we can use Eq.3.12 with D_B^{fit}=-25.3 mm et B^{fit}=0.56 T to have the energy of the protons which deposited their energy in the IP according to their position.

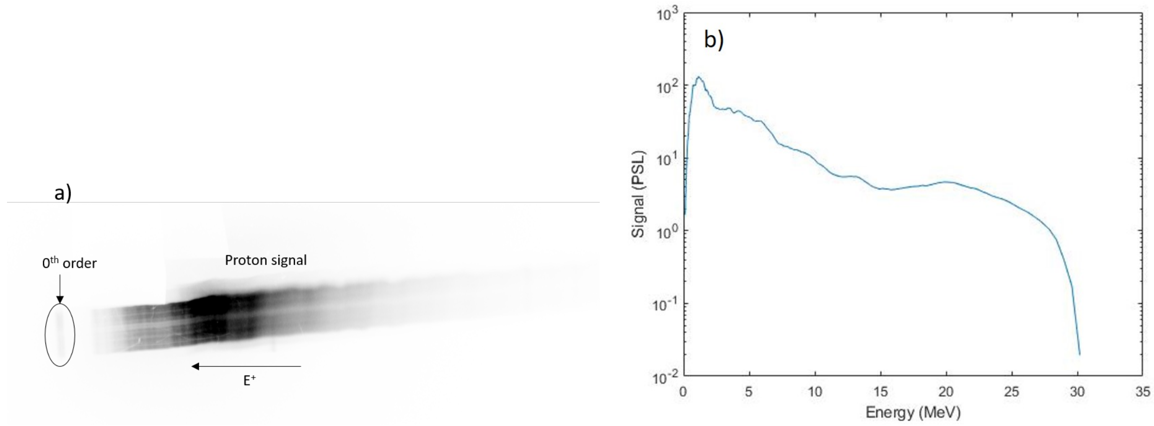

Figure 3.24: *IP scan for shot 9 and corresponding PSL spectrum.*

The scan of the IP gives us an image of quantum levels (QL). This image is represented in Fig.3.24a. From this, we can calculate a PhotoStimulated Luminescence (PSL) value which is a function of the deposited energy. This PSL value is given by the equation(175) :

$$PSL = \left(\frac{R}{100}\right)^2 \times \frac{4000}{S} \times 10^{L\times\left(\frac{QL}{2^G-1}-\frac{1}{2}\right)} \tag{3.13}$$

This PSL value along the axis normal to the slit for shot 9 is shown in Fig.3.24b. For low energy deposition the PSL value is proportional to the energy deposited by the particle of interest. However, for ions, the energy deposition density is too high and the relation between the PSL and the ion kinetic energy is a bit more complicated. We published an empirical formula(176) inspired by Birks' formula(128) to retrieve the PSL value induced by an ion. This empirical approach seems accurate for light ions, up to carbon, and the PSL value is then given by :

$$PSL(E) = A\int_0^W \frac{\frac{dE_{dep}}{dz}(E,z)}{1+B\frac{dE_{dep}}{dz}} e^{-\frac{z}{L}}\, dz \tag{3.14}$$

Where PSL is the PSL value deposited by one ion, A a parameter equal to $2.4.10^{-4}$ $PSL.keV^{-1}$, W the width of the active layer equal to 50 μm, E_{dep} is the energy deposited by the ion, B another parameter equal to 0.15 $Å.eV^{-1}$ and L the absorption length of the scanning photons (2-3 eV) estimated by Bonnet(179) to be equal to 44 μm. The energy deposited by the ions according to the depth can be calculated using SRIM(127). This gives us the PSL response of the TR image plates which is shown in Fig.3.25a. Kojima et al(178) have shown that this approach is also accurate for protons and carbon ions with energies lower than respectively 0.2 MeV and 1 MeV. For heavier ions, Nishiuchi et al(180) have a proposed a more general formula :

$$PSL(E) = \int_0^W \frac{dE_{dep}}{dz}(E,z)\left[\frac{A_1 e^{-\frac{z}{L}}}{1+B\frac{dE_{dep}}{dz}} + A_2\right] dz \tag{3.15}$$

Where A_1 and A_2 are parameters without fixed values yet but $A_1 \gg A_2$. In order to get the best accuracy possible, we decided to use an empirical formula specific to the protons stated by Mancic et al(181), as follows :

$$PSL(E) = 0.22039 e^{-\frac{(E-1.5049)^2}{1.18422^2}} \qquad for\ E \leq 2.11\ MeV \tag{3.16}$$

$$PSL(E) = 0.33357 E^{-0.91377} \qquad for\ E > 2.11\ MeV \tag{3.17}$$

Where E is the proton energy in MeV. This model is also presented in Fig.3.25a and a recent paper by Martin et al(182) have tested it satisfyingly.

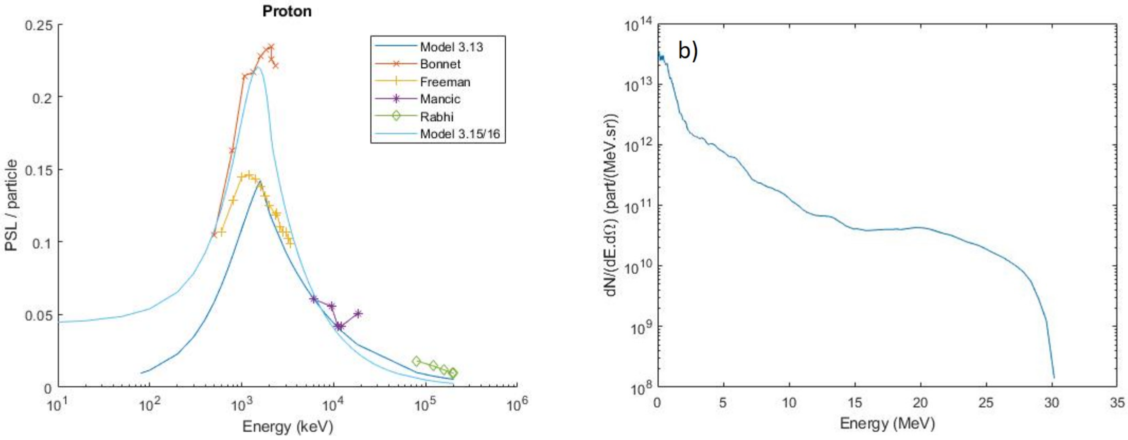

Figure 3.25: *a) PSL per particle calibration for the TR images plates. The blue curves represents the result of the empirical models presented respectively by the Eq.3.14 and 3.16/3.17. Other curves represent experimental datasets from experimental works lead by Bonnet(169), Freeman(183), Mancic(181) and Rabhi(184). b) Angular energy proton spectrum for shot 9.*

Now that that we have a correspondence between the PSL value and the number of protons detected,we can use geometrical considerations to to get a proton spectrum. Indeed, using the zero order width on the IP, the derivative of Eq.3.12 and the distance between the target and the IP, we can calculate the correspondence between a pixel size and a solid angle. In our case, the zero order width could vary a bit from shot to shot depending on the laser parameter and hence the strength of the x-ray emission. To avoid this dependence, we set it at a mean value of 0.8 mm. The distance between the target and the IP was measured at 692 mm. We can then calculate a energy and angular proton spectrum as shown in Fig.3.25. Using the relation between the proton energy and the emission cone half-angle(166), it is even possible to retrieve an energy proton spectrum or an absolute number of protons. As a safe guard to verify the validity of our process, we can consider the proportion of laser energy transfer to the proton. For instance, for shot 9 presented in Fig.3.25, we find an energy transfer of 3.4%, i.e. 2.07 J out of 61.0 J.

Comparison of the shots

Now that we have proton spectra for each shot, we are able to compare the results obtained from the detector units for shots with different parameters but with the same proton spectrum. We can also define different time cutoff values, i.e. the time at which we start the neutron peaks counting, for each shot and define the latest one as the time cutoff for all shots with the same proton spectrum to compare the shots. Hence, if we look again at the results of detector unit 15 for instance, using the very same thresholds and time cutoff, we can have the resulting histograms shown in Fig.3.26 alongside the corresponding proton spectra.

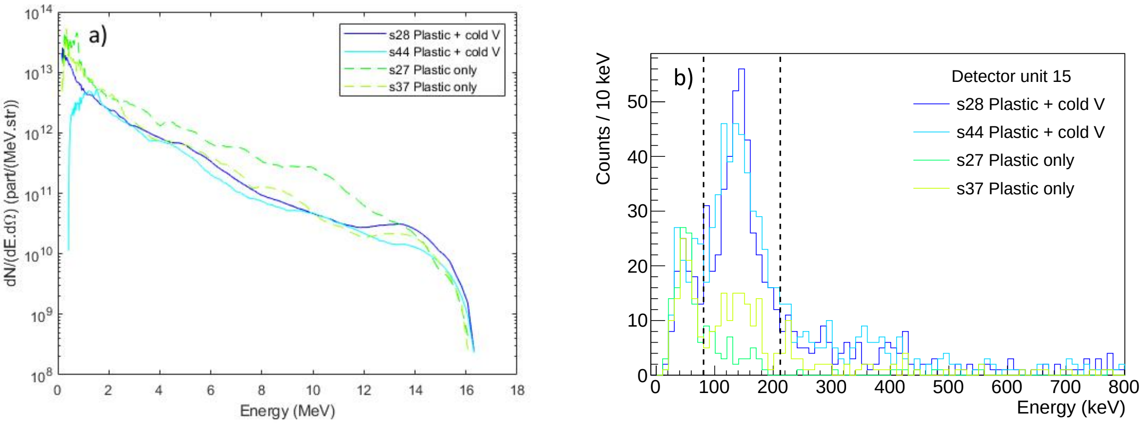

Figure 3.26: *a) Proton spectra for four shots with equivalent laser parameters, two of them with a solid vanadium secondary target, two of them without. b) Histograms of the light collected by the detector unit 15 according to the energy during those four same shots. All the peaks detected before the timestep 170000 are excluded from those histograms. The dashed lines represent the boundaries of the neutron peak we define.*

We clearly see a difference in the results for the "noise" shots, i.e. the ones without the secondary vanadium target, and the "cold" shots with a solid vanadium secondary target. The neutron peaks obtained from shot 28 and 44 with the detector unit 15 have almost the same characteristics in terms of integral, height and width. This is reassuring since the proton spectra obtained for those two shots are very similar. We can then define the boundaries of what we consider to be this neutron peak. We defined it to be between 80 keV and 210 keV as shown by the dashed lines in Fig.3.26b.

However, we see a quite unexpected result for the noise shots. Indeed, even though the proton spectrum associated to shot 27 shows a greater number of emitted protons than for shot 37, it seems that more neutrons are detected during shot 37. Hence, shot 27 seems to show that noise from the sources we already talked about seems really low at the neutron peak energies. However, there is another source of possible noise we did not consider until now. Indeed, during each shot involving a vanadium secondary target, this secondary target is exploded by the primary target hydro expansion and mainly sent in the normal forward direction. A part of this exploded vanadium target can then possibly deposit on the detector PET part hit by the proton beam during the shots. Hence, it is possible that this vanadium deposition become a noise source which increases shot after shot. The histograms shown in Fig.3.27b seem to confirm this supposition. Indeed, no secondary target was used during the three shots considered. However, since the proton spectra for shot 49 is different and especially have an higher energy cutoff, other sources of noises could also explain the difference between shot 37 and shot 49. In the later, for the shots with the same proton characteristics as shots 27 and 37, we will consider the noise level as the mean of those two shots.

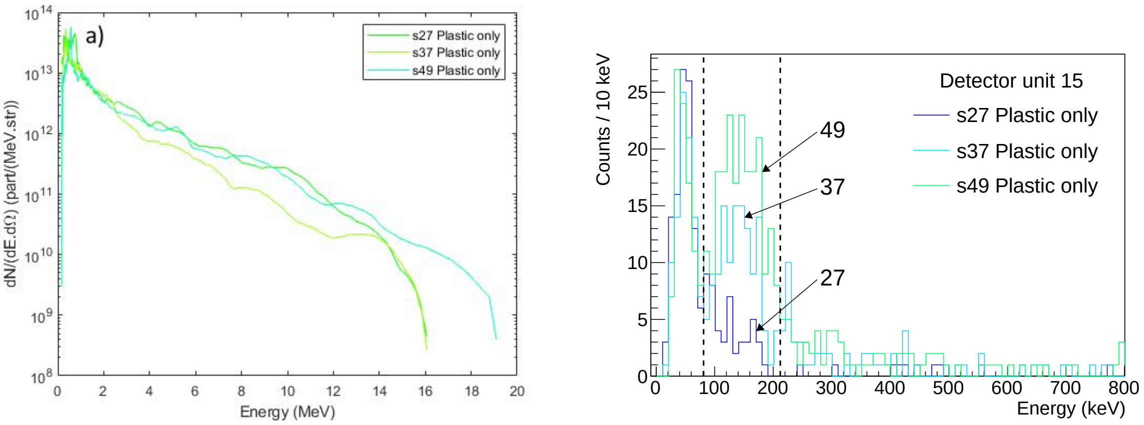

Figure 3.27: *a) Proton spectra for three shots without secondary vanadium target. b) Histograms of the light collected by the detector unit 15 according to the energy during those three noise shots. All the peaks detected before the timestep 170000 are excluded from those histograms.*

As shown in Fig.3.28a, shots 52 and 55 have proton spectrum quite similar to the ones presented in Fig.3.26a, and the ionizing north laser beam was used during those shots. Hence, we can compare the results obtained from those "hot" shots to the noise shots the same way we did with the cold shots. Using the same 170000 timestep as temporal cutoff, we obtain for the detector unit 15 the histograms presented in Fig.3.28. The boundaries set for the neutron peak for the cold shots seems to be still adequate even though the neutron peak is a bit distorted. The main result confirms what could be inferred by the look of the raw traces. It seems, at least for detector unit 15, that there are way less neutron detection events for the hot shots than for the cold ones. For shot 52, the number of detection seems even really close from the noise level.

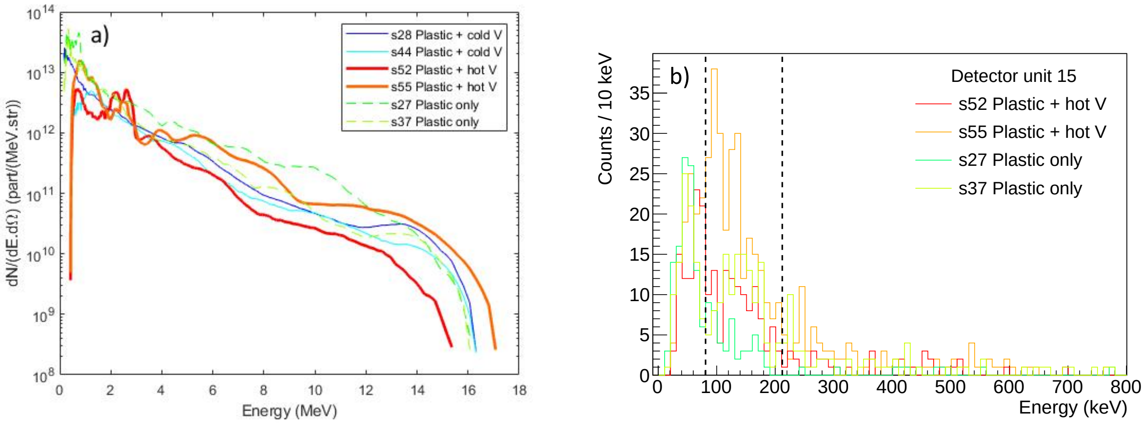

Figure 3.28: *a) Proton spectra for six shots with equivalent laser parameters, two of them with a solid vanadium secondary target, two of them without and two of them with a vanadium secondary target heated by the high-energy ns-duration laser beam. b) Histograms of the light collected by the detector unit 15 according to the energy during the two hot shots and the two noise shots. All the peaks detected before the timestep 170000 are excluded from those histograms.*

Input of Geant4 simulations

To improve those comparisons, we can estimate the number of neutrons we should detect depending on the measured proton spectrum of each shot. To do so, we can in a first time use the TALYS package (82) to have the spectrum and number of neutrons produced according to the proton measurement. During this step, we don't consider any effect due to the temperature of the plasma for the hot shots. The resulting neutron spectrum for the two hot shots and two cold shots are presented in Fig.3.29.

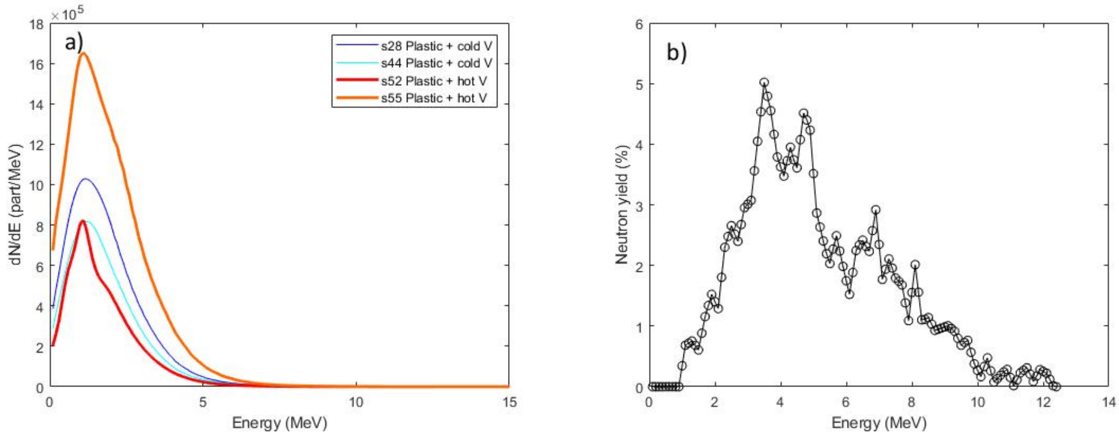

Figure 3.29: *a) Neutron spectrum calculated from the measured proton spectrum thanks to the TENDL data(82), for the two hot shots 52 and 55 and the two cold shots 28 and 44. b) Neutron spectrum of the PuBe neutron source used for the calibration according to Söderström (138).*

From those spectra, we can use Geant4 simulations to calculate two main informations in order to retrieve an actual number of emitted neutrons from the number of detected neutrons. Those two data we are interested in are the total efficiency of the neutron detector for a given neutron spectrum, and the temporal evolution of the detection rate. These efficiencies will have to be compared to the efficiency of the detector calculated with Geant4 using the spectrum of the PuBe neutron source used for the calibration, and to the actual measured efficiency with the source. The detector setup has been reproduced as shown in Fig.3.30.

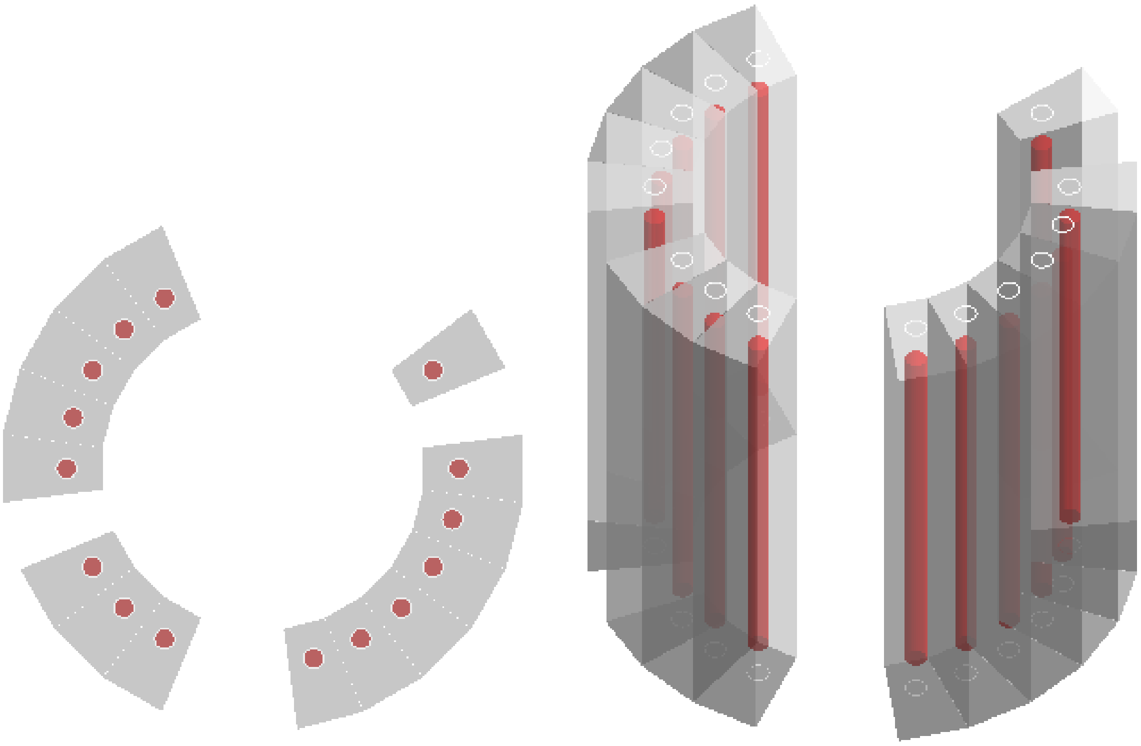

Figure 3.30: *Top view and and side view of the setup used for the Geant4 simulations. HDPE is represented in grey and the scintillators are in red.*

With the same parameters and physics list used during the previous Geant4 simulations and presented in section 2.1.3, and the detector setup reproduced, we ran 10 millions events simulations with the neutron spectra presented in Fig.3.29. According to the TENDL data, the neutron emission is mainly due to compound nuclei and, hence, isotropic. Indeed, for instance, for shot 28, the maximum neutron fluence per energy is equal to $8.27.10^4$ particle.MeV^{-1}.str^{-1} in the forward direction, to $8.12.10^4$ particle.MeV^{-1}.str^{-1} in the backward direction and in between for all the other directions. Then, we didn't take into account the angular differences and used an isotropic neutron source for the simulations. During calibration (which was performed after the experiment), we noticed that, contrary to what happened during the experiment, detector units 1 and 15 seemed damaged and presented an important noise level which prevented most of the neutron detections. Hence, we used simulations with a neutron source corresponding to the PuBe neutron source to retrieve a credible efficiency during the experiment for those two units. As we did earlier in section 2.1.3, we consider the height of the 2310-2320 keV peak in the histogram of deposited energy as representative of the efficiency of the detector. Those detector unit efficiencies are calculated using the following equations :

$$Eff_{unit} = Eff_{2-14/\{8\}} \frac{h_{unit}}{h_{2-14/\{8\}}} \tag{3.18}$$

$$Err_{unit} = Err_{2-14/\{8\}} * \frac{h_{unit}}{h_{2-14/\{8\}}} + Eff_{2-14/\{8\}} * \frac{\sqrt{h_{unit}}}{h_{2-14/\{8\}}} + Eff_{2-14/\{8\}} * \frac{h_{unit}}{h^2_{2-14/\{8\}}} * \sqrt{h_{2-14/\{8\}}} \tag{3.19}$$

Where Eff$_{unit}$ is the calculated efficiency for a given unit for the PuBe neutron source, Eff$_{2-14/\{8\}}$ is the sum of measured efficiencies for all detector unit except 1, 8 and 15, h$_{unit}$ and h$_{2-14/\{8\}}$ the 2310-2320 keV peak height obtained during simulations with a given number of events respectively for one detector unit and for all detector units except 1, 8 and 15, and Err$_{unit}$ and Err$_{2-14/\{8\}}$ are the errors associated respectively to Eff$_{unit}$ and Eff$_{2-14/\{8\}}$. The calculated and measured efficiencies for all detector units for the PuBe neutron source are presented in Fig.3.31. From now on, the measured efficiencies for detector units 1 and 15 are then replaced by the calculated ones.

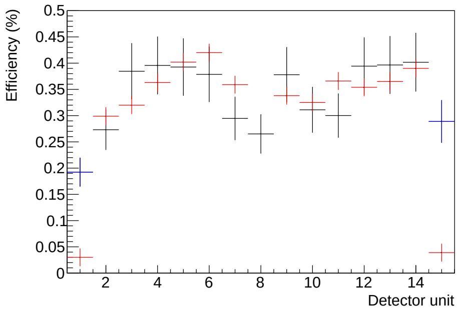

Figure 3.31: *Efficiencies of each detector unit for the PuBe neutron source. The measured efficiencies obtained during calibration are presented in red. The efficiencies calculated thanks to the Geant4 simulations are presented in black for detector units 2 to 14 and in blue for detector units 1 and 15.*

Using the efficiency measured with the PuBe neutron source and the Geant4 simulations presented earlier, we can then calculate efficiencies for the whole detector according to the neutron spectrum. The efficiency values and associated errors have been calculated using the following equations :

$$Eff_{shot} = Eff_{calib} * \frac{h_{shot}}{h_{calib}} \tag{3.20}$$

$$Err_{shot} = Err_{calib} * \frac{h_{shot}}{h_{calib}} + Eff_{calib} * \frac{\sqrt{h_{shot}}}{h_{calib}} + Eff_{calib} * \frac{h_{shot}}{h^2_{calib}} * \sqrt{h_{calib}} \tag{3.21}$$

Where Eff$_{shot}$ is the calculated efficiency for a given shot, Eff$_{calib}$ the measured efficiency with the PuBe neutron source, h$_{shot}$ and h$_{calib}$ the 2310-2320 keV peak height obtained during simulations with a given number of events and with a neutron emission spectrum corresponding to respectively a shot

Neutron spectrum	Number of simulated neutrons	Peak Height	Efficiency (%)
PuBe source	10^6	161231	4.78(62)
Shot 28	10^6	272441	8.09(118)
Shot 44	10^6	273883	8.14(119)
Shot 52	10^6	279388	8.30(121)
Shot 55	10^6	268182	7.97(116)

Table 3.3: *Simulation results and calculated overall efficiencies of the neutron detector for the different neutron spectrum of interest.*

Detector unit	PuBe source	Shot 28	Shot 44	Shot 52	Shot 55
1	0.192(27)	0.355(58)	0.361(59)	0.367(59)	0.356(58)
2	0.299(43)	0.544(88)	0.554(90)	0.566(92)	0.532(86)
3	0.320(40)	0.538(76)	0.537(75)	0.555(78)	0.535(75)
4	0.363(42)	0.594(78)	0.594(78)	0.613(80)	0.588(77)
5	0.402(57)	0.659(104)	0.670(105)	0.683(107)	0.648(102)
6	0.420(48)	0.717(93)	0.710(92)	0.729(95)	0.702(91)
7	0.359(51)	0.613(98)	0.634(101)	0.635(101)	0.609(97)
9	0.338(43)	0.567(81)	0.573(82)	0.580(83)	0.565(81)
10	0.325(53)	0.551(99)	0.550(99)	0.565(102)	0.539(97)
11	0.366(47)	0.628(92)	0.637(93)	0.653(95)	0.623(91)
12	0.354(46)	0.586(85)	0.590(86)	0.592(86)	0.569(83)
13	0.365(35)	0.613(68)	0.608(68)	0.618(69)	0.602(67)
14	0.390(44)	0.645(83)	0.638(82)	0.654(84)	0.626(80)
15	0.289(41)	0.482(77)	0.482(77)	0.492(79)	0.471(75)
All	4.78(62)	8.09(118)	8.14(119)	8.30(121)	7.97(116)

Table 3.4: *Calculated efficiencies for every detector units and shots of interest*

or the PuBe neutron source, and Err$_{shot}$ and Err$_{calib}$ are the errors associated respectively to Eff$_{unit}$ and Eff$_{2-14/\{8\}}$. Since detector unit 8 was non-operational both during the calibration and the experiment, the energy deposition in the corresponding scintillator was also removed from the counting. Those global efficiencies are presented in Table.3.3.

However, to be able to draw conclusions from the signal of only a few detector units, we need calculated efficiencies for each detector units. The same equations presented in Eq.3.20 are used to calculated those unit by unit efficiencies. Those efficiencies are presented in Table.3.4.

This also allows us to have an insight on the efficiency dependence on the neutron energy. As shown in Fig.3.32, the efficiency of the detector mainly decreases when the neutron energy increases. As one could expect, those curves does not depend on the neutron spectrum except for the statistical error. Indeed, for the realistic spectra, there are not enough events to reliably determine those curves for neutron energies higher than 8 MeV. Hence, we also show the same results for a 10 millions events simulation with a flat neutron spectrum from 0 MeV to 16.3.

In order to accurately determine the temporal evolution of the detection rate, especially after hundreds of μs, we need to simulate way more events. Using the shot 28 spectrum, we simulated the emission of 180 millions neutrons. As shown in section 2.1.3, This result doesn't change a lot according to the

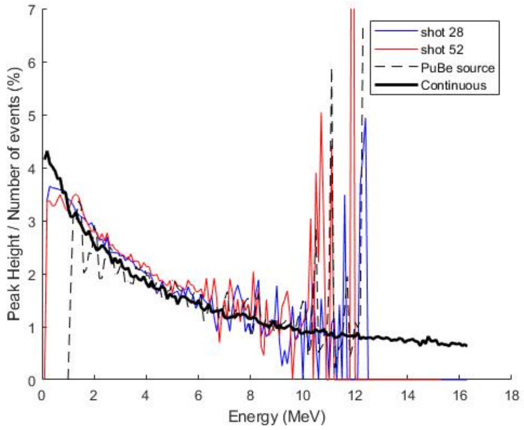

Figure 3.32: *Evolution of the ratio peak height over number of simulated events according to the energy of the incoming particle. Those results have been produced with different neutron spectra. The thick black line especially represents the results coming out of a simulation with a flat spectrum from 0 MeV to 16.3 MeV.*

energy. Besides, the neutron spectrum, for the shots which are considered, are not so different. Hence, we decided to use the same temporal evolution for all the shots. This temporal evolution is shown in Fig.3.33 for the first 300 μs.

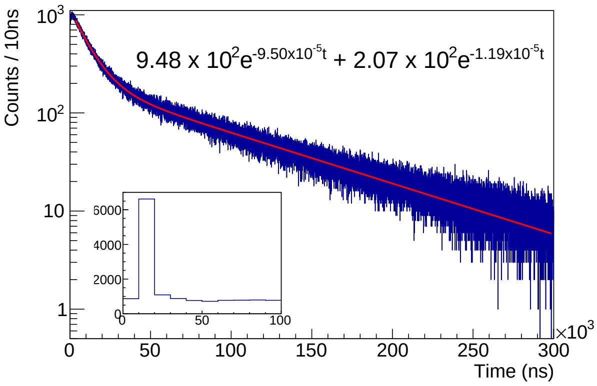

Figure 3.33: *Histogram of energy deposition between 2310 and 2320 keV according to the time of the last interaction depositing energy, from 0 to 300 μs. The red curve represents the fit and the equation written above corresponds to this fit. The zoom-in view shows the first 100 ns and especially the peak representing mainly events where the neutron capture took place without any rebound in the HDPE.*

Using this temporal evolution and the calculated efficiencies, it is possible to retrieve from the count of events in the neutron peaks like the ones shown in Fig.3.26 and 3.28, a number of neutrons produced in the vanadium foil during a shot. The equations used to define the number of neutrons produced in the vanadium foil according to a detector unit, and the associated error, are presented in Eqs.3.23 and 3.24.

Detector unit	Peak		Time cutoff (μs)	Noise shots		Cold shots		Hot shots	
	E_{min}	E_{max}		s27	s37	s28	s44	s52	s55
1	80	180	370	17	19	53	72	62	74
14	60	160	380	13	69	225	229	73	102
15	80	210	230	54	129	403	427	132	275

Table 3.5: *Neutron detection counts for a given set of parameters for the shots of interest. For the parameters, delimitation of the neutron peak and time cutoffs are presented in this table.*

$$n_{unit/shot} = \frac{N_{unit/shot} - N_{unit/noise}}{Eff_{unit/shot}} * \frac{f(1000)}{f(1000) - f(t_{cutoff})} \tag{3.22}$$

$$N_{unit/noise} = \frac{N_{unit/27} + N_{unit/37}}{2} \tag{3.23}$$

$$\begin{aligned} errn_{unit/shot} =& \frac{\sqrt{N_{unit/shot}} + \sqrt{N_{unit/27}}/2 + \sqrt{N_{unit/37}}/2}{Eff_{unit/shot}} * \frac{f(1000)}{f(1000) - f(t_{cutoff})} \\ &+ \frac{N_{unit/shot} - N_{unit/noise}}{(Eff_{unit/shot})^2} * \frac{f(1000)}{f(1000) - f(t_{cutoff})} * \sqrt{Eff_{unit/shot}} \end{aligned} \tag{3.24}$$

Where $n_{unit/shot}$ is the number of neutrons produced during the shot as detected by the detector unit, $N_{unit/shot}$ the count of events in the neutron peak for the detector unit during the shot, $N_{unit/noise}$ the mean count of events in the neutron peak for the detector unit during noise shots, $Eff_{unit/shot}$ the efficiency of the detector unit according to the neutron spectrum calculated for the shot, f(t) is the integral from 0 to t of the histogram represented in Fig.3.33 with t in μs, t_{cutoff} is the cutoff time used in μs, $N_{unit/27}$ and $N_{unit/37}$ are the count of events in the neutron peak during respectively shot 27 and 37 and $errn_{unit/shot}$ is the error associated to $n_{unit/shot}$. As shown in Eq.3.24, we didn't take into account the error induced by the simulated time evolution of the detection rate. Indeed, thanks to the high statistic simulation we did, this error is negligible compared to the other error sources. The results obtained for all the exploitable traces are shown in the very next section.

3.3.3 Results

For a given detector unit, if we are using the very same parameters for the shots 27, 28, 37, 44, 52 and 55 and only keeping results with enough statistics i.e. for which every corresponding traces was usable, we find the results presented in the Tables.3.5 and 3.6. Those results represents the most conservative approach.

It is possible to retrieve more precise results if we adapt some of the parameters for each shot. In particular, the time cutoff doesn't need to be set as late for every shot. Hence, it is possible to retrieve more statistic from more units if we set different time cutoffs for each shot. Of course, the comparison with the noise shots needs to be done with the same time cutoff each time. Those results are presented

Detector	Cold shots		Hot shots	
unit	s28	s44	s52	s55
1	$5.1(25).10^5$	$7.8(31).10^5$	$6.2(27).10^5$	$8.2(32).10^5$
14	$1.62(39).10^6$	$1.67(40).10^6$	$2.8(16).10^5$	$5.5(15).10^5$
15	$1.01(26).10^6$	$1.09(27).10^6$	$1.3(9).10^5$	$5.8(18).10^5$

Table 3.6: *Total number of emitted neutrons according to the measurement of each detector unit for each shot when using conservative parameters.*

Detector	Peak		Time	Noise shots		Cold shots		Hot shots	
unit	E_{min}	E_{max}	cutoff (μs)	s27	s37	s28	s44	s52	s55
1	80	180	250	32	45	124		119	121
5	130	300	430	4	13		44		
			500	3	4	25			
6	130	300	310	15	26	131			
14	60	160	270	28	131		438		
			290	26	120	364			
			310	25	103				139
15	80	210	130	136	280		734		478

Table 3.7: *Neutron detection counts for various time cutoffs for the shots of interest. The delimitation of the neutron peak stays the same.*

in the Tables3.7 and 3.8.

All those results are summed up in Figs.3.34 according to the placement of the detector units during the experiment.

It is important to compare those results with the estimations we can calculate from the measured proton spectrum. Using the same script as the one used for section 3.2.3, i.e., considering the target as solid for every shot, we obtain the following estimations. Cross-sections from TENDL (82) estimates that there should have been a production of :

- $2.66.10^6$ neutrons during shot 28,
- $2.03.10^6$ neutrons during shot 44,
- $1.66.10^6$ neutrons during shot 52,

Detector	Time	Cold shots		Hot shots	
unit	cutoff (μs)	s28	s44	s52	s55
1	250	$4.5(17).10^5$		$4.1(15).10^5$	$4.4(16).10^5$
5	430		$4.5(19).10^5$		
	500	$4.7(22).10^5$			
6	310	$4.9(13).10^5$			
14	270		$1.26(27).10^6$		
	290	$1.21(27).10^6$			
	310				$3.8(15).10^5$
15	130		$6.4(15).10^5$		$3.4(10).10^5$

Table 3.8: *Total number of emitted neutrons according to the measurement of each detector unit for each shot with time cutoffs adapted to each traces.*

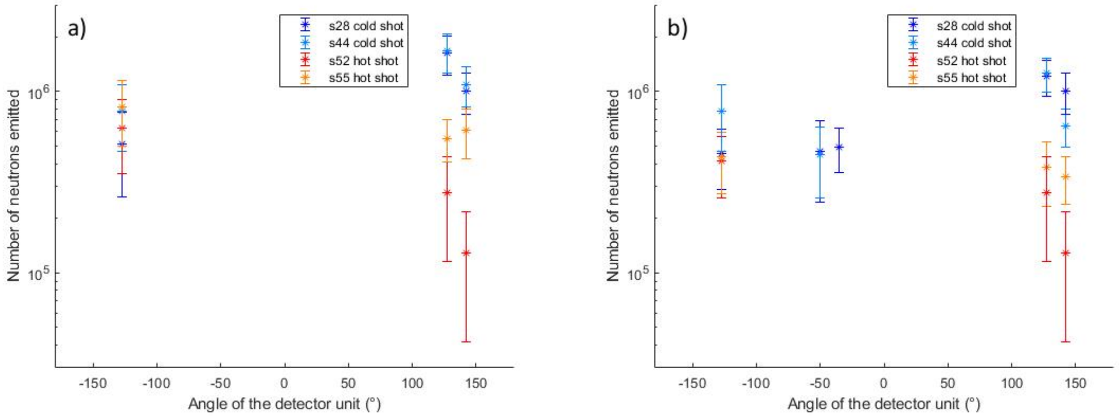

Figure 3.34: *a) Total number of neutrons emitted according to the measurement of each detector using the same analysis parameter for every shot, according to the angle of the detector unit from the picosecond laser direction. b) Total number of neutrons emitted according to the measurement of each detector using the time cutoff adapted to each traces, according to the angle of the detector unit from the picosecond laser direction.*

- 4.39.10^6 neutrons during shot 55.

We can see the ratio of the measurements over the neutron production expectations in Fig.3.35.

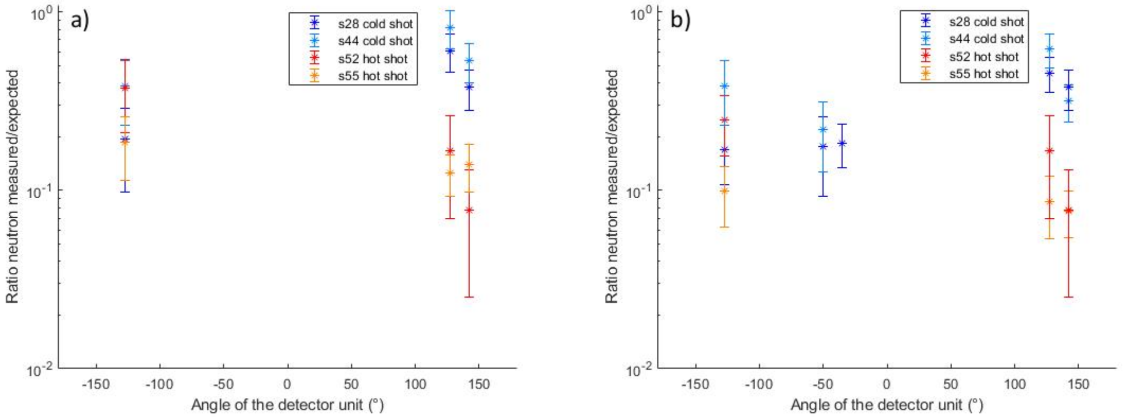

Figure 3.35: *a) Ratio of the total number of neutrons emitted according to the measurement of each detector using the same analysis parameter for every shot, over the estimated neutron production according to the measured proton spectrum, according to the angle of the detector unit from the picosecond laser direction. b) Ratio of the total number of neutrons emitted according to the measurement of each detector using the time cutoff adapted to each traces, over the estimated neutron production according to the measured proton spectrum, according to the angle of the detector unit from the picosecond laser direction.*

3.3.4 Possible explanation

First of all, it seems important to notice that the strongest results presented, i.e. the ones which are deduced from the biggest sample of peaks are the results from detector units 14 and 15. Besides, as it can be seen in Fig.3.35, the results presented by those two detectors for the cold shots are close from what we could expect even though we still detect less neutrons than expected.

An interesting feature of the results for cold shots from detector units 14 and 15 is that when we used the time cutoff "adapted" to the traces, the final number of neutrons decreases. This could be explained by the fact that this adapted cutoff is defined roughly when the peak detection rate seems to start following an exponential decreasing curve. This final number of neutrons decrease could be explained if we defined this time cutoff a bit too low. Looking at the evolution of the peak detection rate only corresponding to energies in the neutron peak could give a more precise result but might also be more difficult since the statistic to define it would be lower.

The main result presented in Fig.3.35 is that we detect way less neutrons during the hot shots than during the cold shots, i.e. when the target is in a plasma state instead of a solid state. If we use the precise parameters, the measured total neutron number is 4.24(309) times higher for the two cold shot in comparison with the two hot shots according to detector unit 14, 4.51(330) times higher according to the detector unit 15 and still 1.59(121) according to detector unit 1.

According to the FSSR measurement, for the shots with the north ns-duration laser beam with an energy around 600 J, the strongest signal recollection corresponds to the emission of a region with a 10^{21} cm^{-3} electron density and a temperature between 1130 and 1200 eV. Sadly, for the shot where the north laser beam had an energy around 100 J, the FSSR measurements were not accurate enough to retrieve such values. According to the NIST Atomic Spectra Database(185), such a temperature corresponds to an ionization rate of 16 for vanadium, the corresponding ionization energy being 1165.2 eV.

Thanks to the MULTI simulations presented in section 3.2.3, and with laser parameters adapted to the ones measured during the experiment, we can see that such an ionization rate and electronic density corresponds to an instant around 2 ns after the irradiation for a mean laser intensity of $6.0.10^{24}$ $W.cm^{-2}$. Finally, with an intensity six times lower, i.e. corresponding to a 100 J north laser beam, we can retrieve a maximum ionization rate of 12.54 for the shots of interest. The evolution of those mean ionization rates is presented in Fig.3.36.

According to the theory, Eq.3.11 gives a screening potential of 245.39 eV for the solid vanadium. With the mean ionization level at its maximum, i.e. 12.54 for the shots of interest, the value of the screening potential drop to 111.60 eV. If we take into account those screening potentials in the calculations of the neutron production during shot 28 for instance, the neutron production change from $2.6630.10^{6}$ to $2.6633.10^{6}$. The screening effect cannot account for the difference between hot and cold shot if those values of screening potential are correct. However, as we have already seen, several publications (152; 173; 159) present experimental results which suggest that the screening potential value is way underestimated by theory. Lipoglasek and Cvetinovic (186) propose an empirical formula to calculate the screening potential value

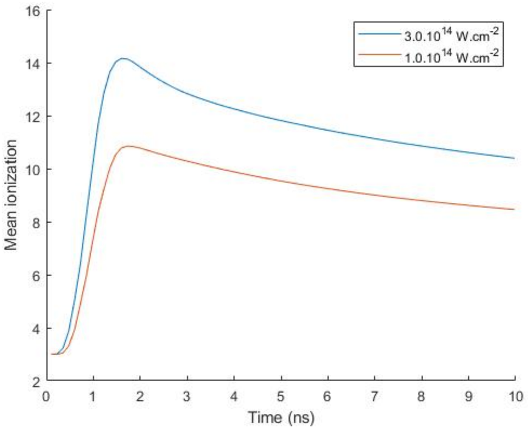

Figure 3.36: *Mean ionization of a 1 μm vanadium target irradiated with an intensity of 1.0.10^{14} W.cm^{-2} according to MULTI simulations.*

with Eq.3.25

$$U_e = Z^2 * U_0 \tag{3.25}$$

Where U_e is the screening potential, U_0=0.8 keV is the maximum electron screening potential measured for the ^{2}H(d,p)^{3}H reaction and Z is the electronic cloud charge of the target nucleus. Using this equation, we found for the screening potential new values of 423.2 keV for the solid vanadium and 87.5 keV for the plasma case. This implies a much greater change in the neutron production. The new estimations become :

- 3.29.10^6 neutrons produced during shot 28,
- 2.57.10^6 neutrons produced during shot 44,
- 1.76.10^6 neutrons produced during shot 52,
- 4.54.10^6 neutrons produced during shot 55.

We can then calculate new ratio of measurements over neutron production expectation as shown in Fig.3.37. Taking into account a strong screening effect reduces the difference observed between the hot and cold shots but is not enough to fully explain it.

To try to explain this difference, we can also consider the difference in stopping power in plasma or solid. Since the foil is only 1 μm thick, we neglected until now its effect on the measurement of the proton spectrum. Since the proton stopping power in a plasma is dependent on many parameters, we can consider an extreme case to see if this can explain the difference between the hot and the cold shots. As extreme case, we decided to consider the stopping power in the solid vanadium according to SRIM (127) to rebuild a more accurate emitted proton spectrum, and the stopping power in the vanadium in a

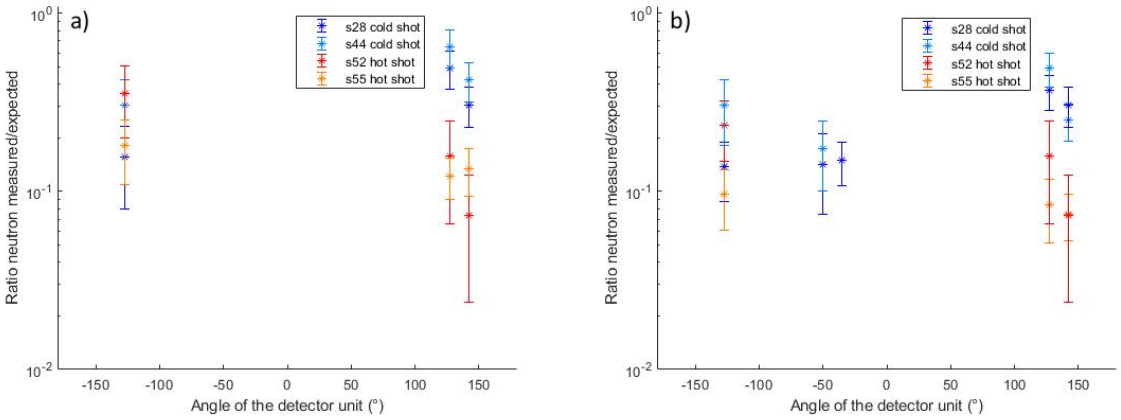

Figure 3.37: *a) Ratio of the total number of neutrons emitted according to the measurement of each detector using the same analysis parameter for every shot, over the estimated neutron production according to the measured proton spectrum and taking into account an important screening effect, according to the angle of the detector unit from the picosecond laser direction. b) Ratio of the total number of neutrons emitted according to the measurement of each detector using the time cutoff adapted to each traces, over the estimated neutron production according to the measured proton spectrum and taking into account an important screening effect, according to the angle of the detector unit from the picosecond laser direction.*

plasma state as null. Indeed, since the proton spectrum measurement is done after them going through the target, the emitted proton spectrum is not exactly the same as the measured one. Using SRIM data, we can rebuild the emitted spectrum for the cold shots as shown in Fig.3.38a for shot 28. Taking into account the important screening potential and the stopping power difference in this extreme case, we found new estimations in the neutron production :

- $3.34.10^6$ neutrons produced during shot 28,
- $2.61.10^6$ neutrons produced during shot 44,
- $1.79.10^6$ neutrons produced during shot 52,
- $4.56.10^6$ neutrons produced during shot 55.

Fig.3.38b shows the ratio of total number of neutrons emitted over the estimated neutron production when taking into account both a strong screening effect and the stopping power in an extreme case. As it could be expected, this doesn't change a lot the resulting ratios and then can't explain the measured difference between the hot and the cold shots.

To conclude, we can't explain the measured difference of neutron production for the solid state and the plasma state. Hence, either there are some unplanned or unknown phenomenon which prevents most of the nuclear reactions to happen if the target is in a plasma state, or the proximity of the nanosecond north beam, through some unknown processes, decreases a lot the efficiency of our detector without totally preventing it to measure any signal.

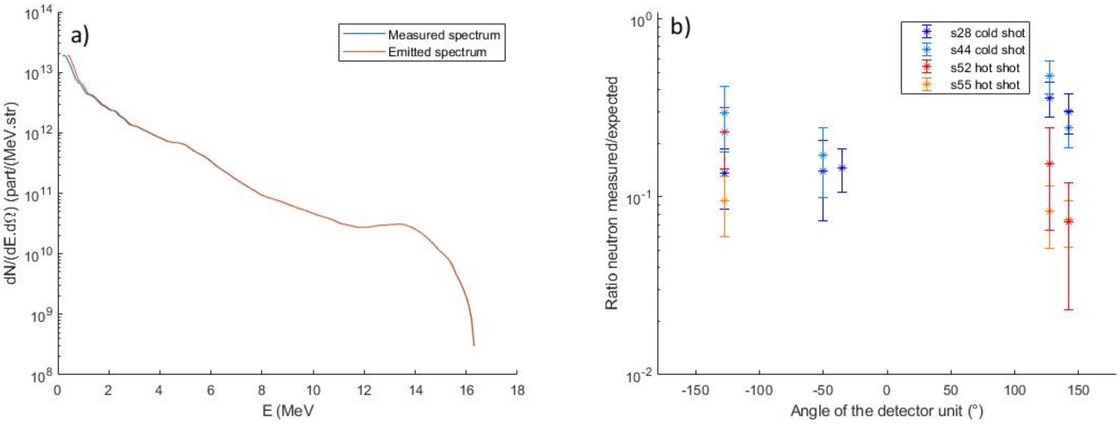

Figure 3.38: *a) Measured angular energy proton spectrum in blue and emitted angular energy proton spectrum calculated thanks to SRIM data(127). b) Ratio of the total number of neutrons emitted according to the measurement of each detector using the time cutoff adapted to each traces, over the estimated neutron production according to the measured proton spectrum and taking into account an important screening effect and the stopping power for cold shots and no stopping power for hot shots, according to the angle of the detector unit from the picosecond laser direction.*

Chapter 4

The Apollon commissioning

In this chapter, we will present another kind of setup that uses parts of the detector we designed and used in the previous chapter. To do so, we have been able to take advantage of the commissioning experiment of the SFA of the Apollon facility which will be presented in a first section. Then, we will introduce the neutron detector setup we used which is totally different from the LULI2000 experiment one, and the preparatory work to characterize this setup. Finally, we will present the results we had during this commissioning experiment, and some complementary studies to understand which improvements need to be done to be able to characterize the neutron beam produced in such a facility.

4.1 Design of the experiment

4.1.1 The Apollon facility

The Apollon facility is a state-of-the-art intense laser system located in the CEA site at Les Ormes des Merisiers and operated by LULI. This system is designed to reach 1 PW in 2019, 4 PW in 2022 and finally 10 PW in 2024. At the end of its development, the Apollon facility will propose to experimenters 4 different laser chains :

- a 10 PW main laser beam F1 with an energy of 220 J and a pulse duration of 22 fs,
- a 1 PW secondary laser beam F2 with an energy of 22 J and a pulse duration of 22 fs,
- a "creation" laser beam F3 with a maximum energy of 250 J and a ns pulse duration,
- a probe laser beam F4 with a maximum energy of 250 mJ and a 20 fs pulse duration.

After the front-end, the amplification system is based on 4 stages of titanium sapphire crystals which can deliver up to 330 J in ns pulses at a rate of one shot per minute. Hence, this laser system has a broad spectrum going from 750 to 900 nm(187). The F3 beam cannot be used at the same time than the F1 beam since it basically corresponds to the same laser beam without compression. At such intensities, the contrast is of prime importance and the goal of the facility is to reach a contrast between 10^{11} and 10^{12} until 100 ps before the main pulse. Besides, it should also be possible to stretch the F1 and F2 laser beam pulses up from 22 fs up to 10 ps.

The facility proposes two different experimental areas, each dedicated to a different focal length of the off-axis parabolas condensing the laser beams in the experimental chamber. The so-called Long Focal Area (LFA) is designed to host electron acceleration and X-ray generation experiments. In this area, the F2 laser beam focal length can either be 3 or 9 m. The F1 laser beam focal length can be either 8 or 20 m and could even reach 32 m in the future. F3 and F4 are not delivered in this area. The highest intensities are reached in the SFA. The F1 and F2 laser beam focal lengths are respectively 1 m and 42 cm in this area. The four laser beams will be available in this area and be sent in an octagonal experimental chamber which can be seen in Fig.4.1. This experimental chamber is 220 cm wide from door to door and 165 cm high.

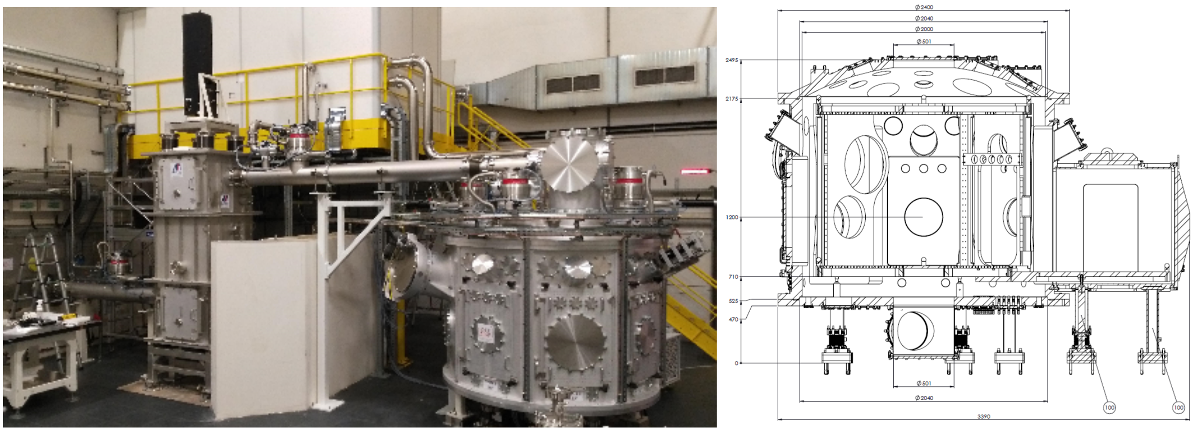

__Figure 4.1:__ Photo of the SFA with the F2 laser beam path and the octagonal experimental chamber and schematic side-view of the experimental chamber.

The F1 laser beam is fixed but all the other can be sent in the experimental chamber with various angles, which allows a large variety of experimental geometries. Besides, the F1 laser beam path is so that a secondary experimental chamber can be installed to have secondary interactions taking place far from the primary interaction.

4.1.2 Setup

This experiment was the first commissioning of the SFA of the Apollon facility. Hence, this was not centered on the neutron beam production and a large variety of diagnostics was installed. A schematic, presented in Fig.4.2, summarizes the experimental setup with all the possible diagnostics used during the campaign(188). Of course, not all those diagnostics could be used during the same shots. However, the target system was the same during the full commissioning experiment.

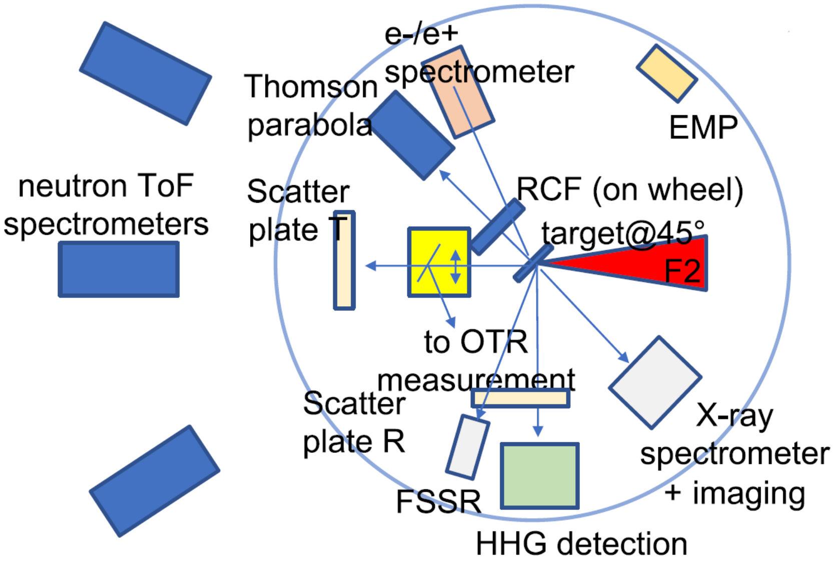

Figure 4.2: *Top-view schematic of the experimental setup(188)*

Diagnostics

To quickly summarize, here is a list of the diagnostics used during the campaign (188) :

- Spectralon scatter plates associated with Basler CMOS cameras positioned outside the experimental chamber were used to measure the scattered light in the direction of laser propagation and in the direction of specular reflection from the target.

- A set of X-ray diagnostics was used to characterize the laser-solid interactions. A Fresnel ultra-high-resolution imager and a X-ray spectrometer using polycapillary X-ray optics, a curved Bragg crystal and a CCD camera, were used to characterize the self-emission of the target at a 10° angle from the target normal on the front face (189; 190). The X-ray range was 4.7 ± 0.1 keV for the Fresnel imager and 4.4 to 6.3 keV for the spectrometer. Besides, a FSSR (167) was installed at a 70° angle from the target normal on the front face and 10 ° down from the equatorial plane, with a spectral range from 1.5 to 1.8 keV. Those three diagnostics were able to measure the temperature of a close to solid density layer, which informs us on the coupling between the hot electrons and the target bulk, respectively for Ti and Al targets. This let us know if the contrast is good enough to prevent a large preplasma to form and then allow an optimal interaction between the laser and the target.

- A high-order harmonic spectrometer, consisting of an extreme ultraviolet grating coupled with a microchannel plate detector, was set in the direction of the specular reflection from the target surface. This was used to study the laser reflection on the plasmatized target front side and demonstrate indirectly the contrast quality (191; 192; 193).

- A set of diagnostics was also used to measure the coherent Optical Transition Radiation (OTR) which is emitted by hot electrons crossing the rear side of the target to reach the vacuum (194; 195). This OTR light was spectrally measured and imaged both at 815 nm and 408 nm, which corresponds here respectively to the fundamental and second harmonic wavelengths of the laser. Those measures inform us on the electron generation on shot and then image the intensity distribution in the laser focal spot.

- Four commercial probes from Prodyn Technologies and the associated recording equipment was installed to measure the EMP. Those equipment are facility equipment and should be able to provide for all future experiments EMP measurements. Since the EMP is strongly correlated with the laser-matter interaction and especially the intensity of the laser beam on target, it provides useful insight on the experimental conditions.

- An electron magnetic spectrometer was used during some shots. This spectrometer was set along the target normal axis on the rear side and could measure electron energies from 3 to 50 MeV. It consisted of a pinhole in front of a pair of magnets creating a 1 T magnetic field, in front of YAG:Ce scintillating crystals associated with RadEye CMOS detectors. Those scintillating crystals convert a part of the energy deposited by the electrons, into visible light with wavelength around 550 nm and this light is then detected by the associated CMOS detectors. Using adequate calibration, this kind of spectrometer can perform quantitative measurements.

- A Thomson parabola was also used during this commissioning experiment and was also set along the target normal axis on the rear side. This parabola is designed to measure both electron and proton/ion signals. After a pinhole, a 1.1 T magnetic field and an electric field up to 10 kV is applied on the particles. The same YAG:Ce scintillating crystals/RadEye CMOS detectors association was used to measure the proton energy depositions. Proton spectra with energy up to around 20 MeV have been measured.

- RCF stacks were used to characterize in energy and angle the proton beam produced. To avoid to open the experimental chamber after each shot, a motorized wheel was used to store up to 10 RCF stacks. This wheel was set so that one RCF stack was 35 mm far from the target along the target normal axis on its rear side. This allowed us to measure proton spectra up to 28 MeV and see angular features insightful about the acceleration process.

- PMTs/scintillator units as described in the previous sections were set at different distances and angles to be used as nToF detectors. The PMTs/scintillator units were not surrounded by HDPE to avoid any delay in the detection of the neutrons. The actual setup of the units array will be presented later.

Target system

The target holder was designed to be a rectangular 5x9 grid with 3 mm diameter coplanar holes. This target holder was made of two parts in between which the targets were set. Such a design allows to have quite an important number of target possibly different without changing the target holder and hence opening the experimental chamber. The target holder was set so that the laser beam had an incidence of 45° on the targets. Besides, its polarization was approximatively 14° relative to the horizontal, i.e. close to the p-polarization.

To be able to remotely align the desired target on the focal plane, we used a system presented in the schematic shown in Fig.4.3. Using two converging laser beams produced by two laser diodes coupled with beam expanders, it is possible to precisely define a point in space by superposing the two focal spots. If we put this point on the focal plane prior to the target alignment, using for instance a wire with its tip at TCC, the focal plan is then the only one parallel to the target holder in which the two beams are superposed. By looking at the light diffused by the target when the two diodes are on it, by superimposing the two spots, it is then possible to position the target along the laser axis with a ±20 μm precision.

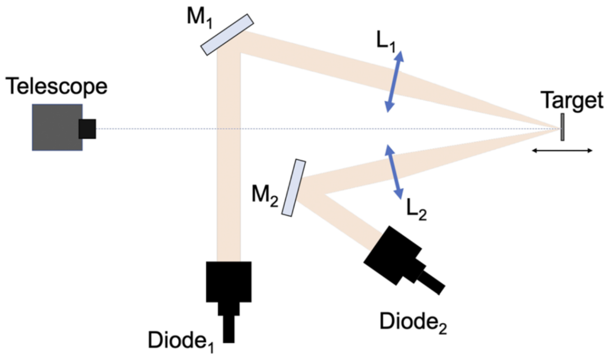

Figure 4.3: Top-view schematic of the target alignment system(188)

Target variety

During this commissioning experiment a large variety of target has been tested. Here is a list of the different types of targets and their application :

- the main point of this campaign was to test the performances of the 1 PW laser beam in regard of proton beam generation. To do so, we used simple aluminum targets with thicknesses ranging from 800 nm to 100 μm.
- in order to use the X-ray diagnostics, we shot 12 μm titanium targets. In the same optic, sandwich targets with the composition CH/Ti/CH and respective thicknesses 2/0.2/2 μm were tried.
- to enhance the proton beam generation, we used 15 μm thick Al with a forest on carbon nanotube on the front face. This carbon nanotube layer was either 60 or 20 μm. Targets with a 50 nm silicon layer followed by a 20 μm gap and a 1.5 μm Al layer was also tried. We also used aluminized mylar target. The PET layer was either 23 or 50 μm with a 20 nm Al layer on the front face.
- to test the neutron beam generation, the pitcher catcher geometry was used. The primary targets were Al targets with a thickness between 0.8 and 3 μm which were the Al targets with the best results in terms of high energy proton generation. The secondary target was either a 1.5 mm thick lithium fluoride (LiF) crystal or a 1 mm thick lead target to study spallation. Some shots with deuterated polyethylen (CD2) targets were also performed.

As we emphasized, a large variety of diagnostics and targets with different goals were present during this campaign. In the later sections, we will focus on the shots were neutrons were emitted and the associated diagnostics used.

4.2 Neutron detectors

4.2.1 Detector configuration

During this commissioning campaign, we decided to use the PMTs/scintillator units without any of the surrounding polyethylene that was used at LULI2000 to thermalize the incoming neutrons. This was motivated by two arguments. First, since the experimental was already crowded with diagnostics, it was out of question to use the same high efficiency setup as we did during the LULI2000 experiment. Second, since we were not looking for high efficiency, it was the opportunity to try and measure a neutron energy spectrum. To do so, we decided to use the PMTs/scintillator units as nToF detectors as was already performed by many groups in similar experiments (196; 197; 198; 199). Setting the units far away from the interaction point had another upside, in the fact that it drastically reduced the EMP and gamma flash the units would had to be subject to. In addition to that, all detector units were inside individual Faraday cages and the power supply and signal cables were protected using metallic sockets. Besides, to protect the detector units from the gamma flash, a 10 cm thick lead wall was set just in front of the units.

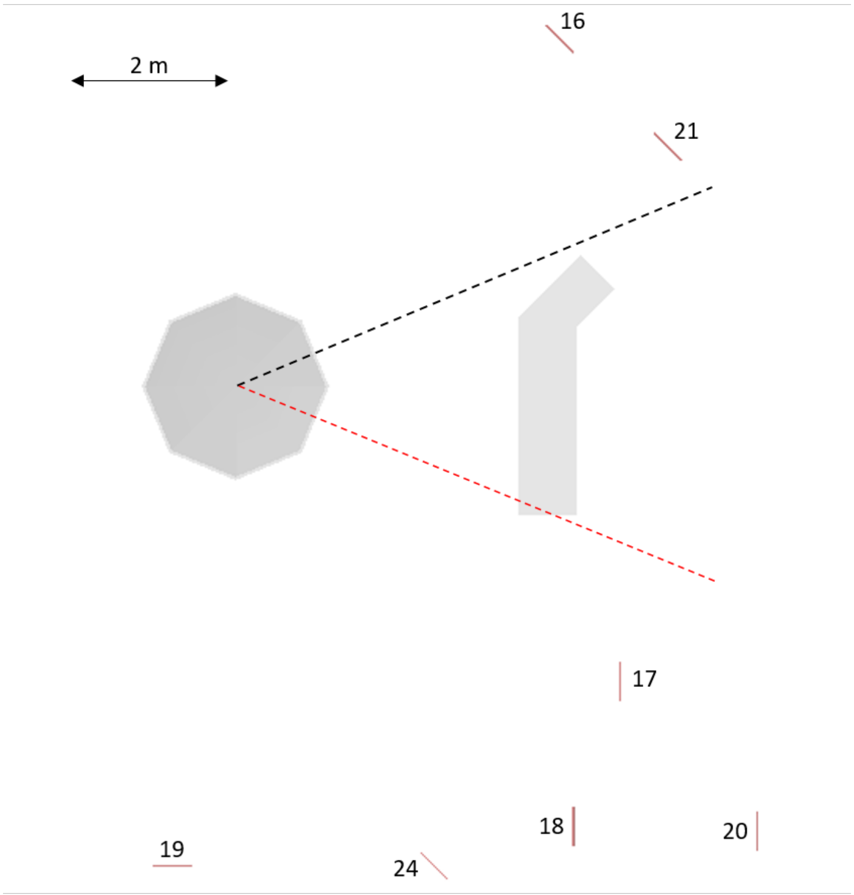

Figure 4.4: *Top-view schematic of the neutron detector configuration. The grey octagon represents the experimental chamber with the concrete wall on its right also in grey. The detector units are in red with their dedicated number next to it. The black dashed line represents the laser direction and the red dashed line the target normal direction. The units 17-20 and 24 face the rear surface of the target.*

There were multiple ideas behind this setup presented in Fig.4.4. The first main goal was to measure the neutron beam at different angles thanks to the units 17, 18, 19, 20 and 24. Putting units 17 and 20 at the same angle from the source but at different distances was set in order to check that the measured signal was really a nToF one. Besides, units 16 and 21 were set near the laser direction to test the effect it would have on the measurement. We indeed expected to see an effect since the gamma and x-ray emission is stronger in this direction (139; 140; 141). The position of each unit according to the experimental chamber center is registered in Table.4.1.

To acquire the signal, we used again a CAEN V1730SB card externally triggered to record 1 ms long traces from each PMTs. For the high voltage power supply of the detector units, we also used a CAEN A7030SN board set in a CAEN SY5527LC power supply to deliver a 1.2 kV tension to each PMT.

Detector unit	Distance (cm)	Angle (°)	Height (cm)
16	605	-69.5	-20
21	629	-51.5	0
17	617	15	-15
20	872	18	-15
18	706	30	-5
24	663	45	0
19	615	75	0

Table 4.1: *Distances from TCC and angles from target normal for each detector unit. The distances are the one projected on the equatorial plane and the angle are given clockwise in the topview. The height is also given according to the TCC height which is 120 cm above the ground.*

4.2.2 Preparatory calculation

The main goal was to be able to characterize the neutron beam produced by the facility. To do so, we used LiF secondary targets to convert part of the protons accelerated by the laser in neutrons. As a secondary aim, we also tried to see if the proton beam produced by the facility was high enough in energy for the spallation process to be interesting to produce neutrons. To study that, we used Pb secondary targets.

First of all, we decided to check what we could expect from time-of-flight measurements, i.e. what would be the energy deposition from the incoming neutron in the scintillators. To do so, a first step is to calculate the number of neutron we expect to generate. To do so, since it was the very first experiment in SFA, we used a proton spectrum created on another facility. We were expecting to be able to reach proton energies up to a few tens of MeV (200; 201). Hence, we decided to use the proton spectrum obtained during shot 9 at the LULI2000 experiment as reference. The number of proton emitted was supposed to be lower since the pulse energy at SFA is lower but the energy range for the protons is the good one. This was indeed demonstrated during the experiment where we recorded peak proton energies up to 25-30 MeV (188). Keeping this in mind, we can calculate the number and spectrum of neutrons emitted during a shot using the TALYS package (82). We neglected here the stopping power in the secondary target. The proton spectrum of reference and the corresponding neutron spectra for 1 mm thick targets of LiF or lead are presented in Fig.4.5.

Using again the TALYS package, it is then possible to calculate a number of reactions depositing energy in a scintillator according to the time. To do so, we considered the main three reactions which can happen for a neutron in a scintillator, i.e. a ^{10}B neutron capture reaction, an elastic collision with a ^{12}C nucleus or an elastic collision with an ^{1}H nucleus. The cross sections of those three reactions are presented in Fig.4.6a. We see that for neutrons in the keV-MeV range, the number of elastic scatterings should be way more important than the number of neutron capture reaction.

For the sake of simplicity, we considered in a first time a 4π spherical thin layer of scintillating EJ-254 material with a radius of 6 m. Besides, in this whole work, we will consider the neutron beam isotropic

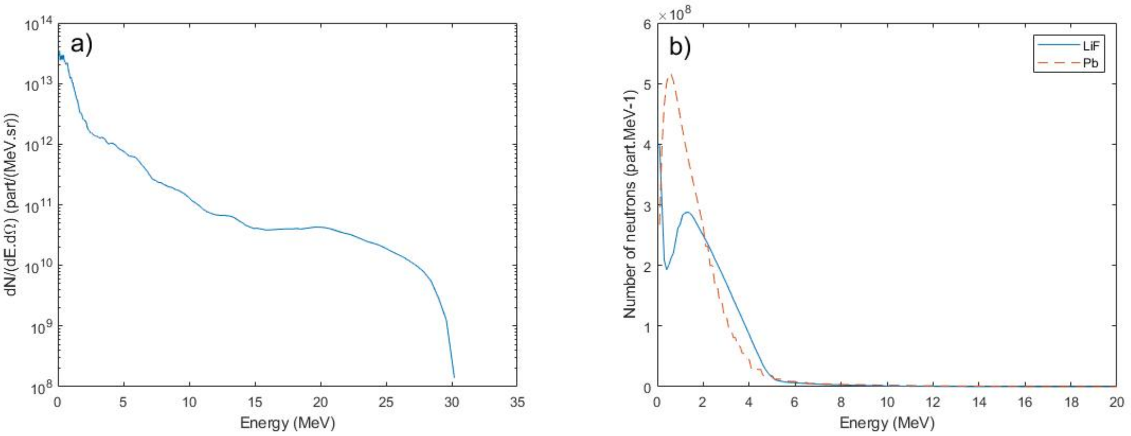

Figure 4.5: *a) Reference proton spectrum for the preparatory calculation. b) Neutron spectra generated by the corresponding proton beam in 1 mm thick Pb or LiF secondary targets.*

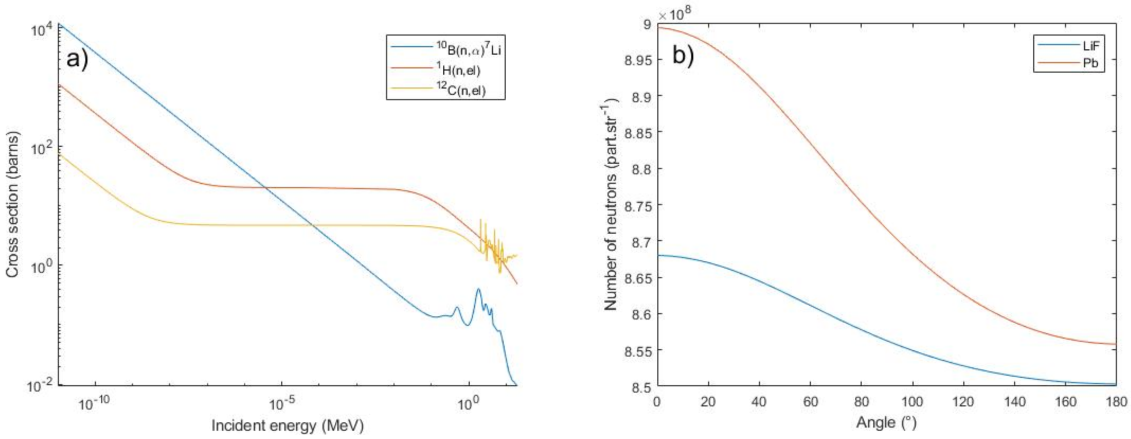

Figure 4.6: *a) Cross-section for the reaction $^{10}B(n,\alpha)^7Li$ and the neutron elastic scatterings on ^1H and ^{12}C nuclei. b) Angular neutron spectra generated by the reference proton beam in 1 mm thick Pb or LiF secondary targets.*

since as, shown in Fig.4.6b, the neutron beam produced by using either the lead or LiF secondary target is almost non-directional. The temporal evolution of the number of deposition of energy by the neutrons produced in lead or LiF secondary target, in this fictional scintillator is presented in Fig.4.7.

As expected, the number of elastic scatterings on ^{12}C or ^{1}H nuclei is way more important than the number of ^{10}B neutron capture. However, what we are interested is not exactly the number of reactions but the energy deposited in the scintillator. For the neutron capture, this corresponds to the kinetic energy of the incoming neutron plus the Q-value of the reaction. However, this is a bit more complicated for the elastic scattering. The amount of energy transferred from the incoming neutron to the nucleus on which it scatters is given by Eq.4.1 (202).

$$E_k = \frac{4Mm_n}{(M+m_n)^2} cos^2\beta \tag{4.1}$$

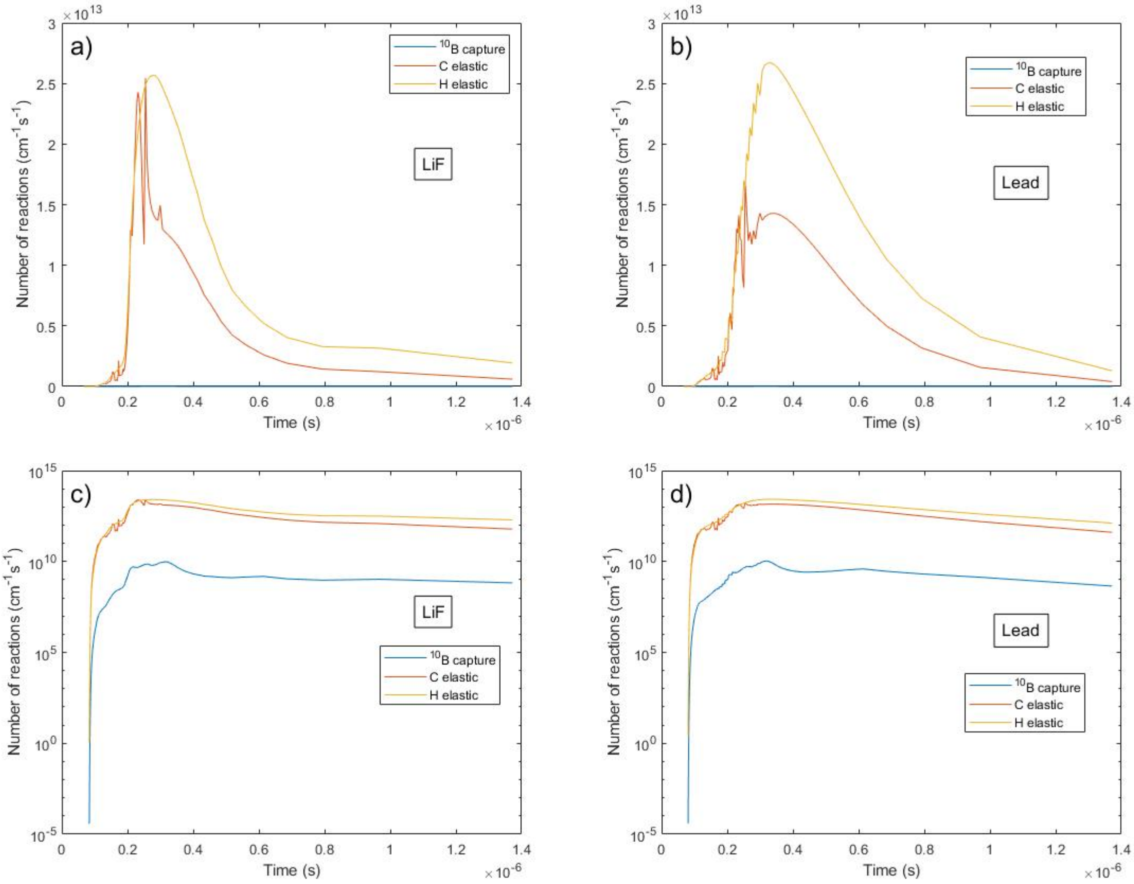

Figure 4.7: *Number of neutron captures or elastic scatterings in a spherical 4π scintillator with a 6 m radius, according to time. a) and c) correspond to a neutron beam produced in a LiF target with a spectrum as presented in Fig.4.5b). b) and d) corresponds to the equivalent with a lead target.*

Where E_k is the proportion of transferred energy, M the mass of the target nucleus, m_n the neutron mass and β the angle in the laboratory referential between the direction of the incoming neutron and the direction of the hit nucleus after the scattering. The energy deposition is then different for each elastic scattering. But for our purpose, we can consider the mean energy deposition over all angles, which can easily be calculated and is given by Eq.4.2.

$$E_{mean} = \frac{2Mm_n}{(M+m_n)^2}E_{inc} \tag{4.2}$$

Where E_{mean} is the mean energy deposition for a given neutron energy E_{inc}. The energy deposition due to each process is showed in Fig.4.8. In addition to that, the scintillation efficiency of the scintillator is not the same whether the energy deposition is done through the kinetic energy of proton, carbon ion or alpha particle and lithium ion produced by the ^{10}B neutron capture. To define this efficiency according to the energy deposited and the nature of the particle through which the energy is deposited, we decided to use an empirical formula defined by Birks (128; 176) and shown in Eq.4.3.

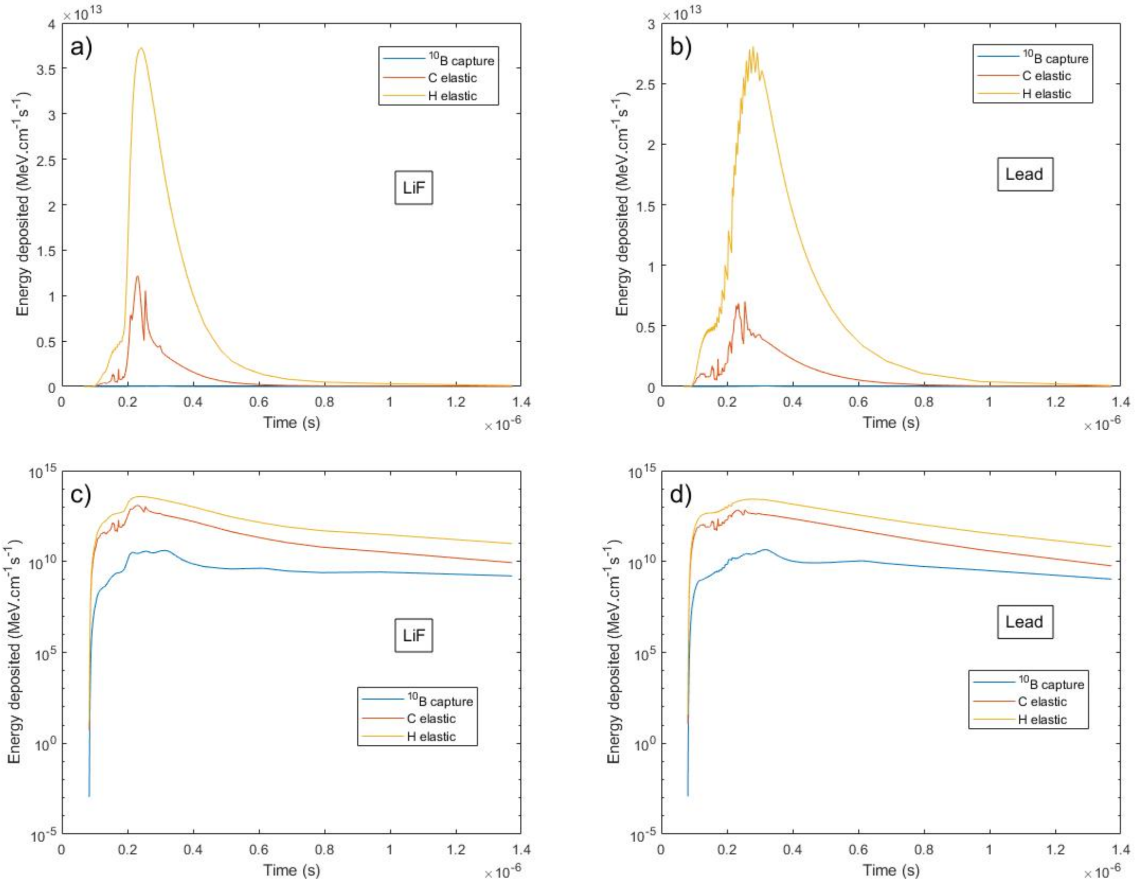

Figure 4.8: Energy deposition from neutron capture or elastic scattering in a spherical 4π scintillator with a 6 m radius, according to time. a) and c) correspond to a neutron beam produced in a LiF target with a spectrum as presented in Fig.4.5b). b) and d) corresponds to the equivalent with a lead target.

$$E_{scint} = A \int_0^W \frac{\frac{dE_{dep}}{dz}(E,z)}{1 + B\frac{dE_{dep}}{dz}} e^{-\frac{z}{L}} dz \tag{4.3}$$

Where E$_{scint}$ is the energy of the scintillated light, E$_{dep}$ is the energy deposited in the scintillator by the proton or any other particle, W is the length travelled by this particle and A, B and L are parameters. From previous works(179; 169), we can set L = 44 μm. We can use SRIM (127) to calculate the energy deposition of any particle along its travel in the scintillator. Besides, trying to match the proton recoil response of EJ254 from the work of Gabella et al (203), and the mean scintillated energy around 100 keV$_{ee}$ for a ^{10}B neutron capture, we can set A = 0.24 keV$_{ee}$.keV^{-1} and B = 0.04 μm.keV^{-1}. The results obtained for those parameters is shown in Fig.4.9

Using this model and those parameters, it is then possible to calculate the scintillated light energy due to each process, as shown in Fig.4.10. We see that the main part of scintillated light is produced through elastic scatterings on ^{1}H nuclei. The scintillated light produced through ^{10}B neutron capture is several orders of magnitude less important. Hence, we won't be able to use the neutron peak to discriminate

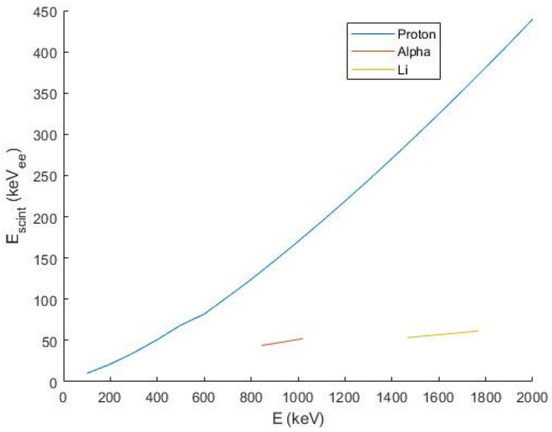

Figure 4.9: *Scintillated light energy according to the energy of the depositing particle and the nature of the particle, for EJ254.*

energy deposition due to neutron from the ones due to others sources. One important feature is also that the energy deposition begins around 100 ns and peaks around 240 and 290 ns depending on the neutron spectrum. Hence, if the detectors units don't recover from the gamma flash and the EMP before those values, we won't be able to measure a spectrum.

Besides, even though the energy deposition is probably over estimated quantitatively since the proton spectrum used here is the one produced at LULI2000, which has more energy than expected at Apollon, it is still interesting to take a look at what energy deposition we can expect in a PMTs/scintillator unit placed 6 m away from TCC. In the best case scenario with the lead target, the energy deposition peaks at 3.5 MeV.cm^{-1}.s^{-1}. For a detector unit placed tangentially at 6 m from TCC, this gives us an energy deposition of 6.1 MeV.ns^{-1}. We don't know how efficient is the conversion to optical photons when the energy is deposited as proton kinetic energy in the matrix. However, this energy deposition is quite important and would compare to neutron detection pile-up if ^{10}B neutron capture was the main process.

After some calculations, it seems that the energy deposited by the neutrons is important enough to be detected. However, on the downside, the energy deposited by a neutron is fluctuating a lot and it won't be possible to use the so-called "neutron peak" to discriminate the energy deposition we are detecting. Besides, the nToF signal begins 100 ns after the laser shot and peaks around 250 ns after the shot. Hence, the recovery time after the gamma flash and EMP is crucial and has to be as low as possible to be able to measure a nToF signal.

4.2.3 Calibration

The same way we calibrated the detector array for the LULI2000 experiment, we had to calibrate those PMTs/scintillator units in energy and efficiency.

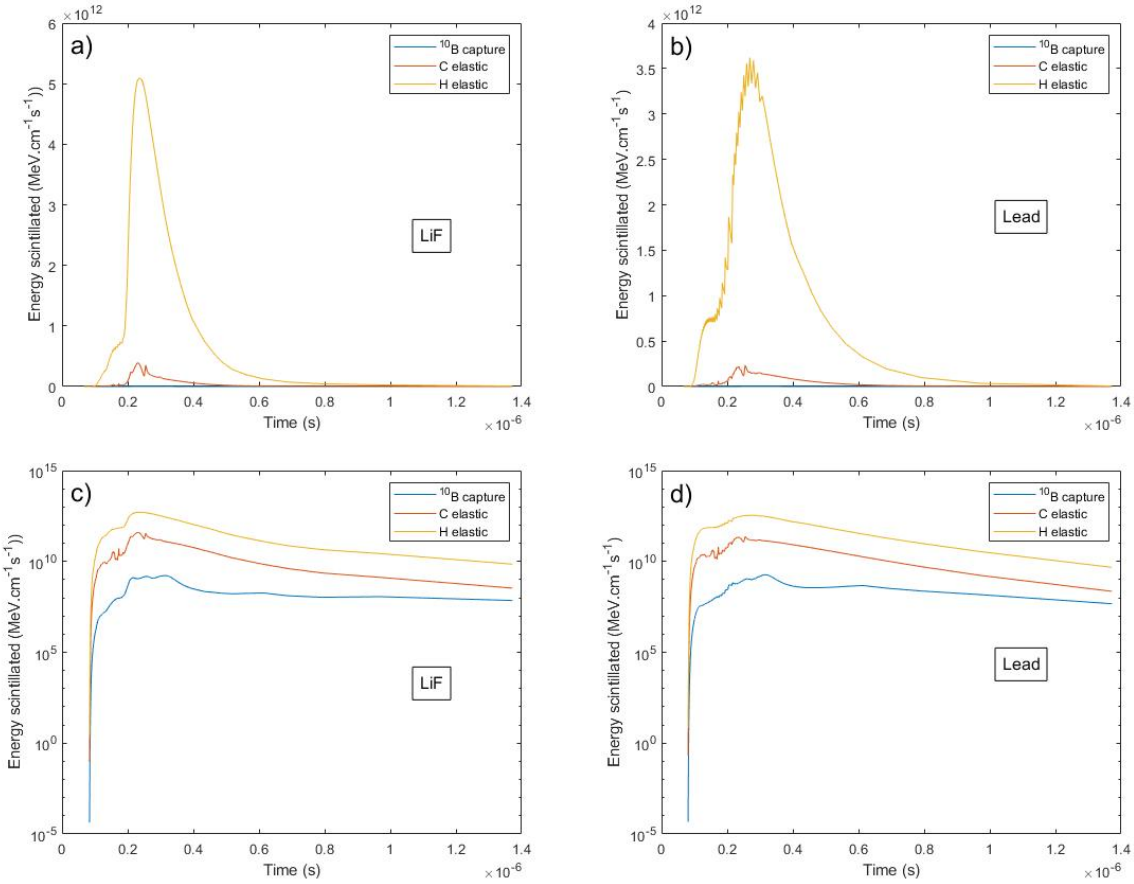

Figure 4.10: Scintillation light energy produced through neutron capture or elastic scattering in a spherical 4π scintillator with a 6 m radius, according to time. a) and c) correspond to a neutron beam produced in a LiF target with a spectrum as presented in Fig.4.5b). b) and d) corresponds to the equivalent with a lead target.

For the energy calibration, the procedure was the very same than the one explained in Section 2.3.2. We used the same ^{137}Cs gamma source which was placed 50 cm high away from the detector units which were laying on concrete floor. As it can be seen in Fig.4.11, the same double Compton edge structure is present in the histograms from individual PMT and totally disappears in the combination of the two measurements once the energy calibration is done.

The calibration factor used as in Eq.2.21 are presented in Table.4.2.

The efficiency calibration was a bit more complicated to do. Indeed, as we have seen it with the preparatory calculations, for keV-MeV range neutrons, we cannot use the neutron peak to discriminate the neutron induced energy depositions from noise and other energy depositions. Since we are mainly interested in the neutron spectrum for the nToF measurement, we decided not to do any efficiency calibration for neutrons this energetic. However, we knew that some neutrons would be thermalized in the concrete walls of the experimental area and sent back to the detector units. To quantitatively measure those neutrons, we decided to do an efficiency calibration of the detector units for thermalized neutrons.

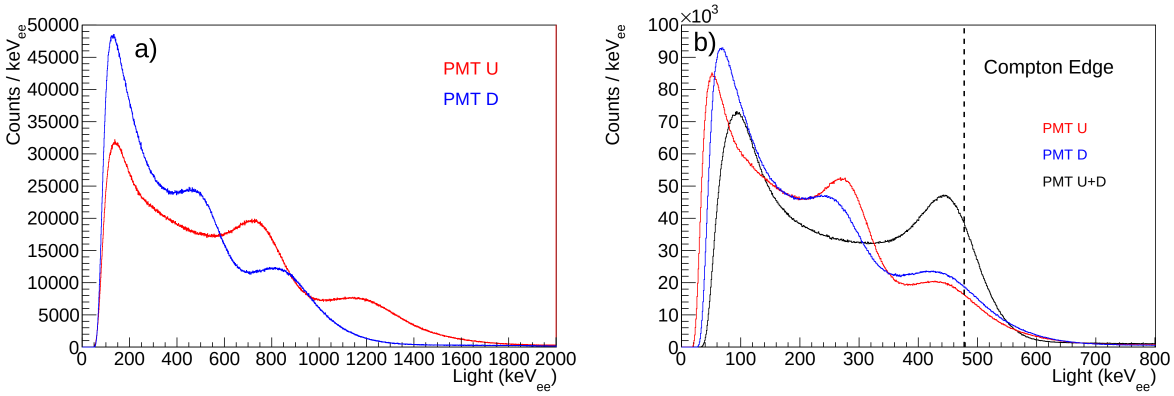

Figure 4.11: *a) Histograms of the light collected by the two individual PMTs of module 20 without any energy calibration. b) Same histograms with an approximate energy calibration in red and blue. In black is the combination of those two histograms recalibrated with the Compton edge energy at 80% height of the Compton distribution.*

Module	A_1	A_2	A_Σ
16	0.0625	0.1255	1.2746
17	0.1092	0.1060	1.2562
18	0.1646	0.0823	1.2431
19	0.1897	0.7267	1.2954
20	0.0938	0.1301	1.2271
21	0.0846	0.1488	1.4292
24	0.0443	0.0730	1.2866

Table 4.2: *Energy calibration factors*

To do so, we used the PuBe neutron source associated with a sphere made of a paraffin and nickel mixture. This composite source has been designed to produce high energy gammas thanks to the neutron capture reaction ^{58}Ni(n,γ)^{59}Ni. The neutron separation energy of ^{59}Ni is 8999.28 keV. Hence, the produced nucleus will decay through the emission of gammas, mainly via a 8999 keV one or two with the energies 8534 keV and a 465 keV, for an incoming neutron with a negligible kinetic energy. The cross section of this neutron capture reaction increases a lot with the decrease of the incoming neutron kinetic energy (81). That is why paraffin is mixed with nickel. It will thermalize the neutron to enhance the neutron capture rate. This has an interesting side effect for our purpose. Indeed, this composite source also emits thermal neutrons besides the high energy gammas.

To retrieve the energy spectrum of the neutrons emitted from this composite source, we used a 10 million events Geant4 simulation. The 8 cm radius sphere has been made from 500 g of Nickel powder and 1.3 kg of paraffin. Besides, a 3 cm diameter cylindrical hole from the side to the center of the sphere has been made to lodge the PuBe neutron source. Using those data and considering the PuBe neutron source as a point-like one, we have been able to retrieve the spectrum presented in Fig.4.12. Besides, from the measured activity of the PuBe neutron source and this simulation, we can infer that the composite source neutron activity is 1.1166(32).10^5 neutrons per second.

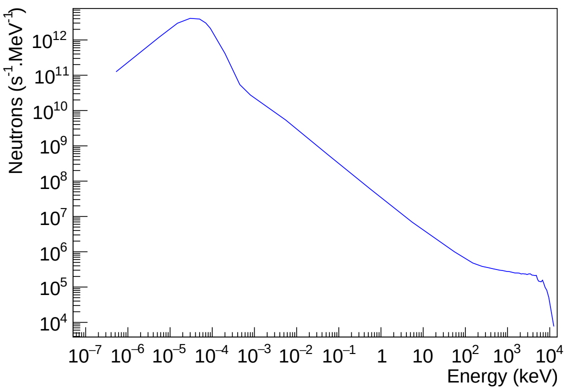

Figure 4.12: *Neutron energy spectrum of the composite source made of the PuBe neutron source and the paraffin nickel mixture sphere.*

Detector unit	PMT1	PMT2
16	87.5	75
17	75	75
18	75	75
19	87.5	87.5
20	75	75
21	75	75
24	150	150

Table 4.3: *Thresholds used during the data acquisition for the efficiency calibration. The thresholds are here defined in term of channel which is related to the voltage by 1 channel = 0.122 mV.*

For the efficiency calibration, we once again used the very same setup than for the energy calibration with the CAEN V1730SB card for data acquisition. For the efficiency calibration of the previous detector, we recorded a set of 1 ms long traces using an external trigger. The data analysis was done later using the same custom script we use for the analysis of experimental data. Here, on the contrary, we used the on-board peak detection and integration. The upside is that we were able to register way more energy deposition which reduces the error on the efficiency measurement. On the downside, this measurement has been done with a set of thresholds we chose but which cannot be changed anymore. Hence, the data analysis will have to be done with this set of thresholds or a new calibration campaign will have to be done if we want to use another set of thresholds. The set of thresholds used is presented in Table.4.3.

The data acquisition lasted 7962 s for detector units 16 and 17, and 8794 s for detector units 18, 19, 20, 21 and 24. Using the energy calibration, we have been able to get for each detector unit the histogram of counts per energy per neutron emitted by the composite source. We fitted this profile using a Gaussian peak for the neutron peak, a decreasing exponential and a constant for the noise induced by the Ni-induced gammas and other sources. Once again, the integral of the Gaussian peak gives us the efficiency of our detectors units in this particular setup. Indeed, Geant4 simulations will be needed to retrieve the actual efficiency for the experimental setup used in SFA. Besides, we assume here that the difference

Detector unit	E (keV$_{ee}$)	ΔE (keV$_{ee}$)	Efficiency (%)
16	96.7(1)	36.9(3)	7.23(10).10^{-3}
17	94.3(1)	31.7(2)	9.38(11).10^{-3}
18	99.8(1)	35.7(2)	9.69(11).10^{-3}
19	100.5(1)	29.3(2)	5.21(8).10^{-3}
20	95.9(1)	37.6(2)	9.31(11).10^{-3}
21	98.8(1)	38.2(3)	7.60(10).10^{-3}
24	95.9(2)	44.4(5)	6.46(11).10^{-3}

Table 4.4: *Efficiency and neutron peak characteristics for the detector units used as nToF, during the calibration with the composite source made of the PuBe neutron source and the paraffin nickel sphere. Errors shown are from the fit of the neutron peak.*

between the on-board integration method and the integration used in our custom analysis script doesn't have any incidence on the efficiency.

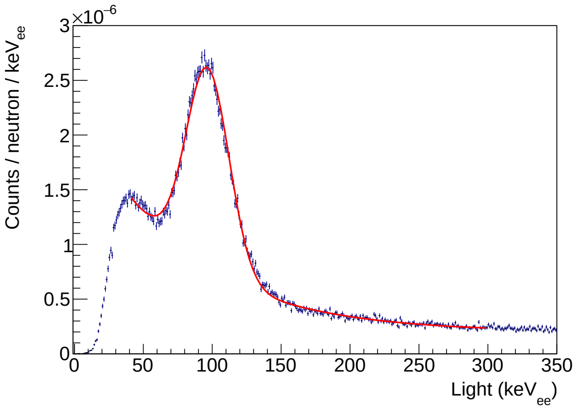

Figure 4.13: *Histogram of the light collected by the detector unit 16 in blue and its fitting function in red.*

Fig.4.13 presents the histogram of the light collected, together with its fit, for the detector unit 16. The advantage in terms of statistics in comparison with the method used for the detector used at LULI2000 is pretty clear if we look at the size difference of the error bars between Fig.4.13 and Fig.2.38. However, we have to keep in mind that it comes with a loss of freedom in the analysis parameters which would have been tragic for the LULI2000 data analysis. Indeed, the unexpected behaviour of the PMTs during the LULI2000 experiment increased a lot the noise level and required a precise adjustment of the thresholds to be able to satisfyingly analyze the data.

Doing this for every detector unit, we have found the desired efficiencies which are presented in Table.4.4.

In summary, as we did for the detector units used during the LULI2000 experiment, we have also calibrated in energy and efficiency those new detector units. However, even more for those units, since the setup during the calibration and the experiment is not the same, Geant4 simulations will be needed to retrieve an actual efficiency for the neutrons which thermalized and/or rebounded in the concrete walls of the experimental area.

4.3 Analysis

During April 2021, we have been able to take part of the SFA commissioning experimental campaign with the neutron detector setup as presented in Section 4.2.1. We will, in this section, present the results obtained during the shots where neutron converters were present behind the proton source target as well as the corresponding shots without the secondary target.

As a first approach, we can take a look at some raw traces. Figs.4.14 shows the example of two traces recorded during shot 323 where neutrons were emitted from a LiF secondary target. First of all, we can see that the peak recorded during the gamma flash / EMP is weaker than what we witnessed during the LULI2000 experiment. As a reminder, detector unit 17 is in the direction normal to the target and detector unit 21 in the laser direction. It also seems that there are more energy depositions in the detector unit 17 in comparison with detector unit 21. Besides, we witness within the detector unit 21 trace a rebound quite similar to what we saw during the LULI2000 experiment but over a shorter timescale. Even though it needs to be confirmed through incoming analysis, it seems with this first glance that it's possible to detect and count the neutrons which thermalize and/or bounce back in the concrete walls.

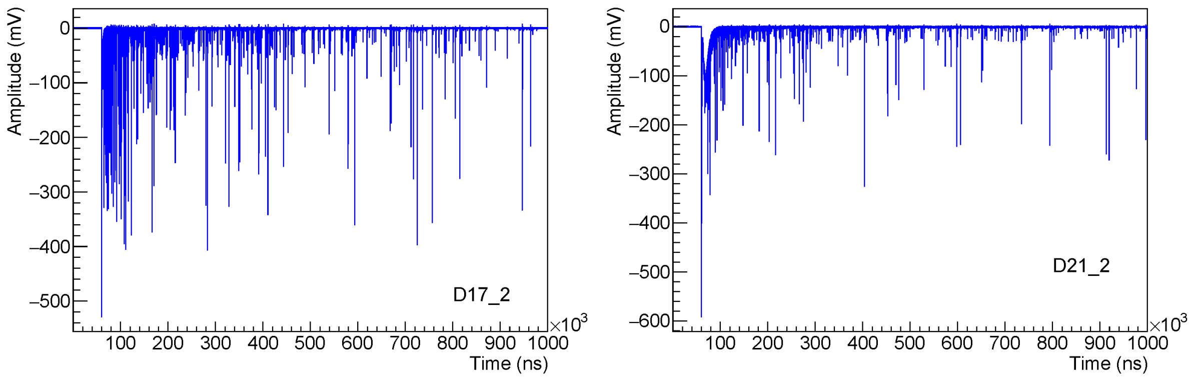

Figure 4.14: *Examples of traces obtained from PMT2 of the detector units 17 and 21 during shot 323. During this shot, the primary target was a 2 μm thick Al foil and the secondary target a 1 mm thick LiF crystal.*

Now, if we zoom in the first μs after the shot as it is done in Figs.4.15, the traces don't look like what we could expect from a clean nToF measurement. In both cases, it seems that there is some kind of rebound between 2 and 4 μs for unit 17 and between 3 and 25 μs for unit 21. However, in both cases, the baseline doesn't come to its preshot value between the first peak and this rebound, and the temporal location of this rebound doesn't match at all both between the units and with what we could have expected from the preparatory calculation.

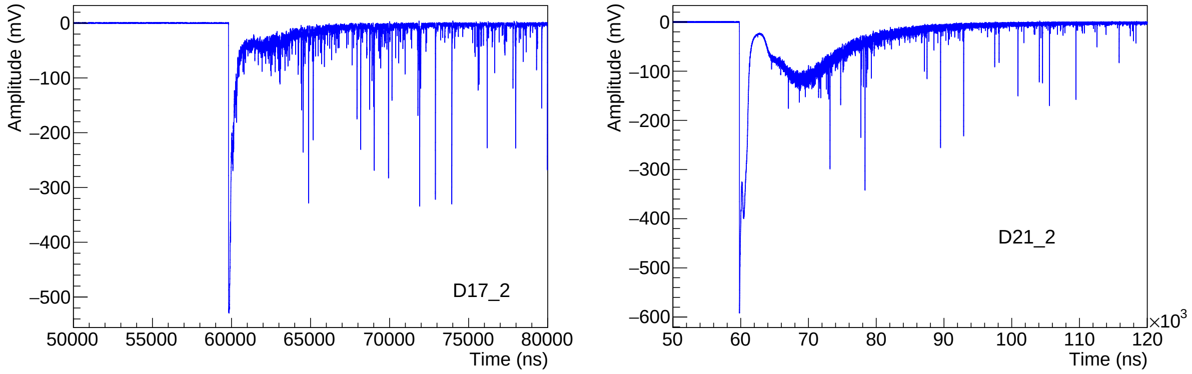

Figure 4.15: *Zoom in the first μs after the shot in the traces obtained from PMT2 of the detector units 17 and 21 during shot 323.*

On the counting part, it seems that the energy deposition counting is possible as soon as 5 μs for unit 17 and around 12 μs for unit 21. Those values are way better than what we had during the LULI2000 experiment, as expected.

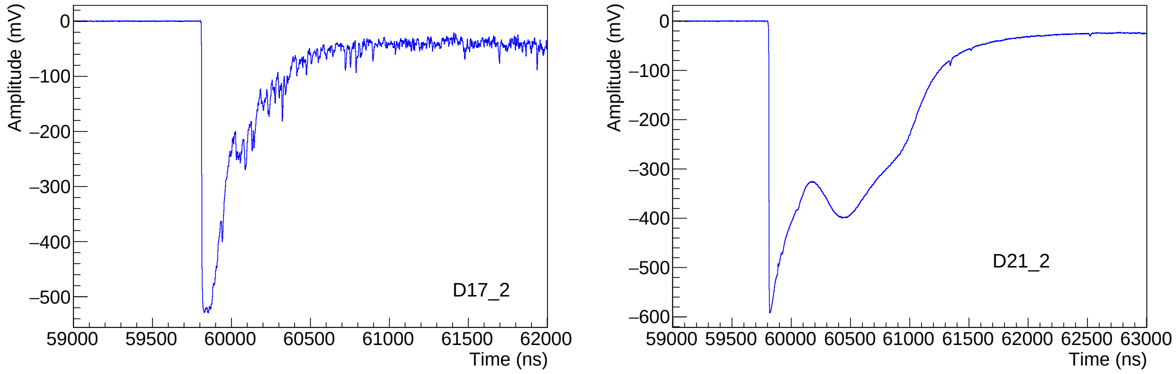

Figure 4.16: *Zoom in the first hundreds of ns after the shot in the traces obtained from PMT2 of the detector units 17 and 21 during shot 323.*

If we zoom around the temporal window during which the energy deposition from direct neutrons should peak, i.e. around 250 ns after the shot, we have two very different behaviours depending on the detector unit position, as it can be seen in Figs.4.16. For detector unit 21, there is a smooth rebound which peaks 400 ns later than what we expected. Besides, the behaviour of the trace a few μs after suggests that it may not correspond to an energy deposition. Comparing it with the trace of the corresponding PMT as shown in Fig.4.17, the total noncorrelation between the two traces seems to confirm that those rebounds are PMT dependent and do not reflect a real energy deposition in the scintillator.

For detector unit 17, there seem to be some peaks at the expected temporal location over a decreasing exponential. Besides, those peaks are present in the traces from both PMTs and are temporally coincident. Hence, those seem to be due to energy depositions in the scintillator. However, they are entangled within

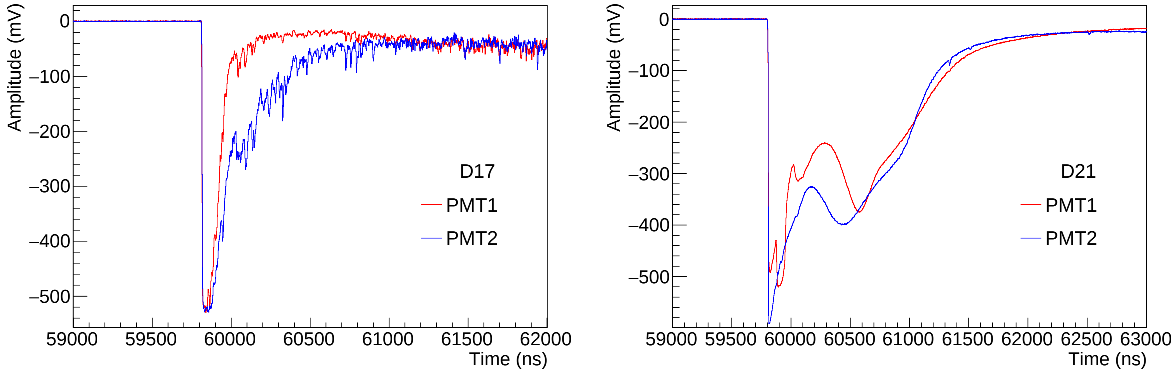

Figure 4.17: *Zoom in the first hundreds of ns after the shot in the traces obtained from both PMTs of the detector units 17 and 21 during shot 323.*

the main gamma flash peak and then, the study of those seems quite complicated. In an attempt to reduce the temporal length of the first peak, we doubled the thickness to 20 cm of the lead wall in front of some detector unit without any apparent result at first glance.

Now, we will analyze in a first time the data we got using the detector units as counters to try and measure the neutron emission during the shots. On a second time, we will study in deeper lengths the behaviour of the PMTs after an overexposure in order to see if we can extract any nToF measurement from the data.

4.3.1 Counter

Geant4 simulations

Before analyzing the experimental data, we decided in a first time to simulate with Geant4 the behaviour of the emitted neutrons in regard of the main features of the experimental area and of the detector units. We first reproduced in Geant4 the setup presented in Fig.4.4.

The experimental chamber was modelled as an octagonal chamber with 3.8 cm thick side walls and 4.5 cm thick roof and floor. The external length of the chamber is 110 cm and its height is 165 cm. The whole chamber is composed of Aluminum 5083 in real life, as in the simulation. Around 150 cm from the chamber is a concrete wall composed of two parts. The first part is 250 cm long and 75 cm thick and the second part is 112.5 cm long and 61 cm thick. There is a 45° angle between the two parts, as shown in Fig.4.4 and the wall is 217 cm tall. For the SFA itself, we considered it as a rectangular cuboid with a 17.79 m length, 14.09 m width and 10 m height. For the walls of this experimental area, we considered 1 m thick concrete walls. The whole geometry is presented in Fig.4.18. Besides, the composition used for the concrete and the Aluminum 5083 is presented in Table.4.5

Using this geometry and the same physics list than the one used for the simulations for the design

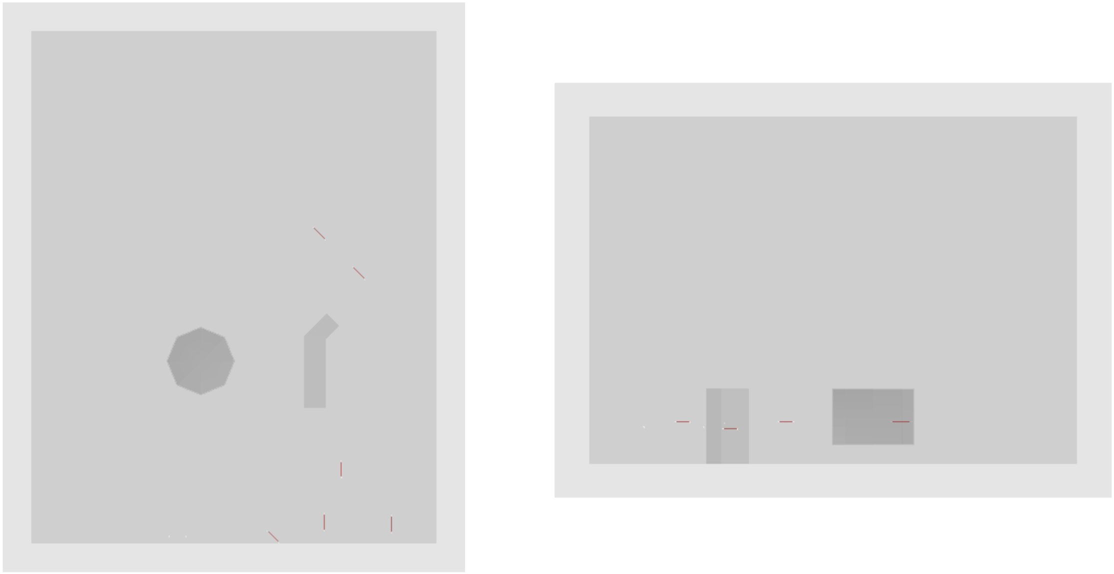

Figure 4.18: *Topview (left) and sideview (right) of the geometry considered for the Geant4 simulations. In red with the white tips are the detector units. The walls of the experimental area are in light gray and the experimental area itself is in gray. The experimental chamber and the concrete wall next to the chamber are in darker gray.*

of the neutron detector, we run a 10 million events simulation. For the neutron energy spectrum, we used one calculated from a LULI2000 proton spectrum sent on a LiF target. Since all the neutrons are being stopped through mainly elastic collision in the concrete walls, this simulation is pretty lengthy and having better statistics would require to do those simulations on a more powerful machine than a personal computer. The first thing we can check is the energy deposition in the detector units. We can also separate those energy depositions in two cases, whether the neutron has rebounded on the concrete walls or it has deposited its energy directly coming in the scintillator, thanks to a flag we set during the simulation. This is represented in Figs.4.19.

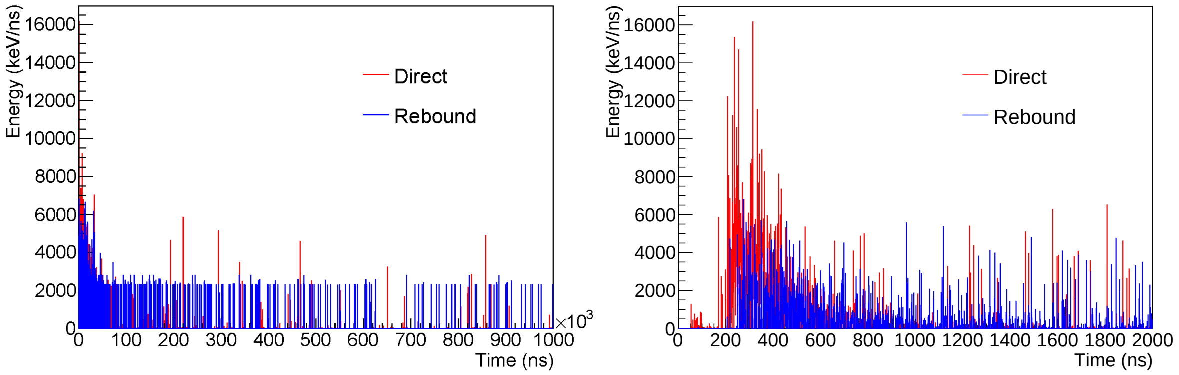

Figure 4.19: *Energy deposited in the scintillators according to time. One figure is over a full ms and the other zooms on the first 2 μs after the neutrons emission. The curves in blue corresponds to the energy deposited by neutrons which went into the concrete wall before coming back to the detector units, and the ones in red to other energy depositions.*

Element	Concrete chemical composition (%)	Al 5083 chemical composition (%)
H	1	
C	0.1	
O	52.9	
Na	1.6	
Mg		4.5
Al	3.4	93.35
Si	33.7	0.4
K	1.3	
Ca	4.4	
Ti		0.15
Cr		0.15
Mn		0.7
Fe	1.4	0.4
Cu		0.1
Zn		0.25
Hg	0.2	

Table 4.5: *Chemical composition of the concrete and Aluminum 5083 considered in the Geant4 simulations.*

One of the first main features we can notice is that, after some time, most of the energy depositions are around 2312 or 2790 keV from neutrons which have rebounded from the walls. Hence, those neutrons thermalized in the walls before coming back to the units with almost no kinetic energy and being captured by a ^{10}B nucleus. Thanks to another flag we used, we can also say that all the non-rebound energy deposition after 62 μs are not induced by neutron collisions. Then, those surely corresponds to gammas produced in the concrete walls through some neutron induced nuclear reaction. Looking at the first 2 μs, we can see that, as expected, the energy deposition in the detector units peaks between 200 and 400 ns after the emission of the neutrons. Also, the energy depositions which happened before 150 ns also doesn't correspond to neutron energy depositions. Then, those surely correspond to gammas produced in the walls of the experimental chamber or in the concrete wall or floor next to it, through some neutron induced nuclear reactions.

Now, we can take a look in particular at the energy depositions due to a ^{10}B neutron capture. We can also separate those depositions whether a rebound in a concrete wall has happened or not. Those histograms are presented Fig.4.20.

We see that, apart for the first μs, there are always more neutron captures due to neutrons which thermalize in the concrete walls than not. Indeed, for 10 million events, we count 1170 captures with a rebound and 177 without. Also, we can see that there are neutron captures from neutrons which didn't go in the walls as late as around 60 μs, which is way later than what we could expect from direct time of flight. Maybe some can come from the concrete wall next to the experimental chamber for which neutrons interacting inside are not considered as rebounded by the simulation. For most of them, it is more likely that they thermalized within the scintillator and then have been captured by a ^{10}B nucleus. We also

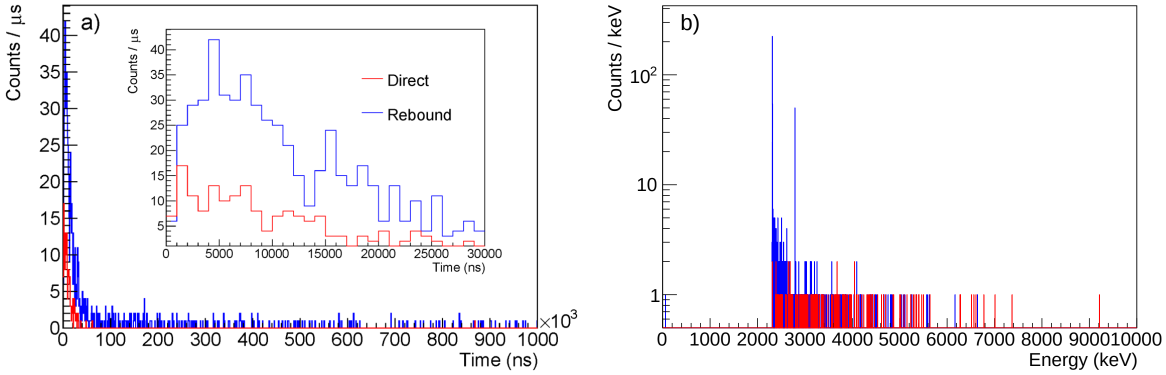

Figure 4.20: *a) Histogram of* ^{10}B *neutron captures in the scintillators according to time over 1 ms and with a zoom over the first 30* μs*. b) Histogram of* ^{10}B *neutron captures in the scintillators according to the energy deposited. The histograms in blue correspond to the energy deposited by neutrons which went into the concrete walls before coming back to the detector units, and the ones in red to other energy depositions.*

confirm, with the histogram in energy, that most of the captured neutrons which have rebounded, come out of the walls with almost no kinetic energy since the energy deposited is often around 2312 or 2790 keV, i.e. the Q-value of the capture reaction.

Now, as we did in Section 2.1.3, we can consider the peak height as representative of the integral of the measured neutron peak. In fact, here we considered the sum of the integrals of the 2010-2020 keV peak and the 2788-2798 keV peak as representative of the efficiency. This is represented in Fig.4.21.

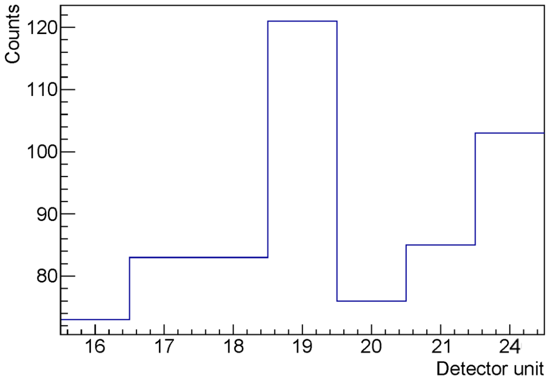

Figure 4.21: *Integral of the two peaks 2010-2020 and 2788-2798 keV in the histogram of energy deposition, according to the detector unit, for the SFA geometry simulation.*

This has to be compared to the setup used for the calibration of the detector units. Hence as shown in Figs.4.22, we reproduced this setup in Geant4 and simulated the interactions with a neutron source with a spectrum similar to the one of the composite neutron source during the efficiency calibration. The neutron source is actually point-like and located 50 cm above the detector units. The detector units were laying on the concrete floor next to each others. In the simulation, we considered a 10 m by 10 m concrete floor with the composition as exposed in Table.4.5.

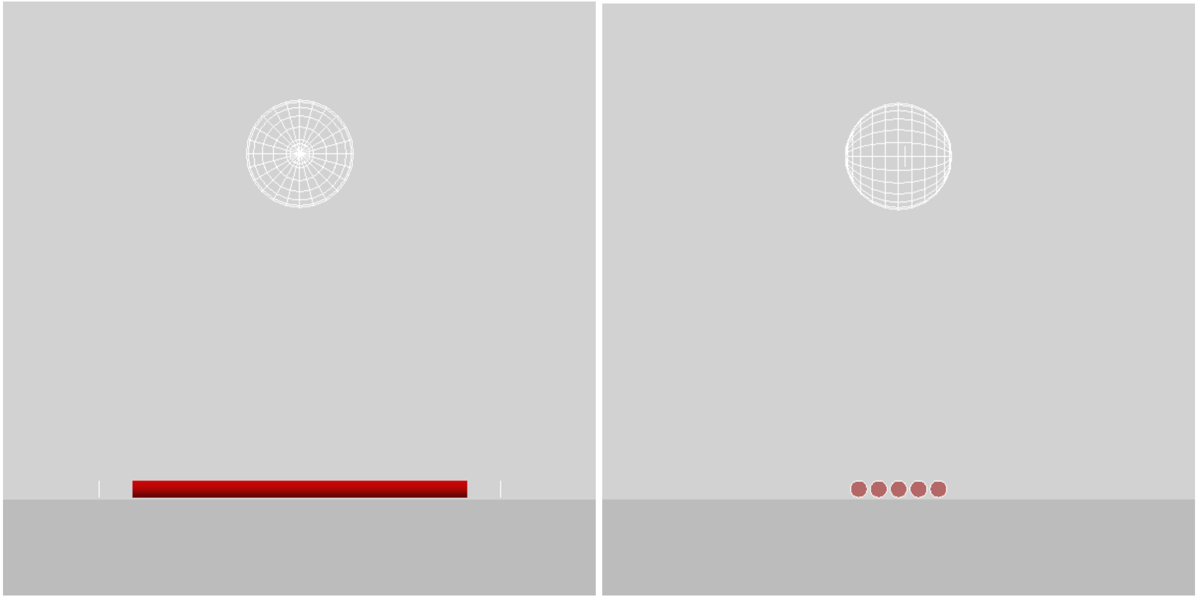

Figure 4.22: Sideviews of the Geant4 geometry used to simulate the efficiency calibration setup using the composite PuBe and paraffin nickel sphere neutron source. The scintillators are represented in red and the concrete floor in dark grey. The white sphere presented in the the sideviews at the composite source location is just for demonstrative purposes and wasn't actually present in the simulation and was replaced by a point-like source with the adequate spectrum.

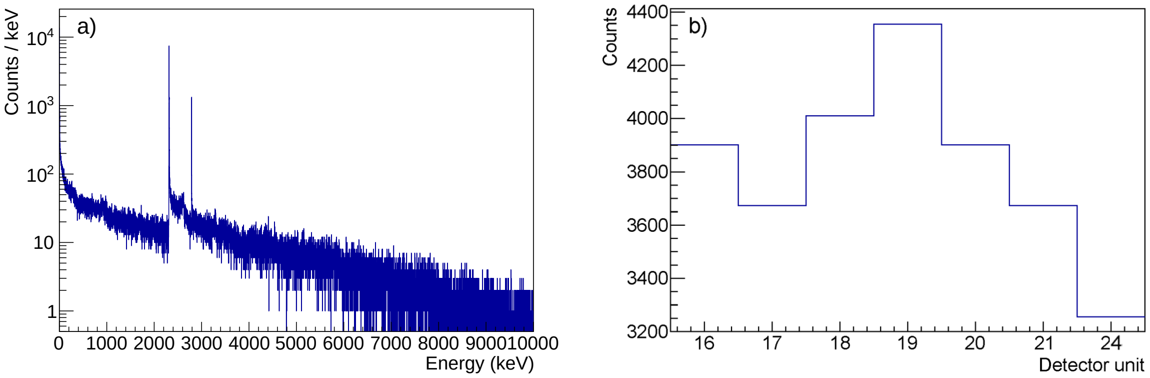

Figure 4.23: a) Histogram of energy deposition in scintillators according to the energy deposited. b) Integral of the two peaks 2010-2020 and 2788-2798 keV in the histogram of energy deposition, according to the detector unit, for the calibration geometry simulation.

Figs.4.23 shows the results for a 10 million events simulation with the composite neutron source.

Experimental data analysis

Now that we have the simulation results for both the calibration and the experimental setup, we can analyze the experimental data to retrieve a number of neutron captures per shot. Since there is still some unresponsive time right after the shot, we need to define a time cutoff as we did for the LULI2000 experiment analysis. However, since the characteristics of the shots are not so different from shot to shot and the behaviour of the detector units mainly depends on their position, we decided for this analysis to define one time cutoff per detector unit, valid for all the shots.

To define those time cutoffs, the easiest is to use a shot with a low emission of neutrons. There is usually a brief surge of peak detection with random energies right before the detector units starts behaving as expected. A two-dimension histogram according to the time and the energy is very helpful to see that transition as shown in Fig.4.24d. For shots with few neutrons, this transition is also very clear in a histogram according to the time as shown in Fig.4.24b which corresponds to shot 326 during which a 3 μm thick Al foil and a 1 mm thick Pb piece were used respectively as primary target and neutron converter.

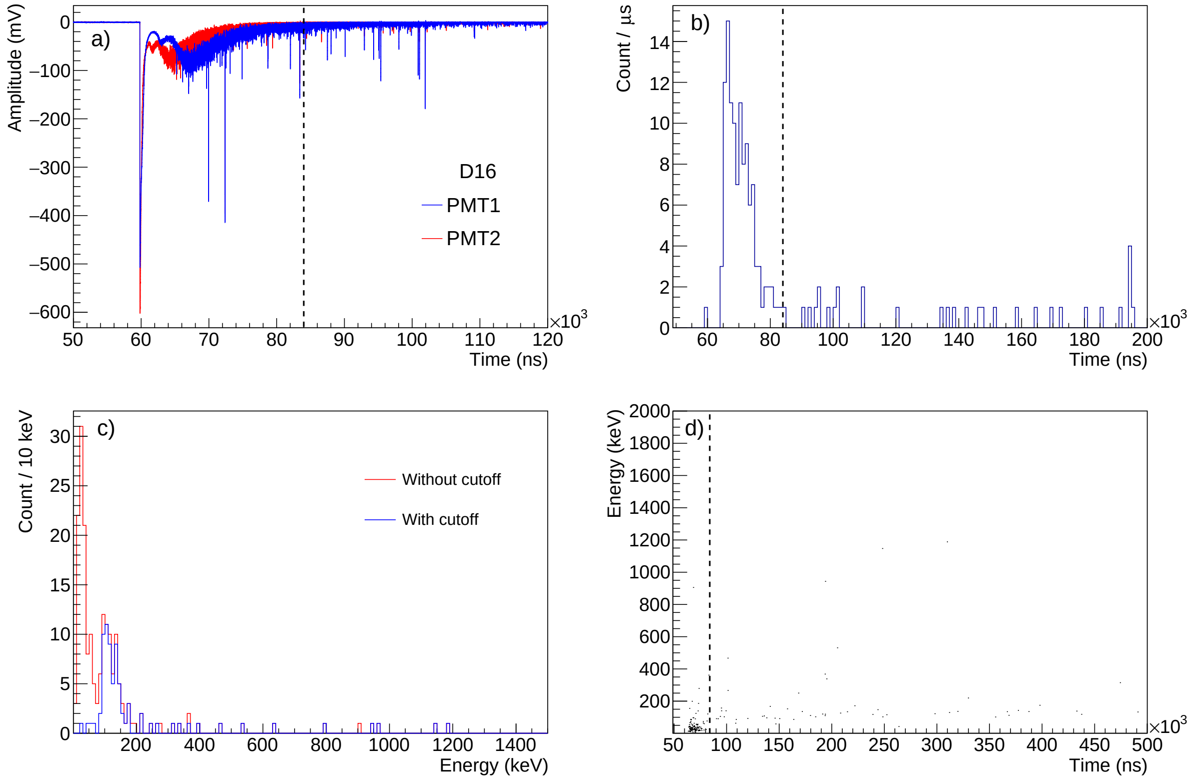

Figure 4.24: *a) Zoom on the raw traces of the two PMTs of detector unit 16 for the shot 326 with the time cutoff represented by the dashed line. b) Histogram of light collected according to the time with the time cutoff represented by the dashed line. c) Histogram of light collected according to the energy with and without taking into account the time cutoff. d) Two dimensions histogram of light collected according to the time and the energy with the time cutoff represented by the dashed line. All the histograms correspond also to the detector unit 16 during the shot 326 which had as primary and secondary target respectively a 3 μm thick Al foil and a 1 mm thick Pb piece.*

The time cutoff values for each detector units for this experiment are presented in Table.4.6.

Using the thresholds set during the calibration and those time cutoffs, for every shot where there is signal, we can see a clear neutron peak without any seenable noise in the low energy part of the

Detector unit	Time cutoff (ns)
16	84000
17	68000
18	70000
19	64000
20	68000
21	96000
24	80000

Table 4.6: *Time cutoff values for every detector unit. The laser pulse arrives on the target approximately 59800 ns after the start of the recording.*

histograms for most of the traces. There are some energy depositions with an energy higher than the neutron peak ones, which surely either correspond to neutrons which also deposed a significant part of their kinetic energy, or to gammas produced in the concrete walls. However, since there are no way to know the origin of those energy depositions, we will only consider the ones in the neutron peak.

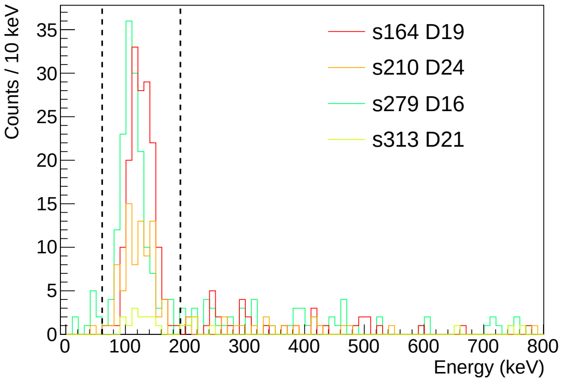

Figure 4.25: *Examples of histogram of light collected according to the energy for various detector units and shots. The dashed lines represents the arbitrary limits of the neutron peaks.*

Since for all the histograms, the neutron peak has similar characteristics as shown in Fig.4.25, we set arbitrarily the neutrons boundaries as 60 to 190 keV. Those values have been set by looking at a large number of histograms to integrate even the largest peaks without integrating the possible residual noise.

In an ideal world, we would have been able to measure the neutron energy spectrum shot to shot with the nToF measurement. Hence, it would have been possible to calculate a counting efficiency adapted to each shot using a Geant4 simulation such as the one we run to obtain Fig.4.21. In fact, since for each event during which energy has been deposited in the scintillators, the original energy of the neutron is recorded, we just need to do a simulation over the whole energy range the neutron produced in the experimental chamber can reach, for each detector setup. If this simulation has enough statistic, we can then calculate an efficiency for any neutron energy spectrum.

However, in our case, we don't have the neutron energy spectrum shot to shot. Hence, we can only assume that the efficiency of the detector units is for every shot near enough the efficiency we can calculate using the energy spectrum we calculated thanks to TALYS data and a proton spectrum generated during the LULI2000 experiment. Even though this is not perfect, this assumption is not unrealistic since RCF measurements during the commissioning experiment have shown us that the spectrum of the protons produced in SFA has also a maximum energy cutoff around 30 MeV and a similar shape. So from now on, we will use the results of the Geant4 simulation presented earlier to calculate an efficiency valid for all the shots.

Now that the time cutoff values have been defined, it is important to update the results from the Geant4 simulation presented in Fig.4.21. This update is presented in Fig.4.26. We see that for some detector units, it doesn't even change anything. This is due to the fact that it takes some time for the neutrons to thermalize in the walls and then be captured to take part in the two peaks. Besides, the statistic in these simulation is not very high. Hence, the change that this time cutoff would induce is not big enough to be seen. However when the time cutoff is higher, we can see the effect that there will be on the final efficiency.

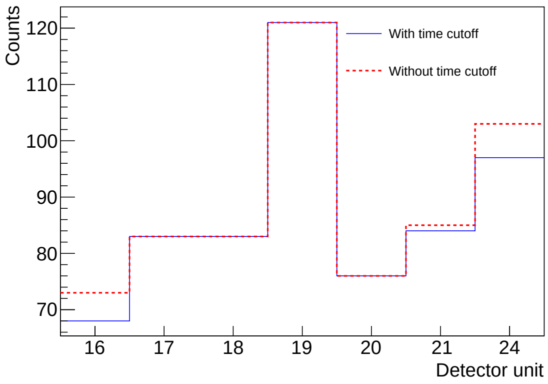

Figure 4.26: *Integral of the two peaks in the histogram of energy deposition according to the detector unit. In red is without the integration of the time cutoff and in blue is with it.*

We can now calculate the efficiency of each detector units using the results presented in Table.4.4, Figs.4.23 and 4.26 and Eq.3.20. Those efficiencies are presented in Table.4.7. It is important to notice that the error presented don't take into account the error which could arise from the change in the neutron energy spectrum.

With those efficiencies, we can then calculate a number of neutrons produced per shot according to each detector unit, considering an isotropic neutron emission, as supported by the results shown in Fig.4.6b. Since Apollon has a repetition rate which can go up to 1 shot per minute, we have been able to make several shots for each configuration along the whole campaign. Figs.4.27 show those results from Al primary target respectively 2 and 3 μm thick and either Pb, LiF or no secondary target.

Detector unit	Efficiency (%)
16	$1.26(19).10^{-4}$
17	$2.12(29).10^{-4}$
18	$2.01(27).10^{-4}$
19	$1.45(18).10^{-4}$
20	$1.81(26).10^{-4}$
21	$2.13(29).10^{-4}$
24	$2.40(33).10^{-4}$

Table 4.7: *Efficiencies of the detector units used as counter for this setup and the adapted time cutoff values.*

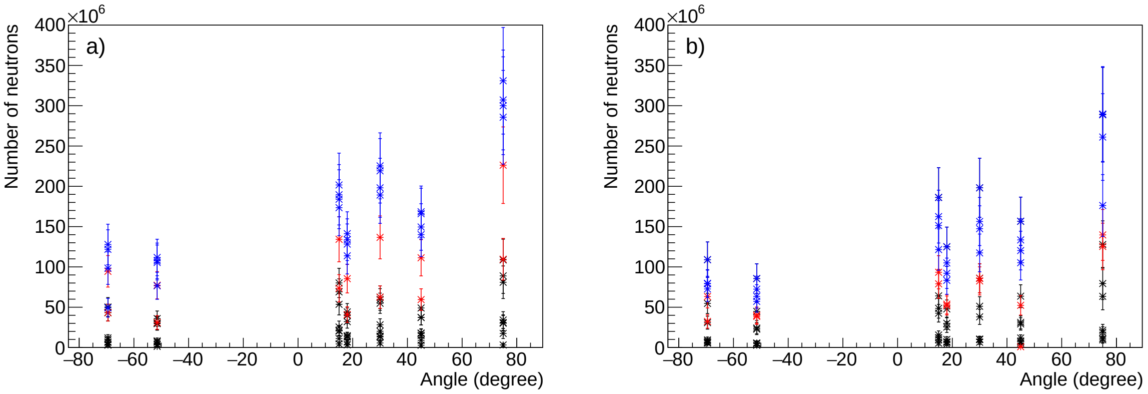

Figure 4.27: *a) Number of neutrons detected according to the detector units placed at different angles from the target normal, when shooting 2 μm thick Al primary targets. b) Number of neutrons detected according to detector unit placed at different angles from the target normal, when shooting 3 μm thick Al primary targets. The blue points correspond to shots with 1.5 mm thick LiF secondary target, the red points to shots with 1 mm thick Pb secondary target and the black ones to shots with no secondary target.*

First of all, the results for the shots with the LiF secondary target are close to the expectations. Indeed, the spectrum calculated during the preparatory calculations gives us a production around 10^9 neutrons per shot. This calculation is based from a proton spectrum obtained at the LULI2000 facility with around 60 J laser pulses. Taking into account that the laser pulse energy during the commissioning experiment was around 12 J, this gives us a production around 2.10^8 neutrons per shot. The results we got are then in total agreement with the expectation or just below for some shots.

For the Pb secondary target, we see that the neutron production varies much more shot to shot. This can be explained by the fact that the neutron production through this process is much more dependant on the proton maximal energy than when we use LiF crystals. Besides, this maximum proton energy has fluctuated during the campaign since there was still adjustments to perform. This shows that for some shots, we already have a proton production with a high enough maximum energy to compete with the neutron production using the LiF converter. Then, we should have even better results in the future when the proton production and its maximum energy will be stabilized and enhanced through the use of plasma mirrors for instance.

We also see that even without secondary target, we have a neutron production which can vary, depending on what else is in the chamber and of course the proton energy spectrum. As with the LiF and the Pb shots, there is for some shots the presence of a clear neutron peak which eliminates the possibility for this to be simply noise.

In addition to that, we can see that the two units 16 and 21 near the laser direction, i.e. -45°, show results a bit inferior than the rest of the other detector units. It would have been good to switch at some point those units with two other units to see if this is due to some imprecision in the efficiency calibration, as it probably is the case between units 17 and 20 respectively at angles 15° and 18°, or if this is a consequence of their proximity with the laser direction and the consequential stronger gamma flash received by those two units.

To conclude, we have been able to retrieve from the data a measurement of the neutron production for each shot. Even though the precision of this measurements can be improve through several ways which have already been exposed, the results are in agreement with the calculated expectations.

4.3.2 Study of PMT saturation

To better understand the behaviour of the PMTs after an overexposure, we ran some tests using one of the PMTs, some optical densities (ODs) and a ps laser. The setup we used is shown in Fig.4.28.

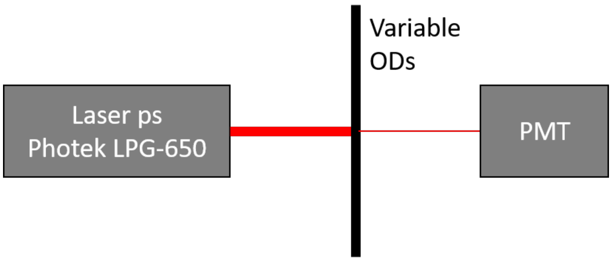

Figure 4.28: *Setup used to test the PMT behaviour when saturation occurs.*

The laser pulse energy ranges from 8 to 125 pJ. Actually, this laser varies its energy mainly by increasing the pulse duration, as shown in Fig.4.29. In addition to this, we also used ODs stack up to 5.17 to reduce the laser pulse intensity from no reduction to $10^{5.17}$, i.e. $1.48.10^{5}$. The energy received by the PMT was then going from $5.4.10^{-17}$ J to $1.25.10^{-12}$ J. Hence, thanks to the tuning of the laser and a set of ODs, we were able to test the PMT response from too low signal to be detected up to the saturation of the PMT.

In order to avoid any effect of the pulse duration, all the raw traces presented in this section have been produced only using the switch position 16 of the laser. Hence, the laser pulse duration was always 800 ps and the energy varied only thanks to the use of various sets of ODs. However, for the results which needed more different energies presented in Figs.4.33 and 4.34b, we used all the switch positions and

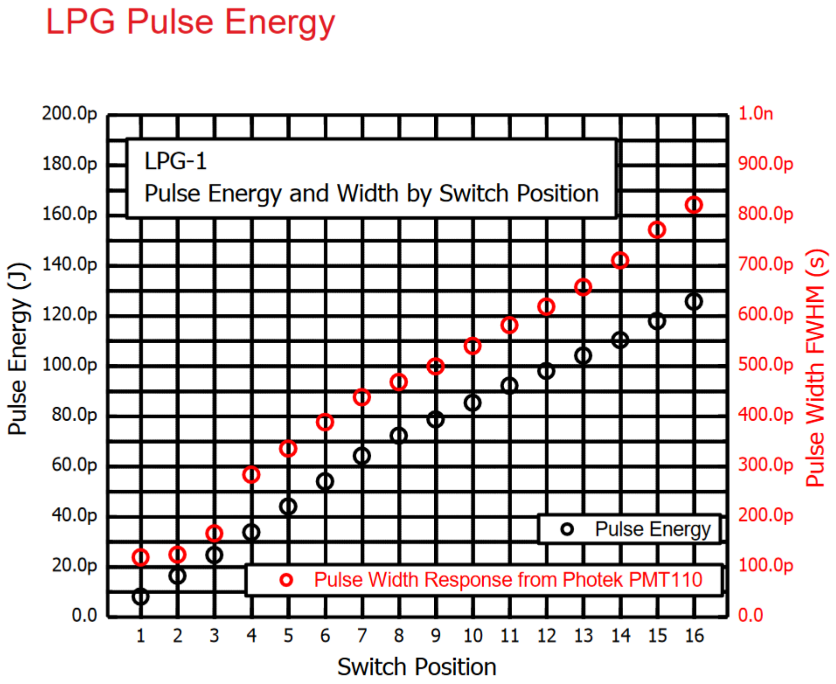

Figure 4.29: *Width and energy of the pulses generated by the Photek LPG-650 laser according to the switch position.*

then varied the pulse duration from 120 to 800 ps.

Besides, the laser wavelength was 650 nm which is not the optimum but is still in the range of what the PMT can accept as shown by Fig.4.30. Also, to see if there is any effect on a second energy deposition if this one is near enough a first energy deposition, we decided to send two pulses next to each other. Due to the repetition rate of the Photek LPG-650 laser being limited to 300 kHz , we could not sent pulses separated by less than 3.3 μs.

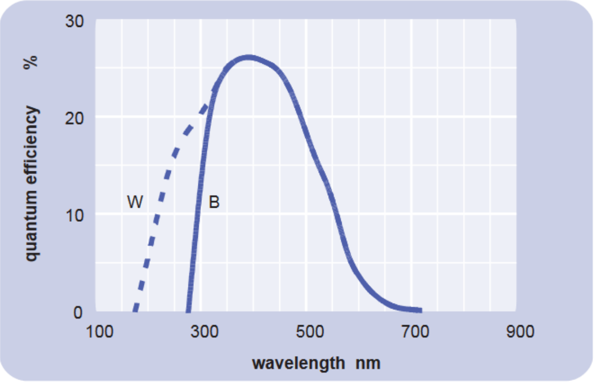

Figure 4.30: *Spectral response of the 9112B PMT as provided by the manufacturer. The curve B corresponds to the 9112B model.*

First of all, we can compare the traces obtained with no OD to some traces obtained during the experimental campaign. Such a comparison is presented in Figs.4.31.

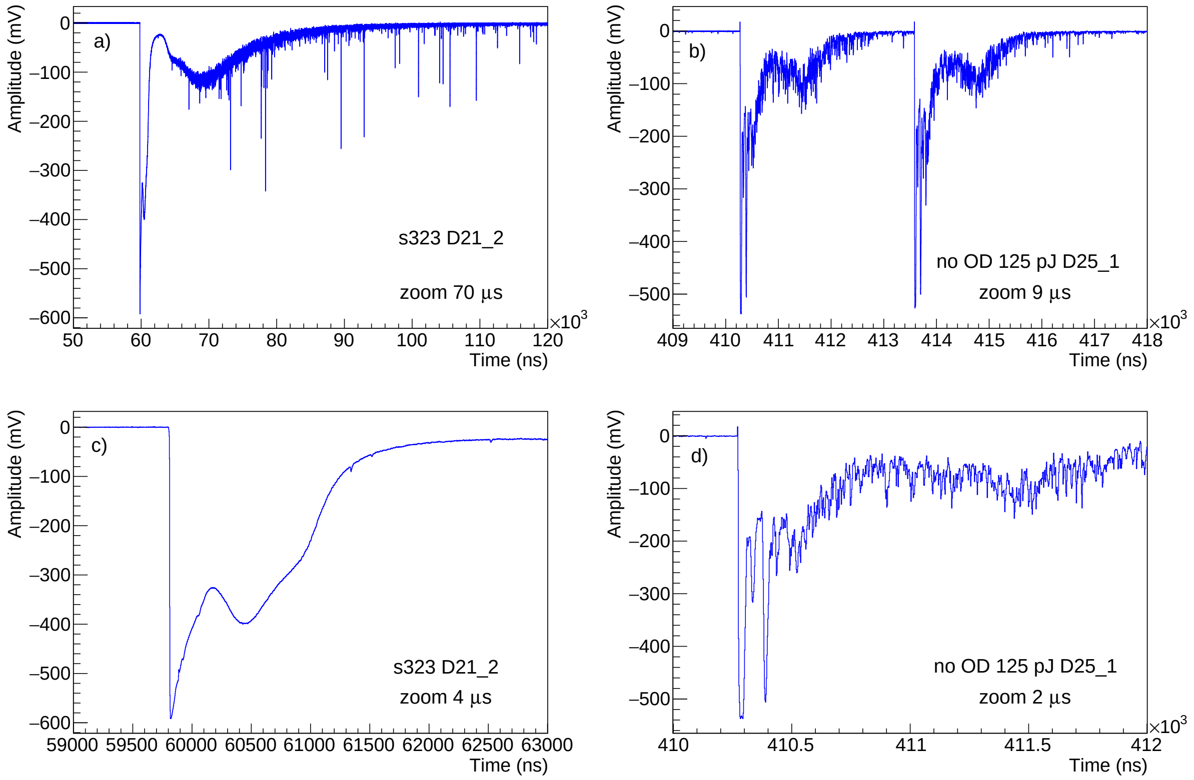

__Figure 4.31:__ Different zooms on the raw traces from the down PMT of detector unit 21 during shot 323 of the SFA commissioning (a and c) and from the up PMT of detector unit 25 during test with the laser pulse generator and no OD (b and d).

One of the first conclusion we can draw is that the rebounds seen during the experimental shots seem to have indeed an electronic origin that doesn't correspond to any nToF measurement. Besides, even without any ODs, the PMT 25U is not as saturated during the tests as PMT 21D was during the experimental shots. This can be seen in Fig.4.31b by the fact that it takes only 3 μs for the signal to come back to the baseline in this test when it took around 38 μs for the experimental example as it can be seen in Fig.4.31a. However, the temporal response of the PMT seems to be similar except that it takes place on a shorter timescale. We won't be able to see the effect of a saturation on a second light measurement since the PMT has time to come back to a normal state before our laser pulse generator can send a second pulse as shown in Fig.4.31b.

There is however some noticeable differences between the two traces. First of all, for the test trace shown in Fig.4.31d, the signal is very shaky almost directly after the peak, contrary to the smooth evolution of the signal happening during a few μs with the experimental trace shown in Fig.4.31c. Besides, for the test trace, there is a second peak taking place around 100 ns after the main one and with almost the same amplitude. Since, as shown in Fig.4.32, this peak reduces and disappears when we put some ODs between the laser pulse generator and the PMT, it seems that it is due to the saturation of the PMT.

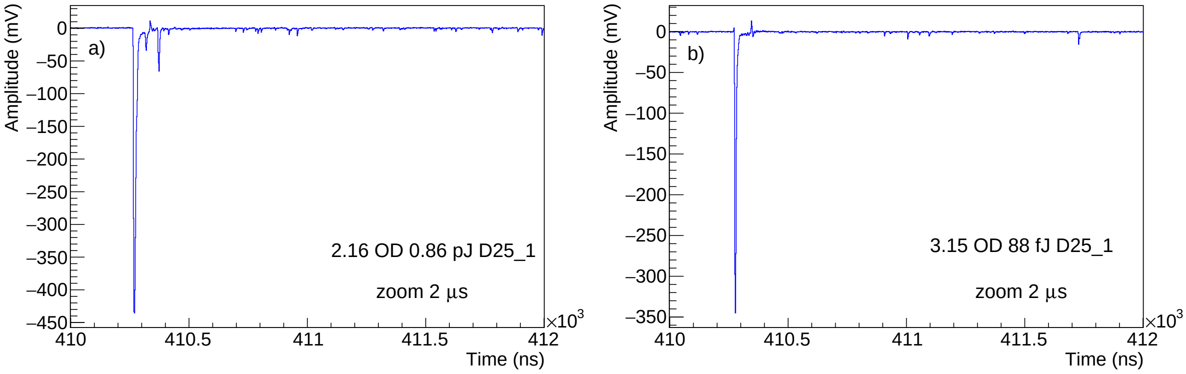

Figure 4.32: *Zooms on raw traces from the up PMT of detector unit 25 during test with the laser pulse generator and a) 2.16 OD or b) 3.15 OD.*

However, we don't see it on the experimental traces even though the saturation is stronger. An explanation could be found in the fact that the light exposure is only over a maximum of 800 ps with the laser pulse generator, as shown in Fig.4.29, when it could be longer with the scintillator during the experimental shots. Indeed, even though the rise and decay time for EJ-254 scintillator is only of a few ns as shown in Table.2.1 in nominal conditions, the overload of energy deposition due to the gamma flash could increase those values (204) and/or the size of the scintillator and the reflective paper used to coat it could allow some photons to travel a relatively long distance and then increase the time it takes for a part of the scintillation light to reach the PMTs (205). Hence a longer light exposition could explain the non presence of this second peak in the experimental shot, which would be absorbed in the main first peak.

Overall, we have seen that we are not able to reproduce exactly the same saturation traces the PMTs exhibited during the experiment. However, we can still analyze the PMT response according to the pulse energy and try to understand what is happening during the saturation.

First of all, we verified that, as we supposed until now, there is a linear relation between the light energy received and the peak integral obtained on the voltage trace. Figs.4.33 shows that that assumption is correct at least up to approximately 10 fJ deposited in 800 ps. As a reminder, a neutron capture produces around 100 keV$_{ee}$ of light, i.e. 16 fJ, distributed between two PMTs over several ns. Indeed, we don't exactly know the temporal width of the light signal after a ^{10}B neutron capture since the 24 ns shown in Fig.2.36 includes also the temporal width added by the electron cascade in the PMTs. According to the manufacturer, the signal FWHM for a single electron at the start of the cascade in a PMT 9112B is 3.1 ns. Hence, we can reasonably assume a 20 ns temporal width for the mean 8 fJ light pulse received by each PMT after a neutron capture. For only a 800 ps long pulse, this would place us at 0.64 fJ on the x-axis in Fig.4.33. Taking into account the quantum efficiency of the PMT shown in Fig.4.30, this places us at

16 fJ which is at the limit of what we presented. Hence, the amount of light collected by a PMT after a neutron capture in the associated scintillator seems to correspond to the linear part, i.e. the PMTs work in their nominal state during a neutron detection.

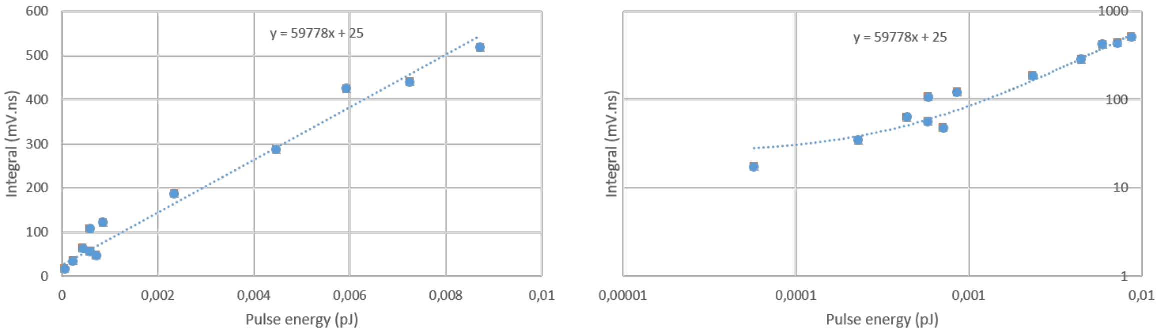

Figure 4.33: *Integral of the peak recorded by PMT 25U according to the laser pulse energy for energies up to 8.7 fJ.*

Additionally, if we remove some ODs and increase the energy received by the PMT, we know can consider two different integrals. Indeed, we can integrate only the main peak or we can also integrate the electronic rebound that follows. An example of the time windows used for the two integration and the evolution of both integrals are presented in Fig.4.34. The integral of the main peak alone cannot be fitted satisfyingly with either a linear or logarithmic or power trend curve. However if we add the rebound in the integration, we see that the behaviour can be fitted with a power trend curve. This fit is not perfect since the r^2 here is equal to 0.9846 but this can give us a first estimation of the energy received by the PMT even if this one is not working at its nominal parameters.

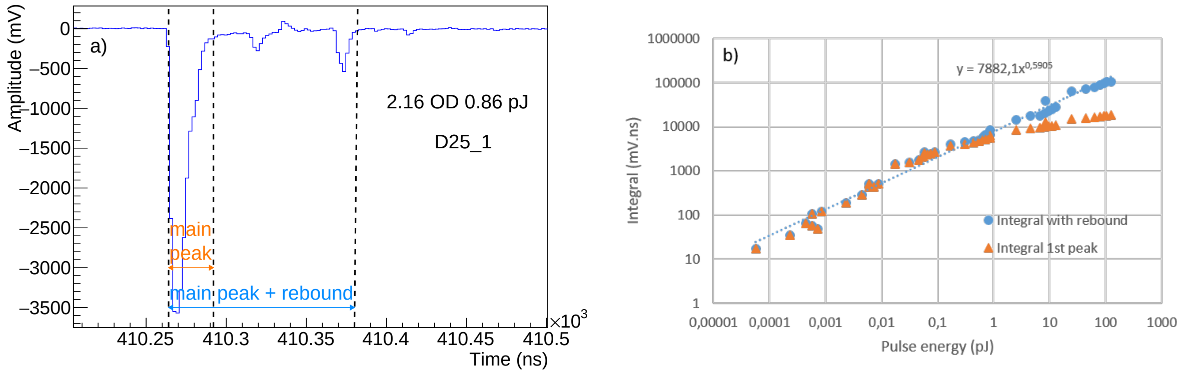

Figure 4.34: *a) Example of time windows used for the integration of the peaks recorded on PMT 25U traces. The orange one corresponds to the main peak alone and the blue one to the main peak with the following rebound. b) Integral of the peak recorded by PMT 25U according to the laser pulse energy for energies up to 125 pJ. Both the integrals of the main peak alone and the main peak with the rebound are presented, respectively in orange and blue.*

To try and prevent this saturation, a first approach is to protect the detector units from this surge of energy deposition after the shot. It is likely that this massive energy deposition is mainly due to gammas and x-rays since other energy depositing particles apart from neutrons, are mainly stopped by the experimental chamber walls. Indeed, the fact that the detector units in the laser direction are more affected than the ones in the direction normal to the target tends to confirm this suspicion. Hence, a way to protect the detector unit would be to stop most of the gammas and x-ray using lead for instance. However, during the commissioning experiment, when we doubled the thickness of lead in front of some detector units, it actually worsened the situation as it can be seen in Figs.4.35.

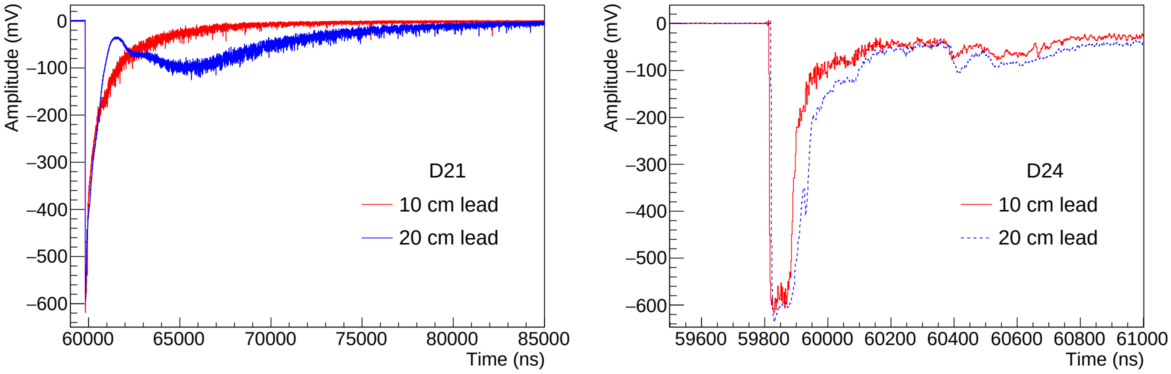

Figure 4.35: *Raw traces for PMT down of detector units 21 (left) and 24 (right) for shot 212 (red) and shot 254 (blue). Between those two shots, the lead thickness in front of those detector units increased from 10 cm to 20 cm. The other parameters were the same for those two shots. The primary target was a 2 μm thick Al target and there was no secondary target.*

In order to find a better solution, we can try to understand what is the reason of this rebound by taking a look directly at how a PMT is built. Fig.4.36 shows the electronic schematic of the PMT with its associated voltage divider C673A. From this, we can understand that when an important luminous signal excites the cathode K, this will induce an important electron cascade which is amplified dynode after dynode. At some point, the electron flow is so important that there is an induced current in the interstage circuit countering the current provided by the high voltage supply. This happens firstly at the last dynode d10 since this is the one where the electron flow is the highest. This causes a change in the interstage voltages. The voltage between the dynodes near the anodes will decrease. If the supply voltage can compensate it, this will also result in higher voltages between the dynodes near the cathodes but the overall voltage can decrease if the capacity of the power supply is exceeded (206). Since the voltage between the last dynodes and the anode is diminished, the resulting signal out of the PMT is diminished the same way, possibly down to zero.

To help the power supply compensate this effect, capacitances are installed on the last three dynodes. This indeed helps increase the saturation threshold. However, at some point, the dynode currents is so strong that even the capacitance near the last dynode cannot counteract the voltage decrease and the signal out of the PMT plummets. Hence, when the electron cascade finally diminishes its intensity, the

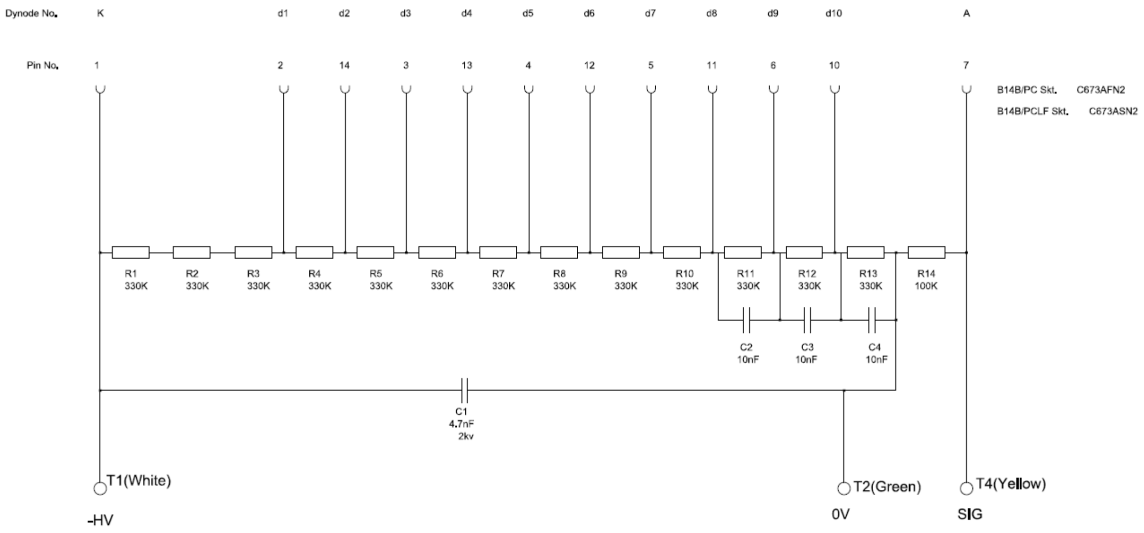

Figure 4.36: Electronic schematic of the PMT 9112B with its associated voltage divider C673A. Compliment of ET Enterprise.

last capacitor takes up its role of "electron reservoir" and increases again the signal out of the PMT. This should be the cause of this observed rebound. If we take this logic even further, the little rebound in the middle of the flat baseline between the first main peak and the main rebound as it can be seen in Fig.3.18 for PMT down of detector unit 13 could be explained by the same effect on the capacitor associated to the dynode 9.

To verify those assumptions and try to remove this rebound, we decided to remove capacitors C3 and C4 from some voltage dividers and tested the results with the same setup as presented in Fig.4.28. These tests have been run on the same PMT up of the detector unit 25. The resulting traces for the test with a 125 pJ pulse energy is presented Fig.4.37.

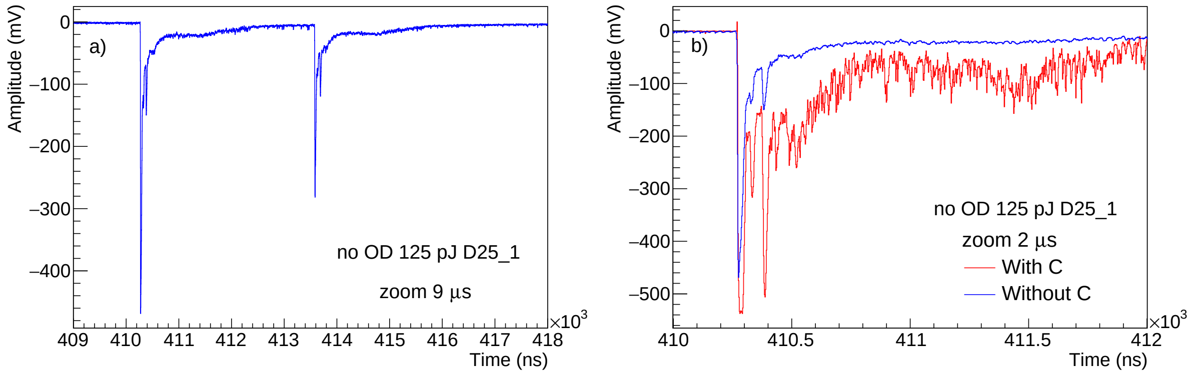

Figure 4.37: Zooms on a raw trace from the up PMT of detector unit 25 without the two last capacitances when receiving two 650 nm laser pulses with an energy of 125 pJ each with a 3.3 µs delay between them. a) shows a zoom on a 9 µs time window and b) shows a comparison between the cases with and without the capacitances on a 2 µs time window zoom.

When comparing the raw trace for the same parameters, i.e. no ODs and a 125 pJ laser pulse, with the last two capacitances, in Fig.4.31b and d, and without, in Fig.4.37a and b, the first result is that the capacitors seems indeed responsible for the observed rebounds. Besides, the peak induced by the 125 pJ laser pulse doesn't seem to exceed 130 ns in duration, even taking into account the second peak, in the case without the capacitances. Even though the voltage is not totally back at the original baseline, it seems flat enough over time to allow an nToF measurement. On the downside, as it can be seen in Fig.4.37a, the second laser pulse coming 3.3 μs after the first one induces a way less important peak. Hence, even though the PMT almost came back to its baseline, it doesn't seem to be responded nominally even after 3 μs which is in this regard worse than with the capacitors. It would be interesting to see how this second peak behaves as the time between the two pulses decreases, but we are already at the limit allowed by the laser pulse generator. A different laser would be needed to check that. However, we can check how long it takes for the PMT to come back to its nominal behaviour after the first 125 pJ pulse, without the two last capacitances on the voltage divider.

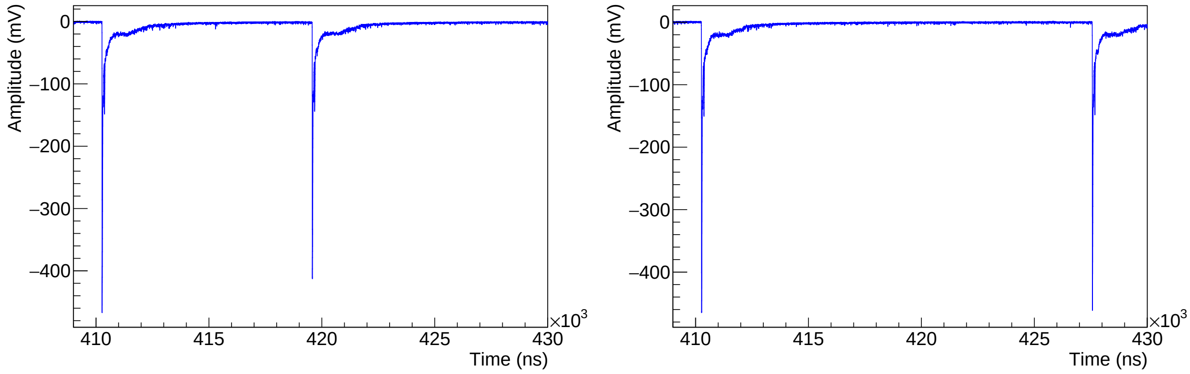

Figure 4.38: *Zoom on raw traces from the up PMT of detector unit 25 without the two last capacitances when receiving two 650 nm laser pulses with an energy of 125 pJ each. The delays between the two pulses are 9.3 μs (left) and 17.3 μs (right). The temporal window for both zoom is 21 μs long.*

Figs.4.38 shows some traces of the test we run to find out the recovery time necessary for the PMT to behave nominally again without the two last capacitances on the voltage divider. For a 125 pJ 650 nm 800 ps pulse, this recovery time is around 15 μs which is way longer than what it was with the capacitors as shown in Fig.4.31. However, even though the PMT doesn't behave nominally, it seems able to detect the energy deposition. Hence, if we are able to reliably know the efficiency of a PMT during its recovery time, we would be able to perform nToF measurement.

Another possible solution we didn't have time to look into yet, is the possibility to use some gate preventing the PMT to amplify any incoming signal before the gate allows it. We could then block any light coming to the PMTs during the main gamma flash and then allow the neutron detection right after. This whole solution relies on how fast it would possible to allow the PMTs to detect signal. For instance, Photek sells gating modules which prevents the electrons produced by a photocathode to reach their associated MicroChannel Plate detector, until the gate is turned on. This switch can be done in 8 ns depending on the solution. If implemented on the PMT we have, such a technology could solve this PMT saturation problem.

There is also the possibility to use a voltage divider with different resistance. ET enterprise commercializes another voltage divider for this PMT model, called C673B. It changes the value of the resistance R13 and R14 as shown in Fig.4.36 to respectively 660 kΩ and 1.32 MΩ. This has for consequence to reduce the overall gain of the PMT. This should then reduce the saturation limit and could improve the situation. Besides, it shouldn't prevent the detector units to still work as counter since we have seen that the detected signal for neutron capture is well above the noise level but this would have to be tested. The main downside of this solution is that it would decrease the detectable nToF signal at least as much as it would decrease the gamma flash induced saturated signal.

Looking at the PMT behaviour when it saturates, we have better understood the cause of this behaviour and proposed some solutions. With a better understanding of the PMTs, we can now try to retrieve some nToF information from the data acquired during the SFA commissioning experiment.

4.3.3 nToF analysis

As we have seen, the time window during which nToF signal should be measured is overloaded from consequences of the gamma flash. Hence, trying to retrieve some nToF data will imply a somewhat complicated analysis. First of all, we can take a look at an example from two shots with similar characteristics but for the neutron converter presence. Figs.4.39 shows the raw traces from shot 323 and 321 which have the same characteristics except for the presence of a LiF secondary target. As a reminder, Fig.4.19 presents the energy deposited in the scintillators according to time during a full ms and its first 2 μs for a neutron spectrum generated using a LiF converter, according to Geant4 simulations. The results we obtained in this section should correspond at least time-wise to this simulation. A copy of this histogram on the first 2 μs with also a focus on detector unit 17 is presented in Fig.4.40b for comparison with the results obtained during this analysis.

A first approach would be to consider the traces obtained during s321 as baselines for s323 nToF study. However, as shown in Fig.4.40a, even if we can see some coincidence between the results from the two PMTs, especially around 200 ns after the gamma peak, the resulting signal is way too noisy to conclude anything.

To reduce this noise, we can try to fit the traces from shot 321 and then use this fit as baseline to study shot 323. As shown in Figs.4.41, this improves the obtained result, but this one is still too noisy to

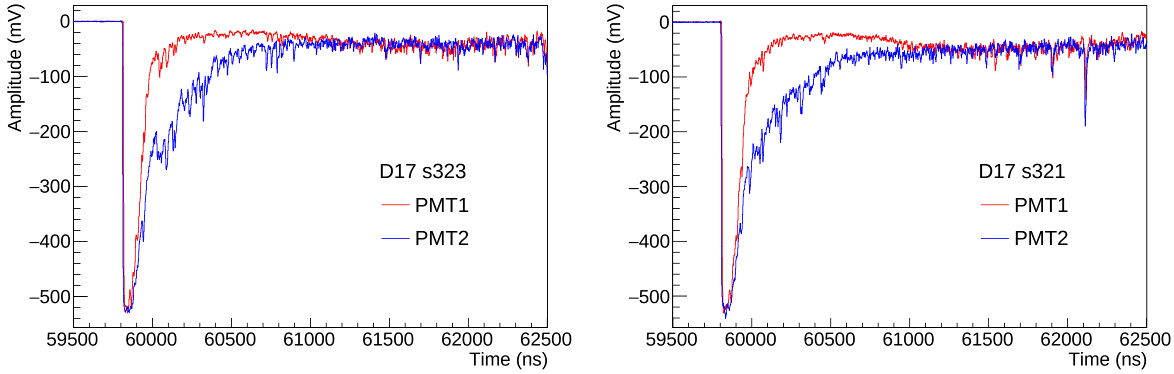

Figure 4.39: *Zoom around the gamma peak on the raw traces from the two PMTs of detector unit 17 during shots 323 (left) and 321 (right). The primary target was a 2 μm thick Al target for both shots and a 1 mm thick LiF neutron converter was additionally present during shot 323.*

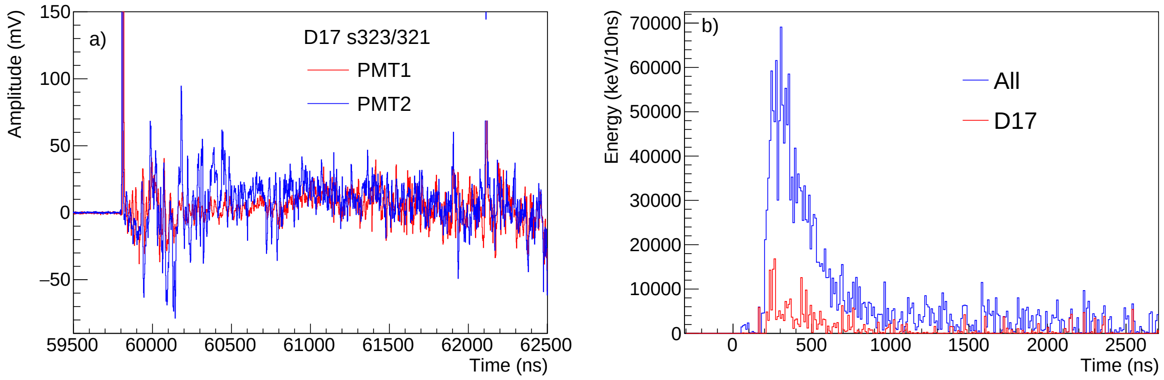

Figure 4.40: *a) Signal obtained from detector unit 17 for shot 323 when subtracting the signal from shot 321 which is hence considered as a baseline. The primary target was a 2 μm thick Al target for both shots and a 1 mm thick LiF neutron converter was additionally present during shot 323. b) Energy deposited in all the scintillators (blue) and in the scintillator of detector unit 17 (red) according to the time, according to Geant4 simulations using an isotropic neutron source with an energy spectrum calculated using a proton spectrum obtained at the LULI2000 facility and TALYS data considering a 1 mm thick LiF neutron converter.*

retrieve a clear neutron energy spectrum. Indeed, even though the traces from the two PMTs of detector unit 17 during shot 323 share some features, they are too affected by the noise to be exploitable. It seems then impossible to retrieve shot to shot a neutron energy spectrum from the data we have from the commissioning experiment.

However, even though shot to shot results seem out of reach, we can try to retrieve a mean energy spectrum from shots with the same characteristics. Indeed, the statistic obtained through the addition of shots should reduce the noise. The different traces with their corresponding mean traces are presented in Figs.4.42 for PMT up of detector units 17 and 19 for the shots with either only a 2 μm Al target or a 2 μm Al target and a LiF neutron converter. We can see that the variance between the traces is not the same depending on the PMT and/or its position. We also see that the noise is indeed reduced on the

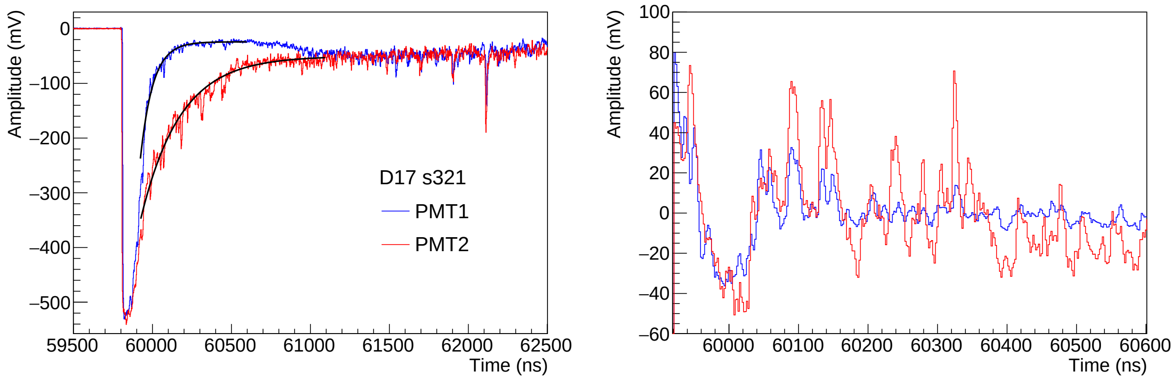

Figure 4.41: *Fit of a part of the traces from the PMTs of detector unit 17 for shot 321 (left). Signal obtained from detector unit 17 for shot 323 when subtracting the fits from shot 321 (right).*

mean trace even if the statistic of only 4 shots for the case 2 μm Al + LiF impacts this noise reduction.

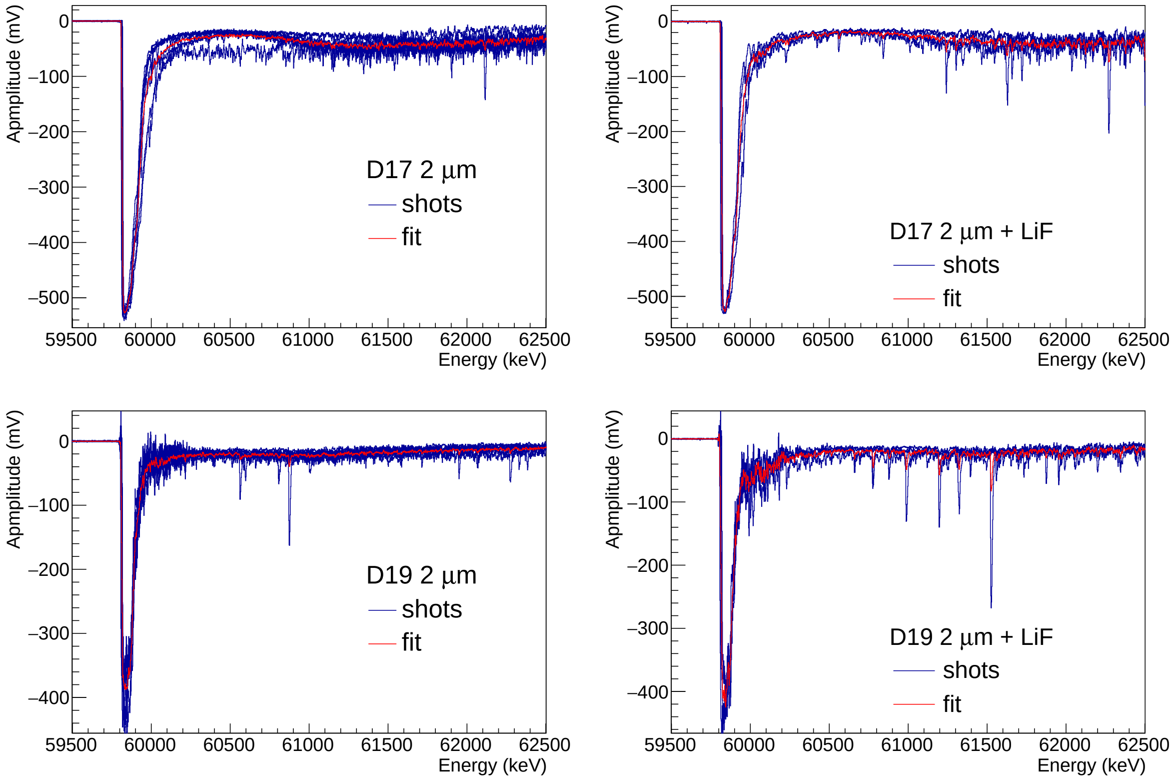

Figure 4.42: *Traces (blue) and mean trace (red) for PMT up of the detector unit 17 and 19 for the shots with either only a 2 μm Al target, i.e. shots 163, 172, 173, 207, 210, 212, 254 and 321, (left) or a 2 μm Al target and a 1 mm thick LiF neutron converter, i.e. shots 168, 180, 183 and 323 (right). All those shots had the same parameters otherwise. Especially, those shots were at best focus in regard of reaching the maximum proton energy.*

We can try to subtract the mean "noise" obtained with the shots on Al target alone to the mean traces obtained from the shots with the neutron converter. This should gives us the closest we can get from an nToF measurement meaned on all the shots with the same characteristics. To get an idea on the statistic we are using, there are 2 shots with 2 μm Al and Pb (174, 322), 4 shots with 2 μm Al and LiF (168, 180, 183, 323) and 8 shots only with 2 μm Al (163, 172, 173, 207, 212, 254, 321). There are also 7 shots with 3 μm Al and Pb (166, 175, 255, 256, 281, 314, 326), 8 shots with 3 μm Al and LiF (167, 181, 182, 257, 282, 315, 319 ,327) and 13 shots only with 3 μm Al (164, 165, 170, 171, 205, 206, 208, 209, 316, 317, 318, 320, 328). All those shots had the same parameters apart from the ones specified. Especially, those shots were at best focus in regard of reaching the maximum proton energy.

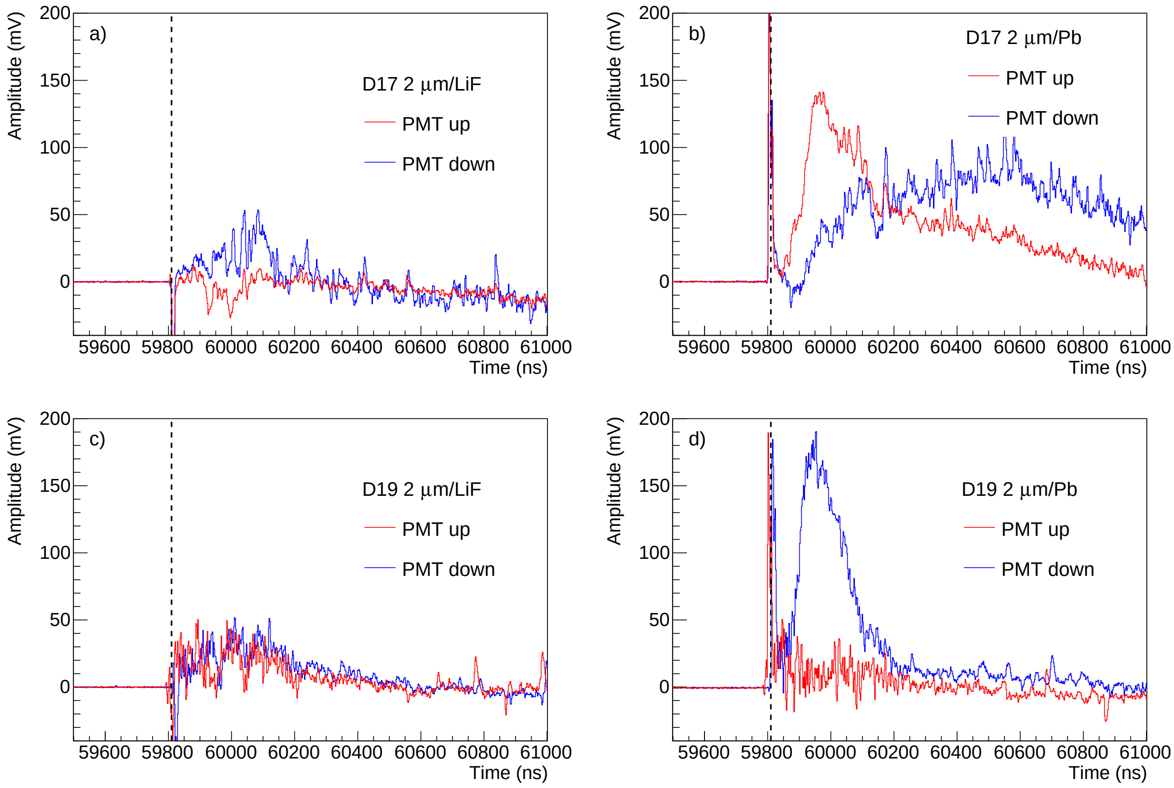

Figure 4.43: *Results for both PMTs up (red) and down (blue) of the detector unit 17 (up) and 19 (down) for the shots with a 2 μm Al target and either a LiF (left) or Pb (right) neutron converter. The mean traces for the shots with only the Al target have been subtracted to the ones with neutron converter to obtain these results. The black dashed line symbolizes the approximate time the gamma flash start.*

Figs4.43 and 4.44 shows the subtraction of the mean "noise" obtained from the shots only with an Al target, to the mean signal obtained from the shots with an Al target and either a 1 mm thick LiF or 1.5 mm thick Pb neutron converter, for detector units 17 and 19. We present here results for the cases with the most number of shots, i.e. either a 2 or 3 μm thick Al primary target. Even for the detector units 17 and 19 which are less affected by the gamma flash than other ones, we don't have any coincident signal clear enough to retrieve a neutron spectrum, even with the help of several shots.

To conclude, we have not been able to get any nToF measurement from this campaign. Hopefully, the improvements proposed in Section 4.3.2 will allow to get those during the following campaigns.

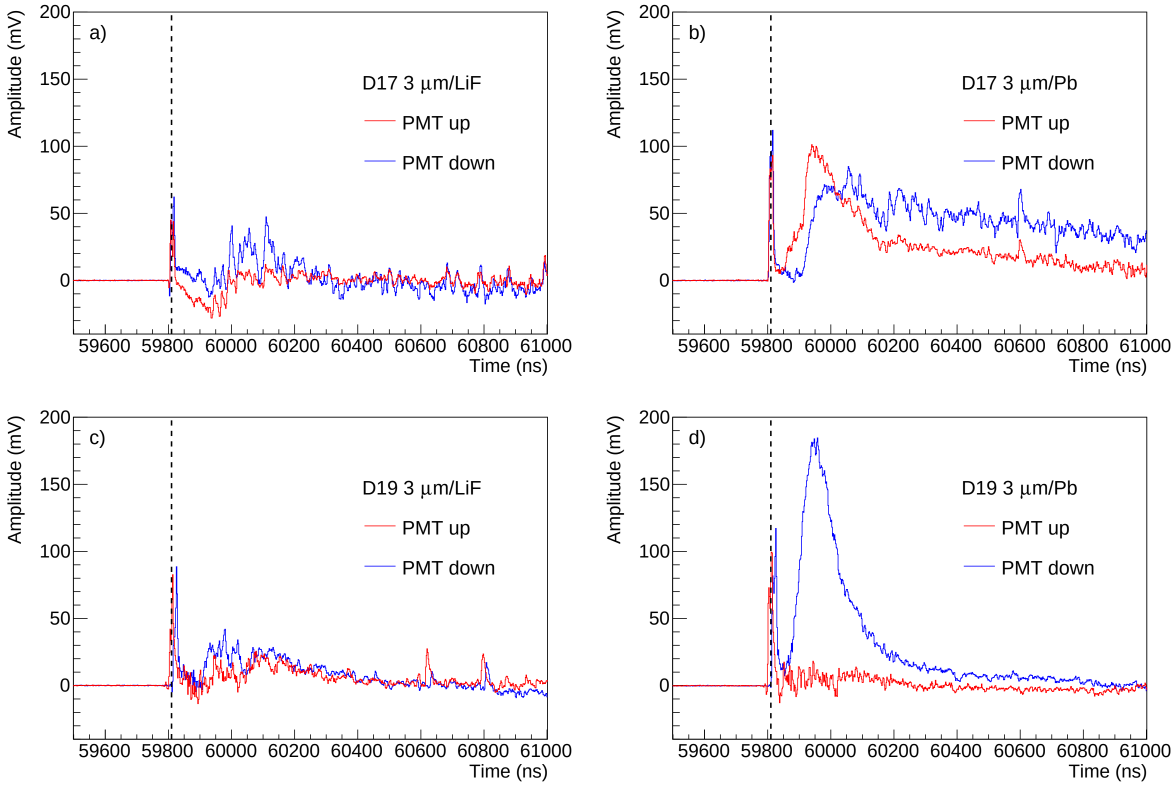

Figure 4.44: *Results for both PMTs up (red) and down (blue) of the detector unit 17 (up) and 19 (down) for the shots with a 3 µm Al target and either a LiF (left) or Pb (right) neutron converter. The mean traces for the shots with only the Al target have been subtracted to the ones with neutron converter to obtain these results. The black dashed line symbolizes the approximate time the gamma flash start.*

However, even if improvements can still be implemented, the counting part of the detector array has been able to measure the numbers of neutrons that were expected to be produced. It demonstrated the possibility to use this detector array in the Apollon environment successfully.

Conclusions and perspectives

The development of diagnostics for nuclear physics in the environment of high intensity lasers is important to develop the possibilities offered by this field in the upcoming laser facilities in France, in Europe and some other countries around the world. This thesis work focused in particular on the development of neutron diagnostics in the context of nuclear astrophysics. We developed a neutron counter from commercially available parts, and all the necessary scripts and simulations to analyze the experimental and retrieve an actual number of neutrons. We also started developing an nToF detector which also can be used as well as a neutron counter thanks to the presence of large volumes of concrete around the experimental target chamber.

The first chapter introduced the notions necessary to understand the production of protons and neutrons at present and upcoming laser facilities. It also presented nuclear astrophysical notions such as the nucleosynthesis and especially the r-process and showed how its study could be rendered possible by high intensity lasers.

The second chapter was dedicated to the conception of a high efficiency neutron counter, from the very beginning to its building and calibration. During this chapter, we:

- found solutions using commercially available parts to build a detector that would be able to endure the high intensity laser environment,
- built a prototype to test our concept both with radioactive sources and in real conditions,
- developed and used Geant4 simulations to understand and optimize the detector dimensions,
- and ran calibrations using gamma and neutron sources and developed the adequate scripts to analyze the calibration data.

The third chapter presented the commissioning experiment of the neutron counter, developed in the previous chapter, at the LULI2000 experiment. The detector being thought for facilities such as Apollon where the EMP is not as powerful as it is at facility like LULI2000, the noise was a real problem during this campaign. We anyway demonstrated that it was possible to detect and count neutrons using this diagnostic during shots with a full intensity ps beam. The results obtained for some of the detector units, which also corresponds to the most statistically strong data, are indeed in the order of magnitude of what we expected as neutron production. We also showed that less neutrons were emitted or at least detected when the secondary target was heated by a ns laser pulse. The amplitude of this decrease is yet unexplained.

The fourth chapter showed how we took advantage of the SFA commissioning campaign to try to use some of our detector parts both as counter and nToF diagnostics. We showed that we were partly able to characterize a neutron beam production by using the detector units as counter. The results showed by the detector units used as counter matched the expectations. However, we did not succeed to perform an nToF measurement during this campaign. Tests were run afterwards to understand why and possible solutions are discussed. A part of the solutions have already been implemented and still have to be tested in real conditions. All the scripts have otherwise been developed and are ready to analyze such data.

To conclude, we have developed a new neutron diagnostic adapted to the high intensity laser environment and commissioned it during full experimental campaigns. This include the material side with the building from commercial parts but also the numerical side with the development of several scripts to calibrate and analyze the detector units depending on its use.

There is of course still a lot of possible improvements, especially on the nToF part. Thankfully, there is another PhD student now working on what is left to do and who ran the tests with me after the SFA commissioning. The main improvement to do in the near future are :

- run the Geant4 simulation with the PMTs/scintillator assembly on a more powerful machine over a wide range of neutron energy in order to have more statistics and hence a more precise counting efficiency, whatever the neutron energy spectrum is.
- qualify the recovering behaviour of a PMT after saturation when the two last capacitors have been removed.
- implement a fast gate on the PMTs to prevent them from seeing the gamma flash.

On another topic, it would also be interesting to do an experiment similar to the one conducted at the LULI2000 facility, but with additional diagnostics to see what is really happening around the two targets to see if the observed decreased can be explained or if it really is due to the plasma state of the target.

Bibliography

[1] M. Passoni, L. Bertagna, and A. Zani, *Target normal sheath acceleration: theory, comparison with experiments and future perspectives*, New Journal of Physics **12**, 045012 (2010).

[2] M. Borghesi, A. Bigongiari, S. Kar, A. Macchi, L. Romagnani, P. Audebert, J. Fuchs, T. Toncian, O. Willi, S. Bulanov, et al., *Laser-driven proton acceleration: source optimization and radiographic applications*, Plasma Physics and Controlled Fusion **50**, 124040 (2008).

[3] G. S. Bauer, *Physics and technology of spallation neutron sources*, Nuclear Instruments and Methods in Physics Research Section A: Accelerators, Spectrometers, Detectors and Associated Equipment **463**, 505–543 (2001).

[4] B. Martinez, S. Chen, S. Bolaños, N. Blanchot, G. Boutoux, W. Cayzac, C. Courtois, X. Davoine, A. Duval, V. Horny, et al., *Numerical investigation of spallation neutrons generated from petawatt-scale laser-driven proton beams*, Matter and Radiation at Extremes **7**, 024401 (2022).

[5] P. Hill and Y. Wu, *Exploring laser-driven neutron sources for neutron capture cascades and the production of neutron-rich isotopes*, Physical Review C **103**, 014602 (2021).

[6] C. Iliadis, *Nuclear physics of stars*, John Wiley & Sons (2015).

[7] S. Agostinelli, J. Allison, K. a. Amako, J. Apostolakis, H. Araujo, P. Arce, M. Asai, D. Axen, S. Banerjee, G. Barrand, et al., *GEANT4—a simulation toolkit*, Nuclear instruments and methods in physics research section A: Accelerators, Spectrometers, Detectors and Associated Equipment **506**, 250–303 (2003).

[8] J. P. Gordon, H. J. Zeiger, and C. H. Townes, *Molecular microwave oscillator and new hyperfine structure in the microwave spectrum of N H 3*, Physical Review **95**, 282 (1954).

[9] T. MAIMAN, *Stimulated Optical Radiation in Ruby*, Nature **187**, 493–494 (1960).

[10] A. Javan, W. R. Bennett Jr, and D. R. Herriott, *Population inversion and continuous optical maser oscillation in a gas discharge containing a He-Ne mixture*, Physical Review Letters **6**, 106 (1961).

[11] C. N. Danson, C. Haefner, J. Bromage, T. Butcher, J.-C. F. Chanteloup, E. A. Chowdhury, A. Galvanauskas, L. A. Gizzi, J. Hein, D. I. Hillier, et al., *Petawatt and exawatt class lasers worldwide*, High Power Laser Science and Engineering **7**, e54 (2019).

[12] E. Brookner, *Phased-array radars*, Scientific American **252**, 94–103 (1985).

[13] D. Strickland and G. Mourou, *Compression of amplified chirped optical pulses*, Optics communications **55**, 447–449 (1985).

[14] M. Perry, B. Shore, R. Boyd, and J. Britten, *Multilayer dielectric gratings: Increasing the power of light*, Science & Technology Review **9**, 25–33 (1995).

[15] R. Baumgartner and R. Byer, *Optical parametric amplification*, IEEE Journal of Quantum Electronics **15**, 432–444 (1979).

[16] R. Danielius, A. Piskarskas, A. Stabinis, G. Banfi, P. Di Trapani, and R. Righini, *Traveling-wave parametric generation of widely tunable, highly coherent femtosecond light pulses*, JOSA B **10**, 2222–2232 (1993).

[17] D. Papadopoulos, J. Zou, C. Le Blanc, L. Ranc, F. Druon, L. Martin, A. Fréneaux, A. Beluze, N. Lebas, M. Chabanis, et al. *First commissioning results of the Apollon laser on the 1 PW beam line*. In *2019 Conference on Lasers and Electro-Optics (CLEO)*, pages 1–2. IEEE, (2019).

[18] P. Sprangle, G. Joyce, E. Esarey, and A. Ting, *Laser wakefield acceleration and relativstic optical guiding*, AIP Conference Proceedings **175**, 231–239 (1988).

[19] F. Amiranoff, S. Baton, D. Bernard, B. Cros, D. Descamps, F. Dorchies, F. Jacquet, V. Malka, J. Marques, G. Matthieussent, et al., *Observation of laser wakefield acceleration of electrons*, Physical Review Letters **81**, 995 (1998).

[20] W. Lu, M. Tzoufras, C. Joshi, F. Tsung, W. Mori, J. Vieira, R. Fonseca, and L. Silva, *Generating multi-GeV electron bunches using single stage laser wakefield acceleration in a 3D nonlinear regime*, Physical Review Special Topics-Accelerators and Beams **10**, 061301 (2007).

[21] C. E. Clayton, J. Ralph, F. Albert, R. Fonseca, S. Glenzer, C. Joshi, W. Lu, K. Marsh, S. F. Martins, W. B. Mori, et al., *Self-guided laser wakefield acceleration beyond 1 GeV using ionization-induced injection*, Physical review letters **105**, 105003 (2010).

[22] A. Debus, R. Pausch, A. Huebl, K. Steiniger, R. Widera, T. E. Cowan, U. Schramm, and M. Bussmann, *Circumventing the dephasing and depletion limits of laser-wakefield acceleration*, Physical Review X **9**, 031044 (2019).

[23] J. Palastro, J. Shaw, P. Franke, D. Ramsey, T. Simpson, and D. Froula, *Dephasingless laser wakefield acceleration*, Physical review letters **124**, 134802 (2020).

[24] E. Clark, K. Krushelnick, J. Davies, M. Zepf, M. Tatarakis, F. Beg, A. Machacek, P. Norreys, M. Santala, I. Watts, et al., *Measurements of energetic proton transport through magnetized plasma from intense laser interactions with solids*, Physical Review Letters **84**, 670 (2000).

[25] R. Snavely, M. Key, S. Hatchett, T. Cowan, M. Roth, T. Phillips, M. Stoyer, E. Henry, T. Sangster, M. Singh, et al., *Intense high-energy proton beams from petawatt-laser irradiation of solids*, Physical review letters **85**, 2945 (2000).

[26] A. Macchi, M. Borghesi, and M. Passoni, *Ion acceleration by superintense laser-plasma interaction*, Reviews of Modern Physics **85**, 751 (2013).

[27] S. Wilks, W. Kruer, M. Tabak, and A. Langdon, *Absorption of ultra-intense laser pulses*, Physical review letters **69**, 1383 (1992).

[28] S. P. Hatchett, C. G. Brown, T. E. Cowan, E. A. Henry, J. S. Johnson, M. H. Key, J. A. Koch, A. B. Langdon, B. F. Lasinski, R. W. Lee, et al., *Electron, photon, and ion beams from the relativistic interaction of Petawatt laser pulses with solid targets*, Physics of Plasmas **7**, 2076–2082 (2000).

[29] F. Beg, A. Bell, A. Dangor, C. Danson, A. Fews, M. Glinsky, B. Hammel, P. Lee, P. Norreys, and M. Tatarakis, *A study of picosecond laser–solid interactions up to 10^{19} W cm^{-2}*, Physics of plasmas **4**, 447–457 (1997).

[30] K. Quinn, P. Wilson, C. Cecchetti, B. Ramakrishna, L. Romagnani, G. Sarri, L. Lancia, J. Fuchs, A. Pipahl, T. Toncian, et al., *Laser-driven ultrafast field propagation on solid surfaces*, Physical review letters **102**, 194801 (2009).

[31] M. Haines, M. Wei, F. Beg, and R. Stephens, *Hot-electron temperature and laser-light absorption in fast ignition*, Physical Review Letters **102**, 045008 (2009).

[32] Y. Ping, R. Shepherd, B. Lasinski, M. Tabak, H. Chen, H. Chung, K. Fournier, S. Hansen, A. Kemp, D. Liedahl, et al., *Absorption of short laser pulses on solid targets in the ultrarelativistic regime*, Physical review letters **100**, 085004 (2008).

[33] P. A. Norreys, M. Santala, E. Clark, M. Zepf, I. Watts, F. Beg, K. Krushelnick, M. Tatarakis, A. Dangor, X. Fang, et al., *Observation of a highly directional γ-ray beam from ultrashort, ultraintense laser pulse interactions with solids*, Physics of Plasmas **6**, 2150–2156 (1999).

[34] M. Santala, M. Zepf, I. Watts, F. Beg, E. Clark, M. Tatarakis, K. Krushelnick, A. Dangor, T. McCanny, I. Spencer, et al., *Effect of the plasma density scale length on the direction of fast electrons in relativistic laser-solid interactions*, Physical Review Letters **84**, 1459 (2000).

[35] M. Roth and M. Schollmeier, *Ion Acceleration—Target Normal Sheath Acceleration*, CERN Yellow Reports **1**, 231–231 (2016).

[36] J. Adam, A. Héron, and G. Laval, *Dispersion and transport of energetic particles due to the interaction of intense laser pulses with overdense plasmas*, Physical review letters **97**, 205006 (2006).

[37] A. Link, R. R. Freeman, D. Schumacher, and L. Van Woerkom, *Effects of target charging and ion emission on the energy spectrum of emitted electrons*, Physics of Plasmas **18**, 053107 (2011).

[38] J. Fuchs, P. Antici, E. d'Humières, E. Lefebvre, M. Borghesi, E. Brambrink, C. Cecchetti, M. Kaluza, V. Malka, M. Manclossi, et al., *Laser-driven proton scaling laws and new paths towards energy increase*, Nature physics **2**, 48–54 (2006).

[39] P. Mora, *Plasma expansion into a vacuum*, Physical Review Letters **90**, 185002 (2003).

[40] P. Mora, *Collisionless expansion of a Gaussian plasma into a vacuum*, Physics of plasmas **12**, 112102 (2005).

[41] P. Mora, *Thin-foil expansion into a vacuum*, Physical Review E **72**, 056401 (2005).

[42] J. Fuchs, Y. Sentoku, E. d'Humières, T. Cowan, J. Cobble, P. Audebert, A. Kemp, A. Nikroo, P. Antici, E. Brambrink, et al., *Comparative spectra and efficiencies of ions laser-accelerated forward from the front and rear surfaces of thin solid foils*, Physics of plasmas **14**, 053105 (2007).

[43] M. Allen, P. K. Patel, A. Mackinnon, D. Price, S. Wilks, and E. Morse, *Direct experimental evidence of back-surface ion acceleration from laser-irradiated gold foils*, Physical review letters **93**, 265004 (2004).

[44] A. Macchi, F. Cattani, T. V. Liseykina, and F. Cornolti, *Laser acceleration of ion bunches at the front surface of overdense plasmas*, Physical review letters **94**, 165003 (2005).

[45] Y. Sentoku, T. Cowan, A. Kemp, and H. Ruhl, *High energy proton acceleration in interaction of short laser pulse with dense plasma target*, Physics of plasmas **10**, 2009–2015 (2003).

[46] A. Robinson, D. Kwon, and K. Lancaster, *Hole-boring radiation pressure acceleration with two ion species*, Plasma Physics and Controlled Fusion **51**, 095006 (2009).

[47] A. Robinson, P. Gibbon, M. Zepf, S. Kar, R. Evans, and C. Bellei, *Relativistically correct hole-boring and ion acceleration by circularly polarized laser pulses*, Plasma Physics and Controlled Fusion **51**, 024004 (2009).

[48] B. Qiao, M. Zepf, M. Borghesi, and M. Geissler, *Stable GeV ion-beam acceleration from thin foils by circularly polarized laser pulses*, Physical review letters **102**, 145002 (2009).

[49] X. Yan, C. Lin, Z.-M. Sheng, Z. Guo, B. Liu, Y. Lu, J. Fang, J. Chen, et al., *Generating high-current monoenergetic proton beams by a circularlypolarized laser pulse in the phase-stableacceleration regime*, Physical Review Letters **100**, 135003 (2008).

[50] A. Macchi, *Theory of light sail acceleration by intense lasers: an overview*, High Power Laser Science and Engineering **2** (2014).

[51] A. Macchi, S. Veghini, T. V. Liseykina, and F. Pegoraro, *Radiation pressure acceleration of ultrathin foils*, New Journal of Physics **12**, 045013 (2010).

[52] A. Robinson, M. Zepf, S. Kar, R. Evans, and C. Bellei, *Radiation pressure acceleration of thin foils with circularly polarized laser pulses*, New journal of Physics **10**, 013021 (2008).

[53] M. Tamburini, T. Liseykina, F. Pegoraro, and A. Macchi, *Radiation-pressure-dominant acceleration: Polarization and radiation reaction effects and energy increase in three-dimensional simulations*, Physical Review E **85**, 016407 (2012).

[54] T. Esirkepov, M. Borghesi, S. Bulanov, G. Mourou, and T. Tajima, *Highly efficient relativistic-ion generation in the laser-piston regime*, Physical review letters **92**, 175003 (2004).

[55] A. Henig, S. Steinke, M. Schnürer, T. Sokollik, R. Hörlein, D. Kiefer, D. Jung, J. Schreiber, B. Hegelich, X. Yan, et al., *Radiation-pressure acceleration of ion beams driven by circularly polarized laser pulses*, Physical Review Letters **103**, 245003 (2009).

[56] S. Kar, K. Kakolee, B. Qiao, A. Macchi, M. Cerchez, D. Doria, M. Geissler, P. McKenna, D. Neely, J. Osterholz, et al., *Ion acceleration in multispecies targets driven by intense laser radiation pressure*, Physical Review Letters **109**, 185006 (2012).

[57] I. J. Kim, K. H. Pae, I. W. Choi, C.-L. Lee, H. T. Kim, H. Singhal, J. H. Sung, S. K. Lee, H. W. Lee, P. V. Nickles, et al., *Radiation pressure acceleration of protons to 93 MeV with circularly polarized petawatt laser pulses*, Physics of Plasmas **23**, 070701 (2016).

[58] L. O. Silva, M. Marti, J. R. Davies, R. A. Fonseca, C. Ren, F. S. Tsung, and W. B. Mori, *Proton shock acceleration in laser-plasma interactions*, Physical Review Letters **92**, 015002 (2004).

[59] D. Haberberger, S. Tochitsky, F. Fiuza, C. Gong, R. A. Fonseca, L. O. Silva, W. B. Mori, and C. Joshi, *Collisionless shocks in laser-produced plasma generate monoenergetic high-energy proton beams*, Nature Physics **8**, 95–99 (2012).

[60] M. Zepf, E. Clark, F. Beg, R. Clarke, A. Dangor, A. Gopal, K. Krushelnick, P. Norreys, M. Tatarakis, U. Wagner, et al., *Proton acceleration from high-intensity laser interactions with thin foil targets*, Physical review letters **90**, 064801 (2003).

[61] S. Chen, M. Vranic, T. Gangolf, E. Boella, P. Antici, M. Bailly-Grandvaux, P. Loiseau, H. Pépin, G. Revet, J. Santos, et al., *Collimated protons accelerated from an overdense gas jet irradiated by a 1 μm wavelength high-intensity short-pulse laser*, Scientific Reports **7**, 1–12 (2017).

[62] P. Antici, E. Boella, S. Chen, D. Andrews, M. Barberio, J. Böker, F. Cardelli, J. Feugeas, M. Glesser, P. Nicolaï, et al., *Acceleration of collimated 45 MeV protons by collisionless shocks driven in low-density, large-scale gradient plasmas by a 10^{20} W/cm^2, 1 μm laser*, Scientific Reports **7**, 1–9 (2017).

[63] A. Pak, S. Kerr, N. Lemos, A. Link, P. Patel, F. Albert, L. Divol, B. Pollock, D. Haberberger, D. Froula, et al., *Collisionless shock acceleration of narrow energy spread ion beams from mixed species plasmas using 1 μm lasers*, Physical Review Accelerators and Beams **21**, 103401 (2018).

[64] L. Yin, B. Albright, B. Hegelich, and J. Fernández, *GeV laser ion acceleration from ultrathin targets: The laser break-out afterburner*, Laser and Particle Beams **24**, 291–298 (2006).

[65] S. Palaniyappan, B. M. Hegelich, H.-C. Wu, D. Jung, D. C. Gautier, L. Yin, B. J. Albright, R. P. Johnson, T. Shimada, S. Letzring, et al., *Dynamics of relativistic transparency and optical shuttering in expanding overdense plasmas*, Nature Physics **8**, 763–769 (2012).

[66] X. Yan, T. Tajima, M. Hegelich, L. Yin, and D. Habs, *Theory of laser ion acceleration from a foil target of nanometer thickness*, Applied Physics B **98**, 711–721 (2010).

[67] B. Hegelich, I. Pomerantz, L. Yin, H. Wu, D. Jung, B. Albright, D. Gautier, S. Letzring, S. Palaniyappan, R. Shah, et al., *Laser-driven ion acceleration from relativistically transparent nanotargets*, New Journal of Physics **15**, 085015 (2013).

[68] P. L. Poole, L. Obst, G. E. Cochran, J. Metzkes, H.-P. Schlenvoigt, I. Prencipe, T. Kluge, T. Cowan, U. Schramm, D. W. Schumacher, et al., *Laser-driven ion acceleration via target normal sheath acceleration in the relativistic transparency regime*, New Journal of Physics **20**, 013019 (2018).

[69] D. Jung, L. Yin, D. Gautier, H.-C. Wu, S. Letzring, B. Dromey, R. Shah, S. Palaniyappan, T. Shimada, R. Johnson, et al., *Laser-driven 1 GeV carbon ions from preheated diamond targets in the break-out afterburner regime*, Physics of plasmas **20**, 083103 (2013).

[70] J. Park, S. S. Bulanov, J. Bin, Q. Ji, S. Steinke, J.-L. Vay, C. G. Geddes, C. B. Schroeder, W. P. Leemans, T. Schenkel, et al., *Ion acceleration in laser generated megatesla magnetic vortex*, Physics of Plasmas **26**, 103108 (2019).

[71] F. Merrill, D. Bower, R. Buckles, D. Clark, C. Danly, O. Drury, J. Dzenitis, V. Fatherley, D. Fittinghoff, R. Gallegos, et al., *The neutron imaging diagnostic at NIF*, Review of Scientific Instruments **83**, 10D317 (2012).

[72] D. Casey, J. Frenje, M. Gatu Johnson, F. Séguin, C. Li, R. Petrasso, V. Y. Glebov, J. Katz, J. Knauer, D. Meyerhofer, et al., *Measuring the absolute deuterium–tritium neutron yield using the magnetic recoil spectrometer at OMEGA and the NIF*, Review of Scientific Instruments **83**, 10D912 (2012).

[73] R. Lerche, V. Y. Glebov, M. Moran, J. McNaney, J. Kilkenny, M. Eckart, R. Zacharias, J. Haslam, T. Clancy, M. Yeoman, et al., *National Ignition Facility neutron time-of-flight measurements*, Review of scientific instruments **81**, 10D319 (2010).

[74] L. Disdier, J. Garconnet, G. Malka, and J. Miquel, *Fast neutron emission from a high-energy ion beam produced by a high-intensity subpicosecond laser pulse*, Physical review letters **82**, 1454 (1999).

[75] L. Willingale, G. Petrov, A. Maksimchuk, J. Davis, R. Freeman, A. Joglekar, T. Matsuoka, C. Murphy, V. Ovchinnikov, A. Thomas, et al., *Comparison of bulk and pitcher-catcher targets for laser-driven neutron production*, Physics of Plasmas **18**, 083106 (2011).

[76] L. Vassura. *Generation and characterization of short-duration and high-brightness laser-driven neutron sources*. PhD thesis, ECOLE POLYTECHNIQUE, (2015).

[77] W. Qi, X. Zhang, B. Zhang, S. He, F. Zhang, B. Cui, M. Yu, Z. Dai, X. Peng, and Y. Gu, *Enhanced photoneutron production by intense picoseconds laser interacting with gas-solid hybrid targets*, Physics of Plasmas **26**, 043103 (2019).

[78] X. Jiao, J. Shaw, T. Wang, X. Wang, H. Tsai, P. Poth, I. Pomerantz, L. Labun, T. Toncian, M. Downer, et al., *A tabletop, ultrashort pulse photoneutron source driven by electrons from laser wakefield acceleration*, Matter and Radiation at Extremes **2**, 296–302 (2017).

[79] I. Pomerantz, E. Mccary, A. R. Meadows, A. Arefiev, A. C. Bernstein, C. Chester, J. Cortez, M. E. Donovan, G. Dyer, E. W. Gaul, et al., *Ultrashort pulsed neutron source*, Physical review letters **113**, 184801 (2014).

[80] Y. Arikawa, M. Utsugi, M. Alessio, T. Nagai, Y. Abe, S. Kojima, S. Sakata, H. Inoue, S. Fujioka, Z. Zhang, et al., *High-intensity neutron generation via laser-driven photonuclear reaction*, Plasma and Fusion Research **10**, 2404003–2404003 (2015).

[81] D. A. Brown, M. Chadwick, R. Capote, A. Kahler, A. Trkov, M. Herman, A. Sonzogni, Y. Danon, A. Carlson, M. Dunn, et al., *ENDF/B-VIII. 0: The 8th major release of the nuclear reaction data library with CIELO-project cross sections, new standards and thermal scattering data"*, Nuclear Data Sheets **148**, 1–142 (2018).

[82] A. Koning, D. Rochman, J.-C. Sublet, N. Dzysiuk, M. Fleming, and S. Van der Marck, *TENDL: complete nuclear data library for innovative nuclear science and technology*, Nuclear Data Sheets **155**, 1–55 (2019).

[83] Y. Yamagata, K. Hirota, J. Ju, S. Wang, S.-y. Morita, J.-i. Kato, Y. Otake, A. Taketani, Y. Seki, M. Yamada, et al., *Development of a neutron generating target for compact neutron sources using low energy proton beams*, Journal of Radioanalytical and Nuclear Chemistry **305**, 787–794 (2015).

[84] R. Garoby, A. Vergara, H. Danared, I. Alonso, E. Bargallo, B. Cheymol, C. Darve, M. Eshraqi, H. Hassanzadegan, A. Jansson, et al., *The European spallation source design*, Physica Scripta **93**, 014001 (2017).

[85] D. Filges and F. Goldenbaum. *The Accelerator-Based Neutron Spallation Sources*. In *Handbook of Spallation Research*, pages 505–559. John Wiley & Sons, Ltd, (2009).

[86] D. Filges and F. Goldenbaum. *The Spallation Process*. In *Handbook of Spallation Research*, pages 1–61. John Wiley & Sons, Ltd, (2009).

[87] G. Rudstam, *Systematics of spallation yields*, Zeitschrift für Naturforschung A **21**, 1027–1041 (1966).

[88] J. M. Carpenter, *Pulsed spallation neutron sources for slow neutron scattering*, Nuclear Instruments and Methods **145**, 91–113 (1977).

[89] V. Hornỳ, S. N. Chen, X. Davoine, L. Gremillet, and J. Fuchs, *High-flux neutron generation by laser-accelerated ions from single-and double-layer targets*, arXiv preprint arXiv:2202.06549 (2022).

[90] M. Günther, O. Rosmej, P. Tavana, M. Gyrdymov, A. Skobliakov, A. Kantsyrev, S. Zähter, N. Borisenko, A. Pukhov, and N. Andreev, *Forward-looking insights in laser-generated ultra-intense γ-ray and neutron sources for nuclear application and science*, Nature communications **13**, 1–13 (2022).

[91] M. Günther, O. Rosmej, P. Tavana, M. Gyrdymov, A. Skobliakov, A. Kantsyrev, S. Zähter, N. Borisenko, A. Pukhov, and N. Andreev, *New insights in laser-generated ultra-intense gamma-ray and neutron sources for nuclear applications and science*, arXiv preprint arXiv:2012.10752 (2020).

[92] F. Negoita, M. Roth, P. G. Thirolf, S. Tudisco, F. Hannachi, S. Moustaizis, I. Pomerantz, P. McKenna, J. Fuchs, K. Sphor, et al., *Laser Driven Nuclear physics at ELINP*, arXiv preprint arXiv:2201.01068 (2022).

[93] A. F. Lifschitz, X. Davoine, E. Lefebvre, J. Faure, C. Rechatin, and V. Malka, *Particle-in-cell modelling of laser–plasma interaction using Fourier decomposition*, Journal of Computational Physics **228**, 1803–1814 (2009).

[94] A. Coc and E. Vangioni, *Primordial nucleosynthesis*, International Journal of Modern Physics E **26**, 1741002 (2017).

[95] B. D. Fields, *The primordial lithium problem*, Annual Review of Nuclear and Particle Science **61**, 47–68 (2011).

[96] H. Palme, K. Lodders, and A. Jones, *Solar system abundances of the elements*, Planets, Asteriods, Comets and The Solar System, Volume 2 of Treatise on Geochemistry (Second Edition). Edited by Andrew M. Davis. Elsevier, 2014., p. 15-36 **2** (2014).

[97] C. Fröhlich, G. Martinez-Pinedo, M. Liebendörfer, F.-K. Thielemann, E. Bravo, W. Hix, K. Langanke, and N. T. Zinner, *Neutrino-induced nucleosynthesis of $A>$ 64 nuclei: the ν p process*, Physical Review Letters **96**, 142502 (2006).

[98] B. J. Shappee, K. Stanek, C. S. Kochanek, and P. Garnavich, *Whimper of a bang: documenting the final days of the nearby type Ia supernova 2011fe*, The Astrophysical Journal **841**, 48 (2017).

[99] D. Maoz, F. Mannucci, and G. Nelemans, *Observational clues to the progenitors of type Ia supernovae*, Annual Review of Astronomy and Astrophysics **52**, 107–170 (2014).

[100] J. J. Cowan, F.-K. Thielemann, and J. W. Truran, *The r-process and nucleochronology*, Physics Reports **208**, 267–394 (1991).

[101] T. A. Thompson, A. Burrows, and B. S. Meyer, *The physics of proto-neutron star winds: implications for r-process nucleosynthesis*, The Astrophysical Journal **562**, 887 (2001).

[102] M. Dominik, K. Belczynski, C. Fryer, D. E. Holz, E. Berti, T. Bulik, I. Mandel, and R. O'shaughnessy, *Double compact objects. I. The significance of the common envelope on merger rates*, The Astrophysical Journal **759**, 52 (2012).

[103] K. L. Heyde. *The nuclear shell model.* In *The Nuclear Shell Model*, pages 58–154. Springer, (1994).

[104] J. Harvey, *Experimental neutron resonance spectroscopy*, Elsevier (2012).

[105] F. Graziani, M. P. Desjarlais, R. Redmer, and S. B. Trickey, *Frontiers and challenges in warm dense matter*, Springer Science & Business (2014).

[106] M. Koenig, A. Benuzzi-Mounaix, A. Ravasio, T. Vinci, N. Ozaki, S. Lepape, D. Batani, G. Huser, T. Hall, D. Hicks, et al., *Progress in the study of warm dense matter*, Plasma Physics and Controlled Fusion **47**, B441 (2005).

[107] J. Fernandez, C. Barnes, M. Mocko, and L. Zavorka. *Time and space-resolved thermometry using neutron resonance spectroscopy (NRS): Requirements and prospects for laser-driven neutron sources.* In *APS Division of Plasma Physics Meeting Abstracts*, volume 2018, pages PO8–003, (2018).

[108] S. H. Glenzer and R. Redmer, *X-ray Thomson scattering in high energy density plasmas*, Reviews of Modern Physics **81**, 1625 (2009).

[109] P. Fowler and A. Taylor. *Temperature imaging using epithermal neutrons.* In *Report of a Workshop on Neutron Resonance Radiography Held at the Los Alamos National Laboratory*, pages 46–80, (1987).

[110] H. Stone, M. Tucker, F. Meducin, M. Dove, S. Redfern, Y. Le Godec, and W. Marshall, *Temperature measurement in a Paris-Edinburgh cell by neutron resonance spectroscopy*, Journal of Applied Physics **98**, 064905 (2005).

[111] V. Yuan, J. D. Bowman, D. Funk, G. Morgan, R. Rabie, C. Ragan, J. Quintana, and H. Stacy, *Shock temperature measurement using neutron resonance spectroscopy*, Physical review letters **94**, 125504 (2005).

[112] D. Higginson, J. McNaney, D. Swift, T. Bartal, D. Hey, R. Kodama, S. Le Pape, A. Mackinnon, D. Mariscal, H. Nakamura, et al., *Laser generated neutron source for neutron resonance spectroscopy*, Physics of plasmas **17**, 100701 (2010).

[113] J. C. Fernández, C. W. Barnes, M. J. Mocko, and L. Zavorka, *Requirements and sensitivity analysis for temporally-and spatially-resolved thermometry using neutron resonance spectroscopy*, Review of Scientific Instruments **90**, 094901 (2019).

[114] D. C. Swift and J. M. McNaney, *Comment on "Requirements and sensitivity analysis for temporally-and spatially-resolved thermometry using neutron resonance spectroscopy"[Rev. Sci. Instrum. 90, 094901 (2019)]*, Review of Scientific Instruments **92**, 037101 (2021).

[115] K. Nedunchezhian, N. Aswath, M. Thiruppathy, and S. Thirugnanamurthy, *Boron neutron capture therapy-a literature review*, Journal of clinical and diagnostic research: JCDR **10**, ZE01 (2016).

[116] J. A. Coderre and G. M. Morris, *The radiation biology of boron neutron capture therapy*, Radiation research **151**, 1–18 (1999).

[117] B. Bayanov, V. Belov, E. Bender, M. Bokhovko, G. Dimov, V. Kononov, O. Kononov, N. Kuksanov, V. Palchikov, V. Pivovarov, et al., *Accelerator-based neutron source for the neutron-capture and fast neutron therapy at hospital*, Nuclear Instruments and Methods in Physics Research Section A: Accelerators, Spectrometers, Detectors and Associated Equipment **413**, 397–426 (1998).

[118] V. Valkovic. *CHAPTER 5 - Measurements of Radioactivity*. In *Radioactivity in the environment: physicochemical aspects and applications*, pages 117–258. Elsevier, (2000).

[119] S. N. Ahmed. *Gas-filled detectors*. In *Physics and engineering of radiation detection (Second Edition)*, pages 157–231. Academic Press, (2015).

[120] M. Arai. *Experimental techniques*. In *Experimental Methods in the Physical Sciences*, volume 44, pages 245–320. Elsevier, (2013).

[121] T. Crane and M. Baker, *Neutron detectors*, Passive Nondestructive Assay of Nuclear Materials **13**, 1–28 (1991).

[122] R. Pringle, L. D. Black, B. Funt, and S. Sobering, *A new quenching effect in liquid scintillators*, Physical Review **92**, 1582 (1953).

[123] S. Moser, W. Harder, C. Hurlbut, and M. Kusner, *Principles and practice of plastic scintillator design*, Radiation Physics and Chemistry **41**, 31–36 (1993).

[124] E. Garwin and A. Roder, *EMISSION SPECTRA OF PLASTIC SCINTILLATORS*, (1971).

[125] E. Technology, *Boron loaded plastic scintillator EJ-254*, https://eljentechnology.com/images/products/data_sheets/EJ-254.pdf (2022).

[126] NNDC, *NuDat 3*, https://www.nndc.bnl.gov/nudat3/ (2022).

[127] J. P. Biersack and L. Haggmark, *A Monte Carlo computer program for the transport of energetic ions in amorphous targets*, Nuclear instruments and methods **174**, 257–269 (1980).

[128] J. B. Birks, *Scintillations from organic crystals: specific fluorescence and relative response to different radiations*, Proceedings of the Physical Society. Section A **64**, 874 (1951).

[129] J. Allison, K. Amako, J. Apostolakis, H. Araujo, P. A. Dubois, M. Asai, G. Barrand, R. Capra, S. Chauvie, R. Chytracek, et al., *Geant4 developments and applications*, IEEE Transactions on nuclear science **53**, 270–278 (2006).

[130] J. Allison, K. Amako, J. Apostolakis, P. Arce, M. Asai, T. Aso, E. Bagli, A. Bagulya, S. Banerjee, G. Barrand, et al., *Recent developments in Geant4*, Nuclear Instruments and Methods in Physics Research Section A: Accelerators, Spectrometers, Detectors and Associated Equipment **835**, 186–225 (2016).

[131] J. Tain, J. Agramunt Ros, A. Algora, and A. E. Tarifeño Saldivia, *The BRIKEN Project: extensive measurements of ß-delayed neutron emitters for the astrophysical r process*, Acta physica polonica B **49**, 417–428 (2018).

[132] A. Tarifeño-Saldivia, J. Tain, C. Domingo-Pardo, F. Calviño, G. Cortés, V. Phong, A. Riego, J. Agramunt, A. Algora, N. Brewer, et al., *Conceptual design of a hybrid neutron-gamma detector for study of β-delayed neutrons at the RIB facility of RIKEN*, Journal of instrumentation **12**, P04006 (2017).

[133] A. Tolosa-Delgado, J. Agramunt, J. L. Taín, A. Algora, C. Domingo-Pardo, A. I. Morales, B. Rubio, A. Tarifeño-Saldivia, F. Calviño, G. Cortes, et al., *Commissioning of the BRIKEN detector for the measurement of very exotic β-delayed neutron emitters*, Nuclear Instruments and Methods in Physics Research Section A: Accelerators, Spectrometers, Detectors and Associated Equipment **925**, 133–147 (2019).

[134] S. Nutter, Y. Amare, T. Anderson, D. Angelaszek, N. Anthony, G. Choi, M. Copley, S. Coutu, L. Derome, L. Eraud, et al., *Measurement of delayed fluorescence in plastic scintillator from 1 to 10 μs*, Nuclear Instruments and Methods in Physics Research Section A: Accelerators, Spectrometers, Detectors and Associated Equipment **942**, 162368 (2019).

[135] Y. Amare, T. Anderson, D. Angelaszek, N. Anthony, K. Cheryian, G. Choi, M. Copley, S. Coutu, L. Derome, L. Eraud, et al., *The boronated scintillator detector of the ISS-CREAM experiment*, Nuclear Instruments and Methods in Physics Research Section A: Accelerators, Spectrometers, Detectors and Associated Equipment **943**, 162413 (2019).

[136] M. Berge, J. Hubbell, S. Seltzer, J. Chang, J. Coursey, R. Sukumar, D. Zucker, and K. Olsen. *XCOM: Photon Cross Sections Database (NIST Standard Reference Database 8 (XGAM))*.

[137] L. Swiderski, M. Moszyński, W. Czarnacki, J. Iwanowska, A. Syntfeld-Każuch, T. Szczęśniak, G. Pausch, C. Plettner, and K. Roemer, *Measurement of Compton edge position in low-Z scintillators*, Radiation measurements **45**, 605–607 (2010).

[138] P.-A. Söderström, C. Matei, L. Capponi, E. Açıksöz, D. Balabanski, and I.-O. Mitu, *Characterization of a plutonium–beryllium neutron source*, Applied Radiation and Isotopes **167**, 109441 (2021).

[139] J. Vyskočil, O. Klimo, and S. Weber, *Simulations of bremsstrahlung emission in ultra-intense laser interactions with foil targets*, Plasma Physics and Controlled Fusion **60**, 054013 (2018).

[140] J. Vyskočil, E. Gelfer, and O. Klimo, *Inverse Compton scattering from solid targets irradiated by ultra-short laser pulses in the* 10^{22}*–*10^{23} W/cm^2 *regime*, Plasma Physics and Controlled Fusion **62**, 064002 (2020).

[141] B. Martinez, E. d'Humières, and L. Gremillet, *Synchrotron radiation from ultrahigh-intensity laser-plasma interactions and competition with bremsstrahlung in thin foil targets*, Physical Review Research **2**, 043341 (2020).

[142] J.-L. Dubois, F. Lubrano-Lavaderci, D. Raffestin, J. Ribolzi, J. Gazave, A. C. La Fontaine, E. d'Humières, S. Hulin, P. Nicolaï, A. Poyé, et al., *Target charging in short-pulse-laser–plasma experiments*, Physical Review E **89**, 013102 (2014).

[143] A. Poyé, S. Hulin, M. Bailly-Grandvaux, J.-L. Dubois, J. Ribolzi, D. Raffestin, M. Bardon, F. Lubrano-Lavaderci, E. D'Humières, J. J. Santos, et al., *Physics of giant electromagnetic pulse generation in short-pulse laser experiments*, Physical Review E **91**, 043106 (2015).

[144] C. Brown Jr, E. Bond, T. Clancy, S. Dangi, D. Eder, W. Ferguson, J. Kimbrough, and A. Throop, *Assessment and mitigation of electromagnetic pulse (EMP) impacts at short-pulse laser facilities*, Journal of Physics: Conference Series **244**, 032001 (2010).

[145] M. Cerchez, R. Prasad, B. Aurand, A. Giesecke, S. Spickermann, S. Brauckmann, E. Aktan, M. Swantusch, M. Toncian, T. Toncian, et al., *ARCTURUS laser: a versatile high-contrast, high-power multi-beam laser system*, High Power Laser Science and Engineering **7** (2019).

[146] J. Ehlert, M. Piel, F. Boege, M. Cerchez, R. Haas, G. Iliakis, R. Prasad, O. Willi, and C. Monzel, *An experimental platform for studying the radiation effects of laser accelerated protons on mammalian cells*, AIP Advances **11**, 065208 (2021).

[147] M. Janecek, *Reflectivity spectra for commonly used reflectors*, IEEE Transactions on Nuclear Science **59**, 490–497 (2012).

[148] CAEN, *User Manual UM5960 CoMPASS Rev. 12*, (2020).

[149] F. Barker, *Electron screening in reactions between light nuclei*, Nuclear Physics A **707**, 277–300 (2002).

[150] C. Spitaleri, C. Bertulani, L. Fortunato, and A. Vitturi, *The electron screening puzzle and nuclear clustering*, Physics Letters B **755**, 275–278 (2016).

[151] C. Casella, H. Costantini, A. Lemut, B. Limata, R. Bonetti, C. Broggini, L. Campajola, P. Corvisiero, J. Cruz, A. D'Onofrio, et al., *First measurement of the d (p, γ) 3He cross section down to the solar Gamow peak*, Nuclear Physics A **706**, 203–216 (2002).

[152] C. Rolfs and E. Somorjai, *Status report on electron screening*, Nuclear Instruments and Methods in Physics Research Section B: Beam Interactions with Materials and Atoms **99**, 297–300 (1995).

[153] H. Assenbaum, K. Langanke, and C. Rolfs, *Effects of electron screening on low-energy fusion cross sections*, Zeitschrift für Physik A Atomic Nuclei **327**, 461–468 (1987).

[154] E. Salpeter, *Electron screening and thermonuclear reactions*, Australian Journal of Physics **7**, 373–388 (1954).

[155] A. Cvetinović, J. Gajević, A. Likar, M. Lipoglavšek, P. Pelicon, T. Petrovič, and A. S. Ortiz. *Electron screening effect in (p, n) and (p, γ) reactions*. In *AIP Conference Proceedings*, volume 1595, pages 238–241. American Institute of Physics, (2014).

[156] P. Prati, C. Arpesella, F. Bartolucci, H. Becker, E. Bellotti, C. Broggini, P. Corvisiero, G. Fiorentini, A. Fubini, G. Gervino, et al., *Electron screening in thed+ 3He fusion reaction*, Zeitschrift für Physik A Hadrons and Nuclei **350**, 171–176 (1994).

[157] S. Engstler, A. Krauss, K. Neldner, C. Rolfs, U. Schröder, and K. Langanke, *Effects of electron screening on the 3He (d, p) 4He low-energy cross sections*, Physics Letters B **202**, 179–184 (1988).

[158] V. Bystritsky, V. Bystritskii, G. Dudkin, M. Filipowicz, S. Gazi, J. Huran, A. Kobzev, G. Mesyats, B. Nechaev, V. Padalko, et al., *Measurement of astrophysical S factors and electron screening potentials for d (d, n) 3He reaction In ZrD2, TiD2, D2O, and CD2 targets in the ultralow energy region using plasma accelerators*, Physics of Atomic Nuclei **75**, 53–62 (2012).

[159] V. Bystritsky, V. Bystritsky, G. Dudkin, M. Filipowicz, S. Gazi, J. Huran, B. Nechaev, V. Padalko, S. Parzhitskii, F. Pen'kov, et al., *Experimental observation of electron screening for the D (p, γ) 3He nuclear reaction in titanium Deuteride TiD*, Physics of Particles and Nuclei Letters **11**, 467–472 (2014).

[160] C. Spitaleri, A. Mukhamedzhanov, L. Blokhintsev, M. L. Cognata, R. Pizzone, and A. Tumino, *The Trojan horse method in nuclear astrophysics*, Physics of Atomic Nuclei **74**, 1725–1739 (2011).

[161] M. Aliotta, C. Spitaleri, M. Lattuada, A. Musumarra, R. Pizzone, A. Tumino, C. Rolfs, and F. Strieder, *Improved information on electron screening in 7Li* (p, α) α *using the Trojan-horse method*, The European Physical Journal A-Hadrons and Nuclei **9**, 435–437 (2000).

[162] S. Romano, L. Lamia, C. Spitaleri, C. Li, S. Cherubini, M. Gulino, M. La Cognata, R. Pizzone, and A. Tumino, *Study of the 9Be* (p, α) *6Li reaction via the Trojan Horse Method*, The European Physical Journal A-Hadrons and Nuclei **27**, 221–225 (2006).

[163] K. Kettner, H. Becker, F. Strieder, and C. Rolfs, *High-Z electron screening: the cases 50V* (p, n) *50Cr and 176Lu* (p, n) *176Hf*, Journal of Physics G: Nuclear and Particle Physics **32**, 489 (2006).

[164] K. Krushelnick, E. Clark, Z. Najmudin, M. Salvati, M. Santala, M. Tatarakis, A. Dangor, V. Malka, D. Neely, R. Allott, et al., *Multi-MeV ion production from high-intensity laser interactions with underdense plasmas*, Physical Review Letters **83**, 737 (1999).

[165] M. Almassarani, S. Meng, B. Beleites, F. Ronneberger, G. G. Paulus, and A. Gopal, *Parametric Study of Proton Acceleration from Laser-Thin Foil Interaction*, Plasma **4**, 670–680 (2021).

[166] P. Bolton, M. Borghesi, C. Brenner, D. Carroll, C. De Martinis, F. Fiorini, A. Flacco, V. Floquet, J. Fuchs, P. Gallegos, et al., *Instrumentation for diagnostics and control of laser-accelerated proton* (*ion*) *beams*, Physica Medica **30**, 255–270 (2014).

[167] J. Geindre, P. Audebert, A. Rousse, J. Gauthier, A. Y. Faenov, T. Pikuz, S. Pikuz, and T. Shelkovenko, *FSSR mica spherical crystal spectrometer with CCD detector for high-resolution x-ray spectroscopy of femtosecond laser produced plasma*, Physica Scripta **53**, 645 (1996).

[168] A. Meadowcroft, C. Bentley, and E. Stott, *Evaluation of the sensitivity and fading characteristics of an image plate system for x-ray diagnostics*, Review of scientific instruments **79**, 113102 (2008).

[169] T. Bonnet, M. Comet, D. Denis-Petit, F. Gobet, F. Hannachi, M. Tarisien, M. Versteegen, and M. Aleonard, *Response functions of Fuji imaging plates to monoenergetic protons in the energy range 0.6–3.2 MeV*, Review of Scientific Instruments **84**, 013508 (2013).

[170] P. McKenna, K. Ledingham, J. Yang, L. Robson, T. McCanny, S. Shimizu, R. Clarke, D. Neely, K. Spohr, R. Chapman, et al., *Characterization of proton and heavier ion acceleration in ultrahigh-intensity laser interactions with heated target foils*, Physical Review E **70**, 036405 (2004).

[171] S. Bolanos, R. Smets, S. Chen, A. Grisolet, E. Filippov, J. Henares, V. Nastasa, S. Pikuz, R. Riquier, M. Safranova, et al., *Laboratory evidence of the halting of magnetic reconnection by a weak guide field*, arXiv preprint arXiv:1909.01684 (2019).

[172] R. Ramis, R. Schmalz, and J. Meyer-ter Vehn, *MULTI—A computer code for one-dimensional multi-group radiation hydrodynamics*, Computer Physics Communications **49**, 475–505 (1988).

[173] A. Cvetinović and M. Lipoglavšek. *Electron screening in Titanium*. In *Journal of Physics: Conference Series*, volume 1668, page 012010. IOP Publishing, (2020).

[174] G. Hogan, K. Adams, K. Alrick, J. Amann, J. Boissevain, M. Crow, S. Cushing, J. Eddelman, C. Espinoza, T. Fife, et al. *Proton radiography*. In *Proceedings of the 1999 Particle Accelerator Conference (Cat. No. 99CH36366)*, volume 1, pages 579–583. IEEE, (1999).

[175] D. Doria, S. Kar, H. Ahmed, A. Alejo, J. Fernandez, M. Cerchez, R. Gray, F. Hanton, D. MacLellan, P. McKenna, et al., *Calibration of BAS-TR image plate response to high energy (3-300 MeV) carbon ions*, Review of Scientific Instruments **86**, 123302 (2015).

[176] V. Lelasseux and J. Fuchs, *Modelling energy deposition in TR image plate detectors for various ion types*, Journal of Instrumentation **15**, P04002 (2020).

[177] J. Strehlow, P. Forestier-Colleoni, C. McGuffey, M. Bailly-Grandvaux, T. Daykin, E. McCary, J. Peebles, G. Revet, S. Zhang, T. Ditmire, et al., *The response function of Fujifilm BAS-TR imaging plates to laser-accelerated titanium ions*, Review of Scientific Instruments **90**, 083302 (2019).

[178] S. Kojima, T. Miyatake, S. Inoue, T. H. Dinh, N. Hasegawa, M. Mori, H. Sakaki, M. Nishiuchi, N. P. Dover, Y. Yamamoto, et al., *Absolute response of a Fuji BAS-TR imaging plate to low-energy protons ($<$ 0.2 MeV) and carbon ions ($<$ 1 MeV)*, Review of Scientific Instruments **92**, 033306 (2021).

[179] T. Bonnet, M. Comet, D. Denis-Petit, F. Gobet, F. Hannachi, M. Tarisien, M. Versteegen, and M. Aléonard, *Response functions of imaging plates to photons, electrons and 4He particles*, Review of Scientific Instruments **84**, 103510 (2013).

[180] M. Nishiuchi, H. Sakaki, N. Dover, T. Miyahara, K. Shiokawa, S. Manabe, T. Miyatake, K. Kondo, K. Kondo, Y. Iwata, et al., *Ion species discrimination method by linear energy transfer measurement in Fujifilm BAS-SR imaging plate*, Review of Scientific Instruments **91**, 093305 (2020).

[181] A. Mančić, J. Fuchs, P. Antici, S. Gaillard, and P. Audebert, *Absolute calibration of photostimulable image plate detectors used as (0.5–20 MeV) high-energy proton detectors*, Review of Scientific Instruments **79**, 073301 (2008).

[182] P. Martin, H. Ahmed, D. Doria, A. Alejo, R. Clarke, S. Ferguson, J. Fernández-Tobias, R. Freeman, J. Fuchs, A. Green, et al., *Absolute calibration of Fujifilm BAS-TR image plate response to laser driven protons up to 40 MeV*, Review of Scientific Instruments **93**, 053303 (2022).

[183] C. Freeman, G. Fiksel, C. Stoeckl, N. Sinenian, M. Canfield, G. Graeper, A. Lombardo, C. Stillman, S. Padalino, C. Mileham, et al., *Calibration of a Thomson parabola ion spectrometer and Fujifilm imaging plate detectors for protons, deuterons, and alpha particles*, Review of Scientific Instruments **82**, 073301 (2011).

[184] N. Rabhi, D. Batani, G. Boutoux, J.-E. Ducret, K. Jakubowska, I. Lantuejoul-Thfoin, C. Nauraye, A. Patriarca, A. Saïd, A. Semsoum, et al., *Calibration of imaging plate detectors to mono-energetic protons in the range 1-200 MeV*, Review of Scientific Instruments **88**, 113301 (2017).

[185] Y. Ralchenko, A. Kramida, J. Reader, et al., *NIST atomic spectra database*, NIST Standard Reference Database (2006).

[186] M. Lipoglavsek and A. Cvetinović. *Electron Screening in Nuclear Astrophysics*. In *EPJ Web of Conferences*, volume 227, page 01012. EDP Sciences, (2020).

[187] D. Papadopoulos, J. Zou, C. Le Blanc, G. Chériaux, P. Georges, F. Druon, G. Mennerat, P. Ramirez, L. Martin, A. Fréneaux, et al., *The Apollon 10 PW laser: experimental and theoretical investigation of the temporal characteristics*, High Power Laser Science and Engineering **4** (2016).

[188] K. Burdonov, A. Fazzini, V. Lelasseux, J. Albrecht, P. Antici, Y. Ayoul, A. Beluze, D. Cavanna, T. Ceccotti, M. Chabanis, et al., *Characterization and performance of the Apollon Short-Focal-Area facility following its commissioning at 1 PW level*, Matter and Radiation at Extremes **6**, 064402 (2021).

[189] A. Do, M. Briat, S. Baton, M. Krumrey, L. Lecherbourg, B. Loupias, F. Pérez, P. Renaudin, C. Rubbelynck, and P. Troussel, *Two-channel high-resolution quasi-monochromatic X-ray imager for Al and Ti plasma*, Review of Scientific Instruments **89**, 113702 (2018).

[190] P. Renaudin, L. Duthoit, S. Baton, C. Blancard, A. Chaleil, P. Cossé, G. Faussurier, L. Gremillet, L. Lecherbourg, B. Loupias, et al. *Radiative cooling of an Al plasma in an AlTi mixture heated by an ultraintense laser pulse*. In *High Energy Density Physics*, (2019).

[191] S. Kahaly, S. Monchocé, H. Vincenti, T. Dzelzainis, B. Dromey, M. Zepf, P. Martin, and F. Quéré, *Direct observation of density-gradient effects in harmonic generation from plasma mirrors*, Physical review letters **110**, 175001 (2013).

[192] L. Chopineau, A. Leblanc, G. Blaclard, A. Denoeud, M. Thévenet, J. Vay, G. Bonnaud, P. Martin, H. Vincenti, and F. Quéré, *Identification of coupling mechanisms between ultraintense laser light and dense plasmas*, Physical Review X **9**, 011050 (2019).

[193] A. Debayle, J. Sanz, and L. Gremillet, *Self-consistent theory of high-order harmonic generation by relativistic plasma mirror*, Physical Review E **92**, 053108 (2015).

[194] H. Popescu, S. Baton, F. Amiranoff, C. Rousseaux, M. R. Le Gloahec, J. Santos, L. Gremillet, M. Koenig, E. Martinolli, T. Hall, et al., *Subfemtosecond, coherent, relativistic, and ballistic electron bunches generated at ω 0 and 2 ω 0 in high intensity laser-matter interaction*, Physics of Plasmas **12**, 063106 (2005).

[195] C. B. Schroeder, E. Esarey, J. van Tilborg, and W. P. Leemans, *Theory of coherent transition radiation generated at a plasma-vacuum interface*, Physical Review E **69**, 016501 (2004).

[196] M. G. Johnson, J. Frenje, D. Casey, C. Li, F. Séguin, R. Petrasso, R. Ashabranner, R. Bionta, D. Bleuel, E. Bond, et al., *Neutron spectrometry—An essential tool for diagnosing implosions at the National Ignition Facility*, Review of Scientific Instruments **83**, 10D308 (2012).

[197] S. Mirfayzi, S. Kar, H. Ahmed, A. Krygier, A. Green, A. Alejo, R. Clarke, R. Freeman, J. Fuchs, D. Jung, et al., *Calibration of time of flight detectors using laser-driven neutron source*, Review of Scientific Instruments **86**, 073308 (2015).

[198] O. Mannion, J. Knauer, V. Y. Glebov, C. Forrest, A. Liu, Z. Mohamed, M. Romanofsky, T. Sangster, C. Stoeckl, and S. Regan, *A suite of neutron time-of-flight detectors to measure hot-spot motion in direct-drive inertial confinement fusion experiments on omega*, Nuclear Instruments and Methods in Physics Research Section A: Accelerators, Spectrometers, Detectors and Associated Equipment **964**, 163774 (2020).

[199] Z. Chen, X. Zhang, Y. Pu, J. Yan, T. Huang, W. Jiang, B. Yu, B. Chen, Q. Tang, Z. Song, et al., *Ion temperature measurements of indirect-drive implosions with the neutron time-of-flight detector on SG-III laser facility*, Review of Scientific Instruments **89**, 023504 (2018).

[200] W. Hong, S. He, J. Teng, Z. Deng, Z. Zhang, F. Lu, B. Zhang, B. Zhu, Z. Dai, B. Cui, et al., *Commissioning experiment of the high-contrast SILEX-II multi-petawatt laser facility*, Matter and Radiation at Extremes **6**, 064401 (2021).

[201] I. Pomerantz, J. Blakeney, G. Dyer, L. Fuller, E. Gaul, D. Gautier, D. Jung, A. Meadows, R. Shah, C. Wang, et al. *Laser-ion acceleration from transparent overdense plasmas at the Texas Petawatt*. In

Laser Acceleration of Electrons, Protons, and Ions II; and Medical Applications of Laser-Generated Beams of Particles II; and Harnessing Relativistic Plasma Waves III, volume 8779, pages 237–242. SPIE, (2013).

[202] M. F. L'Annunziata, *Nuclear radiation, its interaction with matter and radioisotope decay*, Handbook of Radioactivity Analysis , 1–122 (2003).

[203] G. Gabella, B. L. Goldblum, T. A. Laplace, J. J. Manfredi, J. Gordon, Z. W. Sweger, and E. Bourret, *Neutron response of the EJ-254 boron-loaded plastic scintillator*, IEEE Transactions on Nuclear Science **68**, 46–53 (2020).

[204] P. L. Feng and G. A. Chandler. *Low-Afterglow Scintillators for High-Rate Radiation Detection*. Technical report, Sandia National Lab.(SNL-CA), Livermore, CA (United States), (2015).

[205] J. Zhu, M. Fang, J. Wang, and Z. Wei, *Timing window and optimization for position resolution and energy calibration of scintillation detector*, Proceeding of IBIC, Barcelona, Spain , 11–15 (2016).

[206] A. Duraj, *Active voltage divider for detector*, United States Patent Application Publication , US2010/0288933A1 (2010).

ECOLE DOCTORALE

Titre : Détection de flux neutronique intense en vue d'applications d'astrophysique nucléaire

Mots clés : Laser haute intensité, détection neutron, astrophysique nucléaire

Résumé : Avec l'avènement de lasers multi-PW, il devient possible de générer des faisceaux de particules avec des intensités jamais atteintes jusqu'à présent. En effet, avec des intensités laser aussi importantes, les interactions laser-matière permettent de produire des faisceaux de protons dont l'énergie peut atteindre des dizaines voire des centaines de MeV dans les années qui viennent. Ces faisceaux de protons peuvent alors directement être utilisés à des fins scientifiques, ou une fraction de ceux-ci peut être transformée en faisceau de neutrons en utilisant un convertisseur adéquat. Avec de telles énergies, un proton peut être absorbé par un noyau lourd et produire plusieurs neutrons de plus basse énergie à travers un processus appelé spallation.

Un tel faisceau de neutron pourrait être utilisé pour étudier un processus de nucléosynthèse qui a lieu uniquement avec des flux neutroniques extrêmement importants, le processus r. Ce processus ne peut avoir lieu que lors d'évènements cataclysmiques tels que des supernovæ ou des fusions d'étoiles à neutrons et est vu comme le responsable principal de la création des noyaux les plus lourds. Étudier expérimentalement ce processus est de nos jours extrêmement compliqué de par les flux neutroniques à atteindre mais les faisceaux de neutrons générés par laser pourraient être un début de réponse à ce problème. D'autres applications telles que la neutronthérapie ou la spectroscopie par résonance neutronique pourrait bénéficier de cette nouvelle source.

Mais pour utiliser un tel faisceau de neutron, il est d'abord nécessaire de le caractériser. Dans cette thèse, nous présenterons le développement d'un détecteur de neutrons adapté aux environnements de laser de haute intensité. Ce développement inclut l'essai de prototype, des simulations à l'aide de Geant4 ainsi que la calibration de l'instrument à l'aide de sources de gammas et de neutrons.

Nous présenterons également les résultats obtenus lors de deux campagnes expérimentales utilisant deux versions du détecteur que nous avons développé. Une campagne a eu lieu sur l'installation LULI200 (Palaiseau, France) et utilisait une version haute efficacité du détecteur pour étudier l'influence de l'état du plasma/solide sur des réactions nucléaires. La seconde campagne était celle de la mise en service de l'installation APOLLON (Saint-Aubin, France). Une version temps de vol neutronique du détecteur a alors été utilisée dans la perspective de mesurer à la fois le spectre énergétique et l'intensité des premiers faisceaux de neutrons générés sur l'installation.

Title : Detection of laser-driven high-flux neutrons in view of nuclear astrophysical applications

Keywords : High-intensity laser, neutron detection, nuclear astrophysics

Abstract : With the advent of multi-PW lasers, it becomes possible to create particle beams with intensity never reached before. Indeed, at such high laser intensity, laser-matter interaction allows to produce proton beams with energy as high as several tens of MeV, maybe hundreds of MeV in the next years. Such proton beam can then either be used directly for scientific purposes or a part of it can be converted into a neutron beam using the right kind of converter. With such high energy protons, through a process called spallation, a proton can be absorbed by a heavy nucleus and produced several neutrons with lower energy.

Such a neutron beam could be used to investigate a nucleosynthesis process only happening with tremendous neutron flux, the r-process. This process only happens during cataclysmic events like supernovae or neutron stars collisions. It is seen as the main responsible of the synthesis of the heaviest nuclei. Investigating experimentally this process is nowadays very difficult due to the high neutron flux at play but laser-driven neutron beam could be a way to address this problem. Other applications such as neutron therapy or neutron resonance spectroscopy could benefit from this new source.

To use such a neutron beam, one need at first to characterize it. In this thesis we will present the development of a neutron detector adapted to the high intensity laser environment. This development includes prototype testing, Geant4 simulations and the calibration of the instrument using gamma and neutron sources.

We will also present the results obtained from two campaigns using different versions of the detector we developed. One campaign took place at the LULI2000 (Palaiseau, France) facility and used a high efficiency design to investigate solid/plasma effect on nuclear reaction. The second campaign was the commissioning of the APOLLON facility (Saint-Aubin, France). A neutron time-of-flight version of the detector was used in order to measure both the energy spectrum and the intensity of the first neutron beam generated in this facility.

Institut Polytechnique de Paris
91120 Palaiseau, France